



KATHOLIEKE UNIVERSITEIT LEUVEN
FACULTEIT INGENIEURSWETENSCHAPPEN
DEPARTEMENT ELEKTROTECHNIEK
AFDELING ESAT – DIVISIE INSYS
Kasteelpark Arenberg 10, B-3001 Leuven, België

Metamorphic InGaP/InGaAs multijunction solar cells on germanium substrates

Promotoren:
Prof. Dr. G. Borghs
Prof. Dr. ir. R. Mertens

Proefschrift tot het behalen
van de graad doctor in de
ingenieurswetenschappen

door

Yves MOLS

Oktober 2008

In samenwerking met



imec vzw

Interuniversitair Micro-Elektronica Centrum vzw
Kapeldreef 75
B-3001 Leuven
België



KATHOLIEKE UNIVERSITEIT LEUVEN
FACULTEIT INGENIEURSWETENSCHAPPEN
DEPARTEMENT ELEKTROTECHNIEK
AFDELING ESAT – DIVISIE INSYS
Kasteelpark Arenberg 10, B-3001 Leuven, België

Metamorphic InGaP/InGaAs multijunction solar cells on germanium substrates

Jury:
Prof. Dr. ir. Yves Willems, voorzitter
Prof. Dr. G. Borghs, promotor
Prof. Dr. ir. R. Mertens, promotor
Prof. Dr. ir. J. Poortmans
Prof. Dr. G. Adriaenssens
Prof. Dr. ir. O. Van der Biest
Prof. Dr. ir. P. Heremans, secretaris
Dr. M.R. Leys (imec)
Dr. N. Mason (University of Oxford)

Proefschrift tot het behalen
van de graad doctor in de
ingenieurswetenschappen

door

Yves MOLS

UDC: 621.382

Oktober 2008

In samenwerking met



imec vzw

Interuniversitair Micro-Elektronica Centrum vzw
Kapeldreef 75
B-3001 Leuven
België

© 2008 Katholieke Universiteit Leuven – Faculteit Toegepaste Wetenschappen
Kasteelpark Arenberg 1, B-3001 Heverlee (België)

Alle rechten voorbehouden. Niets uit deze uitgave mag worden vermenigvuldigd en/of openbaar gemaakt worden door middel van druk, fotokopie, microfilm, elektronisch of op welke wijze dan ook zonder voorafgaande schriftelijke toestemming van de uitgever.

All rights reserved. No part of the publication may be reproduced in any form by print, photo print, microfilm or any other means without written permission from the publisher.

Wettelijk depot
D/2008/7515/99

ISBN 978-90-5682-989-6

Voorwoord

Er was eens... nee, toch maar niet. Het begon allemaal in Gent, bij Intec, tijdens mijn eindwerk met de gedachte “met dat ‘coole MOCVD-machien’ wil ik wel leren werken”. Na een eerste jaar ben ik dan ook MOCVD-3, dat naar Imec (Heverlee) verhuisde, gevolgd. Bovendien was er nog een nobel onderwerp als zonnecellen beschikbaar. In eerste instantie draaide het vooral om ruimtetoepassingen, maar tijdens het doctoraat ging de balans meer overhellen naar aardse toepassingen vanwege de verhoogde interesse wereldwijd in energie uit zonlicht d.m.v. concentratorzonnecellen.

Voor het beschikbaar stellen van de infrastructuur wil ik graag Staf Borghs bedanken. Verder wil ik mijn promotoren Staf Borghs en Robert Mertens bedanken die me de mogelijkheid gaven een doctoraat op Imec aan te vatten. Ook niet te vergeten zijn Ingrid Moerman (begeleiding) en Paul Lagasse (infrastructuur) tijdens dat eerste jaartje Gent. Natuurlijk hoort hier ook het Instituut voor de aanmoediging van Innovatie door Wetenschap en Technologie in Vlaanderen (IWT) thuis voor haar financiële steun. De leden van de jury dank ik voor de tijd die ze namen om mijn thesis door te nemen en voor de suggesties die ze deden voor het verbeteren van de tekst.

Ook al was het Intec-jaar vlug voorbij, er zijn veel namen blijven hangen die een bedankje verdienen. Joff (nu ook op Imec), die mij met MOCVD-3 leerde werken en de andere groeiers, op den één Koen, op den drie Mark, Modak en Kristof (Umicore) en op den twee Mister Yu. Verder zijn daar nog Hendrik, Ilse C, Thierry – een tussenschot was nodig om een literatuurlawine van zijn bureau (één van zijn vele) naar het mijne te voorkomen – Steven VP, Steven V, Liesbet, Kristien, Luc, Marc, Bjorn, Hannes en nog andere OCS'ers. Natuurlijk mogen onze administratieve medewerksters, met name Ilse VR, Karien, Ilse M, Isabelle en Bernadette, niet in de lijst ontbreken. Het is altijd een plezier sommigen onder jullie weer te zien tijdens de Gentse Feesten (bijna traditie).

Op Imec heb ik uren doorgebracht in het MOCVD-lab. Dank aan Maarten, Joff, Steven B, Kai, Stefan, Bram, Guy en Daniel om het groeien aangenamer te maken. Verder is er Wim van de gasdetectie die ook altijd bereid was tot een leuk gesprek. Wat gegroeid wordt moet ook geprocesst worden. Dank daarvoor aan de cleanroomcrew (Eddy, Erwin, Stijn, Peter, Patrick L, Johan F, e.a.) voor advies, gesprekken en processtappen die ik niet zelf deed en aan de mensen die analyses voor me uitvoerden.

Een algemeen dankwoordje voor alle collega's van NEXT35 en Solo. Vele leuke momenten heb ik beleefd in de cubicles. Een eerste cubicle was met Giovanni, Kris en Patrick DS. Na een kortstondig verblijf in Imec-4 kwam ik in een nieuwe terecht met Niels, Johan en Eddy waar het ook altijd lachen geblazen was. Nadien kwamen Lu en Jan (thesisstudent) in Eddy's plaats. Bedankt voor alle interessante gesprekken, zowel werkgerelateerd als privé. En uiteraard, het potje Worms af en toe is altijd een hilarisch moment. En occasioneel mocht er ook eens geknald worden.

Een speciaal bedankje gaat nog naar Giovanni en Maarten voor het proeflezen van mijn thesis en naar Jef voor het mee opvolgen van mijn dagelijks werk. Ook Chantal, Marion en Inge dienen vermeld te worden voor alle administratieve werkjes die ze opknaptten.

Ten slotte ben ik ook zeer dankbaar voor de steun die ik altijd gekregen heb van mijn familie en vrienden. In het bijzonder omdat ik altijd een luisterend oor bij hen vond tijdens sommige moeilijke momenten het voorbije jaar.

Yves
November 2007

Short summary

Lattice-matched and metamorphic III-V multijunction solar cell development is described in this thesis. More specifically that of $\text{In}_{0.495}\text{Ga}_{0.505}\text{P}$ / $\text{In}_{0.01}\text{Ga}_{0.99}\text{As}$ and $\text{In}_{0.65}\text{Ga}_{0.35}\text{P}$ / $\text{In}_{0.17}\text{Ga}_{0.83}\text{As}$ dual junction cells on germanium, respectively. Combined with a germanium bottom cell, they can be used as top structure in the mechanical stack under development at imec. Applications for this stack lie in electricity generation in space (e.g. for satellites) or in terrestrial concentration systems. Theoretical calculations show that the lattice-matched cell has upper limit energy conversion efficiencies of 32.5 and 36 % under AM0 and 500×AM1.5D spectral conditions, respectively. For the metamorphic cell this is 34.2 and 41.8 %, respectively.

First two theoretical chapters explain the deposition technique (MOVPE) and the source material selection and review the working principles of solar cell and tunnel junction. Next, the lattice-matched dual junction cell development is presented. The $\text{In}_{0.01}\text{Ga}_{0.99}\text{As}$ and $\text{In}_{0.495}\text{Ga}_{0.505}\text{P}$ single junction cells had a best efficiency of 24.7 and 14.2 %. An AlGaAs tunnel junction with a peak current density of 92 A/cm² was realised. Integrating these components into one device, a tandem cell with 24.3 % conversion efficiency was demonstrated. Finally, an 18.6 % efficient metamorphic dual junction cell is constructed from a 17.0 % efficient $\text{In}_{0.17}\text{Ga}_{0.83}\text{As}$ and a 15.2 % efficient $\text{In}_{0.65}\text{Ga}_{0.35}\text{P}$ single junction cell using an AlGaAs tunnel junction with a peak current density of 13.5 A/cm². To this end, a suitable buffer layer is designed to accommodate the lattice-mismatch and prevent threading dislocations from reaching the active device layers.

Beknopte samenvatting

Roosteraangepaste en metamorfe III-V multi-junctie zonnecelontwikkeling wordt in deze thesis beschreven. Meer specifiek die van $\text{In}_{0.495}\text{Ga}_{0.505}\text{P}$ / $\text{In}_{0.01}\text{Ga}_{0.99}\text{As}$ en $\text{In}_{0.65}\text{Ga}_{0.35}\text{P}$ / $\text{In}_{0.17}\text{Ga}_{0.83}\text{As}$ twee-junctie cellen op germanium. In combinatie met een germanium bodemcel kunnen ze gebruikt worden als bovenste deel in de mechanische stapeling die op imec onder ontwikkeling is. Deze structuur kan toegepast worden voor elektriciteitsproductie in de ruimte (bv. voor satellieten) of in aardse concentratiesystemen. Theoretische berekeningen geven een bovengrens voor de efficiëntie van de roosteraangepaste cel, nl. 32.5 en 36 % onder respectievelijk AM0 en 500×AM1.5D belichting. Voor de metamorfe cel is dat respectievelijk 34.2 en 41.8 %.

Eerst wordt in twee theoretische hoofdstukken de depositietechniek (MOVPE) en de bronmateriaalkeuze verduidelijkt en de werking van de zonnecel en de tunneljunctie behandeld. Vervolgens wordt de ontwikkeling van de roosteraangepaste 2-junctie cel

gepresenteerd. De beste 1-junctie $\text{In}_{0.01}\text{Ga}_{0.99}\text{As}$ en $\text{In}_{0.495}\text{Ga}_{0.505}\text{P}$ cellen hadden een conversie-efficiëntie van 24.7 en 14.2 %. Een AlGaAs tunneljunctie met een piekstroombichtheid van 92 A/cm^2 werd gerealiseerd. Met deze componenten werd een 24.3 % efficiënte tandemcel gemaakt. Ten slotte wordt een 18.6 % efficiënte metamorfe 2-junctie cel gemaakt vertrekkend van een 17.0 % efficiënte $\text{In}_{0.17}\text{Ga}_{0.83}\text{As}$ en een 15.2 % efficiënte $\text{In}_{0.65}\text{Ga}_{0.35}\text{P}$ 1-junctie zonnecel en gebruik makende van een AlGaAs tunneljunctie met een piekstroombichtheid van 13.5 A/cm^2 . Hiervoor werd een geschikte bufferlaag ontworpen om de roostermisaanpassing op te vangen en te vermijden dat dislocaties doordringen in de actieve lagen van de component.

List of acronyms

AM<number>(D/G)	Air Mass <number> (Direct / Global)
APB	Anti-Phase Boundary
APD	Anti-Phase Domain
ARC	Anti-Reflective Coating
BSF	Back Surface Field
C-V	Capacitance – Voltage
CB	Conduction Band
CPV	Concentrator Photovoltaics
DC	Down-converter
DH	Double Heterostructure
EDX	Energy-Dispersive X-ray analysis
EOL	End-of-life
EpiTT	In-situ technique for monitoring substrate temperature and layer growth rate
EQE	External Quantum Efficiency
GEO	Geosynchronous Orbit
I-V (J-V)	Current (density) – Voltage
IMM	Inverted Metamorphic
IQE	Internal Quantum Efficiency
LEO	Low Earth Orbit
LM	Lattice-matched
LMM	Lattice-mismatched
LPE	Liquid Phase Epitaxy
MBE	Molecular Beam Epitaxy
MM	Metamorphic
MO	Metal Organic
MOVPE	Metal Organic Vapour Phase Epitaxy
(RT-)PL	(Room Temperature) Photoluminescence
PV	Photovoltaic
QD	Quantum Dot
QW	Quantum Well
RHEED	Reflection High-Energy Electron Diffraction
RSM	Reciprocal Space Map
SB	Strain-balanced
SEM	Scanning Electron Microscopy
SIMS	Secondary Ion Mass Spectrometry
SL	Superlattice
TB-	Tertiarybutyl-
TD(D)	Threading Dislocation (Density)

TEM	Transmission Electron Microscopy
Ti:Sa	Titanium:Sapphire
TLM	Transfer Length Model
TLV	Threshold Limit Value
TM-	Trimethyl-
TRPL	Time-Resolved Photoluminescence
UC	Up-converter
VB	Valence Band
(HR)XRD	(High Resolution) X-Ray Diffraction

List of symbols

Symbol	Description	Unit
c	Speed of light	m/s
d	Thickness	m
D, D_e, D_h	Diffusion coefficient, of electrons, of holes	m^2/s
E	Energy	eV
E_F, E_{Fn}, E_{Fp}	Fermi level, on n-side, on p-side	eV
E_G	Bandgap energy	eV
\underline{E}	Electric field	V/m
$F(E)$	Fermi-Dirac distribution	-
FF	Fill factor	%
G	Gibbs free energy	J
H	Enthalpy	J
h_c	Critical thickness	m
h	Planck constant	J.s
\hbar	Reduced Planck constant	J.s
$I (J)$	Current (density)	A (A/m^2)
$I_0 (J_0)$	Reverse saturation current (density)	A (A/m^2)
I_{ex}	Excess current	A
$I_l (J_l)$	Light-generated current (density)	A (A/m^2)
I_{mp}	Maximum power point current	A
$I_p (J_p), I_v (J_v)$	Peak, valley current (density)	A (A/m^2)
$I_{sc} (J_{sc})$	Short-circuit current (density)	A (A/m^2)
$I_t (J_t)$	Tunnelling current (density)	A (A/m^2)
I_{th}	Thermal current	A
k	Boltzmann constant	J/K
$k(x)$	Electron wave vector	m^{-1}
K	Reaction equilibrium constant	-
L_D, L_e, L_h	Diffusion length, of electrons, of holes	m
L_d	Dislocation limited diffusion length	m
m^*	Electron effective mass	kg
n_i	Intrinsic carrier concentration	m^{-3}
N_A, N_D	Acceptor, donor concentration	m^{-3}
N_d	Dislocation density	m^{-3}
N_V, N_C	Valence, conduction band effective density of states	m^{-3}
P_{in}	Total incident power	W
q	Elementary charge	C
R_{cell}	Cell reflectance	%
R	Radius of curvature	m
R_s, R_{sh}	Series, shunt resistance	Ω

Symbol	Description	Unit
R_{sheet}	Sheet resistance	Ω
R_{sp}	Specific resistance	$\Omega \cdot \text{m}^2$
S	Entropy	J/K
S	Interface recombination velocity	m/s
T	Absolute temperature	K
T_{gr}	Growth temperature	$^{\circ}\text{C}$
T_{t}	Tunnelling probability	-
V_{gr}	Growth rate	m/s
V_{mp}	Maximum power point voltage	V
V_{oc}	Open-circuit voltage	V
$V_{\text{p}}, V_{\text{n}}$	Amount of degeneracy on p-side, n-side	V
$V_{\text{p}}, V_{\text{v}}$	Peak, valley voltage	V
w	thickness	m
W	Width	m
δ_0	Boundary layer thickness	m
ϵ_s	Static permittivity	F/m
η	Energy conversion efficiency	%
λ	Wavelength	m
μ_i	Chemical potential	J/mol
ρ	Resistivity	$\Omega \cdot \text{m}$
σ_l	Layer stress	Pa
τ	Lifetime	s

Inhoudsopgave

Nederlandse samenvatting

HOOFDSTUK 1	Inleiding	i
HOOFDSTUK 2	Metaalorganische Gasfase Epitaxie	v
HOOFDSTUK 3	Theorie over zonnecel en tunneljunctie	vii
HOOFDSTUK 4	Roosteraangepaste materialen	ix
HOOFDSTUK 5	Metamorfe materialen	xiii
HOOFDSTUK 6	Samenvatting en vooruitblik	xvii

Table of contents

English text

CHAPTER 1	INTRODUCTION	1
1.1	Towards renewable energy production	1
1.2	Solar power	4
1.3	High-efficiency III-V solar cells	7
1.4	The dual junction III-V solar cell	11
1.5	Thesis outline	13
1.6	References	14
CHAPTER 2	METALORGANIC VAPOUR PHASE EPITAXY	17
2.1	Introduction	17
2.2	Principle of operation	18
2.3	Thermodynamics	20
2.4	Metalorganic group-V precursors	23
2.5	Reaction kinetics	26
2.6	The boundary layer	29
2.7	Conclusion	31
2.8	References	32
CHAPTER 3	THEORY OF SOLAR CELL AND TUNNEL JUNCTION	33
3.1	Introduction	33
3.2	Solar cells	34
3.3	The tunnel junction	42
3.4	Conclusions	49
3.5	References	50

CHAPTER 4	LATTICE-MATCHED MATERIALS	51
4.1	Introduction	51
4.2	Growth on germanium	52
4.3	$\text{In}_{0.01}\text{Ga}_{0.99}\text{As}$ single junction solar cell	53
4.4	$\text{In}_{0.495}\text{Ga}_{0.505}\text{P}$ single junction solar cell	61
4.5	Carbon doping and tunnel junctions	88
4.6	The InGaP/GaAs dual junction solar cell on Ge	107
4.7	Summary and conclusions	111
4.8	References	113
CHAPTER 5	METAMORPHIC MATERIALS	117
5.1	Introduction	117
5.2	Buffer layers	118
5.3	$\text{In}_{0.17}\text{Ga}_{0.83}\text{As}$ single junction solar cell	127
5.4	$\text{In}_{0.65}\text{Ga}_{0.35}\text{P}$ single junction solar cell	142
5.5	AlGaAs tunnel junction	146
5.6	$\text{In}_{0.65}\text{Ga}_{0.35}\text{P}/\text{In}_{0.17}\text{Ga}_{0.83}\text{As}$ tandem solar cell	154
5.7	Summary and conclusions	159
5.8	References	160
CHAPTER 6	SUMMARY AND OUTLOOK	163
6.1	Introduction	163
6.2	Results	164
6.3	Outlook	166
6.4	References	171

Nederlandse samenvatting

Metamorfe InGaP / InGaAs multi-junctie zonnecellen op germanium substraten

In deze Nederlandse samenvatting wordt verwezen naar figuren en tabellen in de Engelstalige tekst. Referenties zijn te vinden na het overeenstemmende hoofdstuk in de Engelstalige tekst. De nummering van de hoofdstukken is identiek aan die van de Engelstalige tekst, de paragraafindeling is gewijzigd.

Hoofdstuk 1

Inleiding

1.1 Motivatie: hernieuwbare energie

Energie is een van de pijlers van onze moderne maatschappij. Wij, “beschaafde mensen”, kunnen ons nog nauwelijks een wereld inbeelden zonder generatie en consumptie van energie om ons dagelijkse luxelevens op gang te houden. Overal is energie nodig, zelfs in afgelegen gebieden en tot in de ruimte toe.

De globale vraag naar energie neemt almaar toe terwijl de bevolking aangroeit, de levensstandaard stijgt en expansie-economieën floreren. In 2005 was het globale energieverbruik 15.3 TW en dit wordt verwacht met een kwart toe te nemen tegen 2015 volgens het “World Energy Outlook 2006”-rapport van het Internationaal Energie Agentschap [p.14: 1]. Tegen 2030 zal het gestegen zijn tot 22.7 TW als het huidige energieverbruik wordt aangehouden. Het invoeren van verscheidene beleidsmaatregelen kan dit cijfer reduceren tot 20.4 TW (Figuur 1–1, p.2).

Tegenwoordig zijn we nog sterk afhankelijk van fossiele brandstoffen (olie, aardgas en steenkool). Zij vertegenwoordigen 80 % van het globale energieverbruik. De stijgende vraag naar vooral olie en het feit dat veel bronnen in of nabij conflictgebieden liggen, maakt dat de olieprijs de afgelopen jaren gevoelig gestegen is en ook vatbaar is voor internationale politieke disputen. Echter, de aanwezigheid van onconventionele reserves laat toe nog een hele tijd verder te gaan met de consumptie van fossiele brandstoffen, eens de ontginning economisch rendabel wordt.

Ondanks deze optimistische noot is er een enorm nadeel verbonden aan de verbranding van fossiele brandstoffen, namelijk de productie van CO₂, een broeikasgas. De stijgende CO₂-emissies kunnen een desastreuze impact hebben op het klimaat hier op Aarde met nefaste gevolgen voor onze maatschappij. Om de gevolgen binnen de perken te houden, moet er werk gemaakt worden van “schone” energiebronnen om de CO₂-emissies te verminderen. Hernieuwbare energiebronnen zoals zonne-energie, windenergie, energie uit waterkracht en biomassa en geothermische energie, zijn hiervoor uitermate geschikt. Een combinatie van al deze energievormen zal nodig zijn om onze energiehonger te stillen, maar het grootste potentieel schuilt in zonne-energie, die met een praktisch genereerbaar vermogen van 60 TW in de totale energiebehoefte zou kunnen voorzien. Zonne-energie mag dus beschouwd worden als de belangrijkste techniek en daarom wordt in deze doctoraatsthesis gefocust op energieproductie uit zonlicht.

1.2 Hoogefficiënte III-V zonnecellen

Ondanks alle voordelen – onderhoudsvriendelijk, geen geluidshinder, mogelijkheid tot integratie in gebouwen – resten zonne-energie nog twee uitdagingen: de cel- en systeemkost moet dalen en de energieconversie moet efficiënter gebeuren om een energieprijis te bekomen die competitief is met deze van conventionele energieproductie.

Om de celkost te reduceren kan men verder blijven investeren in de huidige kristallijn siliciumtechnologie en dunnefilmtechnologieën met silicium, II-VI halfgeleiders (CdTe, Cu(In,Ga)Se₂) of organische materialen. De twee laatst vermelde materialen hebben echter nog te kampen met respectievelijk de reproduceerbaarheid van het depositieproces en de stabiliteit van het materiaal. Enkel de siliciumtechnologie is een gevestigde waarde en domineert momenteel de markt voor zonne-energieomzetting. Om op grotere schaal (in centrales) elektriciteit te produceren, is een ander materiaalsysteem, namelijk dat van de III-V halfgeleiders, een betere keuze dan silicium door de veel hogere efficiëntie die deze III-V zonnecellen halen met actuele industriële productietechnieken. III-V zonnecellen zijn wel veel duurder dan silicium zonnecellen, maar wanneer ze gebruikt worden in concentratorsystemen wordt de hogere celkost gecompenseerd door minder en kleinere cellen te gebruiken om eenzelfde vermogen te genereren. Het grootste deel van de systeemkost zit dan vervat in de componenten van het concentratorsysteem, die veel vatbaarder zijn voor prijschaling (Figuur 1-7, p.9). Het gebruik van duurdere zonnecellen is dan geoorloofd om tot een competitieve – zelfs goedkopere – elektriciteitsprijs te komen.

Waar vroeger vooral de ruimtevaart een drijvende kracht was voor de ontwikkeling van hoogefficiënte III-V zonnecellen – kostprijs van de cel is van ondergeschikt belang – is de laatste jaren de ontwikkeling van deze technologie voor aardse toepassingen in concentratorsystemen een extra stimulans geworden. Het succesverhaal bij uitstek tot nog toe was de monolithische InGaP / GaAs / Ge 3-junctie zonnecel. In deze multi-junctie zonnecel zijn alle lagen roosteraangepast aan het substraat. Hierdoor ligt de energiekloofcombinatie vast. Theoretische berekeningen tonen aan dat deze welbepaalde combinatie niet optimaal is (Figuur 1-8, p.12). Daarom wordt er tegenwoordig veel onderzoek verricht naar de zogenaamde metamorfe zonnecellen, waarbij niet alle lagen roosteraangepast aan elkaar hoeven te zijn. Op die manier creëert men een extra vrijheidsgraad in de ontwikkeling van hoogefficiënte zonnecellen door de onderzoeker de mogelijkheid te geven andere energiekloofcombinaties te gebruiken. Andere opties om de efficiëntie te verhogen zijn het aantal juncties vergroten tot 4, 5 of zelfs 6 juncties of het doordachte gebruik van een mechanische stapeling.

Onlangs werd door Spectrolab met hoogefficiënte monolithische III-V 3-junctie zonnecellen voor het eerst de “40 % efficiëntie”-barrière doorbroken. Spectrolab demonstreerde een roosteraangepaste en een metamorfe zonnecel die een efficiëntie van respectievelijk 40.1 en 40.7 % haalden onder concentratie [p.15: 23].

1.3 Doel en opbouw van de thesis

Het doel van deze thesis is in een eerste fase de ontwikkeling van een roosteraangepaste InGaP / GaAs 2-junctie zonnecel op germanium, die na het verwijderen van het substraat gebruikt kan worden in een mechanische stapeling in combinatie met een door imec al ontwikkelde zeer efficiënte germanium bodemcel [p.15: 39]. In een tweede fase is het de bedoeling de overgang te maken naar een metamorfe InGaP / InGaAs 2-junctie zonnecel op germanium om de efficiëntie verder te verhogen.

In het tweede hoofdstuk wordt de gebruikte depositietechnologie, metaalorganische gasfase epitaxie (MOVPE), behandeld. Verder wordt ook de keuze voor bepaalde bronmaterialen toegelicht.

Het derde hoofdstuk bekijkt de werkingsprincipes van de zonnecel evenals deze van de tunneljunctie, een uitermate belangrijke component in een monolithische multi-junctie zonnecel.

De ontwikkeling van de roosteraangepaste InGaP / GaAs 2-junctie zonnecel wordt vervolgens behandeld in het vierde hoofdstuk. Eerst worden de afzonderlijke enkelvoudige cellen besproken. Vervolgens is het de beurt aan de ontwikkeling van de tunneljunctie. Ten slotte wordt de 2-junctie zonnecel gerealiseerd door al deze componenten in één structuur te combineren.

Om de overgang naar de metamorfe materialen mogelijk te maken, wordt in het vijfde hoofdstuk eerst de ontwikkeling beschreven van een gepaste bufferstructuur om het propageren van dislocaties naar de actieve lagen (zoveel mogelijk) te vermijden. Verder volgt dit hoofdstuk eenzelfde verloop als het vierde, namelijk eerst het ontwikkelen van de afzonderlijke componenten en ten slotte de integratie ervan in een metamorfe InGaP / GaAs 2-junctie zonnecel.

Het zesde en laatste hoofdstuk geeft een overzicht van de realisaties van dit werk en blikt ook vooruit naar de toekomst van de III-V zonnecellen en naar mogelijke experimenten om het eigen werk verder te verfijnen.

Hoofdstuk 2

Metaalorganische Gasfase Epitaxie

2.1 Inleiding

De groeitechnologie om multi-junctie zonnecellen te maken moet in staat zijn om bulkmateriaal van hoge kwaliteit te deponeren met abrupte interfaces, gecontroleerde dotering en dikte over grote oppervlaktes en met een aanvaardbare groeisnelheid. Ook moet hij grote volumes aankunnen, kosteffectief zijn en commercieel beschikbaar. Kandidaten zijn o.a. moleculaire bundel epitaxie (MBE), vloeibare fase epitaxie (LPE) en metaalorganische gasfase epitaxie (MOVPE). MOVPE is de geprefereerde epitaxiale groeitechniek voor de fabricage van III-V zonnecellen. MOVPE voldoet aan alle bovenvermelde eisen en het is bovendien een zeer flexibele technologie. Nadelen zijn een klein aantal beschikbare in-situ karakterisatietechnieken en dure, gevaarlijke chemicaliën die strenge veiligheidsmaatregelen vergen.

In dit hoofdstuk wordt een overzicht gegeven van het MOVPE groeiproces en wordt de keuze voor metaalorganen als groep-V bronmateriaal toegelicht.

2.2 Werkingsprincipe

Een (summiere) schematische voorstelling van een MOVPE-reactor is te zien in Figuur 2-1 (p.19). Eerst wordt een substraat in een (drukgergelde) reactor geladen. Vervolgens wordt het substraat opgewarmd. Een dragergas, H_2 , voert de bronmaterialen naar de reactor. Boven het verwarmde substraat worden ze thermisch gekraakt – deels in de gasfase, deels op het oppervlak – waarna de geïntroduceerde atomen ingebouwd worden in het op het substraat groeiende kristalrooster. Dit gebeurt bij temperaturen tussen $550\text{ }^{\circ}\text{C}$ en $750\text{ }^{\circ}\text{C}$ en een druk van 76 torr. De restgassen worden door een ‘scrubber’ gestuurd, alwaar de toxische elementen geadsorbeerd worden door een metaaloxide. Door middel van oxidatie kunnen de toxische elementen later omgezet worden in stabiele oxides, waarbij 50 % van het metaaloxide weer beschikbaar wordt. Wanneer de opnamecapaciteit van de scrubber te laag wordt, worden de afvalproducten verwijderd.

Om stoichiometrisch III-V materiaal te groeien moet de molaire verhouding van groep-V tot groep-III moleculen groter zijn dan 1, omdat de groep-V typisch hoge dampdrukken hebben bij standaard groeicondities. De drijvende kracht voor het MOVPE groeiproces zelf vloeit voort uit de thermodynamica van het systeem ‘dampfase aan de overgang damp-vaste stof, vaste stof’, dat een evenwicht tracht in te stellen tussen de samenstellingen van de verschillende fases. Bij MOVPE is de aangevoerde dampfase gesupersatureerd t.o.v. de vaste stof, m.a.w. het systeem is niet

in evenwicht. Een zeer groot deel van deze supersaturatie wordt echter gebruikt om het massatransport van de dampfase naar de overgang damp-vaste stof doorheen een grenslaag mogelijk te maken. De uiteindelijke afwijking van de evenwichtssituatie is dan zeer klein (zie Figuur 2–3, p.21). Dit chemische potentiaalverschil zorgt dan voor de groei van het kristalrooster. Als de reacties aan het oppervlak veel sneller zijn dan de diffusie door de grenslaag, dan is de groei nagenoeg temperatuursonafhankelijk. Dit is het massatransport gelimiteerd gebied. Beneden een bepaalde temperatuur beperken de reacties de groeisnelheid. Ze daalt dan exponentieel met de temperatuur. Boven een zekere temperatuur treedt desorptie van het oppervlak op. Dit is weergegeven in Figuur 2–4 (p.22).

Voor voorbeelden van mogelijke pyrolysereacties in de reactor verwijzen we naar §2.5 in de Engelse tekst.

2.3 Metaalorganische groep-V precursors

Er zijn verschillende groep-V precursors waaruit men kan kiezen om arsenides en fosfides te groeien. De klassiek gebruikte bronnen zijn arsine (AsH_3) en fosfine (PH_3). Deze hydridegassen zijn uitermate giftig (zie Tabel 2–1, p.25) en worden onder hoge druk in gasflessen opgeslagen. Dit vormt een ernstig risico omdat grote hoeveelheden kunnen vrijkomen bij een ongeval. Daarom opteert imec voor minder giftige metaalorganen als bronmateriaal, nl. tertiair butyl-arsine (TBAs) en tertiair butyl-fosfine (TBP). Bovendien zijn deze bronnen pyrofore vloeistoffen bij kamertemperatuur wat het spreidingsrisico sterk verkleint.

Een bijkomend voordeel van TBAs en TBP is hun lagere pyrolysetemperatuur (50 % gekraakt bij: TBAs 370 °C, AsH_3 560-600 °C, TBP 475 °C en PH_3 640-720 °C) waardoor lagere groeitemperaturen binnen bereik komen. Het verbruik van de metaalorganen is ook lager, wat hun duurdere prijs deels goedmaakt. Bovendien tonen studies ook aan dat een hoge materiaalkwaliteit verkregen wordt en dat minder koolstof en zuurstof in de gegroeide lagen terecht komt [p.32: 3-9].

2.4 Conclusie

MOVPE is de te verkiezen epitaxiale groeitechniek om op een kosteffectieve manier grote volumes uniform III-V materiaal van hoge kwaliteit te deponeren op grote oppervlaktes. Het proces wordt beheerst door de thermodynamica van het systeem door het in een bijna-evenwichtstoestand te houden. Voor een veiliger en efficiënter proces, ook bij lage groeitemperaturen, zijn TBAs en TBP uitstekende alternatieven voor de hydrides.

Hoofdstuk 3

Theorie over zonnecel en tunneljunctie

3.1 Inleiding

Het doel van deze thesis is het maken van monolithische InGaP / InGaAs 2-junctie zonnecellen. Dit impliceert dat er een serieschakeling is van de deuncellen waaruit de multi-junctie zonnecel is opgebouwd. Daarvoor moet een geschikte component tussengevoegd worden, de tunneljunctie.

In een eerste deel van dit hoofdstuk wordt de theorie van de zonnecel behandeld. In het tweede deel volgt de bespreking van de tunneljunctie.

3.2 Zonnecellen

Een zonnecel is een grote pn-junctie die elektriciteit genereert door fotonen met een energie groter dan de energiekloof te absorberen. De gecreëerde elektron-gatparen worden door het intern elektrisch veld van de junctie gescheiden en aan de contacten gecollecteerd, zodat ze vermogen kunnen leveren aan een externe belasting.

De I - V curve van een (ideale) belichte zonnecel, gegeven door

$$I = I_0 \left(e^{\frac{qV}{kT}} - 1 \right) - I_\ell, \quad (3.i)$$

is niets anders dan de donkerstroomcurve van een diode, verschoven over een afstand gegeven door de lichtstroom I_ℓ (Figuur 3-2, p.36) en met I_0 de achterwaartse saturatiestroom. Belangrijke zonnecelparameters zijn de openklemspanning V_{oc} , de kortsluitstroom I_{sc} en de vulfactor FF (verhouding tussen maximaal vermogen en het product $V_{oc} \times I_{sc}$). Het rendement van de zonnecel wordt dan gedefinieerd als de verhouding van het maximaal tot het invallende vermogen

$$\eta = \frac{V_{mp} I_{mp}}{P_{in}} = \frac{V_{oc} I_{sc} FF}{P_{in}}. \quad (3.ii)$$

Door de tegengestelde trends voor V_{oc} en I_{sc} als functie van de energiekloof, bestaat er een optimale energiekloof (1.38 eV) waarvoor het rendement maximaal is. Voor een 1-junctie zonnecel benadert GaAs zeer dicht deze waarde (Figuur 3-4, p.38).

In een echte zonnecel treden natuurlijk ook verliezen op. Zo zijn er voor de kortsluitstroom recombinatie- en optische verliezen. Recombinatie beperkt ook de openklemspanning en de vulfactor. Verder zijn er ook nog serie- en parallelweerstand die de vulfactor verminderen en in extreme gevallen V_{oc} en I_{sc} .

Om het rendement van de zonnecel te verhogen gaat men over naar multi-junctie zonnecellen waarbij meerdere materialen met verschillende energiekloof opeen gestapeld worden, de grootste energiekloof bovenaan. Het invallende spectrum wordt zo efficiënter geabsorbeerd; een kleiner deel van de fotonenergie gaat door thermalisatie verloren waardoor het rendement van de cel toeneemt. De materialen die roosteraangepast aan het substraat gegroeid kunnen worden leiden niet tot optimale energiekloofcombinaties voor meerdere juncties. Daarom wordt er de laatste tijd ook veel aandacht besteed aan metamorfe materialen voor gebruik in concentratorsystemen om toch die optimale combinaties te kunnen benaderen en zeer hoge rendementen te bereiken (Figuur 3-7, p.42).

3.3 De tunneljunctie

De tunneljunctie is de component die de deelcellen van een multi-junctie zonnecel in serie verbindt. De tunneljunctie moet een grote stroom kunnen voeren met slechts een kleine spanningsval over de connectie om het verlies in V_{oc} te minimaliseren. Bovendien moet ze ook dun en zo goed mogelijk optisch transparant zijn voor de materialen die eronder liggen om de I_{sc} -verliezen zoveel mogelijk te beperken.

De tunneljunctie bestaat uit een gedegenereerd gedoteerde pn-junctie waardoor conductie- (CB) en valentieband (VB) elkaar kruisen. De werking ervan is gebaseerd op het tunnelen van elektronen van de CB aan de n-zijde van de pn-junctie naar beschikbare plaatsen met dezelfde energie in de VB aan de p-zijde, of omgekeerd, afhankelijk van de aangelegde spanning. De tunneljunctie heeft een typische $I-V$ karakteristiek. Voor negatieve spanning V tunnelen de elektronen van VB naar CB. Als $V = 0$ zijn er geen vrije plaatsen en loopt er dus geen stroom. Voor toenemende positieve spanning neemt de stroom eerst toe tot een maximum, om daarna af te nemen wegens het “ontkruisen” van de banden (negatieve weerstandsgebied). Bij nog hogere spanningen kan ten slotte de normale diodestroom vloeien. Dit is weergegeven in Figuur 3-11 (p.47) waar ook de verschillende componenten van de totale stroom te zien zijn.

In normale omstandigheden, wanneer de piekstroom lager is dan de fotogegenereerde stroom van de zonnecel, werkt de tunneljunctie bij een kleine positieve spanning. In het andere geval treedt er een grote spanningsval op, wat het rendement van de zonnecel sterk beïnvloedt (Figuur 3-14, p.49).

3.4 Conclusie

Het rendement van een zonnecel kan verhoogd worden door meerdere materialen opeen te stapelen en het invallende spectrum aldus efficiënter te gebruiken. Deze verschillende juncties worden in serie aaneengeschakeld door een tunneljunctie. De optische verliezen moeten zo klein mogelijk zijn en een stroom groter dan de fotostroom moet gevoerd kunnen worden bij een minimale spanningsval.

Hoofdstuk 4

Roosteraangepaste materialen

4.1 Inleiding

Er zijn verscheidene substraten beschikbaar om op te groeien (= epitaxiaalagen deponeren), maar germanium wordt vandaag het meest gebruikt voor de productie van III-V zonnecellen wegens de lage prijs, goede mechanische eigenschappen en de mogelijkheid om in het substraat een extra junctie actief te maken. Door de niet-polaire aard van germanium kunnen tijdens de groei defecten, de zogenoemde anti-fasegrenzen, gevormd worden. Een geschikt nucleatieregime werd echter door imec ontwikkeld in samenwerking met Umicore [p.113: 3], zodat lagen van hoge epitaxiale kwaliteit bekomen worden zonder anti-fasegrenzen.

In dit hoofdstuk bespreken we eerst de realisatie van n-op-p $\text{In}_{0.01}\text{Ga}_{0.99}\text{As}$ en $\text{In}_{0.495}\text{Ga}_{0.505}\text{P}$ 1-junctie zonnecellen. Vervolgens bekijken we intrinsieke koolstofdotering en de ontwikkeling van tunneljuncties. Ten slotte komt de integratie van de afzonderlijke componenten in een roosteraangepaste InGaP / InGaAs 2-junctie zonnecel op Ge aan de beurt.

4.2 $\text{In}_{0.01}\text{Ga}_{0.99}\text{As}$ 1-junctie zonnecel

Het gebruiken van een n-op-p configuratie zou een rendementstoename en meer stralingsharde zonnecellen moeten opleveren. Hiervoor is dus een zo hoog mogelijke n-dotering van het materiaal voor de contactlaag nodig. Door de amfotere aard (incorporatie mogelijk op zowel groep-III als groep-V roosterplaats) van het klassieke n-type dopant Si kan een doteringsniveau van 10^{19} cm^{-3} niet bereikt worden. Dit probleem wordt vermeden door het groep-VI element Se te gebruiken. De hoogste ladingsdragerdichtheid die gehaald werd is $1.29 \times 10^{19} \text{ cm}^{-3}$ (Figuur 4-6, p.56).

Kort voor met dit werk gestart werd, haalde een door imec ontworpen p-op-n $\text{In}_{0.01}\text{Ga}_{0.99}\text{As}$ 1-junctie zonnecel (4 cm^2) een rendement van 24.5 % (AM1.5G) met $J_{sc} = 28.9 \text{ mA/cm}^2$, $V_{oc} = 1.030 \text{ V}$ en $\text{FF} = 82.5 \%$. Momenteel halen onze n-op-p cellen een iets lagere efficiëntie: 23.9 % met $J_{sc} = 29.6 \text{ mA/cm}^2$, $V_{oc} = 0.969 \text{ V}$ en $\text{FF} = 83.4 \%$. Beide cellen hebben een interne kwantumefficiëntie (IQE) van 95 % in het golflengtegebied van 450 tot 850 nm. De $J-V$ en IQE curven van beide cellen worden getoond in Figuur 4-8 en Figuur 4-9 (p.60).

4.3 $\text{In}_{0.495}\text{Ga}_{0.505}\text{P}$ 1-junctie zonnecel

In InGaP en InAlP kan ordening op atomaire schaal optreden, d.w.z. in een bepaalde kristalrichting varieert de compositie van de vaste stof met een periode van twee

roosterafstanden en is gemakkelijk afleidbaar uit een elektronendiffractiepatroon. De groeicondities bepalen de mate van ordening die optreedt; de temperatuur is hierin een belangrijke factor. Voor InGaP houdt ordening ook een wijziging van de energiekloof in, meetbaar via fotoluminescentiemetingen: als functie van de temperatuur wordt een maximum bereikt. Voor InAlP kon dit niet worden nagegaan door de indirecte energiekloof voor de gebruikte samenstelling.

De compositie van InGaP en InAlP kan goed gecontroleerd worden. Het doteren van InGaP met Si, Se (Tabel 4–5, p.65) en Zn (Tabel 4–6, p.65) is betrouwbaar zoals is op te maken uit vergelijking van onze metingen met literatuurwaarden (Figuur 4–14 en 4–15, p.67); voor InAlP was de karakterisering van het doteringsniveau moeilijker (Tabel 4–7, p.73). De niveaus van C en O onzuiverheden in InGaP zijn laag ($< 10^{17} \text{ cm}^{-3}$). In InAlP is de O concentratie $> 5 \times 10^{18} \text{ cm}^{-3}$, de C concentratie $> 10^{18} \text{ cm}^{-3}$; de grote variatie in C concentratie heeft te maken met de gebruikte depositietemperaturen.

Op het oppervlak van InGaP stalen kunnen typische defecten (Figuur 4–17, p.70) voorkomen, waarvan het optreden temperatuursgerelateerd schijnt te zijn. Gemiddelde oppervlakteruwheden van $\leq 1.2 \text{ nm}$ zijn aanvaardbaar. Voor InAlP komen soortgelijke defecten voor. Uit TEM-foto's zijn in de bulk ook lange vlakke defecten zichtbaar, afhankelijk van de groeitemperatuur.

De beste 1-junctie InGaP cel (4 cm^2) heeft een rendement van 14.2 % (AM1.5G) met $J_{sc} = 13.6 \text{ mA/cm}^2$, $V_{oc} = 1.276 \text{ V}$ en $\text{FF} = 82.0 \%$. Uit de J - V curve (Figuur 4–25, p.82) leren we dat de cel nog een iets te hoge serieweerstand heeft en een te kleine parallelweerstand. De IQE van de cel is 90 % in het golflengte-interval 500-600 nm (Figuur 4–26, p.82). De beste cel uit de literatuur heeft een efficiëntie van 18.5 % met $J_{sc} = 15.1 \text{ mA/cm}^2$, $V_{oc} = 1.391 \text{ V}$ en $\text{FF} = 87.9 \%$ [p.114: 18]. Uit fotoluminescentiemetingen als functie van de tijd hebben we een effectieve bulklevensduur (in de p-basis) van 4.94 ns en een recombinatiesnelheid van 3418 cm/s aan de overgang tussen basis en BSF bepaald, wat goede waarden zijn rekening houdend met referenties [p.114: 19,20].

4.4 Koolstofdoting en tunneljuncties

Intrinsieke koolstofdoting van GaAs en AlGaAs neemt toe met afnemende V/III verhouding en dalende groeitemperatuur [p.114: 25 en 27]. Met SIMS werd voor GaAs een maximale C concentratie van $1.5 \times 10^{18} \text{ cm}^{-3}$ ($T_{gr} = 520 \text{ }^\circ\text{C}$) gemeten. Elektrische metingen op deze lagen gaven geen uitsluitsel over activering van de koolstof wat ons doet besluiten, gezien het hoge waterstofgehalte in de lagen, dat C grotendeels door H gepassiveerd is.

Met een TMAI fractie van 0.29 in de gasfase werd een ladingsdragerdichtheid van $1.4 \times 10^{19} \text{ cm}^{-3}$ bereikt bij $542 \text{ }^\circ\text{C}$ voor $\text{V/III} = 9.3$. Ze satureert tussen 6 à $7 \times 10^{19} \text{ cm}^{-3}$ bij

een $V/III = 1.7$ en is voor deze V/III temperatuursonafhankelijk. De C concentratie in de laag kan tot een factor 10 hoger zijn. Waterstof speelt ook hier de rol van passiverend element. De C incorporatie in AlGaAs gaat beter omdat de Al-C binding sterker is dan de Ga-C binding. Voor meer cijfermateriaal over de dotering als functie van temperatuur en V/III verhouding verwijzen we naar Tabel 4-12 (p.93). Bij de hoge C concentraties in de AlGaAs lagen treedt een aanzienlijke roostercontractie op ten gevolge van het kleinere C atoom dat op de plaats van een As atoom komt te zitten (Figuur4-34, p.95).

De eerste tunneljunctie die we realiseerden was een GaAs tunneljunctie met 14 nm Zn:GaAs ($7 \times 10^{19} \text{ cm}^{-3}$) en 14 nm Se:GaAs ($1 \times 10^{19} \text{ cm}^{-3}$). Ze heeft een piekstroombichtheid van 82 A/cm^2 bij 0.24 V, een piek-dalverhouding van 1.2 en een specifieke weerstand van $2.8 \text{ m}\Omega \cdot \text{cm}^2$. Een vergelijking met literatuurwaarden is te vinden in Tabel 4-13 (p.97). De lage piek-dalverhouding doet ons vermoeden dat er veel diepe niveaus zijn in de energiekloof. Als er na het groeien van de tunnellen nog Zn-diffusie is opgetreden tijdens de verdere groei van de structuur, zal dit een verlaging van de piekstroom tot gevolg gehad hebben.

In de tunneljunctie worden ook fotonen geabsorbeerd. Om stroomverliezen dat dit veroorzaakt in de onderliggende deelcel te beperken, gebruiken we liever een hoog-energiekloofmateriaal. Daarom hebben we een AlGaAs tunneljunctie ontwikkeld. De 14 nm dikke laag $p^{++} \text{Al}_{0.3}\text{Ga}_{0.7}\text{As}$ is intrinsiek C gedoteerd tot $2 \times 10^{19} \text{ cm}^{-3}$ ($V/III = 9.3$, $T_{gr} = 542^\circ\text{C}$, TMAI-fractie in de gasfase = 0.41), de 14 nm dikke laag $n^+ \text{Al}_{0.2}\text{Ga}_{0.8}\text{As}$ is Se gedoteerd tot $2 \times 10^{18} \text{ cm}^{-3}$. Tussen GaAs lagen heeft deze tunneldiode een piekstroombichtheid van 17 A/cm^2 bij 0.07 V, een piek-dalverhouding van 11.3 en een specifieke weerstand van $2.6 \text{ m}\Omega \cdot \text{cm}^2$. Integreren we deze tunnellen tussen een structuur om de zonnecel te simuleren, dan daalt de piekstroombichtheid naar 3.9 A/cm^2 bij 0.12 V, waardoor de weerstand met bijna een factor 10 toeneemt. De piek-dalverhouding blijft nagenoeg ongewijzigd. In Tabel 4-14 (p.99) zien we dat onze volledig uit AlGaAs gemaakte tunneljunctie beter is dan soortgelijke componenten die in de literatuur vermeld worden. Voor de hoogtechnologische multi-junctiezonnecellen van vandaag wordt echter gebruik gemaakt van een beter presterende AlGaAs / InGaP combinatie. Door op 630°C te groeien met lagere V/III (1.7) werd een tunneljunctie gerealiseerd met een piekstroombichtheid van 92 A/cm^2 bij 0.53 V, een piek-dalverhouding van 9.2 en een specifieke weerstand van $7.8 \text{ m}\Omega \cdot \text{cm}^2$. De tunneljunctie verdient nog verdere studie. Bovendien is gebleken dat dit een zeer kritieke component is, waarvoor vooral de temperatuur zeer goed controleerbaar moet zijn.

4.5 InGaP/InGaAs 2-junctie zonnecel op Ge

Met de eerstgenoemde AlGaAs tunneljunctie werd een $\text{In}_{0.495}\text{Ga}_{0.505}\text{P} / \text{In}_{0.01}\text{Ga}_{0.99}\text{As}$ tandemcel op germanium gemaakt. Deze zonnecel werd gekarakteriseerd door het National Renewable Energy Laboratory (NREL, Golden, Co, USA). Het hoogste

rendement dat zij maten was 24.3 % voor een 1 cm² cel. De 4 cm² cel haalde een rendement van 24.0 % (AM1.5G) met $J_{sc} = 12.4$ mA/cm², $V_{oc} = 2.288$ V en FF = 84.4 %. De J - V curve wordt getoond in Figuur 4-46 (p.109). De externe kwantumefficiëntie van de totale cel en van de deelcellen wordt getoond in Figuur 4-48 (p.110) en bedraagt 90 % voor golflengtes tussen 500 en 850 nm. Als we de gemeten reflectie van de cel in rekening brengen, bekomen we een IQE van ongeveer 95 %.

4.6 Samenvatting

Hoge doteerniveaus in GaAs van de orde 10¹⁹ cm⁻³ werden behaald met Se, wat een goed ohms contact mogelijk maakt in de n-op-p structuur. Het rendement voor een dergelijke GaAs 1-junctie zonnecel bedraagt 24 %. De beste InGaP 1-junctie zonnecel (4 cm²) heeft een rendement van 13.6 %. Een goede effectieve bulklevensduur (4.94 ns) werd gemeten in het p-type materiaal van de basis; de recombinatiesnelheid aan de overgang met het BSF was lager dan vermeld in de literatuur.

Een GaAs tunneljunctie werd gerealiseerd met Zn en Se dotering. Ze heeft een piektunnelstroom van 82 A/cm². Hoge koolstofdotering werd bereikt in AlGaAs voor normale V/III bij lage temperatuur en voor lage V/III zelfs bij normale groeitemperaturen. Een tunneljunctie gegroeid met lage V/III haalt 17.3 A/cm²; in de tandemcel zakt dit tot 4 A/cm². Een AlGaAs tunneljunctie gegroeid met lage V/III bij normale temperatuur en met aangepaste laagdiktes zou 92 A/cm² halen in een tandemcel.

Ten slotte werd een In_{0.495}Ga_{0.505}P / In_{0.01}Ga_{0.99}As 2-junctie zonnecel gemaakt van de afzonderlijke componenten. Het rendement hiervan is 24 % (4 cm²), een veelbelovend resultaat.

Hoofdstuk 5

Metamorfe materialen

5.1 Inleiding

De roosteraangepaste multi-junctiezonnecellen uit het vorige hoofdstuk hebben niet een optimale energiekloofcombinatie. Om een zo hoog mogelijk rendement te halen, zal de samenstelling van de gebruikte materialen aangepast dienen te worden om een betere combinatie te verkrijgen. Dit houdt tevens in dat we van roosteraanpassing moeten afstappen en zogenaamde metamorfe lagen epitaxiaal moeten groeien, omdat er geen geschikte substraten zijn voor deze materialen – met grotere roosterconstante in onze situatie. Om lagen van hoge kwaliteit te deponeren, moet een aangepaste buffer gebruikt worden om de roostermisaanpassing op te vangen en dislocaties te verhinderen door te dringen tot in de actieve lagen van de zonnecel. Een dislocatiedichtheid van 10^6 cm^{-2} of lager is hierbij gewenst [p.160: 2,3].

5.2 Bufferlagen

Als een laag wordt gedeponerd op een substraat met een andere roosterconstante, zal deze eerst elastisch vervormen. Wanneer de opgebouwde spanningsenergie groter wordt dan de vormingsenergie van dislocaties, zal de laag beginnen te relaxeren door het vormen van dislocaties. Veelal leiden ze tot diepe niveaus in de energiekloof met niet-stralende recombinatie tot gevolg. De laagdikte waarbij dislocaties gevormd worden, wordt de kritische laagdikte h_c genoemd en kan berekend worden via het model van Matthews and Blakeslee [p.160: 4]

$$h_c = \frac{a_l}{\kappa\sqrt{2}\pi f} \cdot \frac{1-\nu/4}{1+\nu} \cdot \left[\ln\left(\frac{h_c\sqrt{2}}{a_l}\right) + 1 \right]. \quad (5.1)$$

De hieruit afgeleide waarde voor h_c is een minimum. Vaak kan de gegroeide laag dikker zijn dan de kritische dikte als er nucleatiebarrières voor dislocaties aanwezig zijn; zulke lagen zijn metastabiel. Voor een $\text{In}_{0.17}\text{Ga}_{0.83}\text{As}$ bulklaag op germanium is h_c 7.8 nm.

Het doel van een bufferlaag is de dislocaties te verhinderen door te dringen tot in de actieve gebieden van de zonnecel. Wij hebben de mogelijkheden van stap- en lineair gegradearde buffers bekeken. In het geval van de gestapte buffers worden de dislocaties afgebogen aan de overgangen tussen de verschillende stappen van de buffer. Voor de lineaire buffer zijn die er niet, maar de dislocaties hebben de neiging te propageren in de richting van de kleinste roosterconstante, dus richting substraat.

Tabel 5–2 en 5–3 (p.123) geven een overzicht van de details van de gebruikte buffers en van de meetresultaten. De voornaamste resultaten die daaruit volgen zijn dat een lagere

groei temperatuur de laagkwaliteit vermindert, dat dikke buffers een betere referentielag opleveren en dat lineaire buffers (initieel) iets beter (lijken) zijn dan gestapte. Figuur 5-3 en 5-4 (p.126) tonen TEM-foto's van een doorsnede van een lineaire en een gestapte buffer. Er is te zien hoe de dislocaties afgebogen worden en niet doordringen tot in de lagen boven de buffer; voor een lineaire buffer buigen de dislocaties op willekeurige posities af, terwijl duidelijk te zien is dat dit voor de gestapte buffer aan de stapovergangen gebeurt. Afgaande op deze TEM-foto's is de dislocatiedichtheid van de orde 10^6 cm^{-2} of lager.

5.3 $\text{In}_{0.17}\text{Ga}_{0.83}\text{As}$ 1-junctie zonnecel

De compositie van $\text{In}_x\text{Ga}_{1-x}\text{As}$ kan goed gecontroleerd worden. In de literatuur wordt gemeld dat de dotering gelijkaardig is aan die van GaAs [p.160: 10], dus werden geen aparte doteringscalibraties uitgevoerd.

Uit een X-stralenanalyse van de reciproke ruimte van het kristal kan een ruwe schatting van de dislocatiedichtheid in de bulk van de zonnecel gemaakt worden. Die komt overeen met de hierboven vermelde waarde. In de laag zorgt 110 MPa spanning voor buiging van het substraat.

De gegroeide cellen hebben een bulk indiumconcentratie van 15 tot 17 %. In een eerste experiment werden een lineaire en een stapbuffer gebruikt. Deze laatste had ook nog een uitloei stap ondergaan, waardoor mogelijks de prestatie van deze cellen uiteindelijk minder goed was dan deze gegroeid op de lineaire buffer. In een later experiment werd enkel nog de lineaire buffer gebruikt. Het beste resultaat voor een cel van 4 cm^2 onder AM1.5G belichting is een rendement van 17.3% met $J_{sc} = 36.5 \text{ mA/cm}^2$, $V_{oc} = 0.766 \text{ V}$ en $\text{FF} = 61.7 \%$. De IQE van deze cel ligt boven 95 % in een breed golflengte-interval. De data en curven van alle gemaakte cellen zijn te vinden in de tabellen en figuren op p.133-134. Het verlagen van de serieweerstand van de zonnecellen zal een betere vulfactor en dus beter rendement opleveren.

In Figuur 5-13 (p.139) is een opname van het ruwe oppervlak te zien ten gevolge van de grote roostermisaanpassing (1.14 %) tussen substraat en lagen. Een lasergeïnduceerde stroommeting toont aan dat deze ruwheid niet leidt tot lekpaden.

Via fotoluminescentiemetingen als functie van de tijd is een effectieve bulklevensduur van 18.1 ns in de basis gemeten. De recombinatiesnelheid aan de overgang met het BSF is 1753 cm/s . Uit deze levensduurmeting werd (met een aantal veronderstellingen) een bovengrens voor de dislocatiedichtheid bepaald van $7.2 \times 10^4 \text{ cm}^{-2}$.

5.4 $\text{In}_{0.65}\text{Ga}_{0.35}\text{P}$ 1-junctie zonnecel

De compositie van $\text{In}_{0.65}\text{Ga}_{0.35}\text{P}$ is roosteraangepast aan $\text{In}_{0.17}\text{Ga}_{0.83}\text{As}$. De dotering van $\text{In}_{0.65}\text{Ga}_{0.35}\text{P}$ lijkt gelijkaardig te zijn aan die van $\text{In}_{0.495}\text{Ga}_{0.505}\text{P}$. Voor $\text{In}_{0.64}\text{Al}_{0.36}\text{P}$ wordt hetzelfde aangenomen daar het moeilijk bleek om goede elektrische metingen op deze lagen te verrichten en aldus uitsluitel te krijgen.

De 1-junctie $\text{In}_{0.65}\text{Ga}_{0.35}\text{P}$ zonnecel werd gegroeid op dezelfde lineaire InGaAs buffer als de $\text{In}_{0.17}\text{Ga}_{0.83}\text{As}$ zonnecellen. De cel heeft een rendement van 15.2 % (AM1.5G) met $J_{sc} = 15.4 \text{ mA/cm}^2$, $V_{oc} = 1.228 \text{ V}$ en $\text{FF} = 80.3 \%$. De IQE (Figuur 5–17b, p.145) ligt boven 88 % in het interval 500-700 nm, maar mist een echt vlak stuk. Een verbetering van de materiaalkwaliteit kan hierin verandering brengen en leiden tot een toename van J_{sc} , V_{oc} en FF en dus van het rendement.

Voor het bulkmateriaal van de basis werd een effectieve bulklevensduur van 1.06 ns bekomen en een recombinatiesnelheid van 27562 cm/s aan de overgang met het BSF. Een bovengrens aan de dislocatiedensiteit van $1.3 \times 10^6 \text{ cm}^{-2}$ werd uit de levensduur afgeleid.

5.5 AlGaAs tunneljunctie

In onze aanpak hebben we gekozen voor het integreren van de in het vorige hoofdstuk ontwikkelde tunneljunctie in de tandemcel. Dit wil zeggen dat de AlGaAs-lagen van de tunneljunctie onder trekspanning zullen komen te staan. Met het model van Matthews and Blakeslee berekenen we een kritische dikte van 18 nm voor $\text{Al}_{0.2}\text{Ga}_{0.8}\text{As}$. Onze tunneljunctie is echter 30 nm en zal waarschijnlijk relaxeren, hoewel toch de mogelijkheid bestaat dat ze in een metastabiele toestand blijft. Zoals uit de TEM-foto van de tunneljunctie (Figuur 5–19, p.147) blijkt, relaxeren de lagen inderdaad door het vormen van stapelfouten. Verder zal de energiekloof verkleinen wanneer de lagen onder spanning komen te staan, wat op zijn beurt zal leiden tot een toename van de tunnelstroom.

De AlGaAs tunneljunctie (dezelfde als hoger beschreven in §4.4) werd in een zonnecel simulatiestructuur gebruikt. Dit leidde tot een piekstroom van 13.5 A/cm^2 bij 1.533 V en een piek-dalverhouding van 4.2. In de J - V curve (Figuur 5–21, p.150) is duidelijk te zien dat in de structuur een barrière voor de stroom optreedt waardoor er een grote spanningsval over de tunneljunctie is. Het gebruiken van een ander, Zn-houdend contacteringsmetaal leidde niet tot het oplossen van dit fenomeen. Een niet-ohms contact is dus niet de oorzaak. De analyse van een aantal teststructuren lijkt erop te wijzen dat we het probleem moeten zoeken in het doteringsniveau van de p-type lagen die na de tunneljunctie gegroeid worden. Verder onderzoek moet nog gebeuren om dit probleem op te lossen.

5.6 $\text{In}_{0.65}\text{Ga}_{0.35}\text{P}/\text{In}_{0.17}\text{Ga}_{0.83}\text{As}$ tandemzonnecel

Ondanks het optreden van die stroombarrière in de simulatiestructuur werd toch een metamorfe tandemzonnecel gemaakt. Het is te verwachten dat dit de J - V curve van de cel (Figuur 5–26, p.156) zal beïnvloeden. Inderdaad, de V_{oc} is met 1.664 V lager dan verwachte 1.98 V, die volgt uit de som der V_{oc} 's van de 1-junctie cellen. Dit zal dus een lager rendement tot gevolg hebben. Het beste resultaat is voor een cel van 0.25 cm^2 : 18.6 % met $J_{sc} = 15.8 \text{ mA/cm}^2$, $V_{oc} = 1.680 \text{ V}$ en $\text{FF} = 70.1 \%$. Voor 4 cm^2 hebben we 16.5 % met $J_{sc} = 15.2 \text{ mA/cm}^2$, $V_{oc} = 1.675 \text{ V}$ en $\text{FF} = 57.1 \%$. Naast de standaard MgF_2/ZnS dubbellaags anti-reflectie laag (ARL) werd ook een Si_3N_4 ARL gebruikt voor een snelle test. De rendementen van de zonnecellen met deze Si_3N_4 ARL zijn hoger door een betere FF.

5.7 Samenvatting

Om de grote roostermisaanpassing tussen het substraat en de actieve lagen op te vangen is een geschikte buffer nodig. Lineaire buffers leveren een iets betere materiaalkwaliteit en lijken beter te presteren dan stapbuffers. De dislocatiedichtheid in het materiaal dat op de buffer gegroeid wordt, wordt geschat op 10^6 cm^{-2} of lager.

Een lineaire buffer werd geselecteerd om de $\text{In}_{0.17}\text{Ga}_{0.83}\text{As}$ en $\text{In}_{0.65}\text{Ga}_{0.35}\text{P}$ 1-junctie cellen te groeien. Het beste rendement voor een cel van 4 cm^2 was respectievelijk 17.0 en 15.2 %.

De roosteraangepaste AlGaAs tunneljunctie relaxeert wanneer ze gebruikt wordt in de metamorfe structuur. Er treedt ook een extra stroombarrière op. Een piekstroom van 13.5 A/cm^2 werd bereikt.

De $\text{In}_{0.65}\text{Ga}_{0.35}\text{P} / \text{In}_{0.17}\text{Ga}_{0.83}\text{As}$ 2-junctie zonnecel op Ge die met deze tunneljunctie gemaakt werd, heeft een lagere V_{oc} dan wat mogelijk is. Het beste rendement is 18.6 %. Er werd ontdekt dat het gebruiken van een Si_3N_4 ARL een hogere FF oplevert. Ten slotte zal het oplossen van het probleem met de spanningsval over de tunneljunctie leiden tot betere rendementen.

Hoofdstuk 6

Samenvatting en vooruitblik

6.1 Samenvatting

Volgens het “World Energy Outlook 2006”-rapport van het Internationaal Energieagentschap zal de globale energiebehoefte stijgen van 15.3 TW in 2005 naar 22.7 TW tegen 2030, een doorgedreven energiebeleid niet in acht genomen [p.14: 1].

Fossiele brandstoffen zorgen mee voor het opwarmen van de aarde. Om dit tegen te gaan moeten we op hernieuwbare energiebronnen overschakelen. Van alle mogelijkheden heeft zonne-energie het grootste potentieel; productie van 60 TW is een realistisch cijfer. Alle zonneceltechnologieën zullen dan naast elkaar bestaan, waarbij de omstandigheden de te gebruiken technologie zullen bepalen. In dit werk hebben we ons toegespitst op de ontwikkeling van hoogefficiënte III-V (roosteraangepaste en metamorfe) zonnecellen. Het stapelen van meerdere juncties verhoogt de theoretische efficiëntie van een 1-junctiecel (29 %, AM1.5G) tot meer dan 40 % (AM1.5G). De beste resultaten worden behaald met de InGaP / GaAs / Ge 3-junctie zonnecel.

In eerste instantie hebben we de ontwikkeling van een roosteraangepaste InGaP / GaAs 2-junctie zonnecel op Ge bestudeerd. Deze zal dan (na het verwijderen van het substraat) mechanisch gestapeld worden op imec’s (wereldrecord) Ge cel. Om te beginnen hebben we de GaAs en InGaP n-op-p 1-junctie zonnecellen afzonderlijk ontwikkeld. Voor cellen van 4 cm² halen we respectievelijk een rendement van 23.9 en 13.6 %. Vervolgens werd dan een tunneljunctie, geheel uit AlGaAs (lage optische absorptie; p-type intrinsiek gedoteerd met koolstof) ontwikkeld. In een tandemcel zal deze een piekstroom van 3.9 A/cm² hebben. Ten slotte werden de drie afzonderlijke componenten geïntegreerd in een structuur, de InGaP / GaAs 2-junctie zonnecel op Ge, die een rendement van 24 % haalt.

De energiekloofcombinatie van de roosteraangepaste multi-junctie zonnecel is niet optimaal. Om de efficiëntie verder te verhogen schakelt men over op metamorfe materialen waar men een betere energiekloofcombinatie mee kan realiseren. Dit was het tweede deel van het thesiswerk.

Een geschikte bufferlaag werd ontwikkeld om de roostermisaanpassing te overbruggen en een dislocatiedichtheid van 10⁶ cm⁻² of lager te verkrijgen in de lagen boven de buffer. Op een lineaire buffer werden In_{0.17}Ga_{0.83}As en In_{0.65}Ga_{0.35}P 1-junctie zonnecellen gegroeid met een rendement van 17.0 en 15.2 % (AM1.5G, 4 cm²). Dezelfde AlGaAs tunneljunctie als in de roosteraangepaste aanpak werd hier gebruikt. Ze relaxeert onder de trekspanning met generatie van stapelfouten tot gevolg, maar heeft alsnog een

piekstroom van 13.5 A/cm^2 . Een spanningsbarrière is aanwezig waardoor de V_{oc} van de $\text{In}_{0.65}\text{Ga}_{0.35}\text{P} / \text{In}_{0.17}\text{Ga}_{0.83}\text{As}$ 2-junctie zonnecel die met deze tunneljunctie gemaakt werd, verminderde en het rendement lager uitviel: 18.6 % (AM1.5G, 0.25 cm^2). Bij deze cellen werd ook de gunstige invloed van een Si_3N_4 -laag in de ARL ontdekt (passivatie van defecten).

6.2 Vooruitblik

Nu naast het publiek ook de politiek zich bewust wordt van de mogelijke impact van traditionele energiebronnen op het (toekomstig) klimaat, treedt hernieuwbare energieproductie steeds meer op het voorplan. Zonne-energie met voornamelijk III-V concentrator technologie voorop, kan een sleutelrol spelen in het genereren van elektriciteit aan competitieve marktprijzen.

Derde-generatie zonneceltechnologieën mikken op kostenreductie door een significante toename in efficiëntie waarvoor meerdere energieniveaus nodig zijn. Dit kan door 1) het aantal energieniveaus in de cellen te verhogen, 2) meerdere ladingsdragerparen per hoog-energiefoton of een ladingsdragerpaar met meerdere beneden-bandkloof fotonen te genereren of 3) ladingsdragers te gebruiken voor ze thermaliseren.

Het bekendste voorbeeld van de eerste strategie is de multi-junctie zonnecel. Onlangs werden roosteraangepaste en metamorfe III-V zonnecellen gedemonstreerd die de kaap van 40 % rendement overschreden. De metamorfe $\text{In}_{0.56}\text{Ga}_{0.44}\text{P} / \text{In}_{0.08}\text{Ga}_{0.92}\text{As} / \text{Ge}$ 3-junctie zonnecel realiseerde 40.7 % onder $240\times\text{AM1.5D}$, de roosteraangepaste $\text{In}_{0.495}\text{Ga}_{0.505}\text{P} / \text{In}_{0.01}\text{Ga}_{0.99}\text{As} / \text{Ge}$ 3-junctie zonnecel 40.1 % onder $135\times\text{AM1.5D}$ [p.171: 1]. Een veelbelovende variatie op deze aanpak is de geïnverteerde metamorfe zonnecel (topcel wordt eerst gegroeid op het substraat, dat nadien verwijderd wordt) die 38.9 % haalde onder $81\times\text{AM1.5D}$ [p.171: 3]. Experimentele multi-junctie ontwerpen waarin vier of meer juncties worden gebruikt kunnen een rendement van 45 tot 50 % bereiken. Andere aanpakken zijn de deelcellen mechanisch op elkaar (imec: hybride aanpak) of naast elkaar (DARPA [p.171: 7]) stapelen, waardoor er geen nood meer is aan stroomaanpassing tussen de deelcellen. Ten slotte kan men ook een kwantumput aanbrengen in de bulk van een cel om het absorptievenster van de cel naar langere golflengten uit te breiden als de energiekloof kleiner is dan die van het bulkmateriaal.

De tweede strategie steunt op het gebruik van op- en neer-convertoren om met lage-respectievelijk hoge-energie fotonen extra ladingsdragers in de cel te genereren. De derde strategie maakt gebruik van materialen die een vertraagde thermalisatie van de ladingsdragers vertonen. Beide strategieën zijn nog in de vroege ontwikkelingsfase.

Het is duidelijk dat om in centrales elektriciteit te genereren III-V concentratorcellen uitermate belangrijk zijn. Een eerste betrouwbaarheidstest van concentratorcellen gaf zeer bemoedigende resultaten voor GaAs cellen onder 1000 zonnen [p.171: 10]. De

commerciële toepassing van de technologie zal van het succes van verscheidene projecten met concentratorinstallaties afhangen. Voorbeelden van projecten worden opgesomd op p.169 van de Engelse tekst.

Om de efficiëntie van onze 1-junctie GaAs zonnecel nog iets op te krikken zullen nog kleine aanpassingen aan de structuur moeten worden aangebracht. Voor de InGaP zonnecel dient de invloed van de groeicondities op de kwaliteit van het fosfidemateriaal verder bestudeerd te worden om het rendement te verhogen, o.a. door het bepalen van de levensduur in de emitter en de recombinatiesnelheid aan de overgang tussen emitter en venster. Meer experimenten zijn nodig om de invloed van allerhande parameters op de prestaties van de tunneljunctie beter te leren begrijpen. Ten slotte kan verder aandacht geschonken worden aan de stroomaanpassing van de deelcellen in de tandemstructuur.

In het geval van de metamorfe materialen kunnen eveneens n-type structuren gemaakt worden voor het bepalen van de levensduur in de emitter en de recombinatiesnelheid aan de emitter/venster-overgang. Mogelijk kan ook getracht worden meer controle te krijgen over de residuele spanning in de laag. Voor de tunneljunctie is het nodig de koolstofdoting van metamorf $\text{In}_{0.17}\text{Al}_{0.25}\text{Ga}_{0.58}\text{As}$ te evalueren om ze spanningsvrij in de tandemcel te kunnen integreren. Verder dient ook het barrièreprobleem opgelost te worden om de V_{oc} van de 2-junctie zonnecel en dus het rendement te verbeteren.

Een interessante vernieuwing zou kunnen zijn het ontwikkelen van een dubbellaags ARL waarbij als eerste gedeponeerde laag Si_3N_4 gebruikt wordt om te profiteren van het defectpassiverend effect van de waterstof in dat materiaal.

Dit werk heeft een basis gelegd voor het opbouwen van de praktische kennis betreffende het ontwikkelen van III-V multi-junctie zonnecellen. De eerste resultaten zijn veelbelovend. Verdere experimenten zullen toelaten de groei van de epitaxiale lagen te perfectioneren.

English text

Metamorphic InGaP / InGaAs
multijunction solar cells
on germanium substrates

Chapter 1

Introduction

1.1 Towards renewable energy production

Energy is one of the pillars of our modern society. We, “civilised people”, can hardly imagine a society without generation and consumption of energy to keep our every day life of luxury going. Energy is needed to power all sorts of electrical machinery that make our life so much easier as well as all kinds of electronics, be it for work or pleasure. Energy is needed everywhere, even in extremely remote places such as outer space.

The global energy demand is ever increasing as the population continues to grow, living standards keep rising and economies with large expansion potentials – such as the Chinese – flourish. In 2005 the global energy consumption amounted to 15.3 TW and is projected to grow with one quarter by 2015, according to the “World Energy Outlook 2006” report of the International Energy Agency [1]. By 2030 the demand will have risen to 22.7 TW if the present energy source usage profile is maintained (Figure 1-1, reference scenario). Implementing several policy measures can reduce this number with 10 % to 20.4 TW (Figure 1-1, alternative policy scenario).

At the moment we rely extensively on the availability of fossil fuels: oil, natural gas and coal together constitute 80 percent of global energy consumption (see Figure 1-2a). Although estimates vary, at current annual rates of production about 40 years of oil, 65 years of natural gas and 155 years of coal are left, worldwide [2]. These numbers are based upon the proven reserves of fossil fuel, i.e. those that are recoverable under existing economic and operating conditions. Due to an increased demand from fast

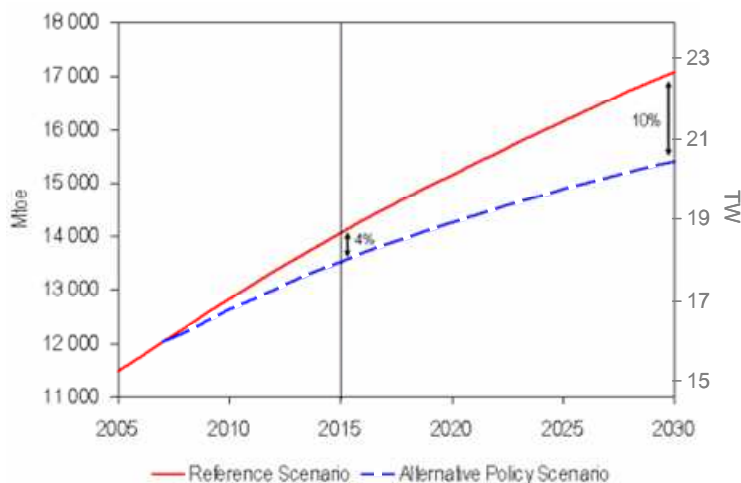


Figure 1-1: Projection of global primary energy demand in megaton oil equivalent (Mtoe) and terawatt (TW) according to the World Energy Outlook 2006. The “reference scenario” assumes the present energy source usage profile is continued whereas in the “alternative policy scenario” several policy measures are implemented.

growing economies and because a large quantity of the oil production is situated in (or near) conflict regions (the Middle East, Nigeria) the price per barrel of crude oil has risen considerably over the past years. But there are other categories of oil reserves besides the proven ones that are left out of the equation and would shed a completely different light on the extent and geological spreading of the oil reserves (see Figure 1-2b). Taking these recoverable and “unconventional” oil reserves (heavy oil, tar sands, oil shale) into account, it is possible the “total” reserves could sustain a continued increase in world oil use beyond the middle of the 21st century on the basis of an assumption of a 2% per annum growth in demand [3]. Nowadays, the oil price is susceptible to Middle-Eastern politics, supply restrictions and heavy new demand. Since we are now already faced with a higher market value of oil, the high production costs for unconventional oil are becoming economically viable. In the future prices can come to depend upon the level of technological advancement for developing these reserves. Apart from oil, for natural gas and coal, too, reserves are present that are unconventional or currently uneconomical to exploit and might become important in the future when energy prices are raised high enough. These resources could extend our fossil fuel energy production with another 500 (gas) and 2000 (coal) years [4].

Despite this seemingly optimistic note (the actual fossil fuel reserves being bigger than generally assumed), there is one enormous drawback on their continued combustion to provide in our energy needs: the production of CO₂, a green house gas, which can dramatically change Earth’s climate with devastating consequences for the world and

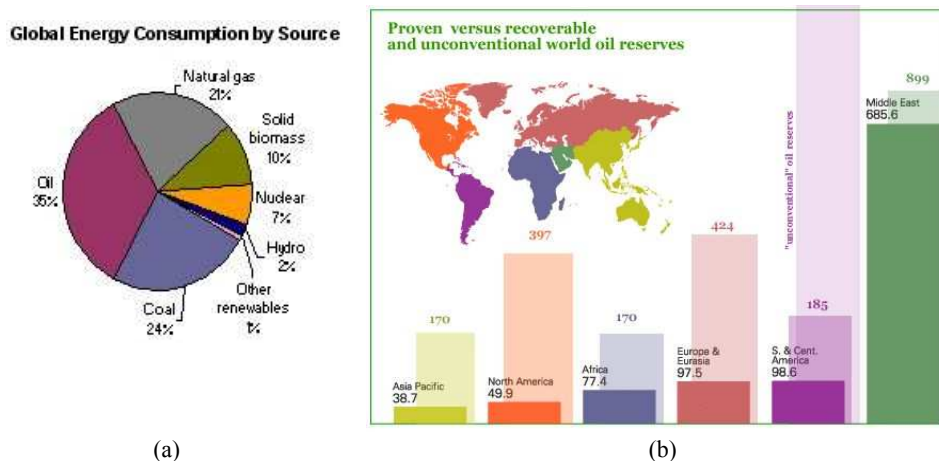


Figure 1-2: (a) distribution of global energy consumption (from [2]), (b) distribution of proven vs. recoverable and unconventional oil reserves in 10^9 barrels (from [3]).

our society [5]. One possibility to reduce CO_2 emissions and at the same time satisfy our energy hunger is to continue using and implement nuclear energy on a larger scale. The world's present measured resources of uranium, even if used only in today's conventional reactors, are enough to last for some 50 to 70 years [6]. Clearly, drawbacks of this technology are the risk of nuclear proliferation and the decommissioning of nuclear waste that may render this technology unsuitable. Obviously, clean energy sources are of dire need.

Renewable energy such as solar energy, wind and water power (Figure 1-3), geothermal and biomass energy, may hold the key to solving the energy puzzle as they are abundant, decentralised and do not produce any CO_2 . Furthermore, we have a long way to go before energy production via nuclear fusion is possible on a large scale. It was only in June 2005 that the Iter (International Thermonuclear Experimental Reactor) international project partners decided to build the first experimental large scale nuclear fusion reactor in Cadarache, France [7].

The practical yearly power production of these renewable energy sources can be estimated [4]. Hydroelectric power has a technically feasible potential of about 1.5 TW. The practical global onshore wind power potential is 2 TW. Including offshore wind farms (production of over 2 TW), increases this number but one has to consider grid proximity. Under very favourable conditions, biomass can produce 7 to 12 TW if one uses all of the cultivatable land not needed to grow food (= 10 % of the total land area). The total of continental and oceanic geothermal power potential amounts to 41.6 TW. Finally, the practical onshore solar power potential is 600 TW. Assuming an overall conversion efficiency of 10 %, 60 TW can be generated annually.

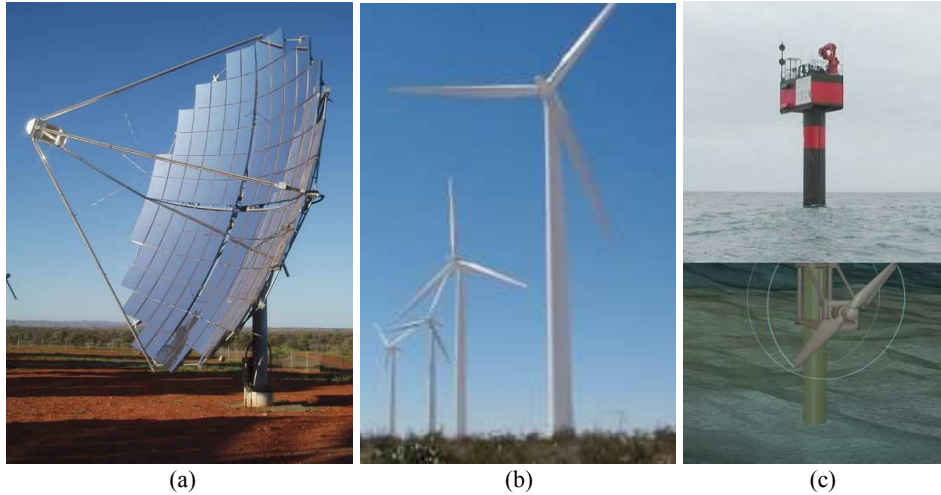


Figure 1-3: A few approaches to renewable energy production: (a) Solar Systems' concentrator module [8], (b) Siemens' wind turbine [9] and (c) Marine Current Turbine's Seaflow turbine [10].

In this work we will concentrate on solar energy production since it has the biggest terrestrial potential and, as such, may be considered as the most important technique to satisfy our future energy needs.

1.2 Solar power

For all its virtues – low maintenance, no noise pollution, esthetical integration into buildings – two main challenges remain for photovoltaics to become wide-spread: on the one hand to reduce the cost of cell (material, processing) and system and on the other hand to enhance the conversion efficiency, in order to reduce the cost per watt. Ultimately, the price for photovoltaic electricity needs to be competitive with the cost for electricity production from fossil fuels.

Reducing the cell cost can be done in several ways. One can continue to make use of the already established silicon solar cells with a market share of over 90 %. This approach can benefit from advances in processing made in other areas of silicon technology (chips, transistors). The current world record conversion efficiency under the AM1.5G spectrum in the laboratory, using high quality monocrystalline silicon, is 24.7 % [11]. To further reduce cell cost one can use lower quality multicrystalline silicon and thinner substrates. The laboratory record for multicrystalline cells is 20.3 % [12] and efficiencies of commercial cells range from 14 to 16 % [13]. On thin substrates (100 μm)

efficiencies of 17 % have been achieved [14]. Also driven by the current shortage in solar grade silicon, a lot of effort is put into the development of thin-film silicon solar cells to reduce the amount of substrate material even further. Thin layers of silicon can be transferred or directly deposited onto foreign low-cost substrates.

Other material systems also make use of thin films deposited onto cheap substrates. Compound semiconductors such as II-VIs (CdTe) and CIGS (Cu(In,Ga)Se_2) have demonstrated efficiencies of 16.5 and 19.5 %, respectively [15,16]. A nice overview of CdTe cell evolution is given in [17] and 18 % efficiency can be expected under a mature technology. However, Cd is not without health risks and assessment thereof has been carried out. It seems that risks are lower than one might assume, based on a simple hazard analysis [18]. CIGS solar cells offer the possibility of high conversion efficiencies at low cost if problems with reproducible deposition of uniformly composed thin films onto large areas can be solved. Recently, a new alloy, ZnMnTe, was developed in which it is possible to split the conduction band by adding oxygen to the alloy. The bands split so that the normally single-band material becomes multi-band, with the energy levels widely spaced to create three energy transitions that fall within the range of the solar spectrum. They hold the prospect of, in theory, reaching more than 50 % conversion efficiency [19].

Organic thin film solar cells are a very promising technology to produce low-cost cells because of the potentially low fabrication cost by using printing techniques that offer cheap mass production. Problems with material stability and large area printing still have to be solved. Although a milestone efficiency of 5 % was reached recently [20], conversion efficiencies will have to be increased to 10 %.

Finally, we come to the III-V material system. Solar cells fabricated with these materials only need to be a few microns thick – owing to the large absorption coefficients due to the direct nature of their bandgap – and, as such, can also be considered thin film cells. Originally, their development was driven by the space industry, where weight reduction of the payload and, hence, higher efficiency cells were more important than cell cost. Nevertheless, III-V solar cells are by far the most expensive ones due to very costly deposition techniques such as Metalorganic Vapour Phase Epitaxy (MOVPE) and Molecular Beam Epitaxy (MBE) for high quality material, due to very expensive precursors and due to the, by comparison, low wafer throughput. However, production scale MOVPE reactors can already hold up to twelve 100 mm wafers (Figure 1-4a) totalling to 942 cm² having (highly) uniform thickness and composition. High efficiency multijunction cells, in which several materials of different bandgap are stacked (monolithically or mechanically) on top of one another, hold the key to competing with – yes, even outperforming – their crystalline silicon and thin-film flat-plate rivals. When combined with optics that concentrate the direct sunlight onto the cells, the higher

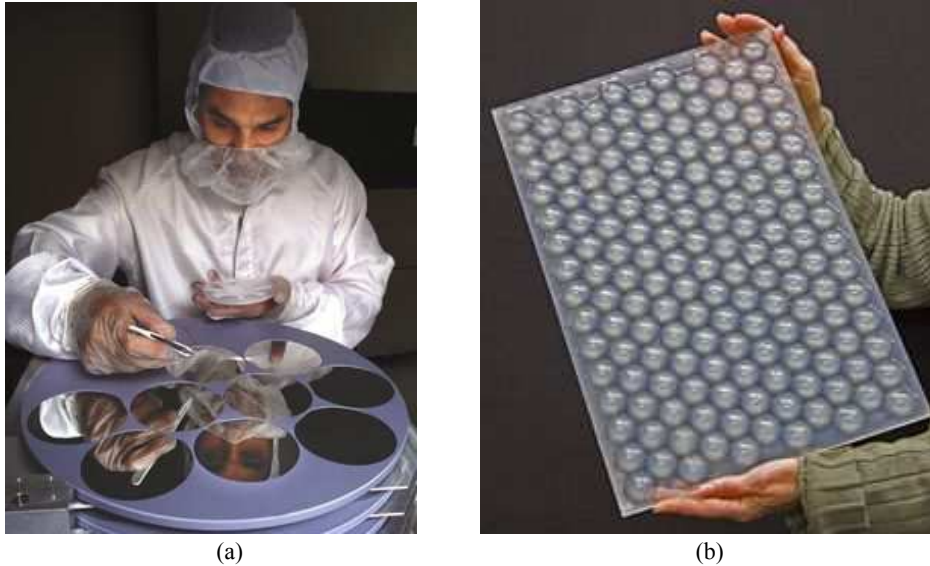


Figure 1-4: (a) Spectrolab wafers being prepared for epitaxial growth, (b) SolFocus' second-generation solar panel

cost of the III-V multijunction cells is offset by the use of fewer cells of smaller area to generate an equivalent power output. Most of the cost is then in lenses or mirrors and in tracking equipment, components which are much more susceptible to economies-of-scale [21]. Concentrator photovoltaics can also benefit from joining forces with the solid-state lighting industry due to their experience concerning certain technological issues such as heating cycle induced problems with bonded parts and protecting devices (cells) from weathering effects [22].

Recently, the “40 % conversion efficiency barrier” was broken and new milestones were set when Spectrolab demonstrated a lattice-matched (LM) and a metamorphic (MM) concentrator cell with an efficiency of 40.1 and 40.7 %, respectively [23]. This breakthrough may lead to systems with an installation cost of only \$3/W, producing electricity at a cost of 0.08-0.10 \$/kWh [24]. A California-based start-up company, SolFocus, says they will manufacture (using Spectrolab multijunction solar cells) first-generation solar systems at \$2/W when it opens its first concentrator plant next year and up-scaling to the gigawatt level will cut the cost to just 0.50 \$/W. They claim that second generation systems (Figure 1-4b) will cut costs even further to as low as 0.32 \$/W [21]. During the past years, all major cell manufacturers – Emcore [25], Spectrolab [26] and Sharp [27] – have received several orders to deliver cells for yet to be installed III-V concentrator systems, showing that this technique is muscling its way into the terrestrial market; partly because of the current shortage of silicon used in more

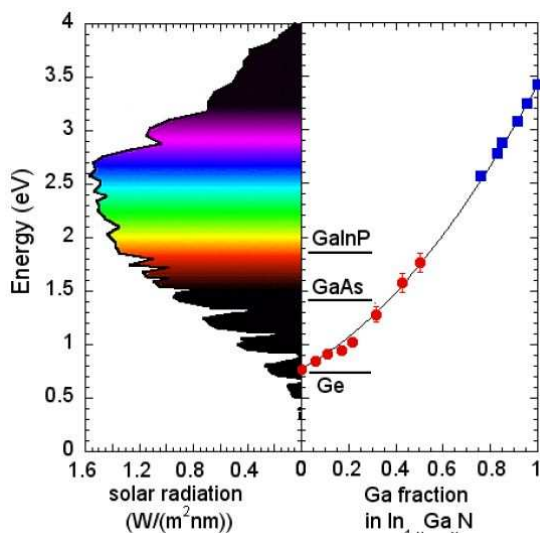


Figure 1-5: Bandgap energies of the InGaN alloy system (data points) cover the entire AM1.5 solar spectrum. The gap energies of conventional multijunction solar cell materials (Ge, GaAs and InGaP) are also shown for comparison. (after [28])

conventional solar panel design, but mainly, I'd like to think, due to their greater potential for utility-scale electricity production.

Great potential could be in store for a subsection of the III-V material system, the III-nitrides. Among their excellent properties are high mobility, an apparent insensitivity to high dislocation densities and their radiation hardness (a superb quality for space applications). Recent re-measurement of the InN bandgap, which turns out to be on the order of 0.7 eV, has prompted several groups [28,29] to look into the feasibility of using InGaN alloys as possible candidates for fabricating high efficiency solar cells because they now cover the full solar spectrum (Figure 1-5). Modelling shows that a 5-junction stack approaches 50 % efficiency. However, achieving p-type doping, obtaining degenerately doped nitride material for tunnel junctions, reducing dislocation densities and choice of substrate are but some of the challenges for this material. Still, this might be a future material to reckon with.

1.3 High-efficiency III-V solar cells

As can be deduced from the previous section, III-V concentrator solar cells are an excellent choice to satisfy the current demand for extra solar power [30] and to deliver the gigawatts that will be needed in the future.

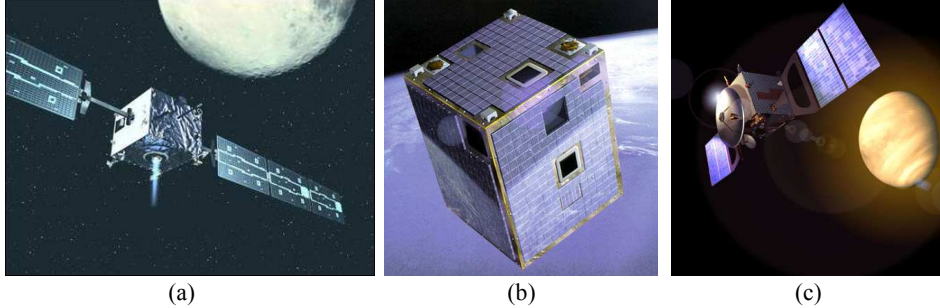


Figure 1-6: (a) *Smart-1 satellite with InGaP/GaAs multijunction solar cells [31], (b) Proba-1 satellite with GaAs solar cells [32] and (c) Venus Express with InGaP/GaAs/Ge triple junction solar cells [33].*

Until recently, space applications (satellites, exploration vehicles, see Figure 1-6) have been the main driving force for the development of high efficiency III-V solar cells. In this market segment the emphasis was mainly on reducing cell weight and increasing efficiency and less on cost reduction of the cell. Nowadays, it costs (on average [34]) \$10,000 to launch a kilogram into a Low Earth Orbit (LEO) and \$22,000 into a Geosynchronous Orbit (GEO). Hence, any mass reduction of the solar panels results in a considerable reduction of launch cost or, alternatively, allows for an increase of the useful payload mass. Furthermore, III-V cells are reliable and offer good radiation hardness, resulting in a high end-of-life (EOL) efficiency.

High efficiency III-V solar cells consist of multiple junctions of semiconductor material with different bandgap stacked on top of each other, with the biggest bandgap on top and the smallest one at the bottom of the stack. In that way, each junction converts a different portion of the solar spectrum into electrical power so that the total conversion is more efficient than by using a single junction. Today's commercially available lattice-matched triple junction space cells – InGaP(1.87eV) / InGaAs(1.41eV) / Ge(0.67eV) triple junction – demonstrate average lot efficiencies ranging from 27.8 to 28.5 % under AM0 conditions [35]. The logical next step in increasing cell efficiency would be to use a 1eV material as the third junction in a quadruple junction cell. Unless the material quality of this 1eV compound, GaInNAs, is improved, this step will be skipped. Instead, moving directly to quintuple (with or without GaInNAs) or even sextuple junction cells (with GaInNAs) is considered. In these cases, current matching requires thinner layers so GaInNAs would generate enough current, in spite of its low minority carrier diffusion length [35]. But increasing the number of subcells makes the fabrication process considerably more complex. The design has to be well thought over since current matching is crucial in a series connected monolithic stack and degradation of the layers also has to be considered in this respect. Nevertheless, a 5-junction cell has already been demonstrated: for an InAlGaP / InGaP / InAlGaAs / InGaAs / Ge cell, a V_{oc} of 5.196 V

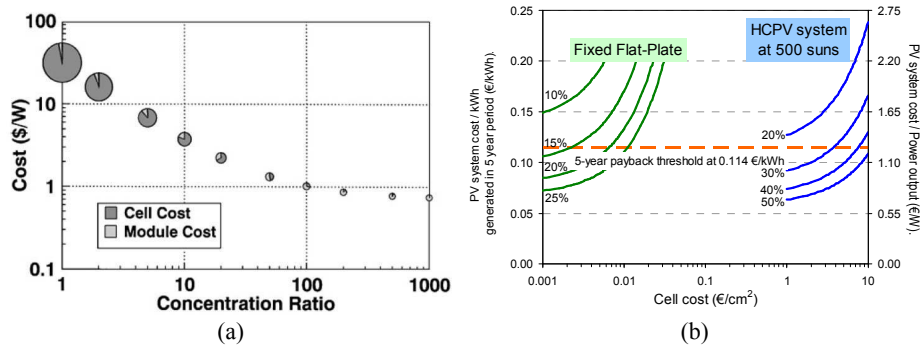


Figure 1-7: (a) Estimated cost for concentrator PV-systems (with share of cell cost) as function of the concentration ratio (b) PV-system cost per kWh with 5 year payback at 0.114 €/kWh (left axis) and PV-system cost per Watt (right axis) as a function of cell cost and cell efficiency, compared for fixed flat-plate and high concentration systems.

was recorded. The other parameters were thought unreliable due to the used spectral conditions [35]. For an InGaP / InGaP / InGaAs / InGaNAs 4-junction cell on Ge, a V_{oc} of 3.90 V was reported. Including an active Ge cell will increase this value to over 4.0 V [36]. However, the question remains whether these multijunction solar cells will have a better EOL performance than triple junction cells.

Over the last few years, the terrestrial solar market has become an additional incentive in multijunction cell development because these cells are the most likely candidates to achieve cost competitive electricity production prices in the near future. In order for this to happen, high-efficiency cells have to be used in concentrator systems with high enough concentration factors. Figure 1-7a shows that increasing the concentration factor reduces the cost, while simultaneously the share of the cell cost in the system cost also decreases [37]. For example, the data in Figure 1-7b (adapted from [38]; dollar is converted to euro) suggests that multijunction cells at 500 suns are cost competitive with fixed flat-plate modules when the cell cost is lower than 4 €/cm² for 30% cells and lower than 8 €/cm² for 40% cells. Price reduction will be an automatic consequence of economies-of-scale when cell production can be ramped up due to an increased demand. Further reduction can be achieved by using terrestrial-grade (=lower quality) germanium wafers and by implementing cell fabrication (= processing) improvements [38].

So far, nothing has been said about the nature of the stack in multijunction solar cells. These cells can be grown monolithically, meaning that all junctions are grown after one another on the same substrate and one ends up with a two-terminal device. A different approach is to take different junctions and stack them mechanically on top of each other. This leads to a 2n-terminal device (n being the number of separate junctions).

To date, the monolithic stacks on germanium give the best results for terrestrial photovoltaic conversion: 40.7 % (see §1.2). For these cells, a low-bandgap bottom cell is obtained by making the germanium active when nucleating growth on the substrate for the deposition of subsequent epitaxial layers. Since monolithic stacking implies a series connection of the cells, only the smallest generated photocurrent can flow through the stack. Thus, current matching has to be ensured between the different junctions to optimise power generation. This is realised by tuning the thickness – hence light absorption, hence photocurrent generation – of the subcells. A good understanding of the radiation induced degradation of each material is also important in case of space application. Radiation will create additional defects in the material, which might compromise the current matching in the long run. Therefore, the individual junctions have to be designed in such a way that the cells still have a respectable EOL performance. In this monolithic approach, interconnection of the components is realised via tunnel junctions that are an integral part of the cell's growth sequence. Special care has to be taken that these tunnel junctions have peak current densities higher than the cell's short-circuit current under optimal concentrator conditions. If not, the cell will not be able to live up to its full potential.

Mechanical stacks have the advantage that individual junctions can be chosen regardless of them being lattice-matched or not, which means there is also a broader choice in available bandgaps. Furthermore, each individual junction can be used to its full potential since there is no more need for current matching between them. On the module level, however, the interconnection scheme becomes somewhat more complex: there is now the need for voltage matching. Naturally, the more terminals one has per stack, the more complex is the interconnection on the module level. Though this might not pose real problems for terrestrial modules, it is not beneficial for space deployment of modules since added interconnection complexity means extra weight.

A compromise can be found by combining the two (extreme) situations discussed above. One can stack a monolithic multijunction solar cell mechanically on top of a bottom device (single- or multijunction cell). This approach to realising high-efficiency multijunction solar cells is part of imec's Solar+ roadmap. We will combine a high-efficiency dual junction monolithic III-V solar cell with a highly efficient thin germanium bottom cell [39], thus forming a four-terminal mechanically stacked high-efficiency multijunction solar cell. In this way, the entire generated photocurrent of the germanium bottom cell can be extracted whereas it would otherwise only partially contribute due to the current matching restriction.

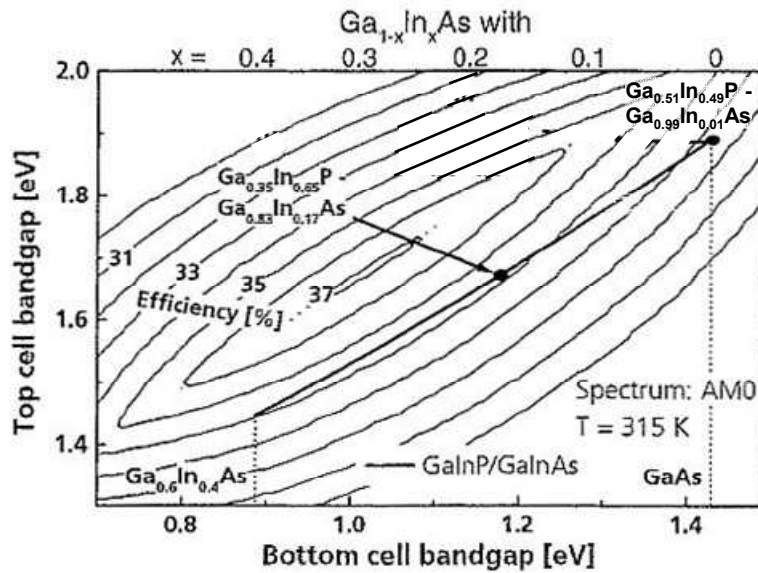
1.4 The dual junction III-V solar cell

Standard state of the art dual (and triple) junction solar cells consist of an InGaP top cell followed by a GaAs cell, grown lattice-matched to a Ge substrate. Germanium has a higher mechanical strength than GaAs, allowing for thinner substrates with the immediate benefit of a 32 % weight reduction on module level for space applications (when using standard substrate thicknesses). Furthermore, Ge substrates are also 2 to 3 times cheaper than GaAs ones.

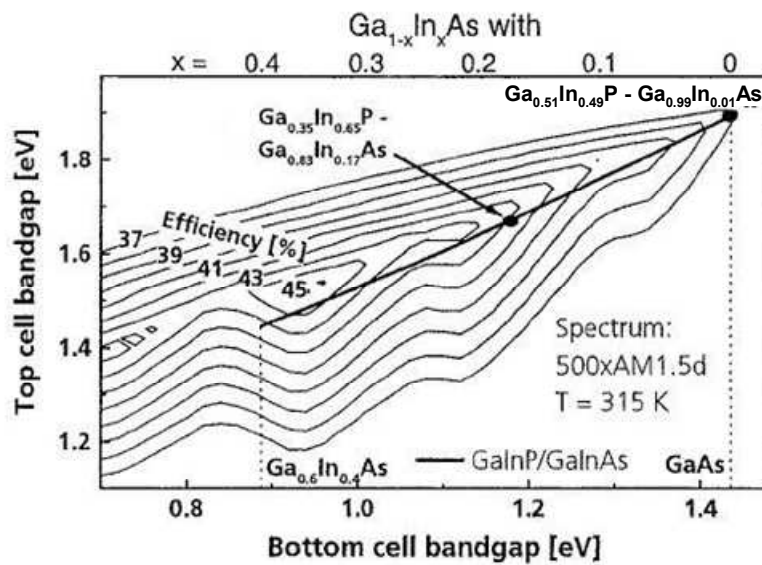
Growing lattice-matched to the substrate leaves you with only one possible material composition and, hence, bandgap combination: $\text{In}_{0.495}\text{Ga}_{0.505}\text{P}$ (1.87 eV, disordered alloy) and $\text{In}_{0.01}\text{Ga}_{0.99}\text{As}$ (1.41 eV). This combination yields a theoretical efficiency of 32.6 % under the AM0 solar spectrum (Figure 1-8a). When used in a concentrator system, the efficiency of this stack is 36.8 % if the light is concentrated 500 times (Figure 1-8b). By relaxing the constraint for lattice-matching between the substrate and the active cell structures the theoretical efficiency limit of the device can be increased even further. A tandem solar cell consisting of an $\text{In}_{0.65}\text{Ga}_{0.35}\text{P}$ (1.68 eV) top cell and an $\text{In}_{0.17}\text{Ga}_{0.83}\text{As}$ (1.18 eV) bottom cell leads to an increase of the theoretical efficiency limit to about 34.2 % (a) and 41.6% (b), a relative increase of approximately 5 % and 13 %, respectively [40]. Increasing this value more is possible by activating the germanium substrate, i.e. creating a third junction in the stack with a bandgap lower than that of InGaAs. This monolithic germanium junction is used in state-of-the-art multijunction devices but is not part of the stack under development at imec.

In the metamorphic approach – where the active device layers are compounds that are lattice-mismatched to the substrate, thus inducing strain relaxation and, consequently, generation of dislocations – a suitable buffer structure has to be used to reduce the number of threading dislocations (TD) propagating into the active cell layers. These TDs cause recombination in the active layers and limit the diffusion length (L_D) in the material when their average spacing is of the order of or less than one L_D . A TD density in the range of 10^5 to 10^6 cm^{-2} is necessary to obtain high efficiencies [41].

This thesis describes the development of a lattice-matched InGaP/GaAs tandem solar cell, an adequate buffer layer and a metamorphic InGaP / InGaAs tandem solar cell on Ge.



(a)



(b)

Figure 1-8: Theoretical efficiency limit of a monolithic dual junction solar cell at (a) AM0 and (b) 500xAM1.5D spectral conditions as a function of the bandgap of top and bottom cell.

1.5 Thesis outline

This first chapter is meant to make the reader aware of the fact that it is necessary to produce energy in a different – a renewable – way instead of using fossil fuels. Apart from solar energy conversion, some other alternatives were briefly mentioned. An overview of the current status of the photovoltaic industry was given and of the capabilities of the III-V sector in more detail.

In the second chapter, the reader will get acquainted with the Metalorganic Vapour Phase Epitaxy (MOVPE) growth technique which is used to deposit all the layers needed for this work. The reason for choosing metalorganic sources for the group-V precursors will be explained.

A third chapter will review the working principles of a solar cell and tunnel junction. The latter is a very important component when you want to make a monolithic multijunction solar cell. The quality of this tunnel junction may influence the performance of the cell in a drastic way.

Then the results concerning lattice-matched devices will be presented in chapter four. The GaAs and InGaP single junction solar cells on germanium will be discussed first. Also, some attention will be given to hydrogen plasma passivation of defects in the grown layers. This is followed by results on the (AlGaAs) tunnel junction. The results on the InGaP/GaAs dual junction cell will conclude the chapter.

For the transition to metamorphic materials an adequate buffer layer is needed. Chapter five will look into buffer layers and the development thereof. The results on metamorphic layers grown on this buffer will also be treated in this chapter. The InGaAs and InGaP single junction metamorphic solar cells on germanium will be discussed first. This is followed by results on the (AlGaAs) tunnel junction sandwiched between metamorphic layers. The InGaP / InGaAs dual junction cell will conclude the chapter.

A final chapter will review the results obtained in the thesis and draw some conclusions. Furthermore, possible future improvements on our own work as well as an outlook into where III-V solar cells are headed will be given.

1.6 References

- [1] <http://www.worldenergyoutlook.org/2006.asp>
- [2] <http://earthtrends.wri.org/updates/node/100>
- [3] <http://www.radford.edu/~wkovarik/oil/>
- [4] N.S. Lewis, "Global energy perspective", <http://nsl.caltech.edu/energy.html>, (2004).
- [5] <http://www.climatecrisis.net/>
- [6] <http://www.world-nuclear.org/info/inf75.htm> (June 2006)
- [7] <http://news.bbc.co.uk/2/hi/science/nature/4627237.stm>
- [8] <http://www.solarsystems.com.au/>
- [9] <http://www.powergeneration.siemens.com/en/windpower/index.cfm>
- [10] <http://www.marineturbines.com/>
- [11] J. Zhao et al., "24.5% efficiency silicon PERT cells on MCZ substrates and 24.7% efficiency PERL cells on FZ substrates", *Progress in Photovoltaics: Research and Applications*, Vol. 7 (6), 471-474 (1999).
- [12] O. Schultz et al., "Thermal oxidation processes for high-efficiency multicrystalline silicon solar cells", *Proceedings of the 19th European Photovoltaic Solar Energy Conference*, 604-607 (2004).
- [13] "A Belgian beauty, Photovoltech starts serial production of attractive back-contact cells", *Photon international*, 32-35, June 2004.
- [14] M.J. McCann et al., "A review of thin-film crystalline silicon for solar cell applications. Part 1: Native substrates", *Solar energy materials and solar cells*, Vol. 68, 135-171 (2001).
- [15] X. Wu et al., "16.5%-efficient CdS/CdTe poly-crystalline thin-film solar cell", *Proceedings of the 17th European Photovoltaic Solar Energy Conference*, 995-1000 (2001).
- [16] M.A. Contreras et al., "Progress towards 20% efficiency in Cu(In,Ga)Se polycrystalline thin-film solar cell", *Progress in Photovoltaics: Research and applications*, Vol. 7, 311-316 (1999).
- [17] D. Bonnet, "The evolution of the CdTe thin film solar cell", *Proceedings of the 19th European Photovoltaic Solar Energy Conference*, 1657-1662 (2004).
- [18] P.D. Moskowitz et al., "Health and Environmental Hazards of CdTe Photovoltaic Module Production, Use and Decommissioning", *Proceedings of the 1st World Conference on Photovoltaic Energy Conversion*, 115-118 (1994).
- [19] <http://compoundsemiconductor.net/articles/news/10/11/1>
http://www.lbl.gov/msd/Pis/Walukiewicz/06/0_2_Walukiewicz.html.
- [20] C.J. Brabec, "Organic photovoltaics: technology and market", *Solar Energy Materials & Solar Cells*, Vol. 83, 273-292 (2004).
- [21] <http://www.technologyreview.com/Energy/17246/page1/>

- [22] <http://compoundsemiconductor.net/articles/magazine/9/11/2/1>
- [23] R.R. King et al., "Metamorphic concentrator solar cells with over 40 % conversion efficiency", Proceedings of the International Conference on Solar Concentrators for the Generation of Electricity or Hydrogen, to be published (2007).
- [24] <http://www.energy.gov/news/4503.htm>
- [25] <http://compoundsemiconductor.net/articles/news/10/2/18/1>
- [26] <http://compoundsemiconductor.net/articles/news/10/8/22/1>
- [27] <http://compoundsemiconductor.net/articles/news/10/11/8/1>
- [28] J. Wu et al., "Superior radiation resistance of $\text{In}_{1-x}\text{Ga}_x\text{N}$ alloys: full-solar-spectrum photovoltaic material system", Journal of Applied Physics, Vol. 94 (10), 6477-6482 (2003).
- [29] C. Honsberg et al., "InGaN – a new solar cell material", Proceedings of the 19th European Photovoltaic Solar Energy Conference, 15-20 (2004).
- [30] <http://www.redherring.com/Article.aspx?a=19186&hed=Three+Huge%26nbsp%3bSolar+Trends>
- [31] <http://smart.esa.int/science-e/www/object/index.cfm?fobjectid=31407&fbodylongid=850>
- [32] http://www.esa.int/SPECIALS/Proba_web_site/ESA6AKTHN6D_0.html
- [33] http://www.esa.int/SPECIALS/Venus_Express/SEMEE3808BE_0.html
- [34] M. Raja Reddy, "Space solar cells – tradeoff analysis", Solar Energy Materials & Solar Cells, Vol. 77, 175-208 (2003).
- [35] M. Meusel et al., "European roadmap for the development of III-V multijunction space solar cells", Proceedings of the 19th European Photovoltaic Solar Energy Conference, 3581-3586 (2004).
- [36] R.R. King et al., "High-voltage, low-current GaInP/GaInP/GaAs/GaInNAs/Ge solar cells", Proceedings of the 29th IEEE Photovoltaic Specialists Conference, 852-855 (2002).
- [37] M. Yamaguchi, "III-V compound multijunction solar cells: present and future", Solar Energy Materials & Solar Cells, Vol. 75, 261-269 (2003).
- [38] R.A. Sherif et al., "The path to 1 GW of concentrator photovoltaics using multijunction solar cells", Proceedings of the 31st IEEE Photovoltaic Solar Energy Conference, 17-22 (2005).
- [39] N.R. Posthuma et al., "Recent progress in the development of a stand-alone germanium solar cell", Proceedings of the 21st European Photovoltaic Solar Energy Conference, 137-140 (2006).
- [40] F. Dimroth et al., "Metamorphic $\text{Ga}_y\text{In}_{1-y}\text{P} / \text{Ga}_{1-x}\text{In}_x\text{As}$ tandem solar cells for space and for terrestrial concentrator applications at $C > 1000$ suns", Progress in Photovoltaics: Research and Applications, Vol. 9, 165-178 (2001).
- [41] S.A. Ringel et al., "Single junction InGaP/GaAs solar cells grown on Si substrates with SiGe buffer layers", Progress in Photovoltaics: Research and Applications, Vol. 10, 417-426 (2002).

Chapter 2

Metalorganic Vapour Phase Epitaxy

2.1 Introduction

The growth technology for multijunction solar cells must be able to grow high quality bulk material, grow abrupt material interfaces, control the doping profile, control the thickness of the deposited layers over large areas, have a reasonable growth rate, be capable of large cell area throughput, be cost effective and be available as a commercial reactor. Possible growth technologies include molecular beam epitaxy (MBE), liquid phase epitaxy (LPE) and metalorganic vapour phase epitaxy (MOVPE).

LPE can easily deal with simple compound systems, e.g. (Al,Ga)As, but not with multiple component systems. Including phosphorus and indium compounds to the (Al,Ga)As system, which is inevitable if one wants to make monolithic multijunction solar cells, only adds to the complexity of the technique. Furthermore, using multiple dopants complicates matters even more. The thickness uniformity of the grown layers is generally poor. MBE, on the other hand, is an excellent growth technology. It allows for deposition of high quality bulk material with sharp interfaces and doping profiles and of uniform thickness. It can also benefit from a diversity of in-situ characterisation techniques (e.g. RHEED). A limited growth rate is a downside to the technology, as well as difficulty in growing phosphorus-containing materials, incapability for large area throughput and maintenance (ultra-high vacuum, downtime). MOVPE is the preferred epitaxial growth technique in industry and research facilities for the fabrication of solar cells in III-V semiconductor material. It has all the above mentioned necessary qualities for uniform device growth, while at the same time being a flexible technology with a relatively simple reactor design. Drawbacks include choice of only few in-situ characterisation techniques and using expensive and dangerous (toxic) chemicals that require stringent safety measures.

In this chapter, a principle-of-operation overview of the MOVPE system will be given. The MOVPE thermodynamics will be summarised to clarify the process' driving force. Reaction kinetics will give us a means to determine the activation energy of the rate-limiting step. Also, the generally accepted reactions that take place during pyrolysis of the precursors are presented. The existence of a boundary layer at the solid/vapour interface is shown and a simple model for calculation of the growth rate derived. The reasons for choosing TBAs and TBP as group-V precursors are clarified. Finally, some short conclusions are drawn. A general reference for this second chapter is G.B. Stringfellow [1], where the interested reader can also find more details.

2.2 Principle of operation

A brief and simple synopsis of the MOVPE growth sequence (= a run) is as follows. A substrate is loaded into a reactor and is heated up. The source materials are transported to it where they are thermally decomposed, partly in the gas phase and partly on the surface. The introduced atoms are then incorporated into a crystal lattice growing on the substrate surface.

An MOVPE system consists of several parts: the interface module (IM), the reactor cabinet, the gas cabinet and the scrubber. The IM is the central nerve system. This is where the communication between the computer and the system takes place. It also houses the different interlocks that enable safe systems operation. The reactor is situated inside a glovebox in the reactor cabinet and is of the vertical type with a close-coupled showerhead above a rotating graphite susceptor (see right hand side of Figure 2-1 for reactor parts). The glovebox is kept under nitrogen to prevent oxygen and water vapour from contaminating the reactor when it is opened to be loaded. A substrate is loaded into the reactor via a load lock, which is first pumped down and then refilled with nitrogen. On a panel of the reactor cabinet one finds the heater and the pressure control unit. The reactor pressure is regulated by adjusting the position of the throttle valve between reactor and turbo pump. All MO-sources are stored in the gas cabinet. Also the gaseous sources (stored in bunkers) enter the system here. All flows are set in this part of the system by means of (input, dilution and output) mass flow controllers, as are the bubbler pressures (by pressure controllers). Which chemicals are sent to the reactor is regulated by the switching manifold. If a source line is not used, it is switched to the vent and sent directly to the waste gas treatment. Waste gasses coming from the reactor are sent through a scrubber. There are two big scrubber columns (to ensure continuous operation) filled with resin, a metal oxide that adsorbs the remaining toxics in the waste gasses. An oxidation process converts the toxics into stable oxides while, at the same time, making 50% of the sites available for adsorption again (= regeneration). The oxides don't desorb and are disposed of once a column of resin is completely full.

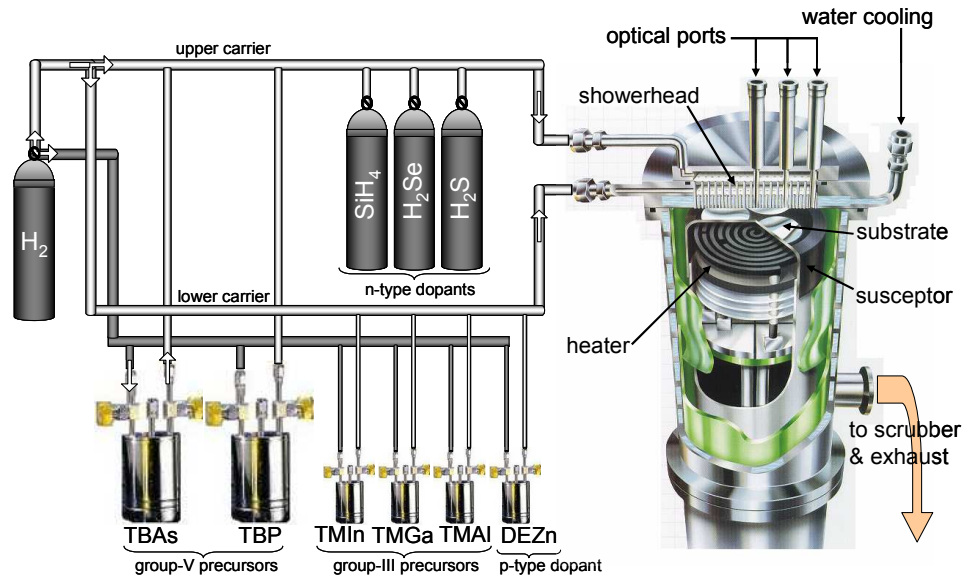


Figure 2-1: Principle of operation of a MOVPE system. The figure gives a schematic representation; for simplicity reasons mass flow and pressure controllers, the vent line and the switching manifold are not shown. The bubblers are placed in thermostatic baths (not shown) to keep them at constant temperature.

After a substrate is loaded into the temperature- and pressure-controlled reactor, the run can be started. First, the pressure is reduced to 76 torr and a low temperature bake-out (300°C) of the substrate is performed. Then the reactor temperature is increased to a standard value between 550°C and 750°C. In case of a germanium substrate, a high temperature bake-out is done to remove the surface oxide. Growth is then carried out at low pressure, 76 torr, after which the reactor is cooled down again. Finally, the substrate, with the deposited layers on it, can be unloaded.

As is clear from the name “III-V” compounds, the matrix elements are selected from the third and fifth column of Mendeleev’s periodic system. They are bound to organic groups to form metalorganic precursors or to hydrogen to form hydrides. The group-III sources we use are trimethylgallium (TMGa), trimethylaluminium (TMAI) and trimethylindium (TMIn). As group-V sources we use tertiarybutylarsine (TBAs) and tertiarybutylphosphine (TBP) instead of the hydrides arsine (AsH_3) and phosphine (PH_3). Dopant sources are diethylzinc (DEZn) for p-type material and silane (SiH_4), hydrogen selenide (H_2Se) or hydrogen sulfide (H_2S) for n-type material. The MOs are either liquid or solid and are kept in stainless steel canisters, also known as bubblers, at a certain temperature and pressure, to obtain the desired equilibrium vapour pressure of the metalorganic material. To transfer the molecules into the reactor, a carrier gas, H_2 , “bubbles” (= passes) through the MO source and, in this way, becomes saturated with

the MO material. The saturated hydrogen flow is then injected into the main carrier lines that go to the reactor (see left hand side of Figure 2-1). The source molecules then enter the heated reactor chamber where they are thermally cracked and adsorbed on the wafer surface. There further reactions cause crystal layers to be grown.

2.3 Thermodynamics

2.3.1 Equilibrium conditions

Thermodynamics provides the basic driving force for epitaxial growth. During MOVPE growth, we have the vapour and the solid phase, i.e. the epitaxial layer being grown. The basic goal of thermodynamics, as applied to epitaxy, is to define the relationship between the compositions of the various phases in an equilibrium system at constant temperature (T) and pressure (P). Equilibrium is the state where the Gibbs free energy (G) is minimal. The Gibbs free energy is defined as:

$$G = H - TS, \quad (2.1)$$

where H is the enthalpy and S the entropy. Since the total free energy for a two-phase (α and β) system $G = G_\alpha + G_\beta$ is minimal at equilibrium, moving an infinitesimally small number of moles of component i , dn_i , between the two phases causes no change in G :

$$\left(\frac{\partial G}{\partial n_i}\right)_{T,P,n_j}^\alpha - \left(\frac{\partial G}{\partial n_i}\right)_{T,P,n_j}^\beta = 0. \quad (2.2)$$

This equilibrium condition can be rewritten for each component in the system as

$$\mu_i^\alpha = \mu_i^\beta, \quad (2.3)$$

where μ_i is called the chemical potential. For an ideal gas mixture and for a non-ideal liquid or solid solution, respectively, μ_i can be expressed as

$$\mu_i = \mu_i^0 + RT \ln \frac{p_i}{p_i^0}, \quad (\text{gas}) \quad (2.4a)$$

$$\mu_i = \mu_i^0 + RT \ln a_i, \quad (\text{solid}) \quad (2.4b)$$

where p_i is the partial pressure of the source molecule, μ_i^0 and p_i^0 are the chemical potential and partial pressure of the equilibrium state of the atom at the vapour/solid interface and a_i is the activity of the elements in the solid.

To grow almost perfectly stoichiometric III-V semiconductor alloys, the molar ratio of group-V to group-III MO molecules in the vapour phase has to be greater than unity. This is because the group-V elements typically have high vapour pressures (e.g. As₄: 0.8 torr at 400 °C), whereas the group-III elements have low ones (e.g. Ga: 2×10^{-7} torr at 700 °C). An excess of group-V species escapes from the solid surface back to the gas

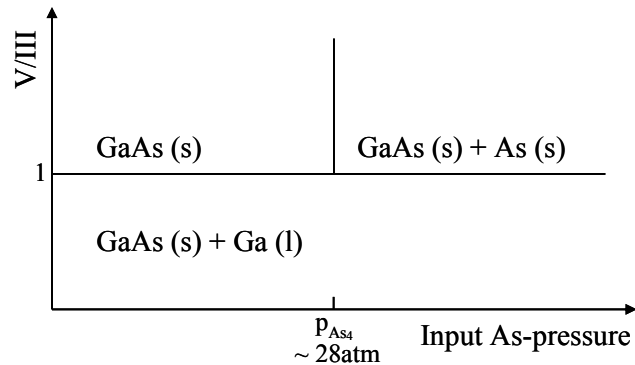


Figure 2-2: GaAs phase diagram appropriate for MOVPE growth. The region containing a single solid GaAs phase and the two two-phase regions are shown.

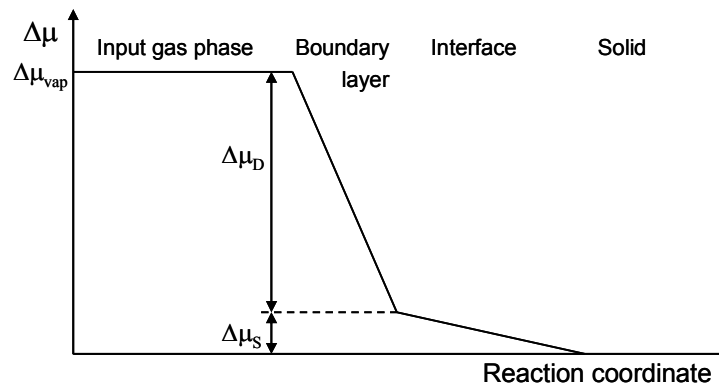


Figure 2-3: Schematic diagram of the chemical potential versus reaction coordinate in the case where $\Delta\mu_s \ll \Delta\mu_D$.

phase, whereas an excess of group-III species would give rise to a second condensed phase. In this way, essentially all group-III atoms are incorporated into the growing solid and a single condensed phase is obtained. This is illustrated for GaAs in Figure 2-2. Under normal MOVPE conditions, the region in the top right corner of the diagram can not be reached.

In the MOVPE process the overall thermodynamic driving force for growth, i.e. the supersaturation of the input vapour relative to the solid, $\Delta\mu_{vap}$, is usually very large. It seems surprising that the condition of thermodynamic equilibrium can still be used to approximate the relation between the composition of the vapour at the solid/vapour interface and the solid. Evidently, the fact that the crystal is steadily formed from the vapour ensures that this condition is not exactly satisfied, but the departure from

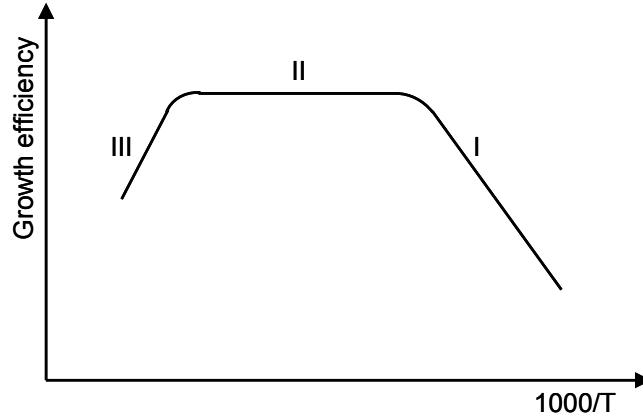


Figure 2-4: Arrhenius plot of the growth efficiency versus reciprocal temperature, showing the different growth regimes: kinetically- (I), mass-transport- (II) and desorption limited (III).

equilibrium, $\Delta\mu_s$, is negligibly small. The supersaturation is nearly entirely used to drive the mass transport process ($\Delta\mu_D$) to the vapour/solid interface. This division of the chemical potential is shown schematically in Figure 2-3 versus reaction coordinate.

When interface kinetics are much faster than diffusion kinetics (the case above), we are in a situation where the growth rate is nearly temperature independent. This is called diffusion or mass-transport limited growth. Below a certain temperature, surface kinetics limits the process, the growth rate decreases exponentially with decreasing temperature. We will come back to this in §4.5.1. Above a certain temperature, the growth rate may be limited by desorption of species from the solid surface. This is schematically illustrated in Figure 2-4.

2.3.2 Solid composition

Since the input vapour is supersaturated, $p_{III}^v p_V^v \gg p_{III}^i p_V^i$, (v : vapour, i : interface), and the V/III ratio is (much) larger than one, $p_{III}^v \ll p_V^v$, the group-III atoms are nearly depleted at the interface, $p_{III}^i \ll p_{III}^v$, whereas the group-V atoms are almost unaffected, $p_V^i \approx p_V^v$. This means that all group-III atoms reaching the vapour/solid interface are incorporated into the growing solid. For a ternary alloy $A_x B_{1-x} C$ with mixing on the group-III sublattice, a distribution coefficient, k , can be defined:

$$k = \frac{x/(1-x)}{p_A^v/p_B^v}. \quad (2.5)$$

In most cases k is almost unity. However, the distribution coefficient can be influenced by higher growth temperatures and strain in the lattice.

2.3.3 Dopant incorporation

Dopant elements for III-V semiconductors are selected from the second, the fourth or the sixth column of Mendeleev's table. An element from the second column (e.g. Zn) is incorporated on the group-III sublattice, thus, having one electron short, gives rise to p-type material. An atom from column six (e.g. Se) is incorporated on the group-V sublattice and, having one excess electron, results in n-type material. Elements from the fourth column can, in principle, be incorporated on either sublattice (= amphoteric behaviour). When it goes on the group-III sublattice, n-type material is obtained. Reversely, on the group-V sublattice p-type material is produced.

Dopant incorporation can also be characterised by a distribution coefficient k , where k equals the ratio of the dopant concentration in the solid to the ratio of the molar flows of dopant to (relevant) matrix element in the vapour phase. The dopant atoms can be divided into two categories according to their equilibrium vapour pressure.

For low vapour pressure dopants incorporated on the group-III sublattice (e.g. Si), the distribution coefficient is inversely proportional to the growth rate and independent of both temperature and p_V^v . However, as we will see later on, SiH_4 does show a temperature dependency due to incomplete pyrolysis at low growth temperatures.

For high vapour pressure dopants two scenarios can be discerned. One, if the dopant is incorporated on the group-III sublattice (e.g. Zn), k is independent of the growth rate, inversely proportional with temperature and proportional with p_V^v . And two, if the dopant is incorporated on the group-V sublattice (e.g. Se), the distribution coefficient is independent of growth rate and inversely proportional with temperature and p_V^v .

2.4 Metalorganic group-V precursors

To grow arsenide and phosphide materials, there are several possible group-V precursors to choose from. The classic sources used by a large number of research groups and by the entire III-V commercial industry, are arsine (AsH_3 , see Figure 2-5) and phosphine (PH_3). The threshold limit values (TLVs, maximum permissible exposure limit based on an eight-hour work day) for AsH_3 and PH_3 are 0.05 and 0.3 ppm, respectively, thus they are highly toxic gasses [2]. In addition, they are stored in pure form in cylinders under high pressure. This signifies a serious threat because the rapid release of large quantities of these sources could affect an entire building or an even larger area in extreme cases. Clearly, the development and use of much less hazardous group-V precursors is a necessity, especially when used near densely populated areas. This approach also permits keeping the cost for adequate safety features acceptable.

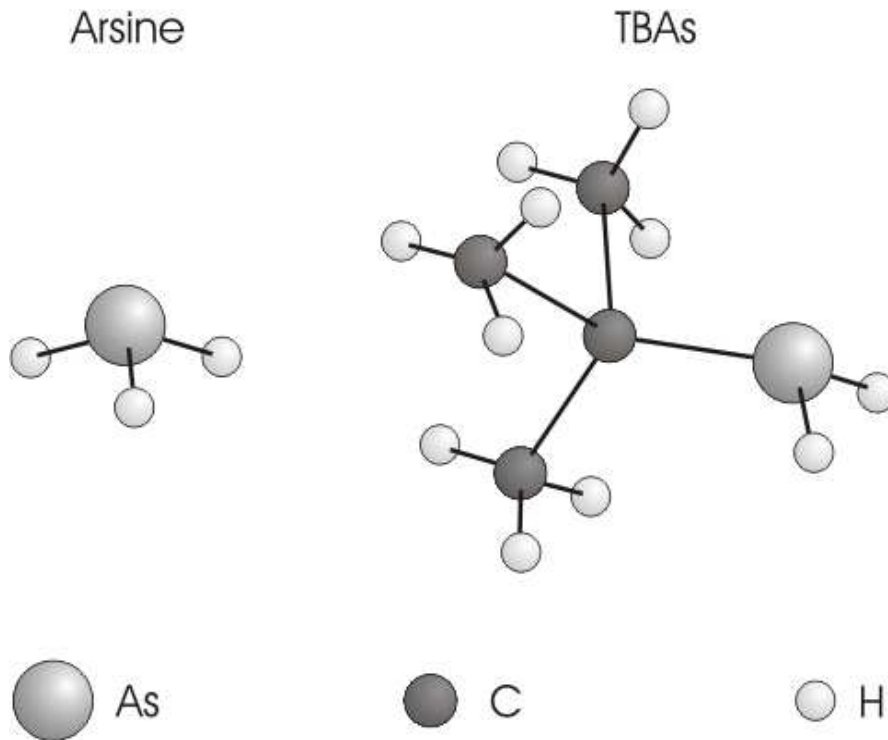


Figure 2-5: Schematic representation of arsine and TBAs molecule. Representations for phosphine and TBP are obtained by substituting a P-atom for an As-atom.

It seems that, in general, the toxicity of As and P sources increases with the number of As–H or P–H bonds. Metalorganic group-V precursors present a good alternative, since one or more H ligands are replaced by organic groups, thus reducing the toxicity of the molecule. The fact that these MO-sources are liquids, with a moderate vapour pressure, is an additional advantage. Computer modelling shows that the spreading of the molecules is 100× slower than for release from a high pressure cylinder, resulting in a dramatic decrease in hazard.

Imec has chosen tertiarybutylarsine (TBAs, see Figure 2-5) and tertiarybutylphosphine (TBP) as group-V MO-precursors in order to run its MOVPE-activities in less hazardous circumstances. As mentioned above, MOs are less toxic and have a much smaller spreading radius than hydrides. TBAs and TBP have the additional advantage of being pyrophoric so, when escaping through a leak, it pyrolyses in air to form a stable oxide, which is even less dangerous than a vapour. The TLV of TBAs is 0.5 ppm, a factor of 10 higher than for AsH₃, no data were found for TBP. In Table 2-1, the TLVs

Table 2-1: Comparison of TLV and LC₅₀ values (in ppm) for AsH₃, TBAs, PH₃ and TBP. The hydrides' lethal dose is also given.

Precursor	TLV [†]	LC ₅₀ [‡]	Lethal dose [#]
AsH ₃	0.05	5-50	500/(1-2)
TBAs	0.5	70	
PH ₃	0.3	11-50	2000/(1-2)
TBP	-	>1100	

[†]Based on an average 8-h work day; [‡]Based on rat mortality after 4-h exposure.

[#]Exposure level in concentration/time (min).

Table 2-2: Properties of group-V precursors. The operating temperatures of the MO-bubblers were chosen to illustrate their vapour pressure.

Precursor	Melting point (°C)	Boiling point (°C)	p (torr) / T (°C) [†]
AsH ₃	-117	-62	11400 / 20
TBAs	-1	69	152.0 / 25
PH ₃	-134	-88	26296 / 20
TBP	4	56.1	355.8 / 25

[†]Gas constants from Akzo Nobel were used to calculate the vapour pressure.

and LC₅₀ values (lethal concentration for 50% of a rat population after several hours of exposure) for AsH₃, TBAs, PH₃ and TBP are compared. For the hydrides the lethal dose is also included. Table 2-2 shows melting and boiling point and the equilibrium vapour pressure at normal operating conditions of the group-V precursors.

Safety is a principal reason for choosing MO-precursors over hydrides. Lower temperatures required for pyrolysis is another. This is an important quality for low temperature growth of fine features in high-performance devices. TBAs pyrolyses at much lower temperatures than AsH₃; pyrolysis is 50% complete at 370°C, compared with 560-600 °C for AsH₃. TBP is 50% pyrolysed at 475°C whereas for PH₃ this is 640-720 °C. From calculations it is noticed that the rate constants for pyrolysis of the hydrides decrease linearly with decreasing reactor pressure. This implies that for high-quality layers at low pressures, hydrides demand much higher V/III ratios than MO-sources, as observed experimentally. A direct consequence is lower consumption of the MO-precursors, which is a bonus: this entails a big cost reduction since the MOs are more expensive than the hydrides.

When growing III-V layers with group-V MO-precursors, we desire a material that is at least of equal quality compared to growing with hydrides, as a reduction in material quality might invalidate the substitution of MOs for hydrides. Several studies were performed to compare the results between layers grown with AsH₃ and layers grown with TBAs. Watkins et al. reported high purity, high mobility InAs layers on GaAs grown at 400°C [3]. Mashita et al. showed lower carbon incorporation for Al_{0.7}Ga_{0.3}As layers grown with TBAs [4]. Low oxygen-content high-quality AlGaAs have been produced at low growth temperatures (625°C) and low V/III ratios (25) [5][6]. Also our own experiments show that carbon and oxygen incorporation in (Al,Ga)As layers is reduced when using TBAs [7]. Substituting TBP for PH₃ resulted in high-quality InP based materials (InP, In(Al,Ga)P) with low oxygen [6][8][9] and low carbon content [9], although some authors report problems related to oxygen impurities [10] or zinc diffusion via group-III interstitials [11].

But, of course, other requirements have to be fulfilled as well in order to be a useful source material. It is preferred that the precursor is a liquid at room temperature with a vapour pressure ≥ 10 -50 torr (see for material properties) to avoid problems with reproducible transport to the reactor and with condensation of the source material in the lines downstream of the bubbler. The precursor must be stable so that it is easily (and economically) synthesized and purified (oxygen). Its shelf lifetime must be measured in years. On the other hand, the molecule must be “unstable” enough to allow for the low temperature pyrolysis, which will be discussed in the next paragraph. Also, parasitic reactions with group-III precursors upstream from the substrate are undesirable.

2.5 Reaction kinetics

Since MOVPE is not an equilibrium process, thermodynamics can only define certain limits for the growth process, e.g. the driving force, maximum growth rate and number and compositions of the equilibrium phases in the bulk or on the surface. To gather information about reaction times, - steps and - rates that are involved in MOVPE growth, a kinetic approach has to be used. Under certain conditions, such as at low temperatures, the thermodynamic equilibrium approximation cannot be used.

In the chemical reactions, the transition from reactants to products is assumed to happen via formation of an activated complex, which requires extra energy, the activation energy E^* . The rates of both the forward and reverse reaction can be written as the product of the concentration and the rate constant, k , which may be expressed in terms of the Arrhenius equation

$$k = A e^{\frac{-E^*}{RT}}, \quad (2.6)$$

where A is the pre-exponential factor and E^* is the activation energy for the reaction. These are not equal for forward and reverse reaction; the values for E^* differ by the thermodynamic enthalpy difference from initial to final state $\Delta H = E_1^* - E_{-1}^*$. The equilibrium constant for the reaction can be written in function of the Gibbs free energy change for the chemical reaction, ΔG :

$$K = e^{\frac{-\Delta G}{RT}}, \quad (2.7)$$

where $\Delta G = \Delta G_1^* - \Delta G_{-1}^*$, the difference between the free energies of activation for the forward and reverse reaction.

One of the most important pyrolysis reactions is homolysis or bond breaking of an AB molecule via an excited transition state AB^* . The first-order rate constant for this step is:

$$k_{AB} = \frac{kT}{h} K_{AB}^*. \quad (2.8)$$

The equilibrium constant for the formation of the excited transition state can be written in terms of the free energy of activation ΔG_{AB}^* (Eq. (2.7)):

$$K_{AB}^* = e^{\frac{-\Delta G_{AB}^*}{RT}}. \quad (2.9)$$

The rate constant can now be written as (using Eq.(2.1))

$$k_{AB} = \left(\frac{kT}{h} e^{\frac{\Delta S^*}{R}} \right) e^{\frac{-\Delta H^*}{RT}}, \quad (2.10)$$

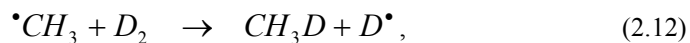
allowing us to identify the pre-exponential factor A as the expression between brackets.

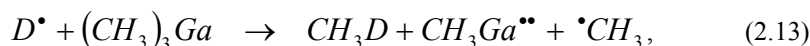
In the heated areas of the reactor the chain of reactions that lead to the deposition of III-V material, are triggered by pyrolysis of the source molecules. This is not simply the sequential, thermally-induced loss of the “organic” radicals but rather an intricate array of reactions, including complex radical reactions. Furthermore, both homogeneous and heterogeneous reactions occur, involving several precursors and their intermediates, in a thermally and compositionally inhomogeneous system. The pyrolysis will also be affected by the reactor pressure, geometry and flow conditions. But mostly the overall reaction rate is often controlled by a rate-limiting step. Under standard growth conditions this is usually the group-III precursor pyrolysis.

The pyrolysis of TMGa for example, is initiated by homolysis of the precursor molecule:



The chain reaction propagates via

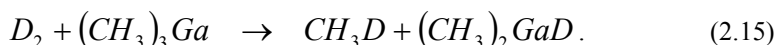




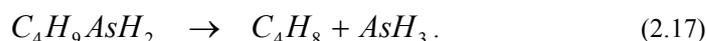
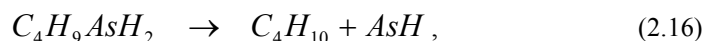
where $CH_3Ga^{\bullet\bullet}$ arrives at the solid surface. The chain is terminated by (for inert ambient)



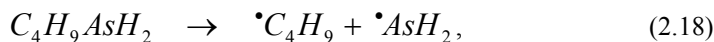
It has to be noted that, in practice, Eq. (2.14) only has a small chance of occurring due to the very large excess of the H_2 ambient in the actual process and it is thus more likely that the chain reaction keeps propagating via Eq. (2.12). The reactions are presented here in a D_2 (deuterium) ambient. Replacing D_2 with H_2 results in a faster reaction Eq. (2.12) due to the lower molecular bond strength and for N_2 or He ambient (inert ambient), the chain cannot propagate via this reaction. This illustrates the involvement and the importance of the carrier gas in the rate determining steps. An alternative explanation of the ambient effect may be that TMGa reacts directly with D_2 (or H_2) by hydrogenolysis:



The earliest pyrolysis studies of TBAs indicated the mechanism to be two parallel unimolecular reactions, a reductive coupling and a β -hydrogen elimination reaction, respectively:



Experiments in D_2 ambient led to the conclusion that TBAs does not react with the ambient. Also the radical attack model is suggested, initiated by homolysis of the TBAs molecule:



whereby C_4H_8 is formed via



and C_4H_{10} by radical attack of the parent molecule:



More recently, the direct loss of H_2 forming C_4H_9As is predicted to have lower activation energy than the three mechanisms mentioned above. Via a β -hydrogen elimination reaction C_4H_8 and AsH are formed, but no unimolecular reaction with low activation energy could be found for the production of C_4H_{10} . A bimolecular reaction was suggested. This model is able to explain many of the experimental observations, but has difficulty explaining the excess C_4H_{10} over C_4H_8 at 1 atmosphere. Clearly, the pyrolysis of TBAs is very complex and it may well be that several of the proposed reactions compete with one another.

When TMGa and TBAs are introduced into the same reactor, it seems logical that they will affect each others decomposition mechanism. A number of observations will now be summarised. The decomposition of TBAs is essentially unaffected by the presence of TMGa. The TMGa pyrolysis is enhanced by adding TBAs, but the decomposition temperature is almost independent of the TBAs/TMGa ratio. No CH_3D (Eqs. (2.12) and (2.13)) and C_2H_6 (Eq. (2.14)) were found when the ambient was D_2 , leading to the conclusion that virtually no independent homogeneous decomposition of TMGa occurs.

We believe that in the reactor the following processes dominate the decomposition of TBAs and TMGa. Since in a real situation TBAs is introduced into the reactor first, independent pyrolysis of TBAs occurs, leading to the presence of H-radicals and AsH_x ($x = \{1, 2, 3\}$) in the ambient. When TMGa is introduced into the reactor, H^\bullet and AsH_x then react with TMGa to produce CH_4 and $(\text{CH}_3)_2\text{Ga}^\bullet$. The decomposition continues resulting in Ga and As being built into the crystal lattice.

2.6 The boundary layer

The reactor we use is a vertical one with a close-coupled showerhead and rotating susceptor whereupon the substrate is placed. This means that the gas, coming out of the showerhead, flows downward and perpendicular to the substrate. The vapour stream is deflected and flows over the substrate. At the interface between the substrate and the vapour, the gas velocity is zero. Due to the gas viscosity and the latter boundary condition, there is a region of decreasing velocity, the boundary layer. On a rotating disk, this gas layer is forced outward by centrifugal force. The hydrodynamic equations can be solved exactly for an infinite disk (a good approximation when the disk radius is much larger than δ_0), giving the surprising result that the boundary layer thickness, δ_0 (Figure 2-6), is independent of z , the position on the susceptor, and is given by

$$\delta_0 \cong 4\sqrt{\frac{\nu}{\omega}}, \quad (2.21)$$

where ν is the kinematic viscosity and ω the angular rotation of the disk. Through this boundary layer mass transport occurs from the input gas phase to the interface with the solid.

For the calculation of the growth rate in the mass-transport limited regime, the boundary layer model is used. It is assumed that the boundary layer is a truly stagnant layer and that mass transport through it is only possible via Fickian diffusion, since the gas phase nutrients are typically very dilute for the MOVPE process. This is not hydrodynamically justified but it has proven to be a useful zeroth order approximation for analysis and interpretation of experimental results. The flux can then be written as

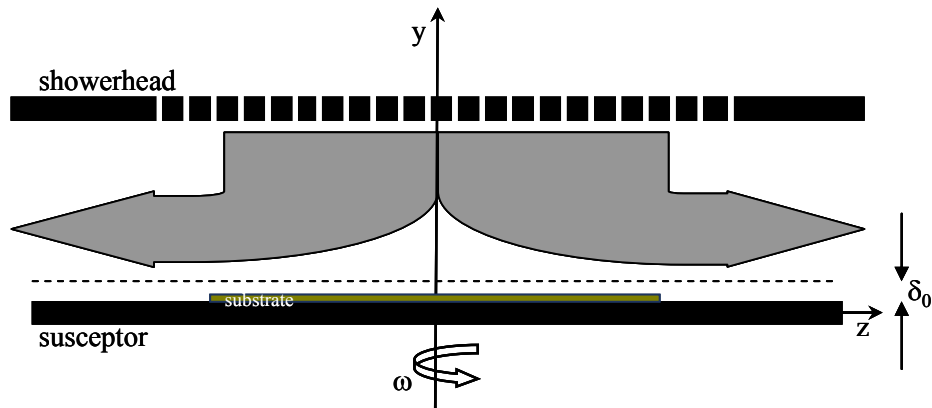


Figure 2-6: Direction of the gas flow in a vertical rotating disk reactor. The dashed line indicates the edge of the boundary layer.

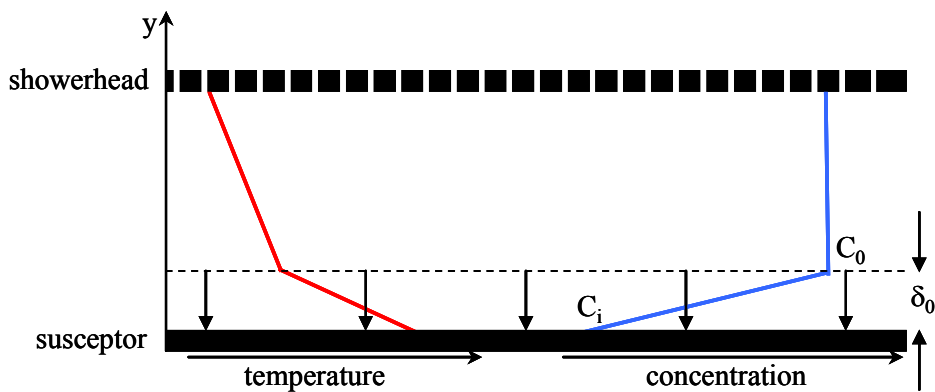


Figure 2-7: Temperature and concentration gradient in function of distance to susceptor.

$$J = -\frac{D(C_0 - C_i)}{\delta_0}, \quad (2.22)$$

with C_0 the concentration of the growth-rate-limiting species in the input gas phase and C_i that at the vapour/solid interface. D is the species' diffusion coefficient. The factor D/δ_0 should be considered as an adjustable parameter. The temperature gradient across the boundary layer (Figure 2-7) is usually approximated by an average temperature and is included in the temperature dependence of the diffusion coefficient. This very simple model cannot account for growth rate non-uniformities and other features encountered in actual MOVPE reactors. These days, finite element simulations are performed that do take into account the temperature gradient across the boundary layer and also the reactor geometry and its influence on the flow patterns.

2.7 Conclusion

In this chapter MOVPE was shown to be the preferred epitaxial technique for deposition of high quality, uniform layers over large areas in a cost effective way and capable of a high throughput and great flexibility in combining several III-V materials.

MOVPE is governed by thermodynamics which provides the overall driving force for the growth process, the supersaturation of the input vapour relative to the solid. Growth is possible by keeping the system in a continuous state of near-equilibrium at the vapour-solid interface. Under standard growth conditions, the growth rate is determined by mass transport through the boundary layer, although (reaction) kinetically limited growth is also possible at low temperatures.

Driven by the need for a safer process, metalorganic group-V precursors (TBAs and TBP) provide a good alternative to replace hydride sources (AsH_3 and PH_3). The ability to grow high-quality low-oxygen and low-carbon content layers makes them truly practical substitutes for a safer and more efficient epitaxial process at reduced temperatures and V/III ratios, even for high-aluminium content layers [6][8].

2.8 References

- [1] Gerald B. Stringfellow, "Organometallic Vapour-Phase Epitaxy: Theory and Practice", 2nd edition, Academic Press, Boston, (1999).
- [2] K.L. Hess and R.J. Riccio, "Integrated safety system for MOCVD laboratory", *Journal of Crystal Growth*, Vol. 77, 95-100 (1986).
- [3] S.P. Watkins et al., "High mobility InAs grown on GaAs substrates using tertiarybutylarsine and trimethylindium", *Applied Physics Letters*, Vol. 66 (7), 882-884 (1995).
- [4] M. Mashita et al., "Comparative study on carbon incorporation in MOCVD AlGaAs layers between arsine and tertiarybutylarsine", *Journal of Crystal Growth*, Vol. 155, 164-170 (1995).
- [5] S. Leu et al., "C- and O-incorporation in (AlGa)As epitaxial layers grown by MOVPE using TBAs", *Journal of Crystal Growth*, Vol. 195, 98-104 (1998).
- [6] W. Stolz, "Alternative N-, P- and As-precursors for III/V-epitaxy", *Journal of Crystal Growth*, Vol. 209, 272-278 (2000).
- [7] J. Derluyn et al., "Comparison of MOVPE grown GaAs solar cells using different substrates and group-V precursors", *Journal of Crystal Growth*, Vol. 247, 237-244 (2003).
- [8] R. Beccard et al., "Replacement of hydrides by TBAs and TBP for the growth of various III-V materials in production scale MOVPE reactors", *Journal of Crystal Growth*, Vol. 170, 97-102 (1997).
- [9] G. Chen et al., "Metalorganic vapour-phase epitaxy of III/V phosphides with tertiarybutylphosphine and tertiarybutylarsine", *Journal of Crystal Growth*, Vol. 270, 322-328 (2004).
- [10] T. Izumiya et al., "The deep levels in InGaAlP epilayers grown by metalorganic chemical vapor deposition using tertiarybutylphosphine", *Journal of Crystal Growth*, Vol. 145, 153-157 (1994).
- [11] M. Mashita et al., "Metalorganic chemical vapor deposition study using tertiarybutylphosphine and tertiarybutylarsine for InAlGaP light-emitting diode fabrication", *Japanese Journal of Applied Physics*, Vol. 36, 4230-4234 (1997).

Chapter 3

Theory of solar cell and tunnel junction

3.1 Introduction

The object of this thesis is to make multijunction solar cells. The first step will be to fabricate lattice-matched solar cells (see Chapter 4). The next step will be to develop a suitable buffer layer so we can make the transition to lattice-mismatched (metamorphic) solar cells in the last step (see Chapter 5). To characterise and evaluate the fabricated solar cells, we need to have an understanding of the working principles of its components. Therefore, in this third chapter, a review of solar cell theory, based on the book by M.A. Green [1], and tunnel junction physics will be presented.

The first part of this chapter is devoted to the solar cell. The characteristic parameters and the equations that govern ideal solar cell operation will be discussed, based on a single junction device. The maximum efficiency of a single junction cell will be calculated under different spectra. Of course, real cells are far from ideal, so the losses that arise through the non-ideality of the device (resistance of bulk material and contact metal, non-radiative recombination) will also be briefly presented. Then, the benefits of using multijunction devices will be shown theoretically, without considering how the subcells are connected. A success story, the monolithic InGaP / GaAs / Ge stack, will be used as an example to motivate the advantages of the transition to metamorphic materials instead of limiting ourselves to lattice-matched materials.

To make a monolithic multijunction solar cell, one needs to series connect the subcells with a special component during growth of the stack to realise a functioning solar cell. Preferably, the voltage drop across that component is small, even when the current

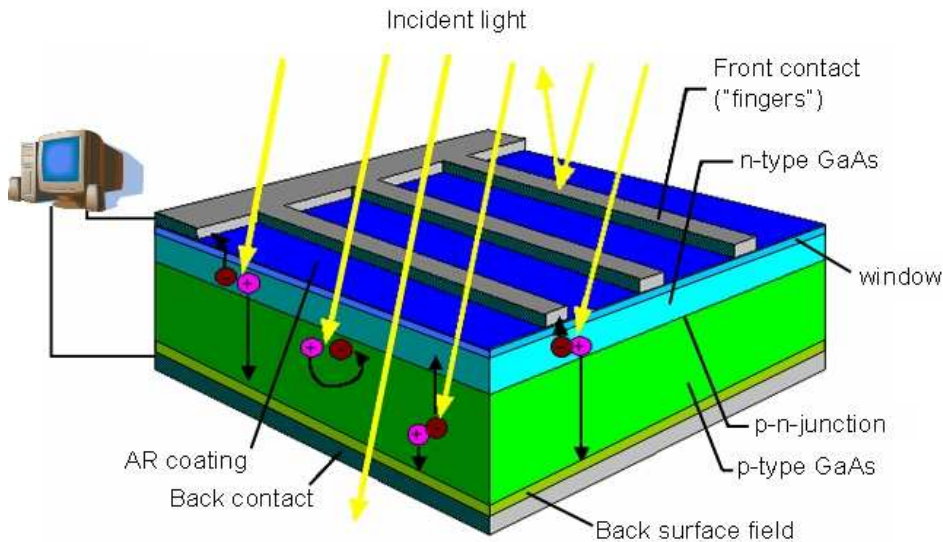


Figure 3-1: Working principle of a GaAs solar cell delivering power to an external load.

through it is very large. To minimise optical losses in the component it has to be thin and made of high-bandgap material. The tunnel junction is the only device that can meet all these requirements. In the second and final part of this chapter we will address how the tunnel junction works. The characteristic parameters and its I - V curve will be discussed. We will also illustrate what happens to the solar cell characteristic when the current generated by the solar cell is larger than the tunnel junction's peak current. The tunnel junction is a very critical component in the monolithic tandem cell. It is very sensitive to the growth conditions. This will become apparent in the next chapter.

3.2 Solar cells

3.2.1 Solar cell parameters

The ideal solar cell

A solar cell is basically a very large area semiconductor p-n junction, that can generate electricity by absorbing the light (photons) impinging on it. Only photons with an energy $h\nu$, larger than that of the solar cell material's bandgap, can be absorbed and, thus, can contribute to the generated photocurrent by creating electron-hole pairs (see Figure 3-1). The energy a photon has in excess of the bandgap is lost through thermalisation of the generated carriers, i.e. relaxation to the band edges by phonon emission. Electrons and holes are separated by the internal electric field and collected by the contacts. Then they can be used to drive an external load.

The dark I - V characteristic of a solar cell is just that of a plain diode (Figure 3-2). The relation between the current density, I , and the voltage, V , is given by

$$I = I_0 \left(e^{\frac{qV}{kT}} - 1 \right), \quad (3.1)$$

where q is the elementary charge, k the Boltzmann constant, T the absolute temperature and I_0 the reverse saturation current, given by

$$I_0 = A \left(\frac{qD_e n_i^2}{L_e N_A} + \frac{qD_h n_i^2}{L_h N_D} \right), \quad (3.2)$$

with A the diode area, (L_e, D_e) and (L_h, D_h) the diffusion (-length, -coefficient) for electrons in p-type and holes in n-type material, respectively, N_A and N_D the acceptor and donor concentration, respectively and n_i the intrinsic carrier concentration of the semiconductor.

When the solar cell is illuminated, electron-hole pairs are generated throughout the volume of the p-n junction, giving rise to an extra current, the light-generated current, I_ℓ . The illuminated I - V characteristic of the solar cell now becomes

$$I = I_0 \left(e^{\frac{qV}{kT}} - 1 \right) - I_\ell. \quad (3.3)$$

This is merely the dark current characteristic shifted down by a current I_ℓ (Figure 3-2), given by

$$I_\ell = qAG(L_e + W + L_h), \quad (3.4)$$

where G is the generation rate throughout the device and W the width of the depletion region. Power extraction from the device is possible in the fourth quadrant.

A solar cell is characterised by three parameters. For an ideal solar cell, the short-circuit current, I_{sc} , of the solar cell is equal to the light-generated current I_ℓ . The open-circuit voltage, V_{oc} , of the cell is found by setting $I = 0$ in Eq. (3.3):

$$V_{oc} = \frac{kT}{q} \ln \left(\frac{I_\ell}{I_0} + 1 \right). \quad (3.5)$$

The maximum power output of the cell is equal to the area of the shaded rectangle in Figure 3-2, determined by the maximum power point (V_{mp}, I_{mp}) . The fill factor, FF, defined as

$$FF = \frac{V_{mp} I_{mp}}{V_{oc} I_{sc}}, \quad (3.6)$$

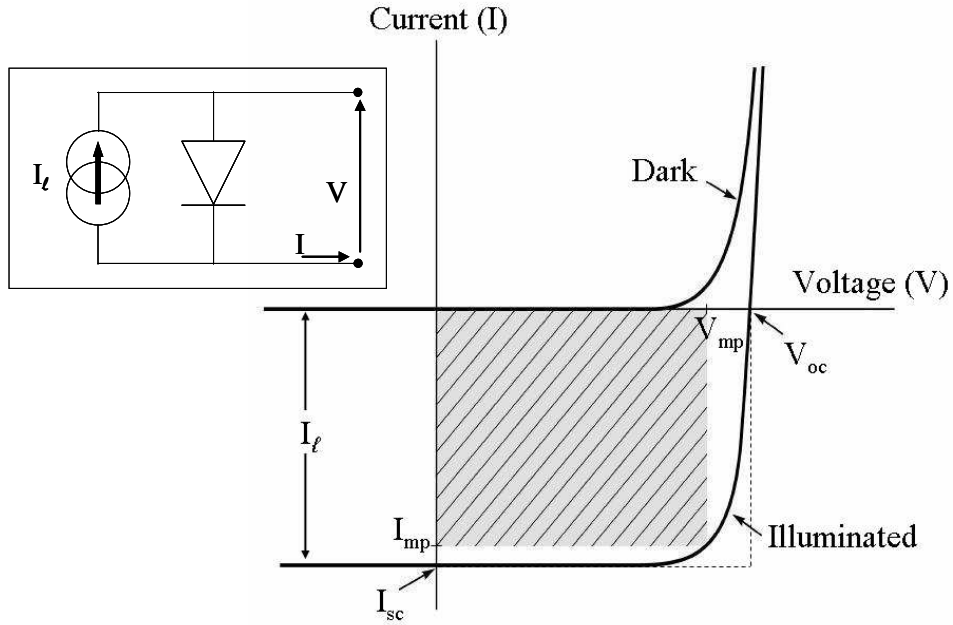


Figure 3-2: Dark and illuminated I - V curve of an ideal solar cell. The saturation current is not visible here. Inset: Equivalent circuit for an ideal single junction solar cell.

is a measure of the “squareness” of the curve. Assuming FF is only a function of V_{oc} (ideal case), an empirical expression describing FF as a function of a normalised voltage v_{oc} , can be derived:

$$FF = \frac{v_{oc} - \ln(v_{oc} + 0.72)}{v_{oc} + 1}, \quad (3.7)$$

where

$$v_{oc} = \frac{V_{oc}}{\frac{kT}{q}}. \quad (3.8)$$

The efficiency, η , is given by

$$\eta = \frac{V_{mp} I_{mp}}{P_{in}} = \frac{V_{oc} I_{sc} FF}{P_{in}}, \quad (3.9)$$

where P_{in} is the total incident power. From the spectral response SR of the solar cell, i.e. the ratio of the current generated by the cell to the power incident on it as a function of wavelength, the external (EQE) and internal (IQE) quantum efficiency can be derived

$$EQE = SR \times \frac{hc}{\lambda q} \quad \text{and} \quad IQE = \frac{EQE}{1 - R_{cell}}, \quad (3.10)$$

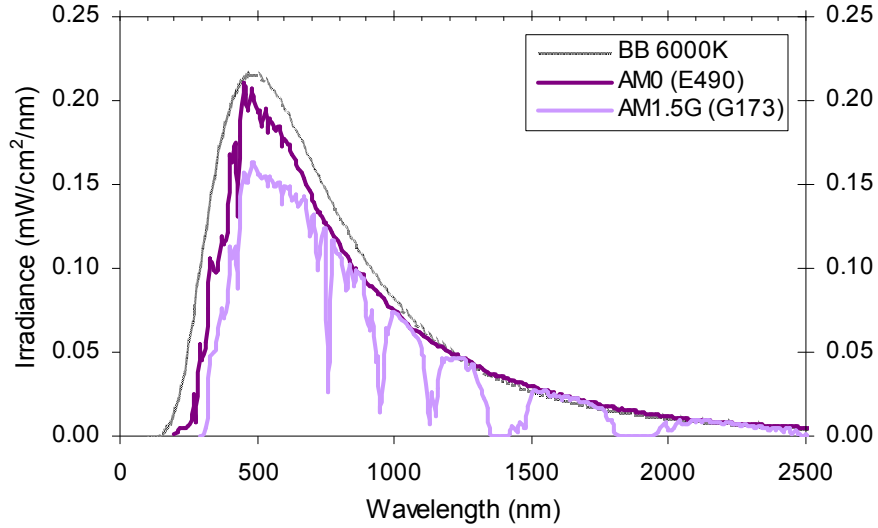


Figure 3-3: Irradiance spectrum of black body at 6000 K and the current reference spectra for AM0 and AM1.5G irradiation.

where R_{cell} is the reflectance of the solarcell.

To calculate the upper limit of the efficiency for a single junction solar cell of material with bandgap E_G , it is assumed that each photon with energy $h\nu \geq E_G$ is absorbed in the material and gives rise to one electron-hole pair that is collected at the cell contacts, thus contributing to I_{sc} . The maximum I_{sc} is calculated by integrating the energy distribution of the impinging light from the shortest wavelength up to the longest wavelength that can be absorbed by the material. The reference spectra AM0 (just outside the atmosphere) and AM1.5G (at the Earth's surface) are shown in Figure 3-3. The short-circuit current increases with decreasing bandgap because more photons are absorbed.

For the calculation of V_{oc} , I_0 is approximated by (unit: Ampère), with A the diode area,

$$I_0 = A \left(1.5 \times 10^5 e^{\left(\frac{-E_G}{kT} \right)} \right). \quad (3.11)$$

The exponential ensures that V_{oc} decreases with decreasing bandgap. Hence, because of the opposing trends for I_{sc} and V_{oc} , it is seen that there will be an optimal bandgap. This is visualised in Figure 3-4, where the maximal efficiency for a single junction solar cell is plotted versus bandgap for the latest AM1.5G [2] and AM0 [3] standards. GaAs is seen to have a near-optimal bandgap (1.424 eV) for light conversion: 28.4 and 25.9 %

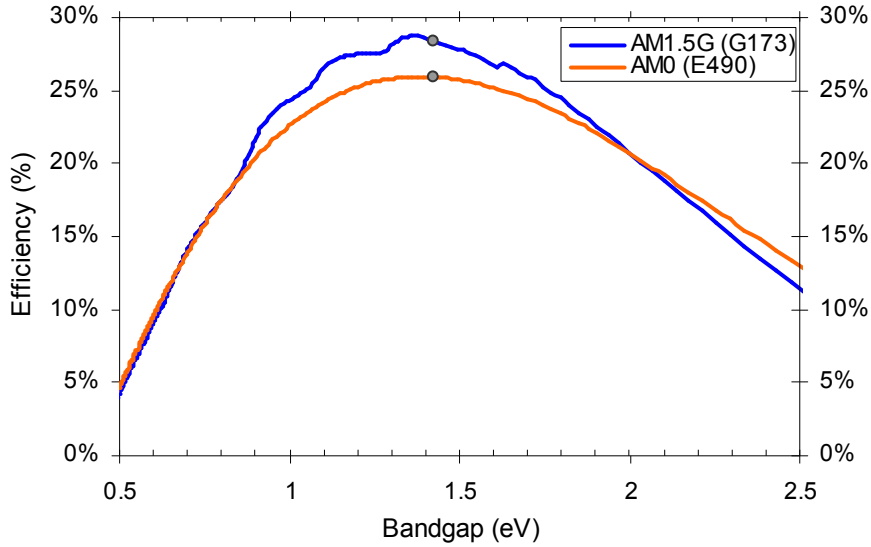


Figure 3-4: Calculated solar cell efficiency limits as a function of bandgap under the current standards for AM1.5G and AM0 illumination. The data points for GaAs are indicated by “•”.

under AM1.5G and AM0 illumination, respectively. The maximum is 28.7 and 26.0 % under AM1.5G and AM0 illumination, respectively, for a bandgap of 1.376 eV.

Losses in real solar cells

For the ideal solar cell it was assumed that the material extended to infinity on both sides of the junction. In real devices this is not so: surfaces set new boundary conditions. As a result, Eq. (3.2) will be modified to

$$I_0 = A \left(\frac{qD_e n_i^2}{L_e N_A} \times F_p + \frac{qD_h n_i^2}{L_h N_D} \times F_n \right), \quad (3.12)$$

where F_p and F_n depend on the surface recombination velocities (expressions can be found in [1]) at the surfaces of the p-type and n-type side, respectively. For high surface recombination velocity F_i is given by $\coth(W_i/L_j)$ and for low surface recombination velocity by $\tanh(W_i/L_j)$ with $(i, j) = \{(p, e), (n, h)\}$ and where W_i represents the width of the quasi-neutral region. From Eq. (3.5) we see that V_{oc} is large for small I_0 and thus for low surface recombination velocities.

Surface recombination is one kind of loss for the short-circuit current. So is bulk recombination. Other important I_{sc} losses are optical in nature and entail reflection (solution: antireflection coatings), grid shadowing (solution: contact design) and finite cell thickness (not all light with energy $>$ bandgap entering the cell is absorbed).

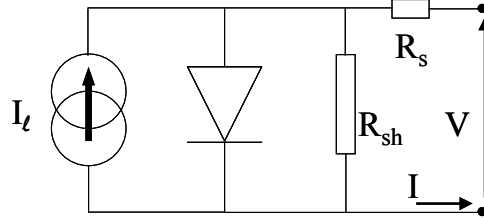


Figure 3-5: Equivalent circuit of a solar cell with series (R_s) and shunt (R_{sh}) resistance.

Both bulk and surface recombination limit V_{oc} but also recombination via impurity levels in the depletion region, is important. Including the latter adds an additional term to the dark I - V curve, which can then be written in the form

$$I = I_0 \left(e^{\frac{qV}{nkT}} - 1 \right), \quad (3.13)$$

where n represents the ideality factor and equals 1 for drift dominated or 2 for recombination dominated current through the depletion region.

Recombination in the depletion region also affects the fill factor. The normalised voltage used to calculate FF via Eq. (3.7), now has to be replaced by

$$V_{oc} = \frac{V_{oc}}{\frac{nkT}{q}}. \quad (3.14)$$

This gives a value that is lower by a factor $1/n$ with respect to the ideal case. A solar cell usually has a parasitic series (R_s) and shunt (R_{sh}) resistance (see Figure 3-5) that act to reduce FF. Expressions for FF can be found in [1]. The main contributors to R_s are the semiconductor's and the metal's bulk resistance and the contact resistance. Large R_s values also reduce the I_{sc} . Leakage across the junction via non-radiative recombination centres or around the edge of the cell are causes for R_{sh} . Small R_{sh} values also reduce the V_{oc} . The effect of R_s and R_{sh} is illustrated in Figure 3-6.

3.2.2 The multijunction solar cell

As shown in Figure 3-4 (p.38), the maximum conversion efficiency for a single junction solar cell is only about 29% under AM1.5G standard illumination. This is far less than the 95 % efficiency (η) of the solar energy conversion process considered as a Carnot engine between the Sun's and the Earth's surface at temperatures T_{Sun} (5800 K) and T_{Earth} (288 K), respectively, which is calculated from

$$\eta = 1 - \frac{T_{Earth}}{T_{Sun}}. \quad (3.15)$$

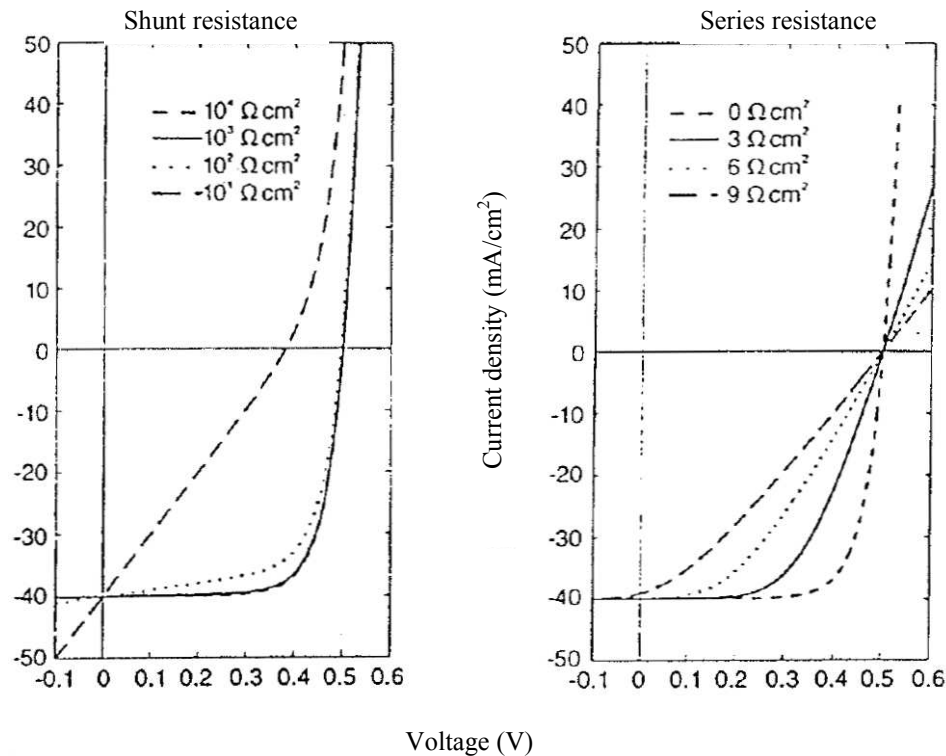


Figure 3-6: Influence of shunt (left) and series (right) resistance on solar cell parameters. A too low shunt resistance decreases the fill factor and in extreme cases V_{oc} . A too high series resistance decreases the fill factor and in extreme cases J_{sc} . (After [4])

The main reason for this is the fact that only photons with energy larger than the material's bandgap are absorbed, generating one electron-hole pair per photon. The electron is excited to the conduction band, where the excess energy is quickly lost when it relaxes back to the conduction band edge by emission of phonons (heat generation).

Allowing the generation of multiple electron-hole pairs by impact ionisation would result in increased efficiency for a single junction cell [5]. Unfortunately, this probability is small. Another approach is to introduce down-conversion [6] of photons with excess energy and up-conversion [7] of photons with sub-bandgap energies.

The most widespread approach is that of using multiple materials with different bandgaps to divide the solar spectrum into portions that are then absorbed more efficiently. These are the so-called multijunction solar cells. Calculations have been

Table 3-1: *The maximal energy conversion efficiency and the corresponding optimal set of bandgaps $E_{G,i}$ ($i=1$ is the top of the stack) for tandem cells with n stacked cells (a) in unconcentrated light and (b) under a maximal concentration of 45900 suns. (After [8])*

(a)					
n	η (%)	$E_{G,1}$ (eV)	$E_{G,2}$ (eV)	$E_{G,3}$ (eV)	$E_{G,4}$ (eV)
1	30	1.3			
2	42	1.9	1.0		
3	49	2.3	1.4	0.8	
4	53	2.6	1.8	1.2	0.8
(b)					
n	η (%)	$E_{G,1}$ (eV)	$E_{G,2}$ (eV)	$E_{G,3}$ (eV)	$E_{G,4}$ (eV)
1	40	1.1			
2	55	1.7	0.8		
3	63	2.1	1.2	0.6	
4	68	2.5	1.6	1.0	0.5

made, showing that the highest efficiency is obtained for a stack consisting of an infinite number of cells and, thus, with a continuously varying bandgap. Efficiencies for a stack with a finite number of cells were also presented [8]. For one sun illumination, an efficiency of 68.2 % is found for an infinite stack of cells and 86.8 % for a maximal concentration of 45900 suns. In Table 3-1, the optimal bandgap combinations and efficiencies are presented for stacks with up to four junctions.

Since we rely on monocrystalline III-V materials, deposited by means of MOVPE, for the high-bandgap junctions of either a monolithic or mechanical stack, two obvious choices remain as substrate for epitaxy: germanium and gallium arsenide. The materials that can be grown lattice-matched to these substrates are limited. That also constrains the number of bandgaps we have at our disposal to make a monolithic lattice-matched (to the substrate) dual or triple junction (active Ge) cell. The most commonly used structure is the InGaP / InGaAs / Ge lattice-matched tandem cell. By relaxing the constraint for lattice-matched growth, a whole new range of bandgaps becomes accessible. Metamorphic materials will offer much greater flexibility of bandgap selection in order to optimise the cell efficiency. But care has to be taken that the increased recombination at dislocations in these lattice-mismatched materials can be controlled. Figure 3-7 [9] shows a contour plot of the ideal efficiencies in the radiative recombination limit for triple junction cells with Ge bottom cell at a concentration of 500 suns. The possibilities for lattice-matched InGaP / InGaAs combinations are shown with increasing degree of lattice-mismatch to the Ge substrate in the direction indicated by the arrow. Also the (dis)order in InGaP (see §4.4.1) is taken into account. With a combination of disordered $\text{In}_{0.65}\text{Ga}_{0.35}\text{P}$ (1.68 eV) and $\text{In}_{0.17}\text{Ga}_{0.83}\text{As}$ (1.18 eV) a conversion efficiency of nearly 54 % is achievable.

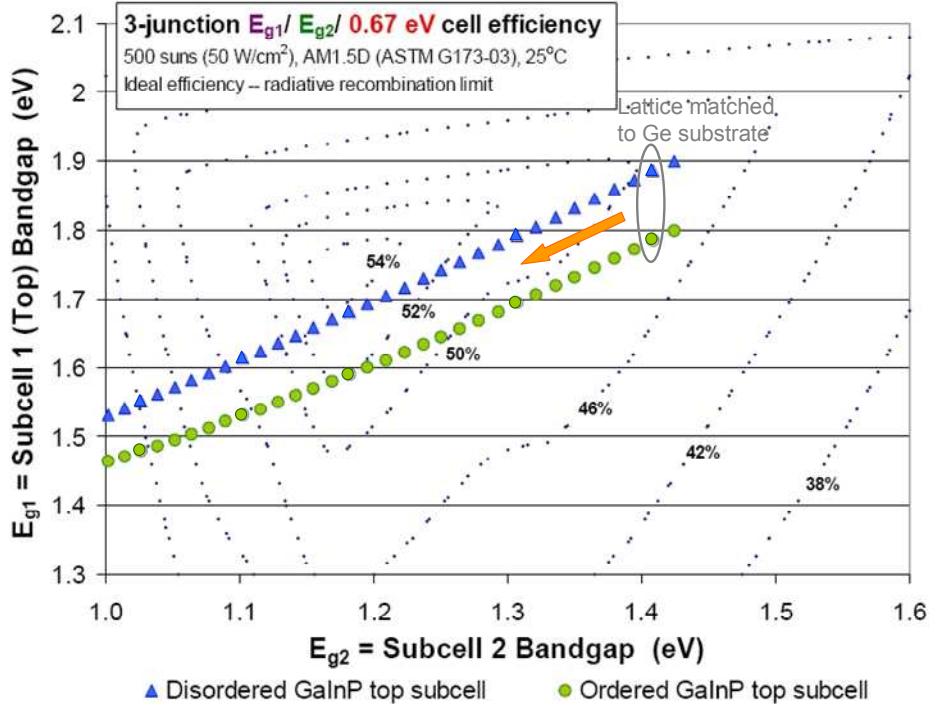


Figure 3-7: Ideal efficiency contour plot for triple junction cells, limited by radiative recombination, at $500\times$ AM1.5D with bottom cell bandgap fixed at 0.67 eV (Ge). \blacktriangle and \bullet represent lattice-matched InGaP / InGaAs combinations with increasing mismatch to the Ge substrate in the direction indicated by the arrow.

The I - V characteristic of a multijunction cell is, in good approximation, the sum of the characteristics of the series connected (single junction) subcells. The open-circuit voltage of the multijunction cell, V_{mj} , equals the sum of those of top and bottom cell, $V_{top} + V_{bottom}$, whereas the short-circuit current I_{mj} equals that of the current limiting cell (in the case of Figure 3-8: the top cell).

3.3 The tunnel junction

The tunnel junction, also known as the Esaki diode, was discovered in 1958 by L. Esaki. It is a simple p-n junction in which both p- and n-sides are degenerate (very heavily doped), so the Fermi level is located within the allowed bands themselves. This is shown in Figure 3-9 in the schematic energy diagram for a tunnel diode in thermal equilibrium (at $T = 0$ K, no voltage bias: $V = 0$). In this case, the Fermi level is constant

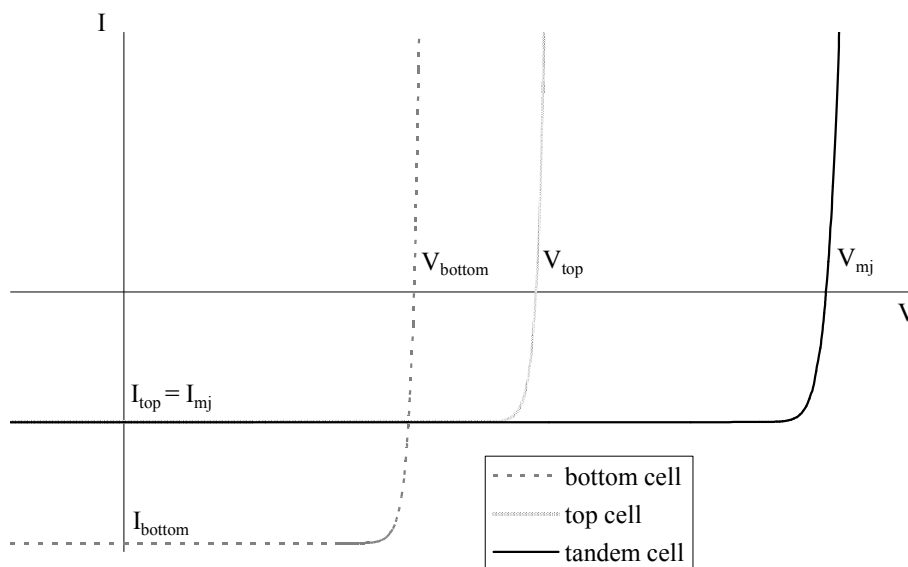


Figure 3-8: Illustration of the determination of the I - V curve of a multijunction cell from those of its components.

across the junction ($E_{Fp} = E_{Fn}$). Above the Fermi level there are no filled states and below there are no empty states. V_p and V_n represent the amount of degeneracy and are dependant on the doping concentrations.

In order for tunnelling to be possible, four conditions have to be fulfilled:

- (1) occupied energy states exist on the side from which the electron tunnels;
- (2) unoccupied energy states exist at the same energy levels as in (1) on the side to which the electron tunnels;
- (3) there is a finite tunnelling probability (low barrier height and small width);
- (4) conservation of momentum during tunnelling process;

It is clear that for a tunnel diode in thermal equilibrium, condition (2) is not fulfilled. Hence, a tunnelling current cannot flow at $V = 0$. When reverse bias is applied ($V < 0$), the bands on the n-side are shifted down over an amount V . There are now electrons on the p-side which satisfy the four tunnel conditions, thus, electrons can tunnel from the valence band into the conduction band. If a forward bias is applied ($V > 0$), the bands on the n-side are shifted up over an amount V . Electrons on the n-side can now tunnel to available states on the p-side. First, the tunnelling current increases with applied bias, as more states on the p-side become available, until it reaches a maximum I_p at a voltage V_p . When the voltage is increased further, the tunnelling current decreases, giving rise to

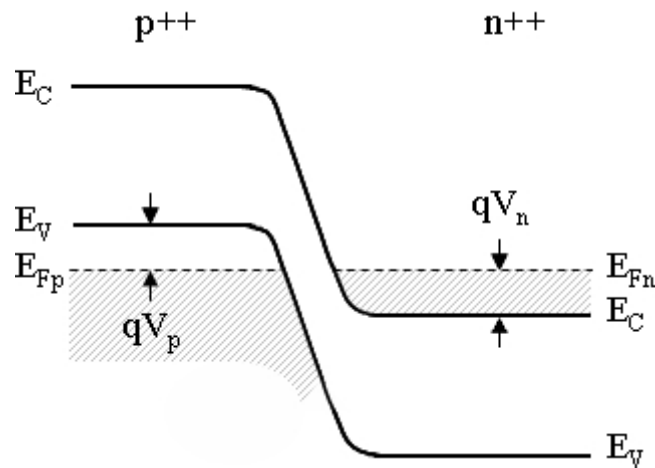


Figure 3-9: Energy diagram of a tunnel diode in thermal equilibrium.

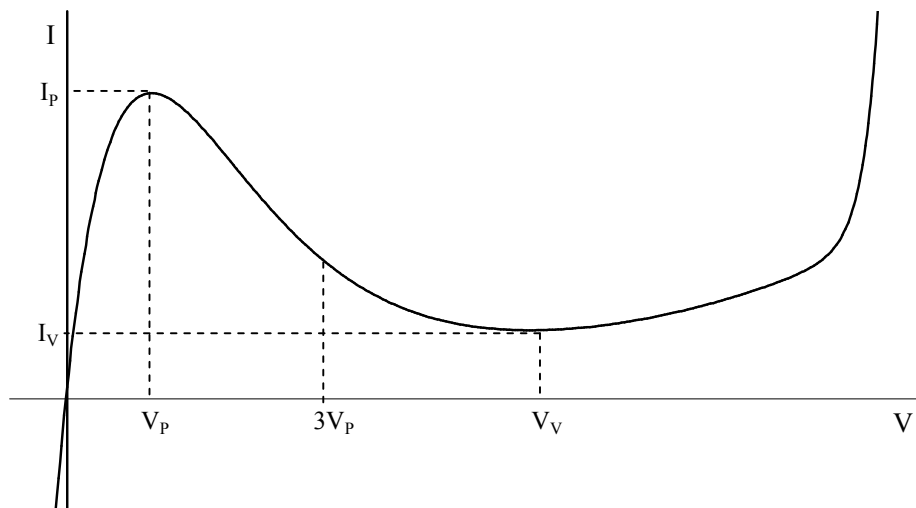


Figure 3-10: Characteristic I - V curve for a tunnel diode. I_p and V_p are the peak current and voltage, respectively, I_v and V_v are the valley current and voltage, respectively.

a negative resistance region. When a forward voltage $V = V_p + V_n$ is applied, the edge of the valence band is aligned with the edge of the conduction band (the bands are uncrossed) and the tunnelling current can no longer flow. Increasing V beyond this point will allow the normal thermal current to flow. This behaviour is illustrated in Figure 3-10 that shows a typical I - V characteristic for a tunnel junction. The characteristic tunnel junction parameters are the peak current I_p , the peak voltage V_p and the valley current I_v . The peak-to-valley ratio is determined by I_p/I_v .

3.3.1 Tunnelling probability and tunnelling current

The probability for tunnelling T_t is finite when the electric field in the depletion region is sufficiently high ($\sim 10^6$ V/cm). For a parabolic energy barrier, T_t can be calculated [10]:

$$T_t \cong \exp\left(\frac{-\pi\sqrt{m^*}\sqrt{E_G^3}}{2\sqrt{2}q\hbar\bar{E}}\right) \times \exp\left(\frac{-2E_\perp}{\bar{E}}\right), \quad (3.16)$$

where

$$\bar{E} = \frac{4\sqrt{2}q\hbar\bar{E}}{3\pi\sqrt{m^*}\sqrt{E_G}}, \quad (3.17)$$

with m^* the electron effective mass, E_G the bandgap, \bar{E} the electric field and E_\perp the energy associated with the momentum perpendicular to the tunnelling direction (transverse momentum). The first factor in Eq. (3.16) gives the tunnelling probability for an electron with no transverse momentum. The second factor is due to the transverse momentum and can act to further reduce the tunnelling probability. To obtain large transmission, m^* and E_G should be small and \bar{E} large.

The tunnelling current, taking the transverse momentum into account, can be calculated from the incident current per unit area in the energy range $dE_x dE_\perp$ [11]

$$dJ_x = \frac{q(m_y^* m_z^*)^{1/2}}{2\pi^2 \hbar^3} dE_x dE_\perp, \quad (3.18)$$

where $E = E_x + E_\perp$ with $E_x = (\hbar^2 k_x^2)/(2m_x^*)$ the energy of the electron in the tunnelling direction. By approximating effective mass m^* as isotropic and equal on both p- and n-side and by using Eq. (3.16), the tunnelling current per unit area, J_t , is obtained

$$J_t = \frac{qm^*}{2\pi^2 \hbar^3} \exp\left(\frac{-\pi\sqrt{m^*}\sqrt{E_G^3}}{2\sqrt{2}q\hbar\bar{E}}\right) \int [F_C(E) - F_V(E)] \exp\left(-\frac{2E_\perp}{\bar{E}}\right) dE dE_\perp, \quad (3.19)$$

with $F_C(E)$ and $F_V(E)$ the Fermi-Dirac distributions. When carrying out the integration over E_\perp , this results in

$$J_t = \frac{qm^*}{2\pi^2 \hbar^3} \exp\left(\frac{-\pi\sqrt{m^*}\sqrt{E_G^3}}{2\sqrt{2}q\hbar\bar{E}}\right) \left(\frac{\bar{E}}{2}\right) D, \quad (3.20)$$

with D (in units eV) an overlap integral which determines the shape of the I - V curve and depends on the temperature and the degeneracy V_p and V_n .

3.3.2 I-V characteristic

The total I - V characteristic of the tunnel junction is the sum of three components: the tunnelling current, the excess current and the thermal current. A first-order approximation for the tunnelling current, I_t , can be given in closed form:

$$I_t = I_p \frac{V}{V_p} \exp\left(1 - \frac{V}{V_p}\right), \quad (3.21)$$

where I_p and V_p are the peak current and voltage (Figure 3-10). V_p can be given by [10]

$$V_p \approx \frac{(V_p + V_n)}{3}. \quad (3.22)$$

The degeneracy on p- and n-side, V_p and V_n , are approximated by

$$V_p \approx \frac{kT}{q} \left[\ln\left(\frac{N_A}{N_V}\right) + 0.35 \frac{N_A}{N_V} \right], \quad (3.23)$$

$$V_n \approx \frac{kT}{q} \left[\ln\left(\frac{N_D}{N_C}\right) + 0.35 \frac{N_D}{N_C} \right], \quad (3.24)$$

where N_A and N_D are the acceptor and donor concentration, respectively, and N_V and N_C the effective density of states in the valence and conduction band, respectively.

As was already mentioned at the beginning of §3.3, for voltages larger than $V_p + V_n$ ($\approx 3V_p$), the valence and conduction band are “uncrossed”. Hence, I_t should be zero and only the normal diode current can flow. In Figure 3-10, the current is obviously not equal to zero. This is due to the excess current I_{ex} , which mainly arises from carrier tunnelling via energy states inside the bandgap. An expression for I_{ex} is

$$I_{ex} = I_V \exp\left[\frac{4}{3} \left(\frac{m_x^* \epsilon_s}{N^*}\right)^{1/2} (V - V_V)\right], \quad (3.25)$$

with I_V and V_V the valley current and voltage (see Figure 3-10), ϵ_s the static permittivity of the semiconductor and $N^* = \left(\frac{1}{N_A} + \frac{1}{N_D}\right)^{-1}$ the effective doping level.

The thermal current is the junction minority carrier injection current

$$I_{th} = I_0 \left(e^{\frac{qV}{kT}} - 1 \right). \quad (3.26)$$

Finally, the total device current I is equal to the sum of Eqs. (3.21), (3.25) and (3.26) (see Figure 3-11):

$$I = I_t + I_{ex} + I_{th}. \quad (3.27)$$

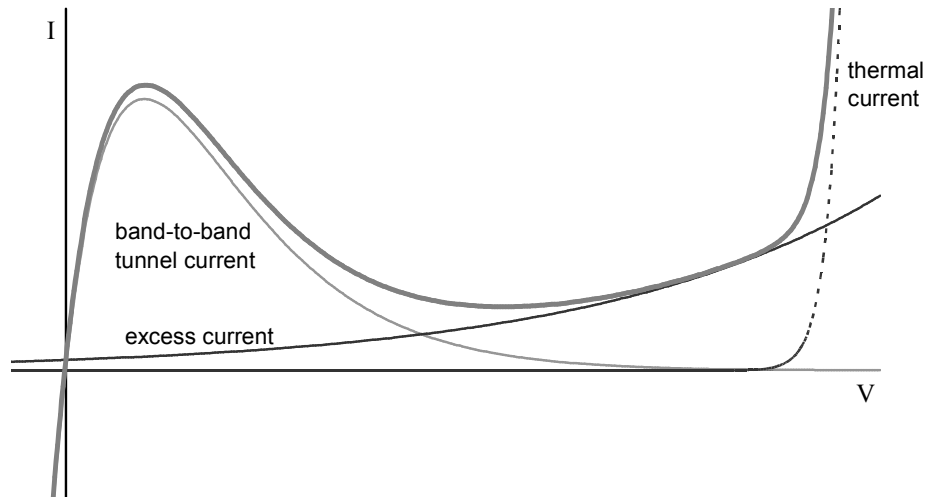


Figure 3-11: *I-V characteristic of the total tunnelling current showing its three components: band-to-band tunnelling current, excess current and thermal current.*

3.3.3 Tunnel junctions in multijunction cells

A monolithic tandem solar cell requires an electrical connection of the subcells in series. Therefore, a component is needed that can, at the same time, pass a high current with only a small voltage drop over the connection – this is extremely important in concentrator applications – and ensure low optical absorption. The first condition is needed to minimise the loss in open-circuit voltage V_{oc} , the second condition to minimise the loss in short-circuit current I_{sc} through absorption of photons that can still contribute to the photocurrent of the cell(s) beneath the tunnel junction.

The tunnel junction is inserted in reverse polarisation between two cells (see Figure 3-12 for an equivalent circuit); for example, if the cells are n-on-p, then the tunnel junction is p-on-n. In that way, when the solar cell is illuminated, the tunnel junction operates in forward bias and electrons can tunnel from occupied states in the conduction band on the n^{++} -side to available states in the valence band on the p^{++} -side of the tunnel junction (see Figure 3-13).

If the tunnel diode's peak current is higher than the cell's short-circuit current, the tunnel junction is operated at low voltages. In that range, the tunnel diode acts as an ohmic resistor. The cell only suffers a minute voltage drop – due to the resistance – that hardly affects cell performance (Figure 3-14, left). When, mostly in the case of application under high concentration, I_p of the tunnel junction is lower than I_{sc} of the tandem, a typical dip can be seen in the cell's *I-V* characteristic (Figure 3-14, right).

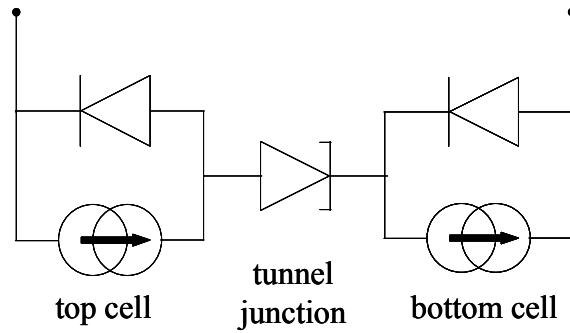


Figure 3-12: Equivalent circuit of a tandem solar cell.

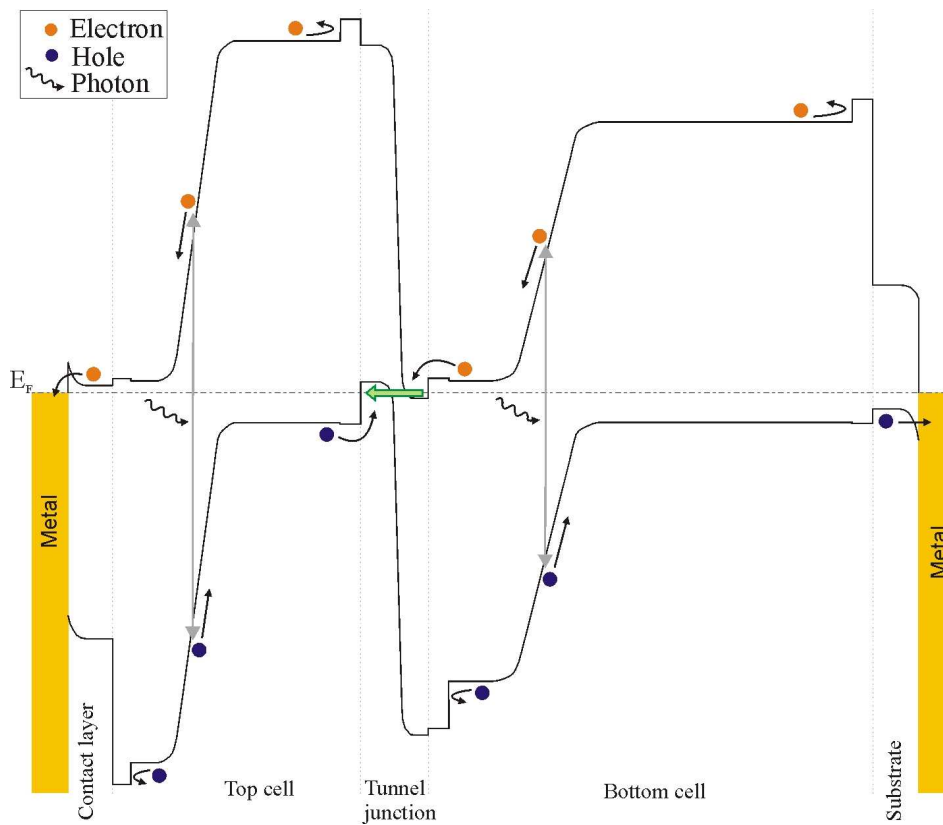


Figure 3-13: Schematic representation of tunnel junction operation when inserted in a tandem cell. Electrons and holes, generated by photon absorption, move in the direction indicated by the black arrows. Electrons can tunnel in the direction of the thick (green) arrow from the n^{++} CB to the p^{++} VB.

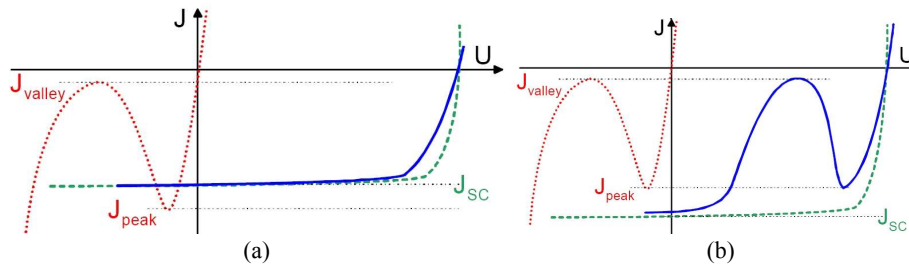


Figure 3-14: Superposition (solid) of I-V characteristics of tunnel diode (dotted) and solar cell (dashed). (a) $J_{sc} < J_p$: only the influence of the ohmic series resistance behaviour of the tunnel diode is reflected in the cell's I-V curve. (b) $J_{sc} > J_p$: the influence of the peak current and the large voltage drop is reflected in the cell's I-V curve.

3.4 Conclusions

In this chapter, the basic equations governing solar cell operation have been reviewed and the characteristic parameters were discussed. Also several loss factors were addressed. It is clear that even though a material with near optimal bandgap for photovoltaic energy conversion (GaAs) is available, the efficiency is limited when using a single junction. Multiple junctions are needed to increase conversion efficiency. In this way, the solar spectrum is divided into portions that are absorbed more efficiently in the different materials (junctions). To make these multijunction cells a reality, a special component is needed to electrically interconnect the subcells in series with a minimal voltage loss while passing high currents and, preferably, without optical losses. The tunnel junction fulfils this task. The device physics were reviewed, the characteristic parameters highlighted and possible problems arising due to insufficient device performance were discussed.

3.5 References

- [1] Martin A. Green, “Solar Cells: Operating Principles, Technology and System Applications”, Prentice-Hall Inc., Englewood Cliffs, (1982).
- [2] <http://rredc.nrel.gov/solar/spectra/am1.5/>
- [3] <http://rredc.nrel.gov/solar/spectra/am0/ASTM2000.html>
- [4] A. De Vos, “Zonnecellen”, course, Universiteit Gent (2000).
- [5] M.A. Green, “Third Generation Photovoltaics: Advanced Solar Energy Conversion”, Springer, Berlin (2003).
- [6] T. Trupke et al., “Improving solar cell efficiencies by down-conversion of high-energy photons”, *Journal of Applied Physics*, Vol. 92 (3), 1668-1674 (2002).
- [7] T. Trupke et al., “Improving solar cell efficiencies by up-conversion of sub-band-gap light”, *Journal of Applied Physics*, Vol. 92 (7), 4117-4122 (2002).
- [8] A. De Vos, “Detailed balance limit of the efficiency of tandem solar cells”, *Journal of Physics D: Applied Physics*, Vol. 13, 839-846 (1980).
- [9] R.R. King et al., “New horizons in III-V multijunction terrestrial concentrator cell research”, *Proceedings of the 21st European PVSEC*, 124-128 (2006).
- [10] S.M. Sze, “Physics of Semiconductor Devices”, 2nd edition, John Wiley & Sons Inc., New York, (1981).
- [11] E.O. Kane, “Theory of tunneling”, *Journal of Applied Physics*, Vol. 32 (1), 83-91 (1961).

Chapter 4

Lattice-matched materials

4.1 Introduction

As can be seen in Figure 4-1, III-V materials span a wide range of bandgaps and lattice constants. Substrates available for lattice-matched growth are GaAs, Ge, InP and GaSb. Both InP and GaSb are not well suited for AM1.5 or AM0 spectra because they lack high-bandgap materials that can be grown lattice-matched to them to realise high efficiency energy conversion. Therefore, GaAs and Ge are left as the best option to realise high-efficiency cells since several materials spanning a broad bandgap range, can be grown lattice-matched to them. As already discussed in §1.3, Ge is a widely used substrate in today's solar cell production because of its low price, good mechanical properties and the possibility of creating an additional active junction in the substrate itself.

As substrates for growth of the III-V materials investigated in this work, gallium arsenide and germanium wafers were used. The decision was made to use 4" Ge wafers as standard substrate. Semi-insulating GaAs wafers were only used for layers that needed electrical characterisation by Hall-Van der Pauw measurements.

In this chapter, we will first comment on the growth on germanium. Then we will discuss the realisation of n-on-p type $\text{In}_{0.01}\text{Ga}_{0.99}\text{As}$ single junction solar cells. Next the development of the n-on-p $\text{In}_{0.495}\text{Ga}_{0.505}\text{P}$ single junction solar cell, grown with TBP as group-V precursor, is treated. Following this, we look into intrinsic carbon doping of AlGaAs and making tunnel junctions. Finally, the realisation of lattice-matched dual junction InGaP / InGaAs solar cells on Ge is presented.

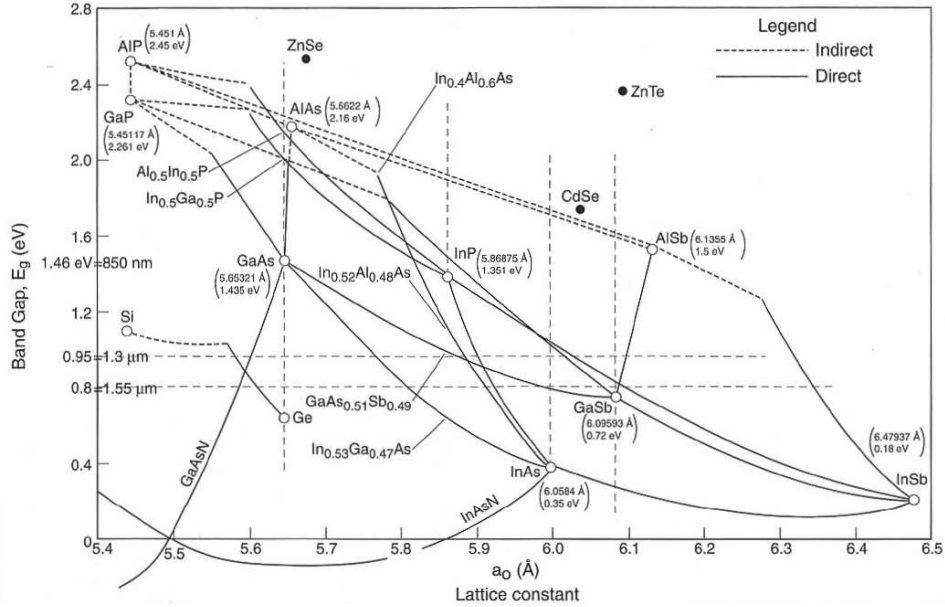


Figure 4-1: Variation of bandgap and lattice constant with alloy composition. Points represent binary, lines ternary and areas between lines quaternary compounds (after [1]).

4.2 Growth on germanium

Due to the non-polar nature of the Ge substrate, problems may arise when growing polar III-V material on it. The occurrence of anti-phase domains (APD) is likely if the proper growth conditions for nucleation of the III-V material are not used. Where APDs come into contact with each other, III-III and V-V bonds exist in the lattice. A two-dimensional structural defect is formed, called anti-phase boundary (APB), as illustrated in Figure 4-2 (left) for GaAs on Ge. The perfect lattice is shown on the right. The solution to growing APD-free material is to use conditions that ensure the formation of double-height steps on the germanium surface. One has to use a high V/III ratio, a relatively low growth rate, a reasonably high temperature and a substrate off-oriented from (001) [2].

A suitable nucleation regime for the growth of GaAs on Ge was developed at Intec (Ghent University) in cooperation with Umicore. Using this nucleation leads to high quality epitaxial layers [3]. The developed technique is now standard in our group. Since we are not troubled by the formation of APD in our material, no further attention will be given to the subject. For more information the reader is referred to [4].

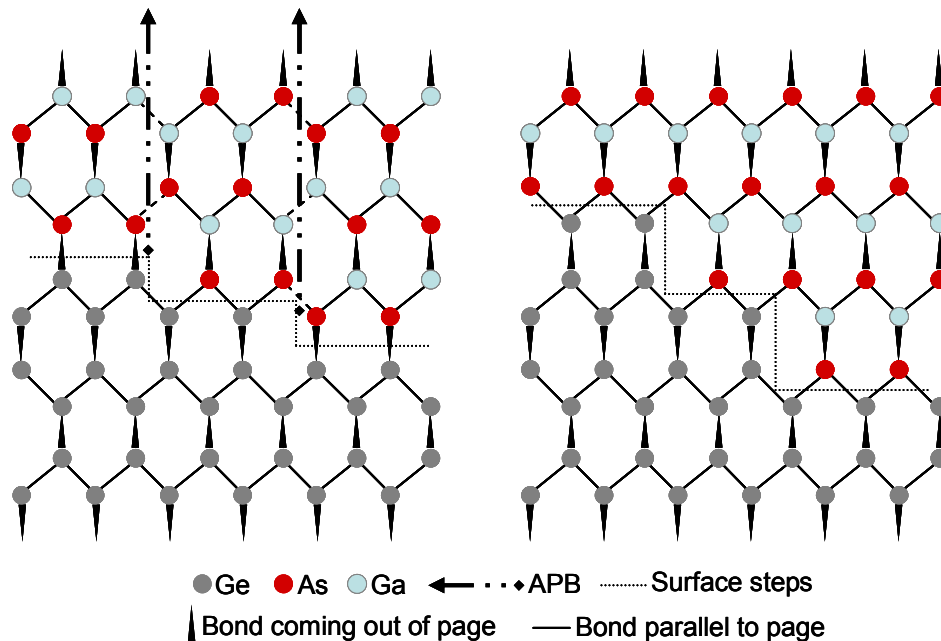


Figure 4-2: Anti-phase domains in GaAs on Ge (left) vs. perfect GaAs lattice on Ge (right).

4.3 $\text{In}_{0.01}\text{Ga}_{0.99}\text{As}$ single junction solar cell

4.3.1 Advantages of n-on-p polarity

Shortly before undertaking this work, the Intec-group successfully grew a p-on-n single junction $\text{In}_{0.01}\text{Ga}_{0.99}\text{As}$ solar cell on Ge – which was designed (Figure 4-3) and processed at imec – with an efficiency of 24.4 % under AM1.5G illumination [5]. However, it is believed that changing to n-on-p configuration will allow an extra increase of the efficiency and produce more radiation resistant cells. 1 % Indium is added to the GaAs to obtain a lattice-match of GaAs on Ge.

Carrier transport takes place in the valence band (VB) for p-type material and in the conduction band (CB) for n-type material. Due to the large difference in the number of occupied states in both levels (the CB is a largely unoccupied energy level whereas the VB is almost completely filled with electrons), the mobility of the majority carriers – for a particular doping level – is much larger in n-type material than in p-type. This means that the sheet resistance R_{sheet} and, hence, the bulk resistivity ρ of an n-type layer with thickness d , is also much lower compared to that of a p-type layer with the same

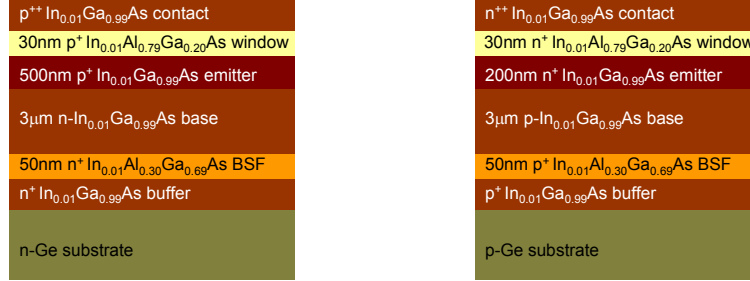


Figure 4-3: Layer structure for p-on-n (left) and n-on-p (right) GaAs solar cell.

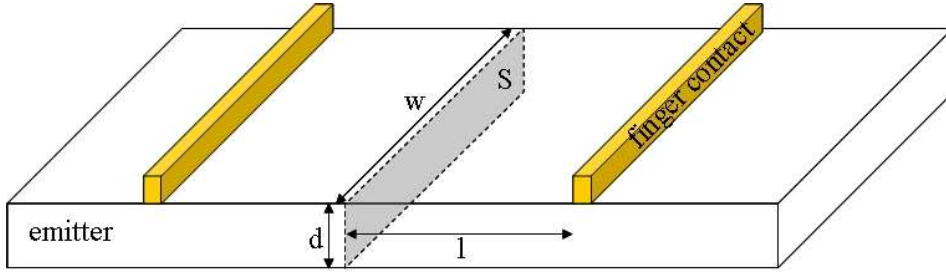


Figure 4-4: Schematic representation of the characteristic dimensions used in the discussion.

thickness. In the emitter there is lateral current conduction towards the grid fingers. If the voltage across the layer is V for a current I , the lateral resistance R of the layer is obtained from Ohm's law: $V = RI$. The resistance can also be described as a function of the bulk resistivity ρ and the sample geometry using Pouillet's third law (characteristic dimensions are shown in Figure 4-4):

$$R = \rho \frac{l}{S} = \rho \frac{l}{wd}, \quad (4.1)$$

with S the cross-section, w the width, d the thickness and l the length of the sample. We now calculate the thickness d_i ($i=\{n,p\}$) needed to pass the same current I through an n-type and a p-type layer that have the same lateral dimensions. From Eq. (4.1) and the ohmic behaviour we get:

$$d_i = \rho_i \frac{l}{wV}, \quad (4.2)$$

where the voltage across the layer was also assumed the same. It follows that

$$\frac{d_n}{\rho_n} = \frac{d_p}{\rho_p}. \quad (4.3)$$

Since we know that $\rho_n < \rho_p$, we conclude that $d_n < d_p$, i.e. to conduct the same current, an n-type layer can be thinner than a p-type layer. Hence, the emitter of an n-on-p solar cell can be thinner than that of a p-on-n cell (Figure 4-3).

Cell performance should benefit from this because the depletion region is moved upwards, closer to the cell's surface where most of the photons are absorbed. Hence, in a shallow junction more electron-hole pairs are generated in the depletion region itself and can immediately be separated by the built-in electric field, thus reducing minority carrier losses. More than half of the incident photons (AM1.5G) with sub-bandgap wavelength are absorbed in a 200 nm GaAs layer. Since the hole diffusion coefficient D_h in n-type material is not large ($\leq 10 \text{ cm}^2/\text{s}$), a reduced (n-type) emitter thickness (200 nm instead of 500 nm) ensures improved hole collection. More minority carriers can then reach the depletion region – where they are transported to the majority region by the electric field – and so fewer holes are lost due to recombination. Also the collection of minority carriers from the p-type base (electrons) is improved because the electron diffusion coefficient D_e is quite large ($\leq 200 \text{ cm}^2/\text{s}$) compared to D_h if the base should be n-type.

Furthermore, it has been observed that carrier removal rates and damage constants for diffusion lengths in n-GaAs (due to 1 MeV electron irradiation) are larger than those in p-type GaAs [6]. Thus, the np-configuration promises a better radiation resistance because the emitter is thin compared to the base. Also, when switching to tandem cells by introducing a InGaP top cell, the radiation resistance of n-p InGaP single junction and InGaP / GaAs tandem solar cells for 3 MeV proton irradiation is observed to be better [7].

4.3.2 High n-type doping

We now need a very highly doped (order 10^{19} cm^{-3}) n-type contact layer for the cells. These high doping levels can not be reached with the classical n-type dopant for arsenides, silicon (Si; source: silane, SiH_4), due to its amphoteric nature; since Si is a group-IV element, it can either go on the group-III or the group-V sublattice. Under normal circumstances, i.e. when the SiH_4 -flux is not too large, Si is preferentially incorporated on group-III sites. The self-compensation is low and the layer is n-type. When the SiH_4 -flux becomes too big, the amphoteric behaviour gets the upper hand: more Si is incorporated on group-V sites, where it acts as a p-type dopant. The self-compensation becomes larger, thus preventing us from reaching higher carrier concentrations. In Figure 4-5 it is seen that at $\text{SiH}_4/\text{III} = 0.01$ we are just reaching the doping level limit, which lies around $5 \times 10^{18} \text{ cm}^{-3}$.

To reach very high doping levels, selenium (Se; source: hydrogen selenide, H_2Se) was studied as a dopant. Since Se is a group-VI element, it can only be built into the lattice on a group-V site and, thus, amphoteric behaviour is avoided. In §2.3.3 dopant incorporation was briefly discussed. Se is a high vapour pressure dopant, so therefore the doping level should be inversely proportional to the growth temperature. In Figure 4-6 it is seen that there is only a small dependency (< factor 2) in the temperature range

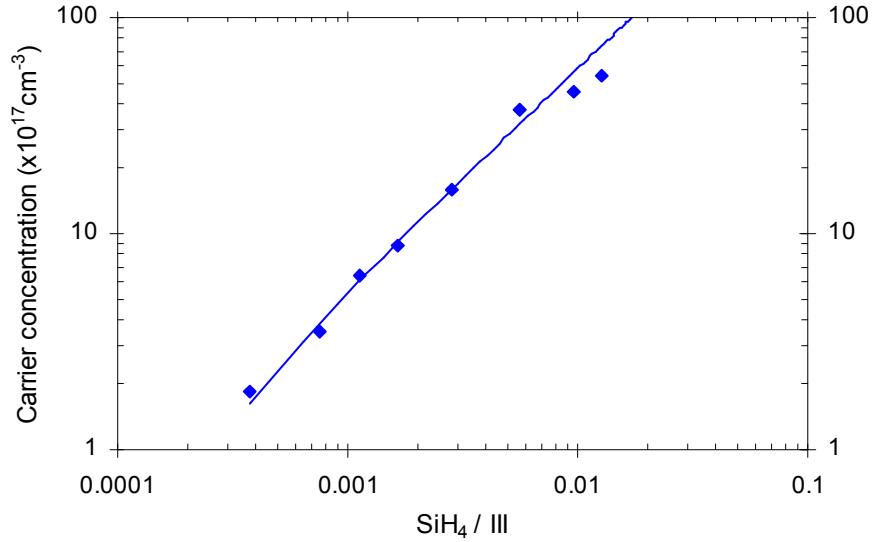


Figure 4-5: Carrier concentration (in units $\times 10^{17} \text{ cm}^{-3}$) in GaAs, determined with room temperature Hall measurements, as a function of the SiH_4/III ratio for layers grown at 660°C with $V/\text{III} = 15.4$ and $V_{gr} = 2.34 \mu\text{m/hr}$.

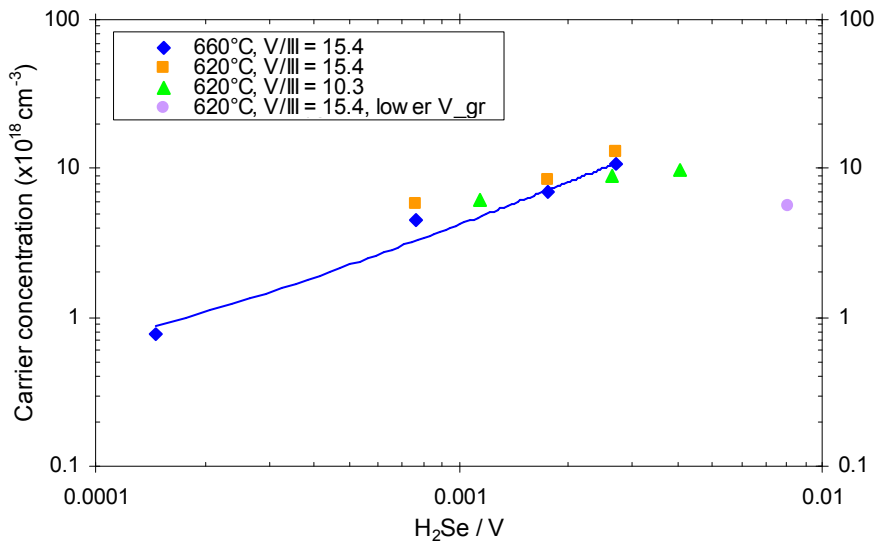


Figure 4-6: Carrier concentration (in units $\times 10^{18} \text{ cm}^{-3}$) in GaAs, determined with room temperature Hall measurements, as a function of the $\text{H}_2\text{Se}/V$ ratio and growth temperature.

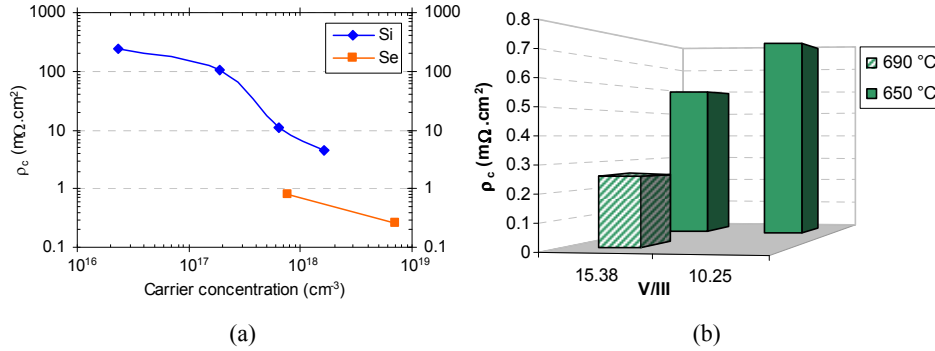


Figure 4-7: (a) specific contact resistance for our Si- and Se-doped layers as function of carrier concentration, (b) specific contact resistance for Se-doped samples as function of V/III ratio and growth temperature.

that was used. Also the influence of p_V^y is rather small in the studied range. Finally, lowering the growth rate (V_{gr}) by a factor of 3 and at the same time reducing p_V^y (by a factor of 3) to keep the V/III ratio constant, resulted in a lower doping level even though H_2Se/V was put to the high value of 0.0081. The highest carrier concentration we obtained is $1.29 \times 10^{19} \text{ cm}^{-3}$ for a layer grown at 620°C with $V_{gr} = 2.34 \text{ }\mu\text{m/hr}$, $H_2Se/V = 0.0027$ and $V/III = 15.4$.

With these very high doping levels we ensure good contact formation. Besides showing ohmic behaviour, the resistive losses due to the contact resistance should be kept as low as possible in order for the cell series resistance not to be dominated by the contacts. For a few samples, both Si- and Se-doped, we determined the specific contact resistance using the 'transfer length model' (TLM) for different carrier concentrations. The contacts that were deposited by evaporation consist of a AuGe/Ni/Au stack (thicknesses: 75/14/20 nm) and were annealed under forming gas at 300°C for 5 minutes. A trend can be observed that for the same carrier concentration, Se-doped samples have a lower contact resistance compared to Si-doped samples (Figure 4-7a). We believe this might be caused by the in-diffusion mechanism of Ge when alloying the contact. In the Si-doped samples there is competition for the same available lattice sites. The lowest value for the samples under test was $0.255 \text{ m}\Omega\cdot\text{cm}^2$ for a Se-doped layer grown at 690°C with $V/III = 15.4$ and a carrier concentration of $7.0 \times 10^{18} \text{ cm}^{-3}$. An indication was also found that layers grown at higher temperature might result in lower contact resistances, as might higher V/III ratios (Figure 4-7b).

4.3.3 Solar cell performance

We will now discuss the performance of the p-n and n-p solar cells. Table 4-1 gives an overview of the structure of the layer stack that was used for each solar cell. Two p-n samples (A & B) and two n-p samples (C & D) are compared.

Table 4-1: Overview of the grown layer stack used in samples A, B, C and D. The dotted line indicates where the dopant type is switched.

Sample	Compound	(doping level)	A	B	C	D
Contact	In _{0.01} Ga _{0.99} As	($\geq 10^{19} \text{ cm}^{-3}$)	300 nm	300 nm	300 nm	300 nm
Window	Al _{0.8} Ga _{0.2} As	($2 \times 10^{18} \text{ cm}^{-3}$)	50 nm	50 nm	50 nm	30 nm
Emitter	In _{0.01} Ga _{0.99} As	($2 \times 10^{18} \text{ cm}^{-3}$)	500 nm	500 nm	200 nm	200 nm
Base	In _{0.01} Ga _{0.99} As	($1 \times 10^{17} \text{ cm}^{-3}$)	3 μm	3 μm	3 μm	3 μm
BSF	Al _{0.3} Ga _{0.7} As	($2 \times 10^{18} \text{ cm}^{-3}$)	50 nm	50 nm	50 nm	50 nm
Buffer	In _{0.01} Ga _{0.99} As	($1 \times 10^{18} \text{ cm}^{-3}$)	600 nm	600 nm	600 nm	600 nm
Substrate			n-Ge	n-Ge	p-Ge	p-Ge

The III-V solar cell research started when the MOVPE reactor was still at Intec (Ghent). This research led to the development of a world record single junction p-n In_{0.01}Ga_{0.99}As solar cell on germanium [5] (sample A). Several months after that, the reactor was moved to Imec (Heverlee). After getting the system back online and conditioning the reactor, the growth process was re-qualified by repeating the recipe that led to the record cell (sample B). The next step was making n-p cells (samples C and D).

The results from these runs are listed for 4 cm² cells in Table 4-2 and the I - V curves are shown in Figure 4-8. From processing to processing, small variations in the anti-reflective coating (ARC) are expected. For samples A and B the ARC was nearly identical. The difference in measured J_{sc} of both cells is explained as follows. The spectral response measurement in Figure 4-9 shows that sample A's absorption edge (885 nm) is at slightly longer wavelength than that of sample B (880 nm). This difference accounts for 0.34 mA/cm² (ideal case), explaining already half of the difference in measured J_{sc} . The remainder could be caused by variations in the position of the cell in the output beam of the solar simulator (WACOM), due to inhomogeneities in the beam's centre and by small variations in the reflectance of the ARC.

A different absorption edge also implies a different bandgap and, hence, a different indium (In) concentration: sample B contains slightly less In than sample A. From the relationship between bandgap and composition of In_{1-x}Ga_xAs, given by [1]

$$E_G = 0.324 + 0.7x + 0.4x^2, \quad (4.4)$$

we calculate 1.1 and 1.6 % In for B and A, respectively. Although cell A has the higher indium content, it has a higher V_{oc} than cell B. This raises the question whether a small amount of strain might be beneficial for the cell performance.

Both cells have a good fill factor, with $FF_B > FF_A$, which seems to confirm that sample A could have an increased I_0 due to a larger lattice-mismatch. Unless of course this effect on FF can be completely attributed to the lower series resistance calculated for

Table 4-2: Overview of solar cell (4 cm^2) parameters. The short-circuit currents listed are – from top to bottom – measured, calculated from EQE (includes shadowing and reflection losses) and from IQE (compensates for shadowing and reflection).

Sample	A	B	C	D
Average reflectance _{450-900nm} (%)	4.1	3.9	5.3	3.0
J_{sc} , measured (mA/cm^2)	28.9	28.2	26.6	29.6
J_{sc} , calculated from EQE (mA/cm^2)	27.6	27.2	25.6	28.5
J_{sc} , calculated from IQE (mA/cm^2)	30.2	29.5	28.3	30.2
V_{oc} (V)	1.030	1.023	1.014	0.969
R_s , upper limit (Ω)	0.446	0.368	0.484	0.377
Fill factor (%)	82.5	83.8	83.2	83.4
Efficiency (%)	24.5	24.2	22.4	23.9

cell B. This calculation is based on a model developed by Kunz and Wagner [8]. Both cell A and cell B have a very good efficiency: 24.5 and 24.2 %, respectively, demonstrating excellent device quality.

Sample C is an n-p $\text{In}_{0.01}\text{Ga}_{0.99}\text{As}$ solar cell. Its short-circuit current is lower than that for a p-n cell (e.g. sample B). This can be partly explained by a 25 % (relative) increase in reflectance for this sample compared to A and B. If we assume sample C has the same reflectance as sample B, then a new EQE can be calculated for cell C. From this new EQE we expect $J_{sc_C} = 26.1 \text{ mA}/\text{cm}^2$. This is still lower than J_{sc} of cell B. Using Eq. (3.5) and the data from Table 4-2 tells us that the lower J_{sc} alone cannot account for the smaller V_{oc} for sample C. It is derived that I_0 is larger for sample C. As can be seen from the internal quantum efficiency (IQE, Figure 4-9), more current is lost for the shorter wavelengths, indicating that the passivation of the front of cell C is not good enough: an increased recombination velocity probably exists at the interface between emitter and window. But again, cell C also shows an excellent fill factor. The efficiency is 22.4 %.

For cell D, a very recent n-p GaAs solar cell, we obtain an efficiency of 23.9 % with, yet again, a good fill factor (83.4 %). Surprising is that this cell not only has a larger J_{sc} but, especially, a lower V_{oc} compared to the other cells. Both seem to indicate a lower bandgap for this cell. The spectral response measurement confirms this assumption because the absorption edge is at longer wavelength (890 nm) compared to the other cells and yields an indium concentration of 2 % versus around 1 % for the other cells. These values can change quite a lot depending on which datapoint is selected as the absorption edge. XRD analysis of solar cell D determines an In content of 1.5 %. The IQE has a value of over 95 % for in the mid-wavelength range, which is an improvement compared to cell C. Also the passivation of the front of the cell is seen to have been significantly improved, being now of comparable level as for the p-n cells. A very recent result is 24.7 % conversion efficiency (confirmed by NREL).

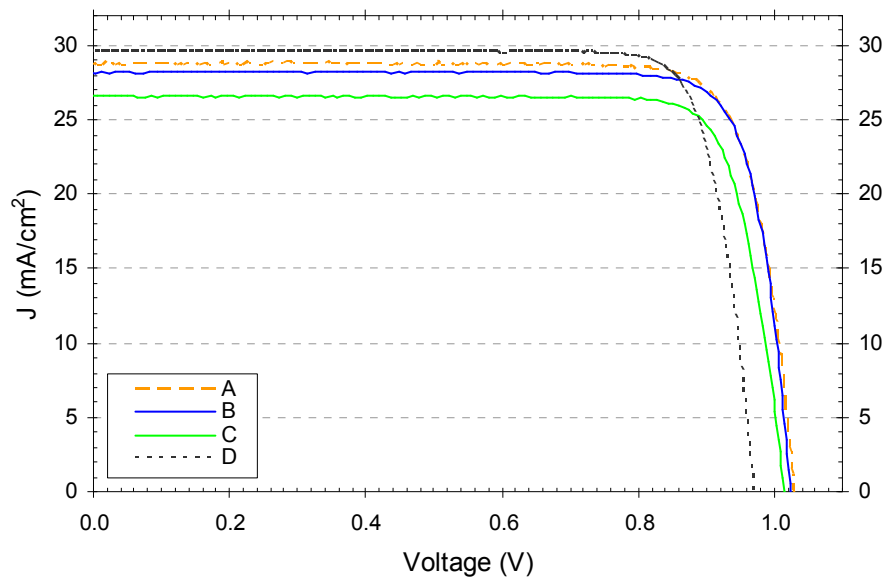


Figure 4-8: *I-V curves of 4 cm² GaAs single junction solar cells under AM1.5G illumination for p-n (A and B) and n-p (C and D) configuration.*

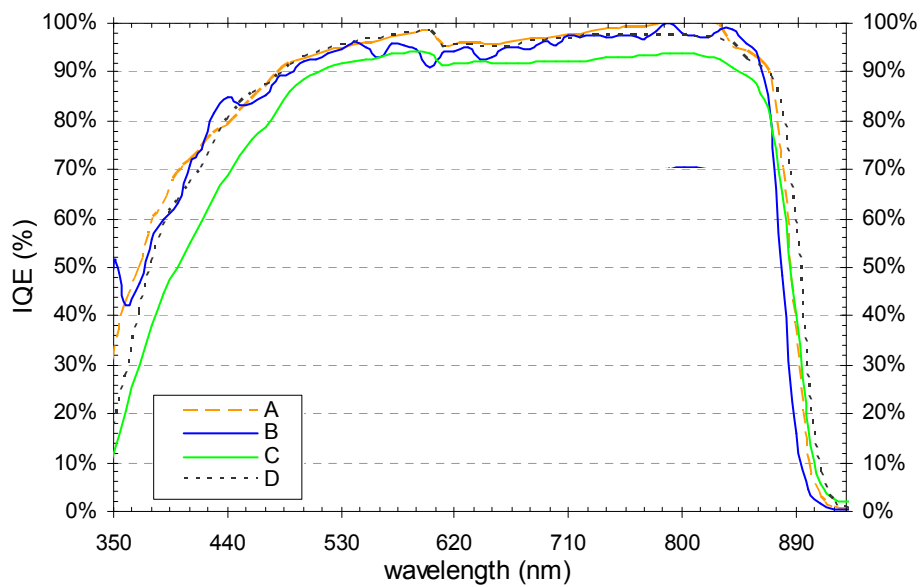


Figure 4-9: *Internal quantum efficiency curves for p-n (A and B) and n-p (C and D) cells (4 cm²), derived from spectral response measurements.*

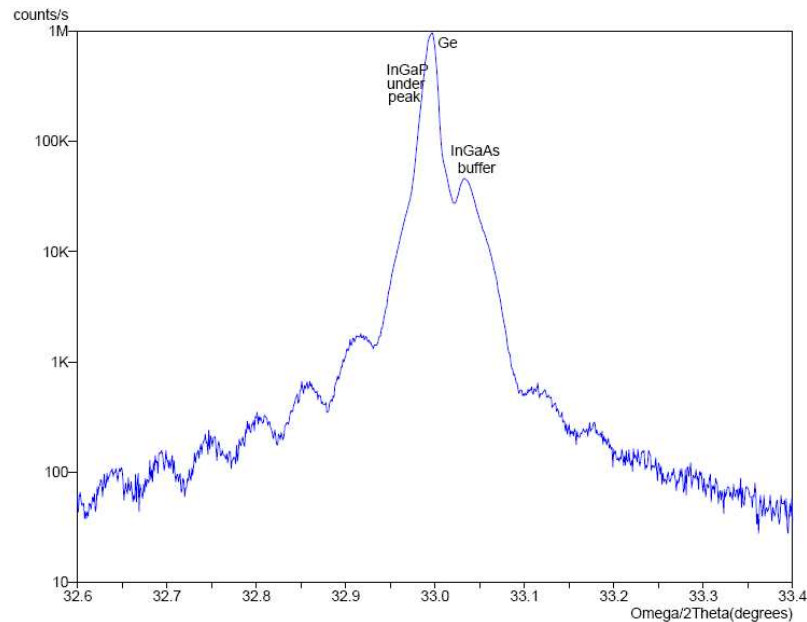


Figure 4-10: $\omega/2\theta$ rocking curve of 1 μm InGaP on Ge.

Table 4-3: Required TMIn/III_{tot} ratio as a function of growth temperature to obtain lattice-matched InGaP on Ge.

T _{set} (°C)	600	650	700	725	750
required TMIn/III _{tot}	0.654	0.694	0.709	0.714	0.718

4.4 In_{0.495}Ga_{0.505}P single junction solar cell

4.4.1 InGaP alloy

Composition and ordering

As was seen in Table 3-1 (p.41), combining GaAs (1.42 eV) and InGaP (1.9 – 1.8 eV, depending on the ordering: see below) will not lead to the most efficient dual junction cell. Here, only lattice-matched materials are considered while developing our first dual junction solar cell know-how, to avoid additional difficulties due to lattice mismatch.

The composition of InGaP is well controlled. The In_{0.495}Ga_{0.505}P compound is lattice-matched to germanium. Figure 4-10 shows a high resolution x-ray diffraction (HRXRD) $\omega/2\theta$ rocking curve for an InGaP layer on (001) Ge 6° off-oriented towards <111>.

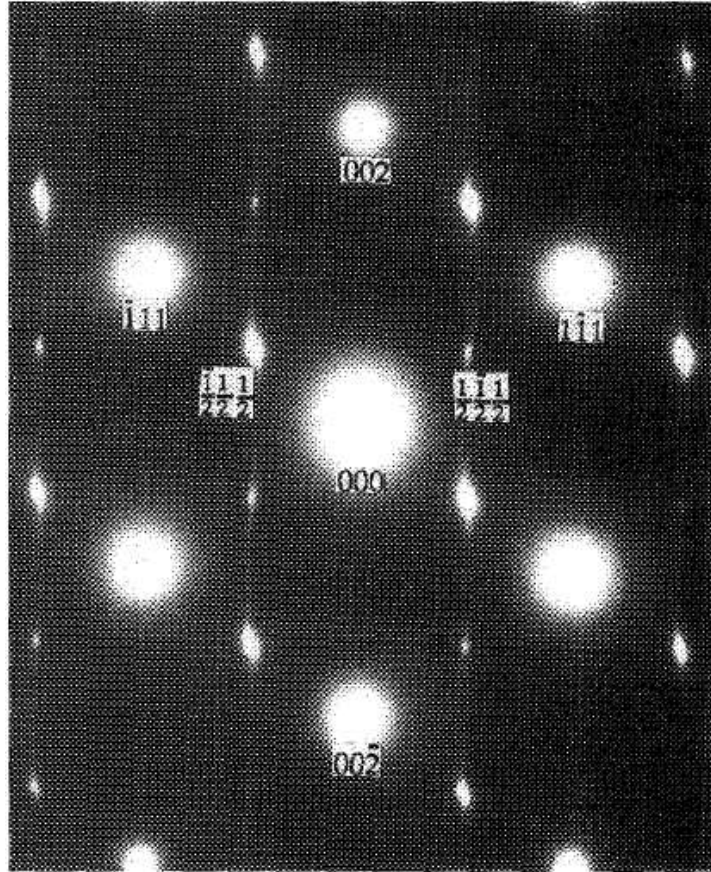


Figure 4-11: $[110]$ -pole electron diffraction pattern for an $\text{In}_{0.5}\text{Ga}_{0.5}\text{P}$ layer. Extra spots are visible at positions halfway from the origin to the spots due to the $\{111\}$ planes in the zinc blende lattice (after [9]).

Due to the higher equilibrium vapour pressure for In compared to Ga in the range of applicable growth temperatures, the In distribution coefficient is seen to be dependent on temperature. In other words, for increasing growth temperatures the $\text{TMIn}/\text{III}_{\text{tot}}$ fraction in the vapour phase has to be increased to maintain the same solid composition (see Table 4-3) due to indium evaporation from the surface. This was also observed by P. Modak [4].

It is well known that atomic ordering occurs in ternary III-V alloys. This phenomenon can significantly influence the fundamental properties of the materials, such as the bandgap energy and the free carrier mobility. Atomic scale ordering means that in the structure the solid composition is modulated along a particular crystallographic direction

Table 4-4: Growth conditions, RT-PL peak wavelength and emission energy and ordering parameter χ for Si-doped InGaP layers on Ge.

Sample	A	B	C	D
Temperature setpoint (°C)	650	650	700	725
V/III	83.4	73.7	83.5	113.2
TMGa ($\mu\text{mol}/\text{min}$)	63.4	96.4	58.1	56.8
TMin ($\mu\text{mol}/\text{min}$)	68.2	95.7	68.2	68.2
Indium content (from HRXRD)	0.498	0.493	0.495	0.496
RT-PL peak wavelength (nm)	661.4	654.5	684.5	667.9
RT-PL emission energy (eV)	1.873	1.893	1.810	1.855
Ordering parameter χ	0.204	0.122	0.430	0.294

in the lattice with a period of two lattice spacings. In the case of completely ordered InGaP, alternating monolayers of InP and GaP would be formed in the $\langle 111 \rangle_A$ direction. Several growth parameters (growth temperature, growth rate and substrate orientation) play a role in the extent of ordering [9]. The occurrence of ordering can easily be proven if in an electron diffraction pattern extra spots with a spacing just $\frac{1}{2}$ that observed for the normal zinc-blende lattice are visible. This is shown in Figure 4-11 for the $[110]$ -pole electron diffraction pattern of an $\text{In}_{0.5}\text{Ga}_{0.5}\text{P}$ layer.

When characterising $\text{In}_x\text{Ga}_{1-x}\text{P}$ with a photoluminescence technique, the lowest emission energies for a given composition x are believed to correspond to the highest degree of ordering. For increasing growth temperature, the degree of ordering first increases to a maximum and then decreases again. At high growth temperature, ordering disappears because above a certain critical temperature the entropy of mixing becomes dominant over the enthalpy of mixing. At low growth temperature, ordering disappears because of a reduced surface mobility of the group-III species, preventing the lower-energy ordered structures to be formed [9]. This behaviour is observed by Schneider et al. [10] and by Zorn et al. [11]. Also of importance are V/III ratio, substrate off-orientation and doping concentration. The degree of ordering is attributed to a change in surface reconstruction from 2×1 (phosphorus rich) to 2×4 (group-III rich) surface reconstruction [11].

Growth conditions and measurement results of our own (Si-doped) InGaP layers are listed in Table 4-4 and shown in Figure 4-12. The room-temperature photoluminescence (RT-PL) emission energy is shown in Figure 4-12a as a function of growth temperature and V/III ratio. Although the nominal In content in all layers is approximately equal, clear differences in emission energy are observed. This is due to the degree of ordering, which can be expressed via an ordering parameter χ ($0 =$ completely disordered; $1 =$ completely ordered) that can be estimated using

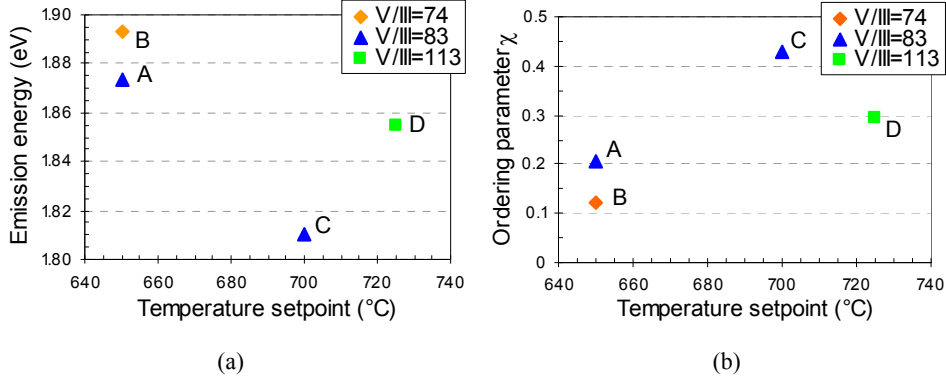


Figure 4-12: (a) PL emission energy and (b) ordering parameter of several Si-doped InGaP layers as a function of growth temperature and V/III ratio.

$$\chi = \sqrt{\frac{\Delta E_G}{471 \text{ meV}}}, \quad (4.5)$$

where $\Delta E_G = E_G^{\text{disordered}} - E_G^{\text{ordered}}$ is the difference between the disordered bandgap and the measured bandgap. The disordered bandgap is derived from the indium content (determined via HRXRD) using an empirical formula, whereas the measured bandgap equals the emission energy from the PL measurement [11]. The ordering parameter is plotted as a function of growth temperature and V/III ratio in Figure 4-12b.

The degree of ordering clearly influences the bandgap; the bandgap decreases with increasing ordering. This effect can be used in both solar cells and LEDs to tune the absorption edge or emission wavelength, respectively.

Dopant and impurity incorporation

Electrical characterisation of the doping level was done via Hall-van der Pauw measurements or via C - V measurements. For the Hall measurements the samples were diced into squares of about 1 cm^2 . Indium dots were pressed onto the corners of the sample, which was subsequently annealed under forming gas at $380 \text{ }^\circ\text{C}$ for 30 s. Sometimes it was impossible to obtain a good contact. C - V measurements were performed on some samples to check the Hall results or on others where no good contact was obtained. A mercury probe was used to make the Schottky contact with the sample.

Table 4-5 and Table 4-6 give an overview of the growth conditions and measurement results for n-type (Si, Se) and p-type (Zn) doped InGaP layers, respectively. There are two temperatures used in the tables. One is the temperature control unit's setpoint T_{set} ,

Table 4-5: Growth conditions and doping concentrations for n-type doped (Si and Se) InGaP layers. T_{gr} values in *italic* are estimated.

Sample	202	205	228	336	599	617	619	372	376	377
dopant	Si	Si	Si	Si	Si	Si	Si	Se	Se	Se
T_{set} (°C)	700	700	650	650	700	700	700	650	650	650
T_{gr} (°C)	<i>650</i>	<i>650</i>	<i>600</i>	<i>600</i>	660	650	650	<i>610</i>	<i>610</i>	<i>610</i>
Si/III, Se/V ($\times 10^{-4}$)	12.0	1.2	11.5	27.9	55.9	58.5	5.9	0.6	3.2	0.1
V/III	36.6	83.5	83.4	73.7	46.8	26.8	26.8	74.2	74.2	74.2
TMGa ($\mu\text{mol}/\text{min}$)	58.1	58.1	63.4	96.4	95.8	87.3	87.3	95.1	95.1	95.1
TMIn ($\mu\text{mol}/\text{min}$)	68.2	68.2	68.2	95.7	95.7	95.7	95.7	95.7	95.7	95.7
N_{Hall} ($\times 10^{18} \text{cm}^{-3}$)	1.2	0.07		0.49	3.3			3.1	14.0	3.8
N_{CV} ($\times 10^{18} \text{cm}^{-3}$)			0.3		6.0	5.0	0.47			
N_{SIMS} ($\times 10^{18} \text{cm}^{-3}$)	0.92	0.08	0.23							
μ_{Hall} (cm^2/Vs)	937	1013		1200	668			439	345	717

Table 4-6: Growth conditions and doping concentrations for p-type doped (Zn) InGaP layers. T_{gr} values in *italic* are estimated. Inconclusive results are marked by “-”.

Sample	219	243	365	369	598	604	605	609	611
T_{set} (°C)	650	650	650	650	700	700	700	700	700
T_{gr} (°C)	<i>600</i>	<i>600</i>	<i>610</i>	<i>610</i>	660	660	660	650	650
Zn/III ($\times 10^{-2}$)	3.14	0.46	4.77	47.4	0.58	5.97	1.49	1.51	1.51
V/III	83.4	84.0	74.2	74.2	46.8	48.5	48.5	48.9	26.8
TMGa ($\mu\text{mol}/\text{min}$)	63.4	57.2	95.1	95.1	95.8	88.8	88.8	87.3	87.3
TMIn ($\mu\text{mol}/\text{min}$)	68.2	61.4	95.7	95.7	95.7	95.7	95.7	95.7	95.7
N_{Hall} ($\times 10^{18} \text{cm}^{-3}$)		0.15	0.25	3.5	-	-	0.28	-	-
N_{CV} ($\times 10^{18} \text{cm}^{-3}$)					0.07	0.60	0.18	0.19	0.16
N_{SIMS} ($\times 10^{18} \text{cm}^{-3}$)	1.53								
μ_{Hall} (cm^2/Vs)		38	215	43	-	-	38	-	-

the other is the surface temperature or actual growth temperature T_{gr} . The latter is obtained from the EpiTT pyrometer signal. This in-situ measurement tool (for T_{gr} & V_{gr}) was installed during the course of this work, so EpiTT data are only available for run numbers beyond 382. T_{gr} values in *italic* are estimations based on observations made on EpiTT-runs. The 10°C difference in T_{gr} for a given T_{set} depends on the substrate used for growth. The higher T_{gr} is on GaAs substrates, the lower on Ge substrates.

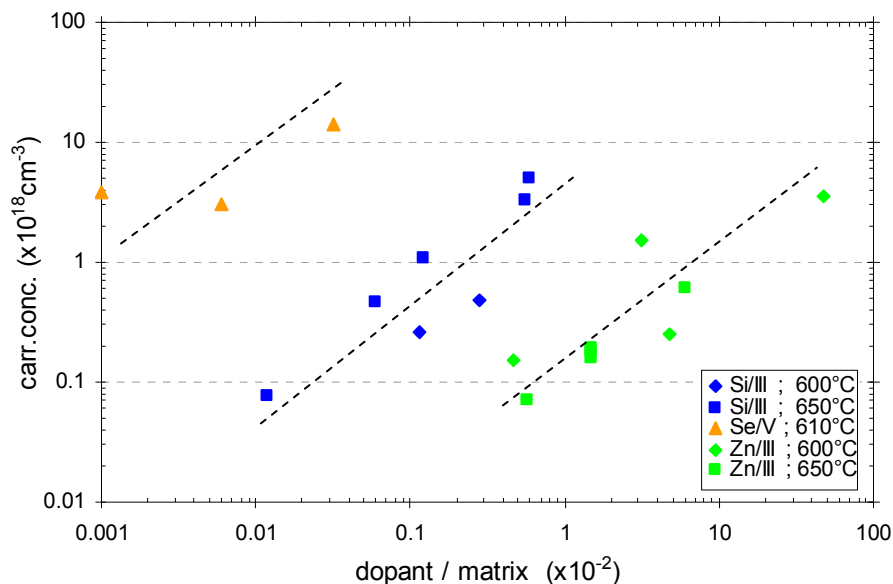


Figure 4-13: *InGaP* carrier concentration as a function of the ratio of dopant / “relevant matrix element(s)” in the vapour phase. The lines are a guide to the eye.

A few samples were selected for secondary ion mass spectrometry (SIMS) – carried out by Procion Analysis, France – as an additional means for checking the doping level and to determine the impurity content in the layers (see Figure 4-16a, b, c and d). They used their *InGaP* standards for quantification of Si and Zn concentrations in the *InGaP* material. As can be seen from Table 4-5, the agreement with the Hall and *C-V* measurements is very good. Since SIMS does not give information on the electrical activity of the dopant element in question (Si), we conclude that the activation degree is 100 per cent. We therefore also assume that the SIMS value for the Zn concentration is definitely an acceptable upper limit estimate of the carrier concentration in the layer.

The doping results are represented graphically in Figure 4-13. For Se-doping a highest value of $1.4 \times 10^{19} \text{ cm}^{-3}$ was reached, for Si a highest value of $5 \times 10^{18} \text{ cm}^{-3}$ was obtained and for Zn $3.5 \times 10^{18} \text{ cm}^{-3}$ was the highest value. The guidelines indicate that the doping behaviour has a linear trend.

When we compare the room temperature Hall mobility data with the values available from literature, we see that our values agree well with the observed trends (see Figure 4-14 and Figure 4-15). However, sample 365 shows an exceptionally high p-type mobility of $215 \text{ cm}^2/\text{Vs}$.

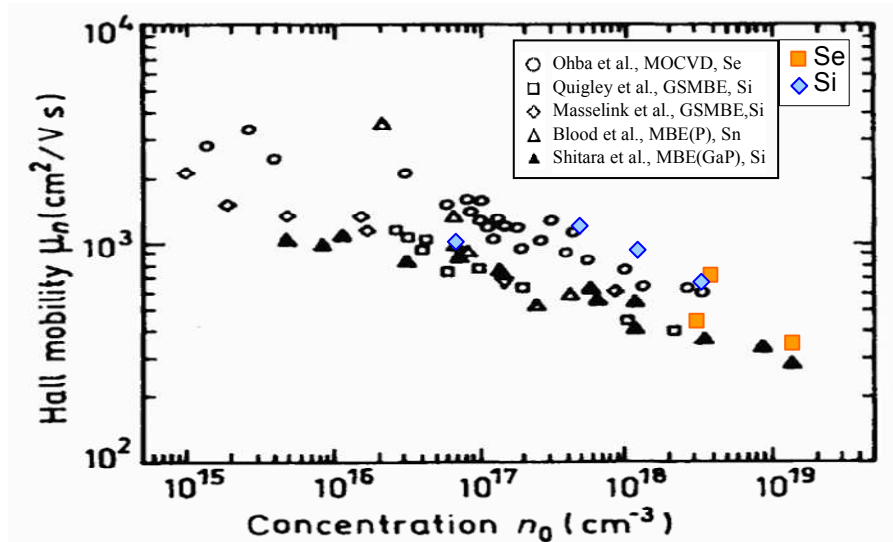


Figure 4-14: Comparison of our room temperature Hall mobility data as a function of carrier concentration for n-type InGaP with values from literature (after [12]).

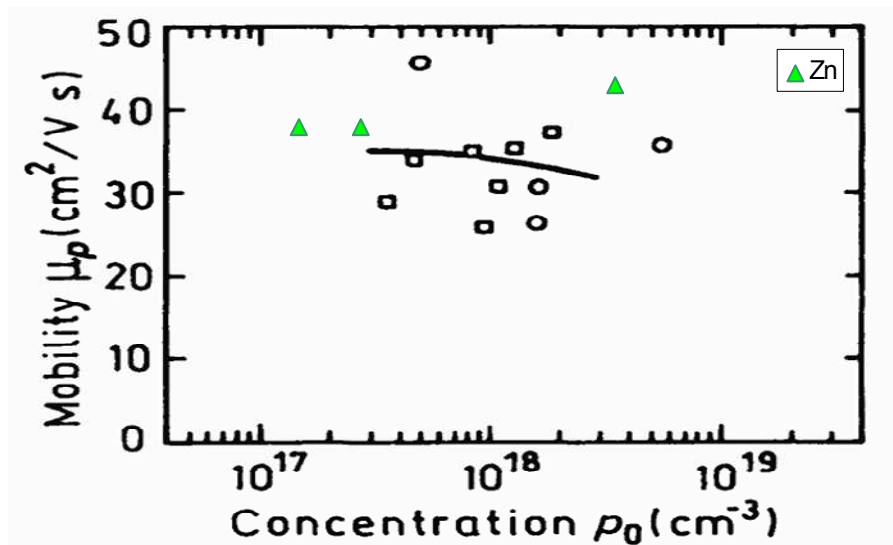


Figure 4-15: Comparison of our room temperature Hall mobility data as a function of carrier concentration for p-type InGaP with values for MOCVD-grown Zn-doped InGaP from literature (after [13]).

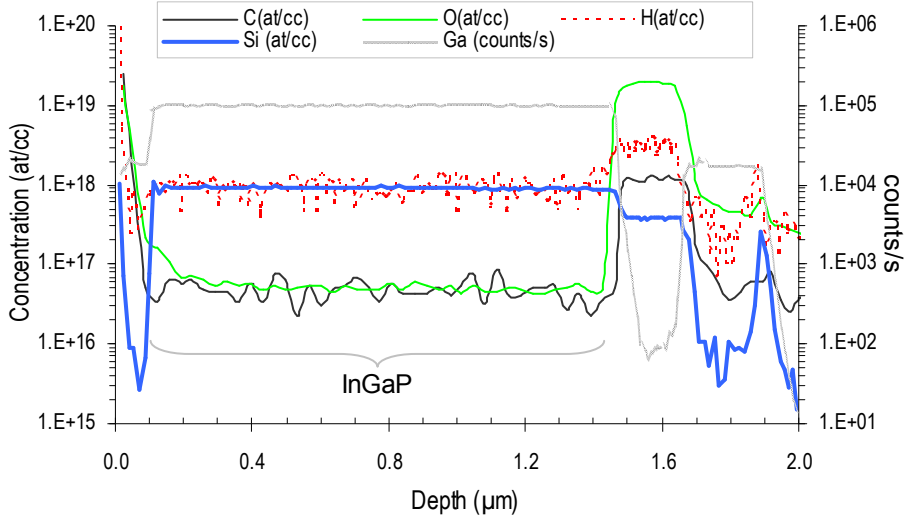
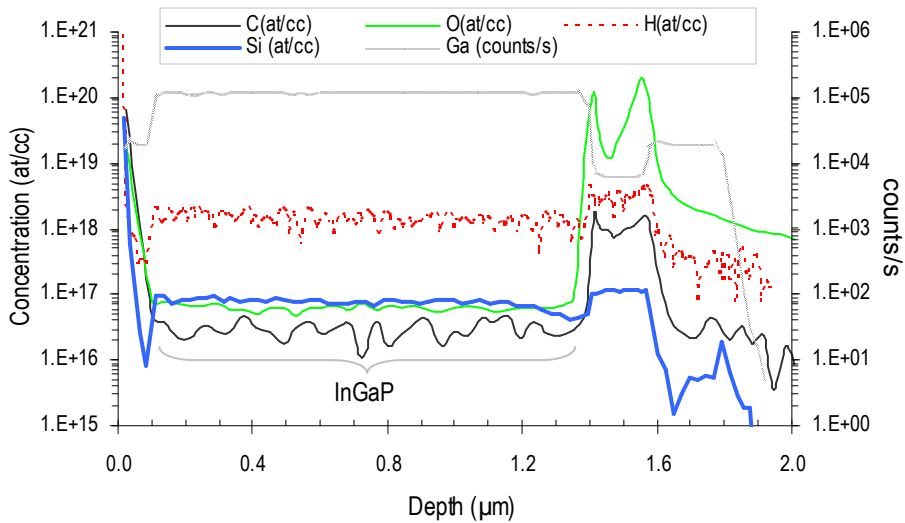
(a) Sample 202: $\text{Si} = 9.2 \times 10^{17} \text{ cm}^{-3}$ (b) Sample 205: $\text{Si} = 8 \times 10^{16} \text{ cm}^{-3}$

Figure 4-16: SIMS profiles of atomic concentrations of dopants and impurities for (a)(b)(c) Si-doped InGaP layers with monitoring of C, O and H, and (d) Zn-doped InGaP.

For the samples analysed with SIMS, also the impurity concentrations of C, O and H in the lattice were determined. Here, we will only discuss the InGaP layer, not the layers grown beneath it. For C, O and H, Probion had no InGaP standards available at that time. However, it turns out that the calibration coefficients are not very different compared to

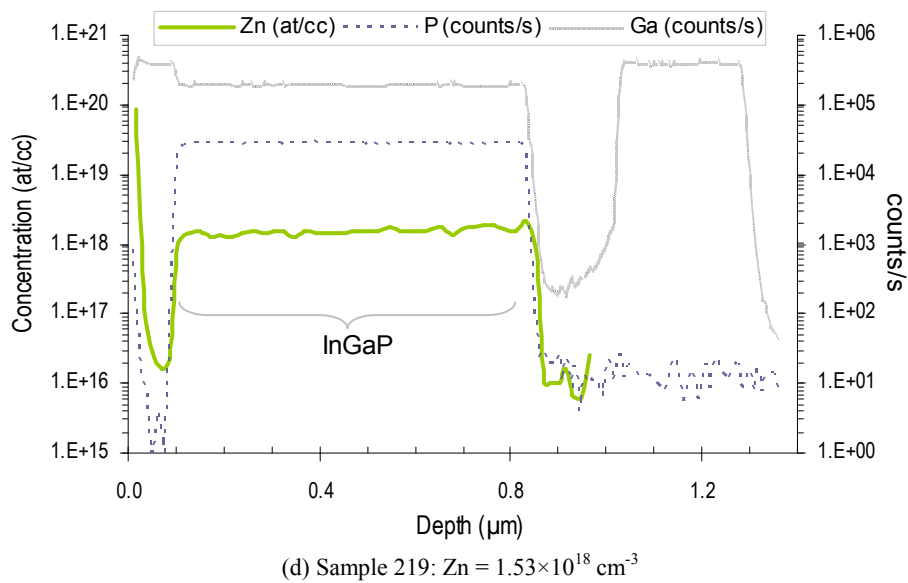
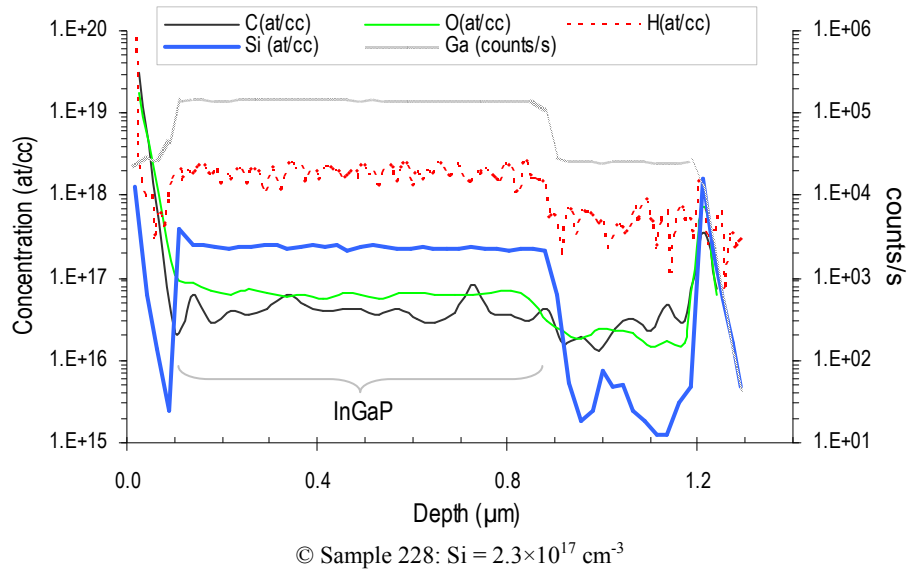


Figure 4-16 – Continued

GaAs, so reasonable estimates were in fact obtained [14]. Therefore, qualitative comparison between different samples is possible. As seen when comparing Figure 4-16a, b and c, the C, O and H concentrations are comparable in all samples. The C and O concentrations are all below 10^{17} cm^{-3} . For the Zn-doped sample, C, O and H were not

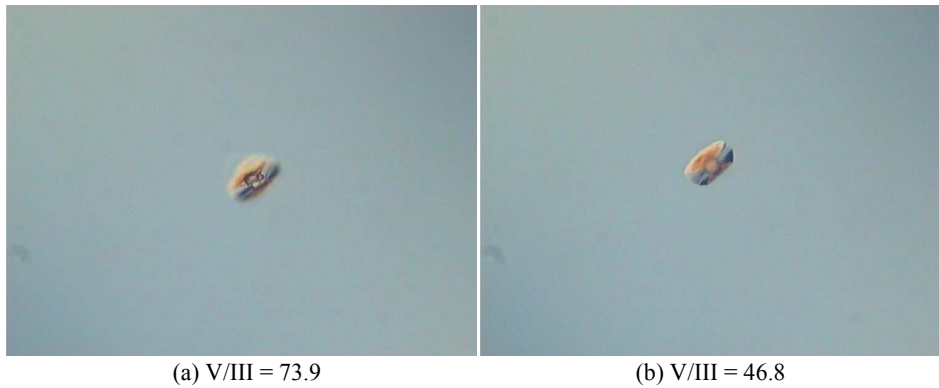


Figure 4-17: Typical defects observed on InGaP layers grown at 630 °C. The average characteristic length and width of the defect are 13 and 7 μm .

accessible because Zn-monitoring requires different analysis conditions. Neither the incorporation of C, O or H was found to be dependent on T_{gr} or on V/III ratio in the temperature range that was used here.

Summarising the previous results, we saw that the Si-, Se- and Zn-concentration is linear in dopant gas flux. The highest values obtained are $1.4 \times 10^{19} \text{ cm}^{-3}$, $5 \times 10^{18} \text{ cm}^{-3}$ and $3.5 \times 10^{18} \text{ cm}^{-3}$ for Se, Si and Zn, respectively. Carbon and oxygen are not incorporated in high concentrations during InGaP growth.

Morphology

On InGaP layers, typical defects can be observed across the entire wafer. Figure 4-17 shows these defects for layers grown at 630 °C with 95.8 and 95.7 $\mu\text{mol}/\text{min}$ of TMGa and TMIn, respectively, and a V/III ratio of 73.9 (fig.a) or 46.8 (fig.b). Obviously, the V/III ratio has no effect on the presence of the defects. When the growth temperature was increased to 650 °C for a V/III = 46.8, no defects were present.

The root mean square (rms) surface roughness of InGaP samples was also measured via scanning white light interferometry (Zygo NewView). Each wafer was analysed on five different spots and the scanned area was $700 \times 530 \mu\text{m}^2$. The average rms roughness for the samples mentioned above was 1.18, 0.95 and 0.84 nm, respectively. The presence of defects in an analysed area obviously has a negative influence on the rms value of that spot. The obtained rms values are quite acceptable.

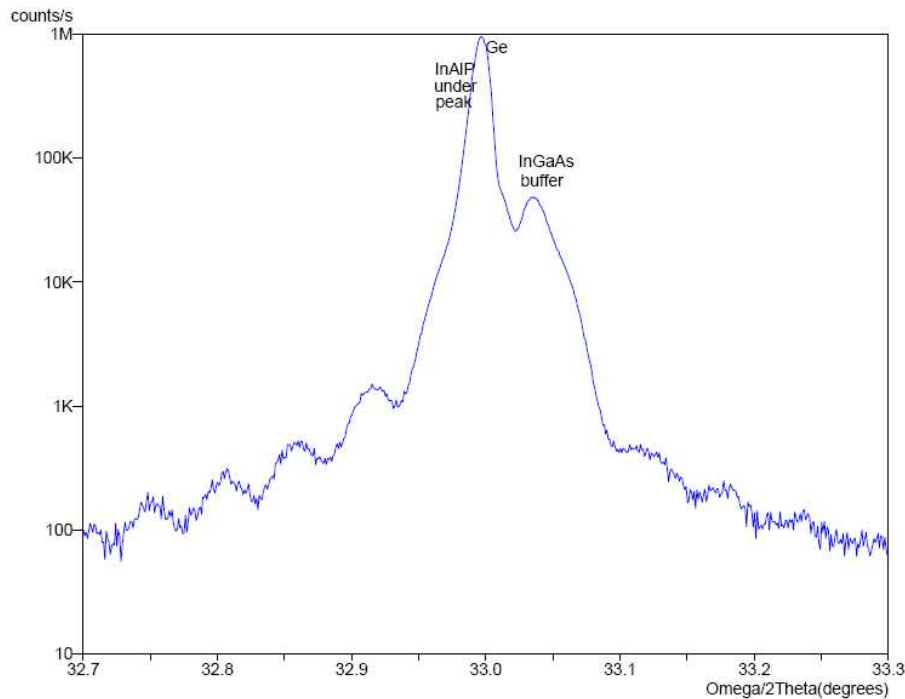


Figure 4-18: $\omega/2\theta$ rocking curve of $1\mu\text{m}$ InAlP on Ge.

4.4.2 InAlP alloy

To reduce surface recombination at the front and rear end of the cell, a window and a back surface field (BSF) are needed to repel minority carriers from those surfaces. A requirement for window and BSF material is that its bandgap is larger than that of InGaP, the cell's bulk material. InAlP (2.35 eV, LM to Ge) is a suitable candidate.

Composition and ordering

The composition of InAlP is well controlled. Lattice-match to germanium is obtained for an $\text{In}_{0.486}\text{Al}_{0.514}\text{P}$ compound. Figure 4-18 shows a HRXRD scan of InAlP on Ge.

Ordering will also occur for this alloy. However, due to the indirect nature of the bandgap for an indium content smaller than 0.56, RT-PL measurements cannot be used to estimate the degree of ordering in our material. However, we did obtain evidence from electron diffraction patterns, performed at imec on our material, that ordering occurs in InAlP. Halfway points are visible in Figure 4-19a, indicating that ordering is present in the material. This sample was grown at 650 °C. In Figure 4-19b these spots are not visible, thus, no ordering is present. That sample was grown at 560 °C. This confirms that when increasing the growth temperature, the degree of ordering increases, as was stated in the InGaP paragraph.

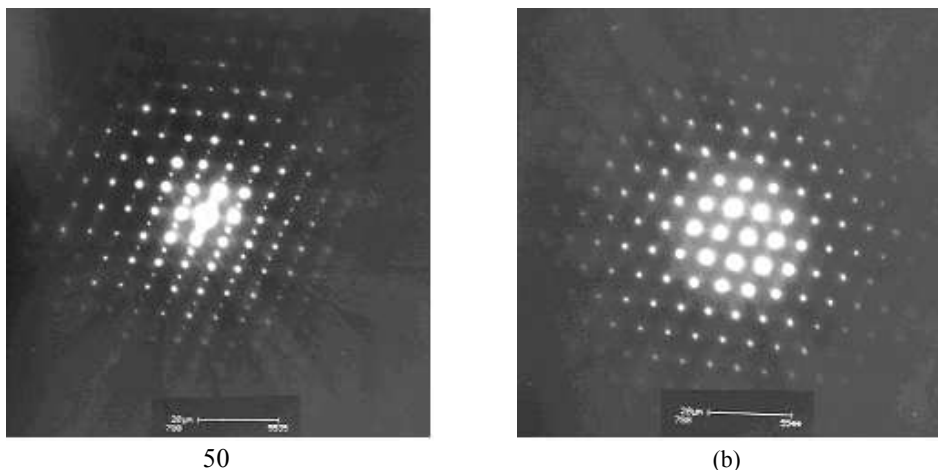


Figure 4-19: *[110]-pole electron diffraction pattern of InAlP (a) grown at 650 °C showing ordering (see halfway points) and (b) grown at 560 °C without ordering.*

Dopant and impurity incorporation

Electrical measurement of the doping level in InAlP layers proved to be much more difficult than for InGaP layers. Growth conditions and results are shown in Table 4-7. The SIMS measurements can be found in Figure 4-21.

Comparing sample 224 with sample 228 (InGaP) shows that the Si concentration in both samples, as determined with SIMS, is comparable. This indicates that the Si incorporation coefficients in both materials are similar. However, due to the high oxygen levels (see below) the actual carrier concentration might be lower.

For Se, Probion did not have an InAlP standard, so the value for samples 237 and 281 are only a rough estimate of the order of magnitude. Caution has to be exerted when comparing these two values since the quantification was done in separate runs. But the difference in H₂Se input by a factor of 10 is reflected in the SIMS values. The Hall and *C-V* measurements for Se-doped sample 601 differ by a factor of 3.5. There are no straightforward conclusions to be drawn regarding Se-doping of InAlP when comparing to InGaP Se-doping.

It is possible to obtain p-type doping in InAlP. The results do not reproduce too well. Whether this is due to the growth or to the measurement is unclear. For decreasing Zn/III ratio the carrier concentration is reduced (samples 600 and 608/612). Reduction of p_V^y also leads to a reduction of the carrier concentration (samples 612 and 614). However, sample 615 shows a completely different result for the same set of growth conditions compared to sample 614. Also, when we compare sample 614 to InGaP

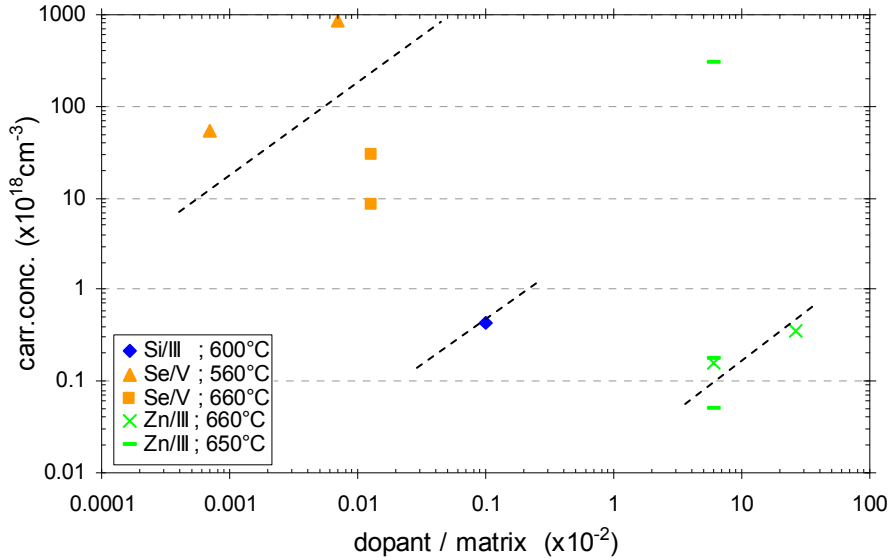


Figure 4-20: *InAlP* carrier concentration as a function of the ratio of dopant / “relevant matrix element(s)” in the vapour phase. The lines are a guide to the eye.

Table 4-7: Growth conditions and doping concentrations for doped *InAlP* layers. T_{gr} values in *italic* are estimated. Inconclusive results are marked by “-”.

Sample	224	237	281	601	600	608	612	614	615
dopant	Si	Se	Se	Se	Zn	Zn	Zn	Zn	Zn
T_{set} (°C)	650	600	600	700	700	700	700	700	700
T_{gr} (°C)	<i>610</i>	<i>560</i>	<i>560</i>	660	660	660	650	650	650
Si/III, Se/V ($\times 10^{-4}$)	10.1	0.70	0.07	1.30					
Zn/III					0.26	0.06	0.06	0.06	0.06
V/III	84.0	84.2	84.2	79.6	79.6	77.9	77.8	40.3	40.3
TMAI ($\mu\text{mol}/\text{min}$)	55.6	35.4	35.4	76.6	76.6	80.5	80.8	79.8	79.8
TMIn ($\mu\text{mol}/\text{min}$)	68.2	40.4	40.4	95.7	95.7	95.7	95.7	95.7	95.7
N_{Hall} ($\times 10^{18} \text{ cm}^{-3}$)				8.5	-	0.16			
N_{CV} ($\times 10^{18} \text{ cm}^{-3}$)				30	0.35	-	0.18	0.05	293
N_{SIMS} ($\times 10^{18} \text{ cm}^{-3}$)	0.43	850	55.5						
μ_{Hall} (cm^2/Vs)				120	-	13			

sample 604 (similar growth conditions), the doping level is a factor 10 lower. Unfortunately, no Zn-doped samples were analysed by SIMS that could shed some light on the matter.

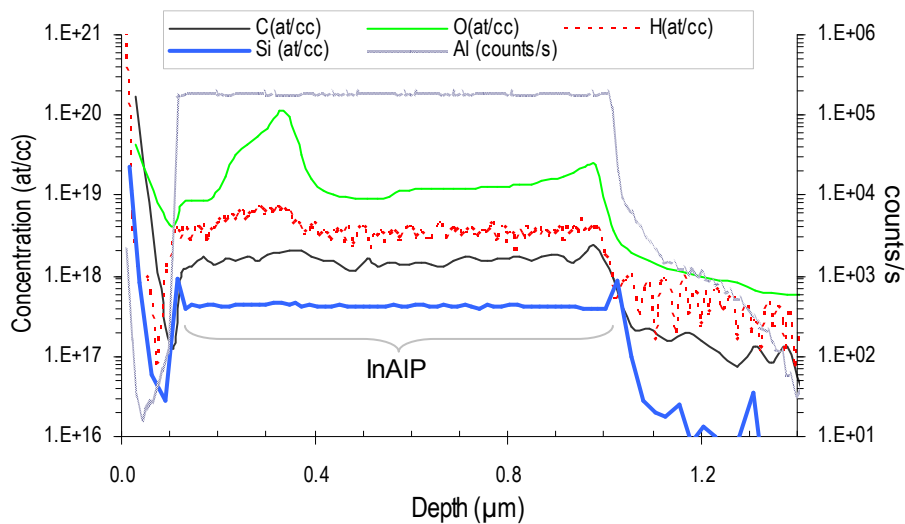
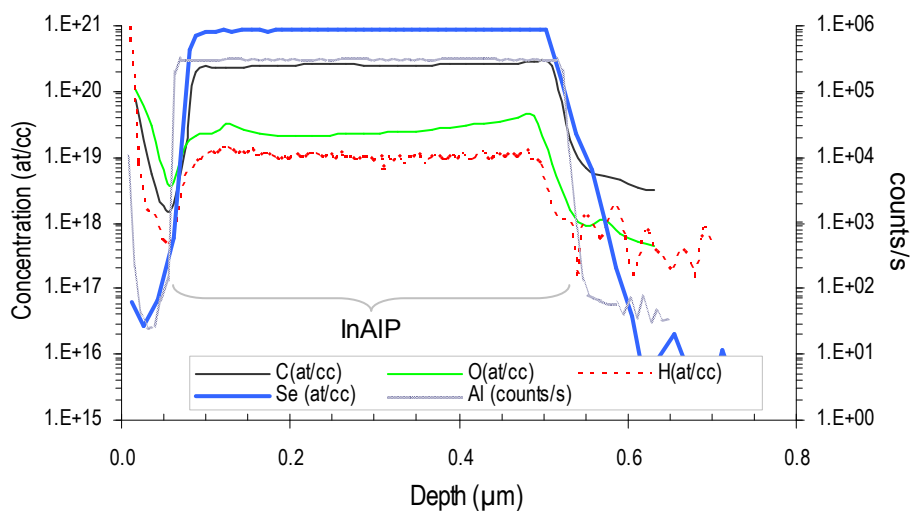
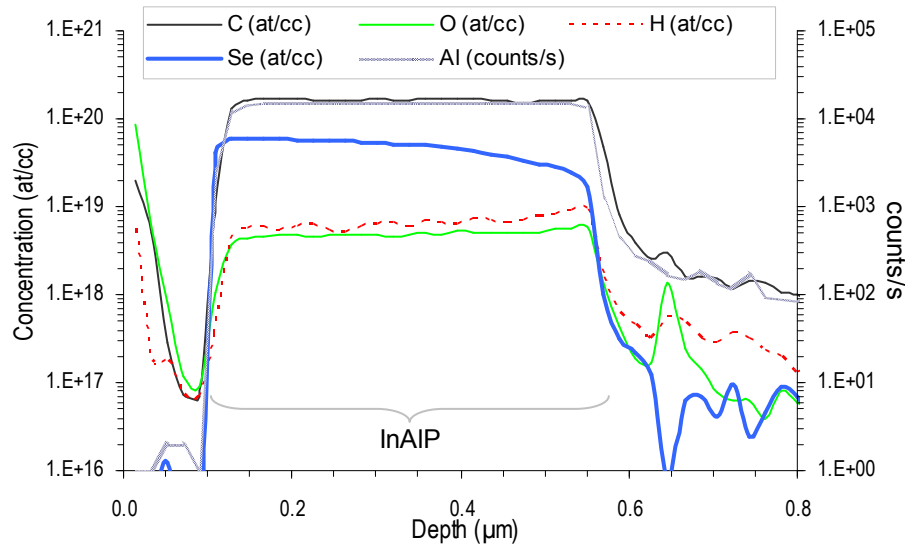
(a) Sample 224: Si = $4.3 \times 10^{17} \text{ cm}^{-3}$ (b) Sample 237: Se = $8.5 \times 10^{20} \text{ cm}^{-3}$

Figure 4-21: SIMS profiles of atomic concentrations of dopants and impurities for (a) Si-doped and (b)(c) Se-doped InAlP layers with monitoring of C, O and H.

The dopant results are presented graphically in Figure 4-20. Temperature dependence of Se-doping can be observed. The guidelines are a very approximate indication for the linearity of the dopant incorporation.



© Sample 281 : Se = $5.55 \times 10^{19} \text{ cm}^{-3}$

Figure 4-21 – Continued

For the C, O and H impurities, Probian did not have the necessary standards needed for quantification but the same remark as for InGaP holds here as well. The values are reasonable estimates. When comparing sample 224 with InGaP sample 228 (both Si-doped with similar growth conditions) we notice that the carbon level in the InAlP is higher by a factor of 20. Clearly, a reduction of 40°C increases the carbon concentration by two orders of magnitude due to the low growth temperature. This might cause compensation in n-type layers if the carbon is electrically active (C most likely occupies group-V sites). The hydrogen concentration seems to remain constant under this temperature change, reducing the probability on a proportional increase of H-passivated carbon complexes.

Now we make some considerations on the oxygen content. The Al atoms are very reactive with oxygen, so it is expected that Al-containing layers exhibit higher oxygen content than layers without aluminium. Indeed, the oxygen values in samples 224 and 237 are very high, between $5 \times 10^{18} \text{ cm}^{-3}$ and $5 \times 10^{19} \text{ cm}^{-3}$. In sample 224 we even observe a strange oxygen spike at a depth of around 300 nm that is rather difficult to explain. Comparison between sample 237 and 281 seems to indicate that the oxygen content in the layer is related to the amount of H_2Se that is introduced.

Summarising we can say that the Si-doping seems to yield a reliable result. As mentioned previously, Zn-doping does not reproduce too well. Due to the lack of standards for Se-doping, no reliable results were obtained. The carbon concentration is

Table 4-8: Overview of the layer stack used for samples A, B, C, D, E and F. The dotted line indicates where the dopant type is switched.

Sample	Compound	(doping level)	A, B, D, E, F	C
Contact	In _{0.01} Ga _{0.99} As	($\geq 10^{19} \text{ cm}^{-3}$)	300 nm	300 nm
Window	In _{0.486} Al _{0.514} P	($2 \times 10^{18} \text{ cm}^{-3}$)	30 nm	–
Emitter	In _{0.495} Ga _{0.505} P	($2 \times 10^{18} \text{ cm}^{-3}$)	100 nm	200 nm
Base	In _{0.495} Ga _{0.505} P	($1 \times 10^{17} \text{ cm}^{-3}$)	1 μm	3 μm
BSF	In _{0.486} Al _{0.514} P	($2 \times 10^{18} \text{ cm}^{-3}$)	50 nm	–
buffer	In _{0.01} Ga _{0.99} As	($1 \times 10^{18} \text{ cm}^{-3}$)	600 nm	600 nm
Substrate			p-Ge	p-Ge

high, on the order of 10^{18} cm^{-3} at 600 °C and even 100× higher for really low growth temperatures. Also the oxygen content in the InAlP is high, with $5 \times 10^{18} \text{ cm}^{-3}$ the lowest value measured. For SIMS analysis performed on Al_{0.85}Ga_{0.15}As, grown using various growth conditions, the oxygen content was $4\text{--}7 \times 10^{18} \text{ cm}^{-3}$. These layers were undoped. For Al_{0.3}Ga_{0.7}As, the lowest oxygen content was $2 \times 10^{18} \text{ cm}^{-3}$ and changing growth conditions had a much larger influence on the oxygen level.

Morphology

From TEM study of two samples it is observed that for the sample grown at 660°C (Figure 4-22, bottom), very long planar defects originate at the InAlP / GaAs interface and run up to the GaAs / InAlP interface, probably causing the slight roughness of the GaAs cap layer. For the sample grown at 560°C (Figure 4-22, top) no such defects are observed. Most of our InAlP layers were grown around 600°C the middle of this temperature range. The same features as for InGaP are observed on the surface. Energy dispersive X-ray analysis (EDX) on those features has shown that they have the same composition as the bulk material.

4.4.3 Solar cell performance

The structures used for the different samples are presented in Table 4-8. The InGaP single junction solar cells that were fabricated on a standard In_{0.01}Ga_{0.99}As buffer (growth on Ge is nucleated with GaAs, followed by the growth of a buffer layer) on Ge all have the np-configuration. Results obtained from 3 MeV proton irradiation experiments indicate that p-type InGaP layers keep a higher minority carrier diffusion length after irradiation than the n-type layer. This is because the electron mobility in the p-type layer is larger than the hole mobility in the n-type layer. These findings suggest that the np-configuration is more radiation resistant than the p-n configuration [7]. The radiation induced defects in InGaP material can be partially recovered by minority carrier injection annealing which results in the (partial) recovery of the solar cell properties [15].

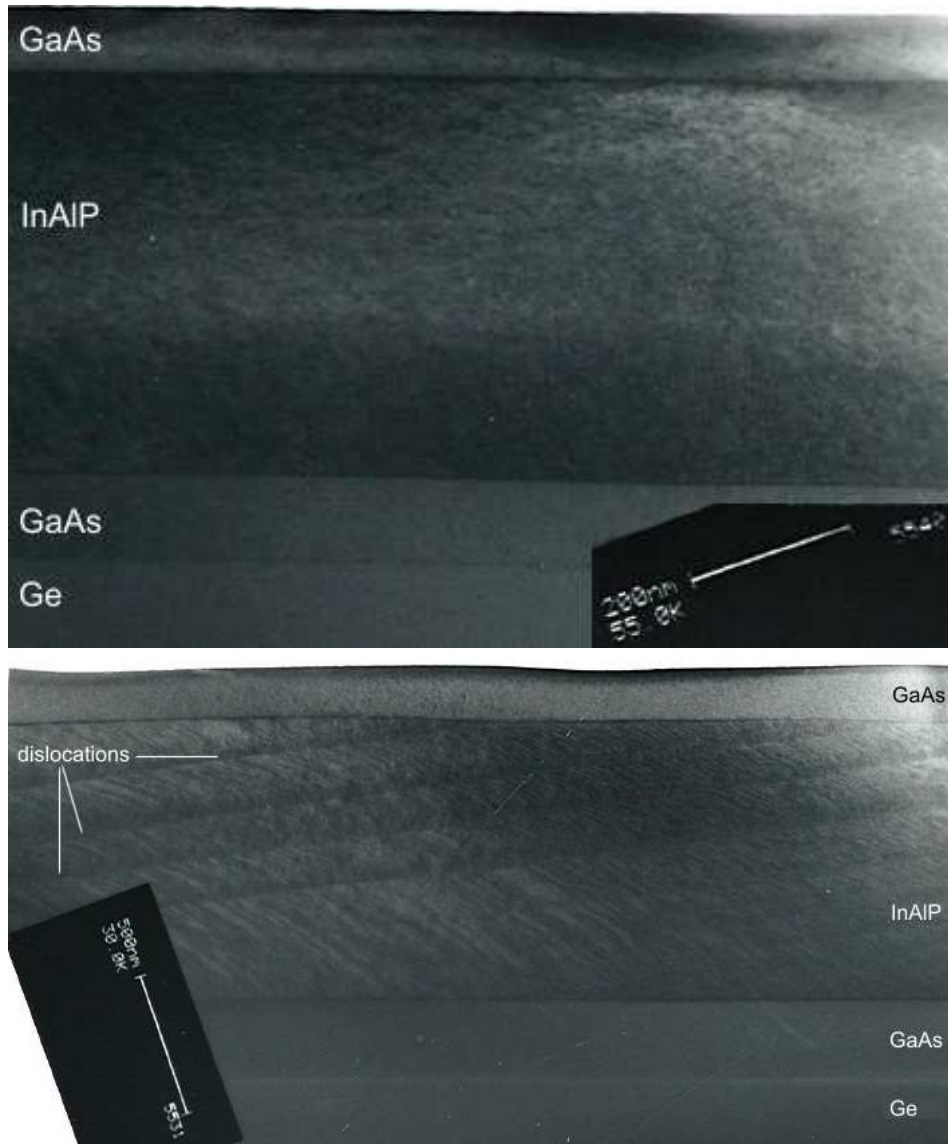


Figure 4-22: TEM images of InAlP on GaAs/Ge without (top) and with (bottom) planar defects.

Growth details

The results of the single junction InGaP solar cells on Ge are presented further on. Table 4-9 summarises the growth conditions of the different samples. Cells on sample A, B and C were fabricated with a wet mesa-etch, those on sample E and F with a dry mesa-etch and both wet and dry were used on sample D. The reason for switching to dry etching of the mesa will become clear in the next paragraph.

Table 4-9: Growth conditions for the InGaP solar cells layers.

Sample	A	B	C	D	E	F
BSF ($1 \times 10^{18} \text{ cm}^{-3}$)						
T _{set} (°C)	600	700		650	670	670
T _{gr} (°C)	560	660		610	630	600
V/III	84.9	169.9		82.1	82.1	82.1
TMIn (μmol/min)	61.4	40.4		95.7	95.7	95.7
TMAI (μmol/min)	62.8	29.3		76.6	76.6	76.6
Zn/III	0.13	0.24		0.28	0.28	0.28
Base ($1 \times 10^{17} \text{ cm}^{-3}$)						
T _{set} (°C)	650	650	650	650	670	670
T _{gr} (°C)	610	610	610	610	630	600
V/III	83.4	84.6	84.6	74.2	74.2	74.2
TMIn (μmol/min)	61.4	61.4	61.4	95.7	95.7	95.7
TMGa (μmol/min)	58.1	55.5	55.5	95.1	95.1	95.1
Zn/III ($\times 10^{-3}$)	4.6	4.7	4.7	4.8	4.8	4.8
Emitter ($1-2 \times 10^{18} \text{ cm}^{-3}$)						
T _{set} (°C)	650	650	650	650	670	670
T _{gr} (°C)	610	610	610	610	630	600
V/III	83.4	84.6	84.6	74.2	73.9	73.9
TMIn (μmol/min)	61.4	61.4	61.4	95.7	95.7	95.7
TMGa (μmol/min)	58.1	55.5	55.5	95.1	95.8	95.8
Si/III ($\times 10^{-3}$)	4.5	4.6	4.6	9.3	9.2	9.2
Window ($3 \times 10^{18} \text{ cm}^{-3}$)						
T _{set} (°C)	600	700		650	670	670
T _{gr} (°C)	560	660		610	630	600
V/III	84.6	165.9		80.8	80.8	80.8
TMIn (μmol/min)	61.4	40.4		95.7	95.7	95.7
TMAI (μmol/min)	64.9	31.0		79.5	79.5	79.5
Si/III, Se/V ($\times 10^{-3}$)	5.6	9.9		0.3	0.3	0.2
Contact ($> 10^{19} \text{ cm}^{-3}$)						
T _{set} (°C)	650	650	650	650	670	670
T _{gr} (°C)	610	610	610	610	630	600
V/III	12.6	12.5	12.5	14.3	14.2	14.2
TMIn (μmol/min)	1.5	2.3	2.3	2.2	3.1	3.1
TMGa (μmol/min)	79.3	79.3	79.3	105.7	105.7	105.7
Se/V ($\times 10^{-3}$)	3.2	3.1	3.1	2.8	2.8	1.6

Sample A, with InAlP grown at 600 °C probably has high oxygen content in the InAlP BSF and window layer and possibly defects crossing the active layers, originating in the InGaP. In sample B the InAlP was grown at a higher temperature, even though this might give rise to planar defects in the InAlP (see Figure 4-22), because it was assumed that increasing the temperature would result in lower oxygen content. To rule out an inoperative InGaP junction, sample C was also grown, where the InAlP BSF and window were omitted. For sample D the InAlP growth temperature was reduced again by 50 degrees. For sample E all growth temperatures were increased by 20 degrees. Although sample F was grown with the same settings as sample E, the EpiTT indicated growth temperatures that were 30 degrees lower.

InGaP etching

Since phosphide-based materials do not etch in a $\text{H}_2\text{SO}_4:\text{H}_2\text{O}_2:\text{H}_2\text{O}$ (1:8:200) solution, which is used for etching the mesa of a single junction GaAs solar cell, an alternative wet etchant was needed for the mesa-etch to separate the cells on the sample. A solution of $\text{H}_3\text{PO}_4:\text{HCl}:\text{H}_2\text{O}$ (1:1:1) was selected because of its selectivity in etching phosphide materials over arsenide materials [16]. The etch rate is approximately 90 nm/min for InGaP at room temperature. Also InAlP can be etched in this solution, since typical etchants for selective etching of InAlP over GaAs are based on $\text{HCl}:\text{H}_2\text{O}$ mixtures.

To etch through the complete stack of the InGaP cell, first the $\text{H}_2\text{SO}_4:\text{H}_2\text{O}_2:\text{H}_2\text{O}$ mixture is used to selectively etch the top InGaAs layer. Then, the sample is put into $\text{H}_3\text{PO}_4:\text{HCl}:\text{H}_2\text{O}$ to etch the phosphide layers. Finally, the sample is put back into $\text{H}_2\text{SO}_4:\text{H}_2\text{O}_2:\text{H}_2\text{O}$ to remove the InGaAs buffer layer. This last step is not really necessary because the junctions are already isolated from each other after the second etch step. As we shall see in the following paragraph, performing this last step might in fact lead to unwanted side effects.

As is seen in Figure 4-23a, underetch has occurred during the mesa-etch, in this case over a distance of 120 μm , when the cell edges are parallel to $\langle 100 \rangle$ directions. If the cell edges are oriented parallel to the $\langle 110 \rangle$ directions, only the corners of the cell area are affected (see Figure 4-23b). Figure 4-24 shows an SEM image of an InGaP sample with the following structure: 300 nm GaAs cap / 700 nm InGaP / 260 nm GaAs buffer / Ge substrate. After a photolithographic step, first the GaAs cap was removed and then the InGaP layer was etched away in $\text{H}_3\text{PO}_4:\text{HCl}:\text{H}_2\text{O}$ in 7 min. The underetch is about 14 μm . From this it is clear that if the sample would again be put into $\text{H}_2\text{SO}_4:\text{H}_2\text{O}_2:\text{H}_2\text{O}$ to etch away the buffer (± 750 nm thick in a real solar cell), also the contact layer under the finger contacts could be etched. It might then occur that the unsupported part of the finger collapses during further processing steps and in that way short-circuits the solar cell if the contact metal touches both emitter and base. Also, if the cell is not aligned with the edges parallel to the $[110]$ directions, the actual solar cell area will be smaller than desired.

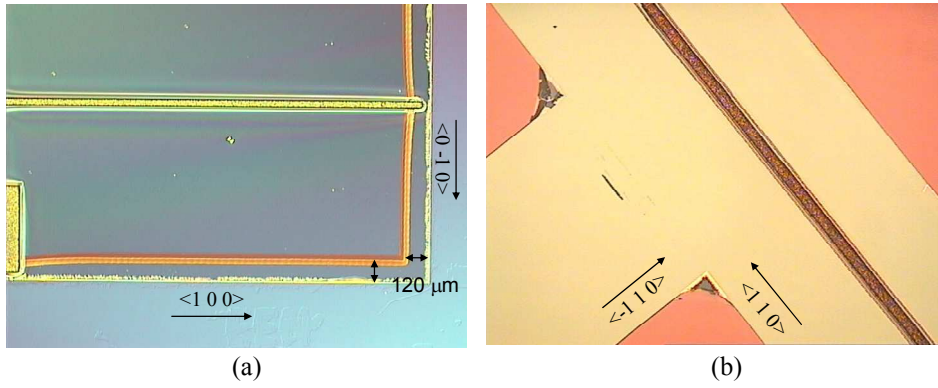


Figure 4-23: Underetch observed after processing of an InGaP single junction cell (a) with the cell edges parallel to the $\langle 100 \rangle$ directions and (b) with the cell edges parallel to the $\langle 110 \rangle$ directions. The darker areas are the cell areas

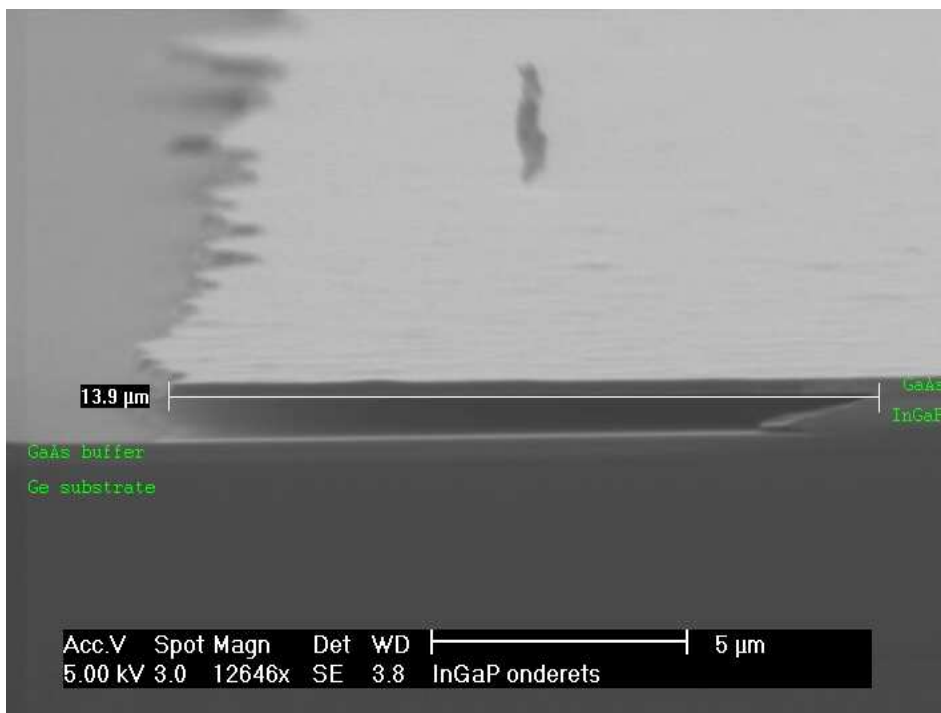


Figure 4-24: SEM image showing underetch due to etching of InGaP in a solution of $H_3PO_4:HCl:H_2O$ (1:1:1).

Table 4-10: Overview of InGaP single junction solar cell parameters. The cell area (in cm^2) is denoted as “_<area>”. The short-circuit currents are – from top to bottom – measured, calculated from EQE (this includes shadowing and reflection losses) and calculated from IQE (this compensates for shadowing and reflection).

Sample	A_1	B_4	B_0.25	C_0.25	D_4	E_4	F_4
Reflectance _{400-670nm} (%)	–	8.7	8.7	13.8	8.9	10.0	3.0
$J_{sc, \text{measured}}$ (mA/cm^2)	0.1	8.4	8.5	7.0	8.3	11.2	13.6
$J_{sc, \text{calculated from EQE}}$ (mA/cm^2)	–	8.3	8.3	5.9	7.4	11.3	13.0
$J_{sc, \text{calculated from IQE}}$ (mA/cm^2)	–	9.4	9.4	7.2	8.6	13.1	14.1
V_{oc} (V)	0.629	1.265	1.279	1.293	1.234	1.271	1.276
$R_{s, \text{upper limit}}$ (Ω)	–	3.641	–	–	2.728	1.714	1.131
Fill factor (%)	47.2	72.3	76.0	64.1	75.1	79.2	82.0
Efficiency (%)	0.02	7.7	8.3	5.8	7.7	11.3	14.2

An alternative to avoid (anisotropic) underetching during the fabrication of the mesa is to use reactive ion etching with a Cl_2 -Ar plasma for stacks containing phosphide material. The plasma conditions are 15sccm Cl_2 and 15sccm Ar at 10 mtorr with an RF-power of 250 W. The plasma is applied during 4 minutes while the sample is actively cooled to 15 °C. In this way, the entire III-V stack is etched away to form the mesa.

Results

The results of the single junction InGaP solar cells on Ge are presented in Table 4-10. Cells on sample A, B and C were processed with a wet mesa-etch, those on sample E and F with a dry mesa-etch and on sample D cells were processed with both. The table only contains the result for the wet processing of D. That of the dry processing is presented later on. In the table, the cell area (in cm^2) is denoted by “_<area>”. This extension will only be mentioned in the text where necessary. The AM1.5G J - V curves are shown in Figure 4-25, the internal quantum efficiency (IQE) in Figure 4-26.

The first attempt at an InGaP solar cell on Ge, sample A, with InAlP grown at 600 °C, showed a very bad J - V characteristic and an efficiency of only 0.02 %. The most likely reasons for this are the high oxygen content in the InAlP BSF and window layer and possible defects crossing the active layers.

For the next attempt, sample B, the InAlP was grown at a higher temperature, because it was assumed that increasing the temperature would result in a lower oxygen content. To rule out an inoperative InGaP junction, sample C was also grown, where the InAlP BSF and window were omitted. Sample C was expected to give a low efficiency because the minority carrier barriers were absent in this cell. As it turned out from the SIMS measurement on an InAlP layer that was grown just before cell B, there already was less oxygen (about a factor of 4 to 6) in the InAlP at 600 °C than at the time cell A was grown (compare Figure 4-21b and c). Cell B was a marked improvement over cell A.

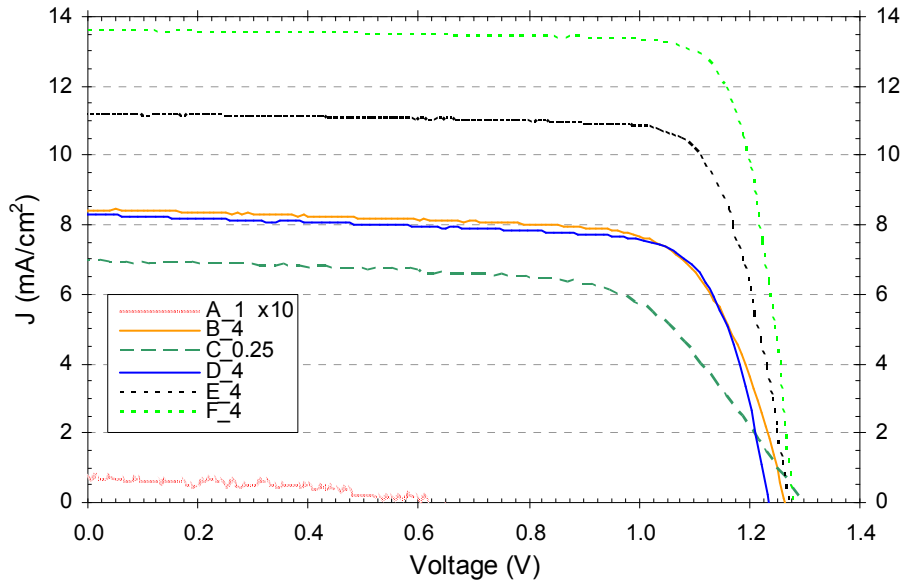


Figure 4-25: Measured I-V characteristics for single junction InGaP solar cells on Ge under AM1.5G illumination. The A₁ curve is magnified 10 times. The cell area (in cm²) is denoted as “_<area>”.

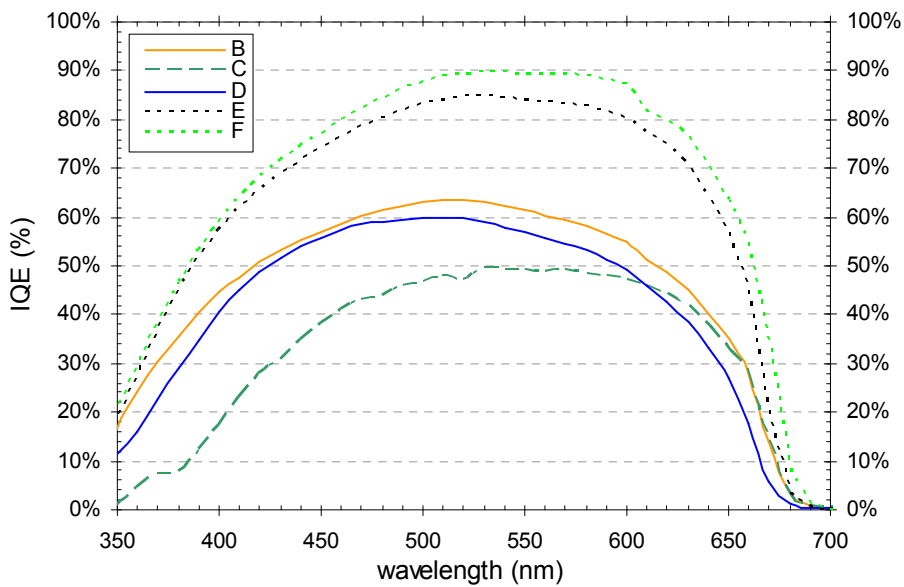


Figure 4-26: Internal quantum efficiency for single junction InGaP solar cells on Ge.

The smaller cell B_0.25 has a higher efficiency, 8.3 %, than the larger cell B_4, 7.7 %, due to higher J_{sc} , V_{oc} and fill factor. As can be clearly seen from the I - V curves, both cells have a shunt resistance that is too low, indicating the existence of defects in the active cell regions. An insufficient material quality is thought to be the main limiting factor on the cell efficiency through enhanced recombination in the bulk of the cell and high recombination velocities at the base/BSF and window/emitter interfaces, yielding an IQE of around 60 %. As expected, cell C showed a lower performance due to the absence of BSF and window, which is clearly visible in the IQE comparison. The IQE for this cell remains below 50 %.

Solar cell D_4, with InAlP grown at lower temperature than for B_4, demonstrates a small improvement in fill factor compared to B_4, which would indicate a slight reduction in depletion region recombination. The J_{sc} is a fraction lower but mainly the V_{oc} is lower due to higher recombination velocities at the back and at the front (see IQE). This gives a comparable efficiency of 7.7 % with an IQE < 60 %.

The layer stack of cell E was grown at 20 °C higher setpoint. Since all other parameters were the same during growth, the higher absorption edge is related to ordering induced bandgap reduction. The major improvement was in J_{sc} , which also led to a substantial improvement of the fill factor approaching decent values. The result was an 11.3 % efficient cell. Better material quality obviously led to fewer defects in the bulk material, increasing the IQE to around 84 %. Shortly before this run, a leak was fixed at the thermocouple which might have lowered the oxygen background in the reactor.

Another possible reason for the reduction of the oxygen background may be the installation of filters in the H₂- and N₂-droppoint in the MOCVD-lab; a modification that was decided upon after the observation of regular H₂O spikes at the H₂-droppoint, caused by the introduction of a new H₂-ring supply.

Finally, solar cell F was grown with the same parameters, although the EpiTT indicated a lower surface temperature T_{gr} . An increased J_{sc} and fill factor – a good value of 82 % was obtained – indicate improved material quality. The resulting efficiency is 14.2 % and the IQE almost attains 90 %.

The parameters for an AM1.5G illuminated ideal single junction InGaP solar cell having a bandgap of 1.877 eV, are presented in Table 4-11. Also shown are the highest reported values found in literature for single junction InGaP solar cells on GaAs. They are from Japan Energy Corporation [17] and Toyota Technical Institute [18].

As was mentioned earlier, using a wet mesa-etch causes serious lateral etching of the InGaP cell. To examine its effects on cell performance, cell D was processed with a wet and a dry mesa-etch. Using the dry mesa-etch slightly improves the IQE (Figure 4-27) at

Table 4-11: Solar cell parameters for an ideal single junction InGaP solar cell, the best values reported in literature on GaAs substrates and Imec's best result on a Ge substrate.

Sample	Ideal solar cell	Japan Energy Corp.	Toyota Techn. Inst.	Imec
Cell area (cm ²)	–	2	10	4
J _{sc} (mA/cm ²)	17.20	14.40	15.12	13.6
V _{oc} (V)	1.464	1.390	1.391	1.276
Fill factor (%)	91.2	86.9	87.9	82.0
Efficiency (%)	23.0	17.4	18.5	14.2

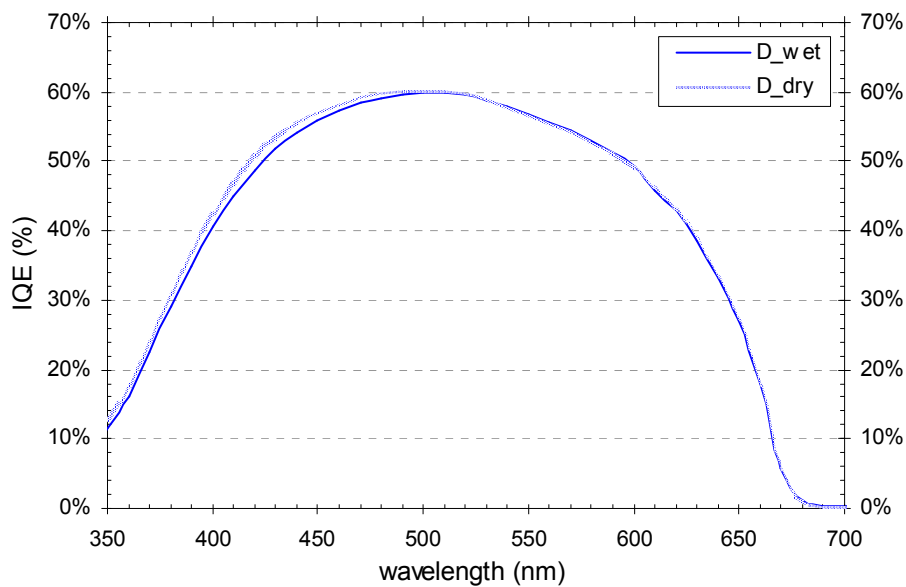


Figure 4-27: Comparison of the IQE of a wet and dry mesa-etched cell.

Table 4-12: Parameters of a wet and dry mesa-etched cell under AM1.5G solar spectrum.

Sample	D_wet	D_dry
Cell area (cm ²)	4	4
J _{sc} (mA/cm ²)	8.31	8.55
V _{oc} (V)	1.234	1.218
Fill factor (%)	75.1	75.1
Efficiency (%)	7.7	7.8

the shorter wavelengths, meaning that something has changed at the front of the cell. This is explained by looking at the wet-etched mesa wall shape (Figure 4-24): more material is etched away at the top, thus, less photons are absorbed compared to the dry etch. This is confirmed by the increased J_{sc} for cell D_dry (Table 4-12).

4.4.4 Time-resolved photoluminescence

The quality of our best single junction InGaP solar cell on germanium is not as good as the best literature values. There is still room to increase J_{sc} and V_{oc} with 1 mA/cm² and 0.1 V, respectively.

In an attempt to improve our understanding of the InGaP material quality, time-resolved photoluminescence measurements were conducted (by Probion Analysis) on InGaP double heterostructures (DH), made specifically for this purpose. The layer stack consisted of our standard GaAs buffer on Ge followed by the InGaP DH, i.e. an InGaP layer, p-type doped to the level of the solar cell's base, clad with InAlP layers, p-type doped to the level of the cell's BSF. Finally, a 40 nm highly doped GaAs cap layer was grown on top of the DH to protect the InAlP barrier from the air and to ensure symmetric boundary conditions on both sides of the InGaP layer, should band bending occur if the InAlP doping level is not high enough. The thickness of the InGaP is varied: 200, 400 and 800 nm is aimed at. From the EpiTT 633 nm reflectance signal, thicknesses of 207, 415 and 830 nm are deduced. The samples are excited by a double Ti:Sa mode locked laser at 400 nm, with pulse duration of 1.5 ps and repetition time of 12 ns. The average power on the samples is 1 mW and the spot diameter 50 μm, resulting in a low carrier creation of 1.2×10^{12} cm⁻². The luminescence is spectrally dispersed with a monochromator equipped with a 75 gr/mm grating and then enters a streak camera with a time resolution of 30 ps for this time range.

It is observed that the signal is weak at the beginning of the excitation – when the laser first strikes the sample – and then increases to stabilise after a few minutes. It is believed that the decay time after one hour of exposition is the relevant measurement. This yields effective lifetimes of 3.60, 2.65 and 1.89 ns for the 830, 415 and 207 nm thick InGaP layer, respectively. The effective lifetime τ_{eff} can be expressed as

$$\frac{1}{\tau_{eff}} = \frac{1}{\tau_{eff_bulk}} + S \frac{2}{w} = \frac{1}{\tau_{rad}} + \frac{1}{\tau_{nonrad}} + S \frac{2}{w}, \quad (4.6)$$

with τ_{eff_bulk} , τ_{rad} and τ_{nonrad} the effective, radiative and non-radiative bulk lifetime, S the interface recombination velocity and w the layer thickness. Plotting $1/\tau_{eff}$ as a function of $2/w$ gives us S as the slope of a linear fit through the data points and τ_{eff_bulk} is obtained from the intercept with the y-axis (see Figure 4-28). We get $\tau_{eff_bulk} = 4.94$ ns and $S = 3417.7$ cm/s. Assuming an electron diffusion coefficient $D_e = 100$ cm²/s [19],

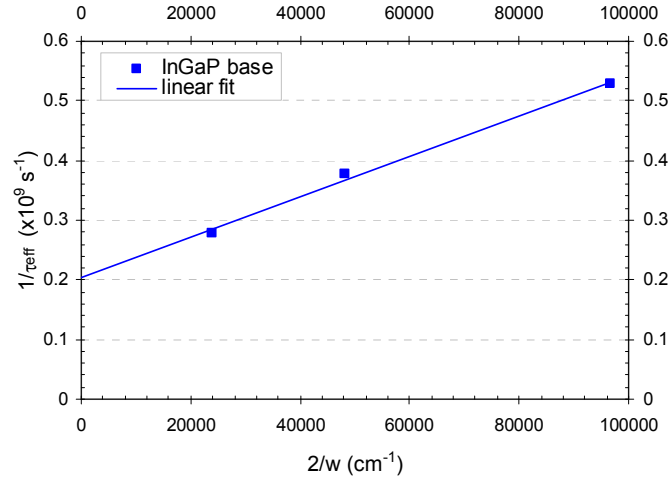


Figure 4-28: $1/\tau_{\text{eff}}$ as a function of $2/w$ for an InGaP base layer clad in InAlP BSF layers.

the electron diffusion length L_e is 7.0 μm . Since the majority carrier concentration created was low, one could make the following approximation: $\tau_{\text{eff_bulk}} \approx \tau_{\text{nonrad}}$.

A first impression would be that this value for S at the base/BSF interface is at least a factor 10 too high when comparing it to values for Si or Ge solar cells. However, Yang et al. [20] report a minority carrier lifetime of 5.1 ns and a recombination velocity at an InAlP / InGaP interface of 5800 cm/s. Furthermore, calculations of the internal quantum efficiency of thin InGaP cells made by Kurtz et al. [19] showed that reduction of S at both BSF and window to below 10^4 cm/s has a negligible effect on the IQE. In this respect, our measured value for S at the base/BSF interface (~ 3420 cm/s) is a good one.

A similar study on the n-type material of the emitter, clad in the InAlP from the window layer, would be an interesting analysis to determine the interface recombination velocity at the front of the cell.

4.4.5 Remote hydrogen plasma passivation

Gorbylev et al. [21] report that hydrogen (or deuterium) passivation at 250 $^{\circ}\text{C}$ for 1 hour passivates both Si donors and Zn acceptors in InAlGaP and InGaP. They also found that new hole traps are generated in p-InGaP. Complete recovery was found to occur after annealing at 450 $^{\circ}\text{C}$. Using a remote-plasma (16 mW/cm 2) at 200 $^{\circ}\text{C}$ and 0.01 torr for 2 hours, Lee et al. [22] observe the passivation of Si donors as well as deep levels near the surface of an InGaP layer. Electrical properties are recovered by rapid thermal annealing at 350 $^{\circ}\text{C}$ for 20 s.

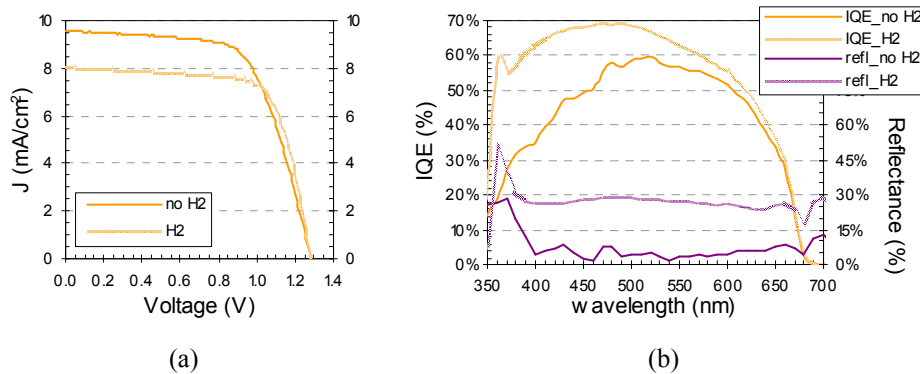


Figure 4-29: (a) I - V characteristics and (b) IQE and reflection curves for cell B before and after remote hydrogen plasma treatment.

Experiments have also been done with a PH_3/H_2 plasma. Akahori et al. [23] used 10 % PH_3 in H_2 in an RF plasma chamber at 0.1 torr and 250 °C for 1 hour. They observed an increase in the PL intensity of $\text{In}_{0.49}\text{Ga}_{0.51}\text{P}$ grown on a GaAs on Si substrate, together with a narrowing of the linewidth, suggesting that defect related non-radiative recombination centres can be effectively passivated. Annealing the passivated sample in H_2 at 450 °C for 10 minutes countered the effects of the hydrogenation. The addition of PH_3 to the H_2 plasma serves to passivate the plasma induced surface damage. Wang et al. [24] have used the same plasma to passivate bulk and surface defect-related non-radiative recombination centres in GaAs solar cells on Si and observed an increase in V_{oc} . Contrary to Akahori et al., the authors didn't see a reduction of the PL intensity upon annealing a single layer in H_2 for 10 minutes at 450 °C. However, annealing a device at this temperature did lead to partial removal of the passivation effect.

An early remote hydrogen plasma passivation experiment was carried out on sample B – prior to having any knowledge about lifetime or interface recombination velocity – in an attempt to improve the characteristics of a finished single junction InGaP solar cell. First, the MgF_2 top layer of the dual layer ARC was removed by rinsing in water and the cell characteristics were measured. Then the cell was placed in a remote 23 % NH_3 in H_2 plasma (100 W) for 1 hour at a temperature below 280 °C. After this treatment the cell was measured again and the resulting data is shown in Figure 4-29. As can be seen, J_{sc} was decreased from 9.59 to 8.04 mA/cm². The reason is increased reflection due to either a damaged ARC or to lack of an ARC and damage to the window layer. The V_{oc} of the passivated cell is slightly reduced from 1.28 to 1.27 V, suggesting the ARC might in fact be gone and the window damaged. The fill factor, however, is increased from 64.4 to 71.1 %. Before passivation the efficiency was 7.9 % and after it was 7.3 %.

From the EQE of the unpassivated cell, $J_{sc} = 7.76 \text{ mA/cm}^2$ is calculated. It is not known why there is such a big difference between the measured J_{sc} and the one calculated from

EQE. If the passivated cell would still have an intact ARC, one can calculate a new EQE starting from its IQE by using the original reflectance and estimate J_{sc} for an undamaged ARC/surface. J_{sc} would be seen to increase from 7.76 mA/cm^2 (from EQE unpassivated cell) to 9.27 mA/cm^2 (using new EQE passivated cell), a 19 % increase in current. Assuming the V_{oc} and the fill factor remain what they are, the new efficiency would be 8.4 %. This demonstrates the ability of remote hydrogen plasma passivation to improve solar cell characteristics.

In our hydrogenation experiment, interface states were most likely passivated. In order to find the optimal parameters for the plasma passivation, a design of experiment was made. Parameters under study are time, temperature and plasma power. Responses that can be used are the PL signal, both at 300 and 80 K. Also SIMS analysis needs to be performed to learn about the diffusion profile. Therefore, deuterium will have to be used in the experiment instead of hydrogen, due to the larger sensitivity of the SIMS measurement for deuterium. A total of 11 runs need to be performed to discover if a certain parameter does indeed affect the outcome. Unfortunately, due to the exuberant amount of downtime of the remote hydrogen plasma system, these experiments could not be carried out.

4.5 Carbon doping and tunnel junctions

In the above two paragraphs, the results on single junction GaAs and InGaP solar cells on Ge were discussed. To combine these separate devices into a lattice-matched tandem cell, an additional component, the tunnel junction, is used. The tunnel junction establishes the electrical series connection between the two subcells, preferably with a voltage drop that is as low as possible. This device is inserted in reverse polarisation with respect to the solar cell structures but this does not mean that it is also reversely biased under operating conditions. Degenerately doped layers are needed to enable tunnelling in this p-n junction. To minimise optical losses for the bottom cell, the layers are also required to be thin.

The highest n-type doping we could achieve in arsenide material was by using Se as a dopant. For the p-type material, high doping levels are obtainable by using Zn but due to its high diffusion coefficient Zn is not particularly suited to be used in a tunnel junction. As mentioned earlier, the layers are thin and the growth of the top cell might cause considerable out-diffusion of the zinc and, thus, result in a reduced effective doping level in the layer after growth. Therefore, an alternative p-type dopant, carbon, is investigated in the following paragraph. Since we do not have a carbon precursor, C from the metalorganic precursors (the group-III sources) is used. This is called intrinsic carbon doping.

4.5.1 Intrinsic carbon doping

GaAs

Intrinsic carbon doping in GaAs is reported to increase with decreasing growth temperature (T_{gr}) and decreasing V/III ratio [25]. Layer stacks were grown on Si-doped GaAs at 610, 580, 550 and 520 °C for SIMS analysis, illustrated in Figure 4-30. The Si-signal is shown as a reference to illustrate where the substrate begins. Each stack consists of an undoped buffer (690 °C, V/III = 12.8) which is identical in all samples. The buffer was intended to be followed by five layers with decreasing V/III ratio: 2.1, 1.7, 1.3, 1.0 and 0.8, respectively. The TMGa flux was set to 79.3 $\mu\text{mol}/\text{min}$ for all layers. Although changing the V/III ratio in this range was not observed to affect the carbon incorporation, a dependency on T_{gr} was found. The carbon level rose from $4 \times 10^{16} \text{ cm}^{-3}$ at 610 °C to $1.5 \times 10^{18} \text{ cm}^{-3}$ at 520 °C. Reducing the growth temperature decreased the growth rate, indicating growth was performed in the kinetically limited regime. The oxygen concentration was constant in all samples at about $7 \times 10^{16} \text{ cm}^{-3}$. The average hydrogen concentration was about 6.5 to $7.2 \times 10^{17} \text{ cm}^{-3}$ throughout the layers under study – i.e. higher than the C concentration – except for those grown at 520 °C, where the value was slightly higher and nearly matched the carbon concentration.

Of course, one could argue that the variation in V/III ratio was too small but (much later) we discovered a communication error in the system software was causing the problem. When switching only one of two TBAs lines to the reactor in the growth recipe (to obtain low V/III ratios), the wrong one was switched in the system, thus resulting in a constant instead of varying V/III ratio. This explains why the carbon incorporation in GaAs was seemingly independent of V/III ratio and why specular layers were obtained for growth with “V/III < 1” at higher temperature.

From the SIMS measurements estimates of the growth rate (V_{gr}) can be made. But to obtain more accurate values, superlattice (SL) structures were grown on GaAs substrates. The SL consisted of 5 periods of GaAs / $\text{Al}_{0.25}\text{Ga}_{0.75}\text{As}$, whereby the GaAs layer was grown at the desired temperature and growth interrupts were used to ramp the temperature between the deposition of each $\text{Al}_{0.25}\text{Ga}_{0.75}\text{As}$ and GaAs layer. Calibration of the GaAs growth rate was performed by determining the layer thicknesses via HRXRD of the SL. Data was gathered for TMGa fluxes of 79.3, 65.0 and 50.0 $\mu\text{mol}/\text{min}$ and a V/III ratio of 7.8, 9.5 and 12.3 respectively and is presented in Figure 4-31. The growth rate is seen to increase with temperature. Below 610 °C the dependency is large, as expected for growth in the kinetically limited regime. Above 610 °C the mass-transport limited regime begins and V_{gr} is relatively independent of T_{gr} . There is also an increase in V_{gr} for increasing TMGa flux which is observed to saturate above a certain flux for low T_{gr} (520 and 526 °C). Saturation of V_{gr} as a function of TMGa flux at a certain T_{gr} is explained due to saturation of the available surface sites. Adding extra TMGa then no longer serves to increase V_{gr} .

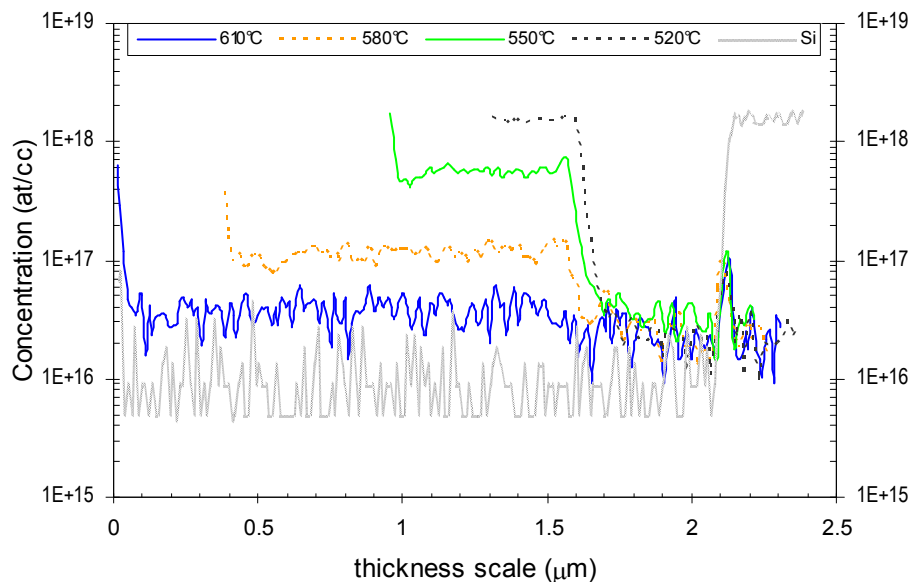


Figure 4-30: Detected carbon signal from SIMS measurement on carbon doped GaAs layers grown at several temperatures. The Si signal illustrates where the substrate starts.

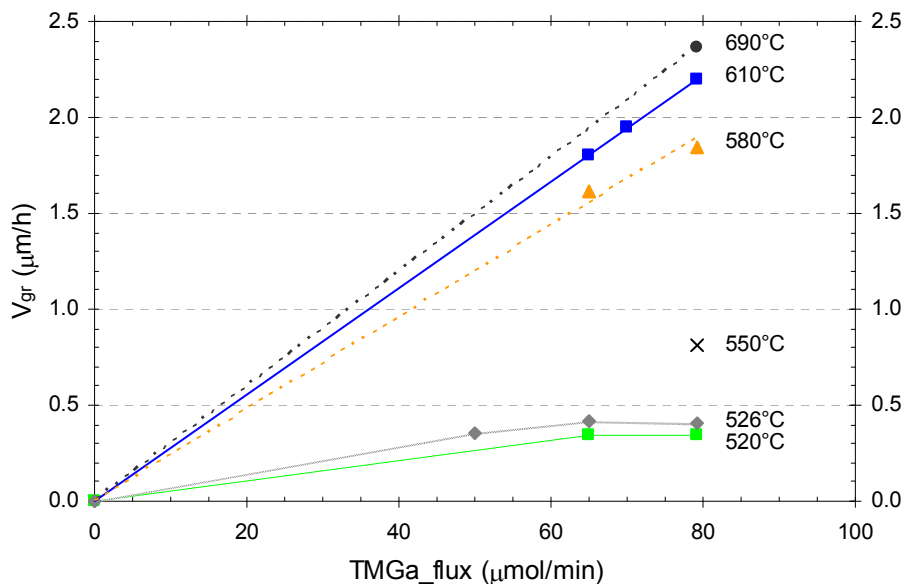


Figure 4-31: GaAs growth rate as a function of TMGa flux and growth temperature. The V/III ratio was not equal for the used fluxes (see text). The lines are a guide to the eye.

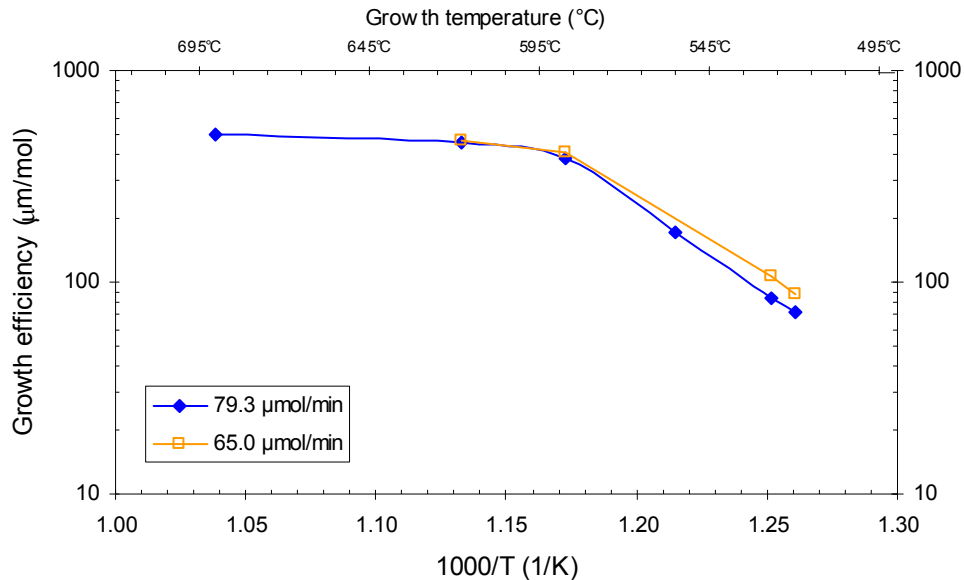


Figure 4-32: Growth efficiency curves for GaAs growth as a function of $1000/T$ and TMGa molar flow. For V/III ratios we refer to the text.

The growth efficiency is defined as the ratio of growth rate over total group-III flux, V_{gr}/III , and is expressed in $\mu\text{m}/\text{mol}$. If the data is plotted as a function of reciprocal temperature (in $1/\text{K}$), the activation energy for the rate limiting step can be determined by fitting an Arrhenius equation to the data in the kinetically limited regime of V_{gr} . Activation energies of 37.8 and 34.6 kcal/mol are calculated for TMGa molar flows of 79.3 and 65.0 $\mu\text{mol}/\text{min}$. Literature values for kinetically limited GaAs growth lie between 25 and 31 kcal/mol [26]. The growth efficiency being higher for smaller molar flow is understandable because the effect of growth rate saturation is then smaller when the growth temperature decreases.

Samples were grown for electrical characterisation. The results were inconclusive, which means that hydrogen in the layers is probably passivating the carbon acceptors present in the material.

AlGaAs

SIMS analysis on one of the SL structures used to calibrate the GaAs growth rate revealed that carbon is more efficiently incorporated in AlGaAs due to the higher Al–C bond strength compared to Ga–C. Intrinsic carbon doping of AlGaAs is reported to increase with decreasing growth temperature and decreasing V/III ratio [27]. Because of the higher AlGaAs bandgap, the optical losses will also be smaller but the tunnelling

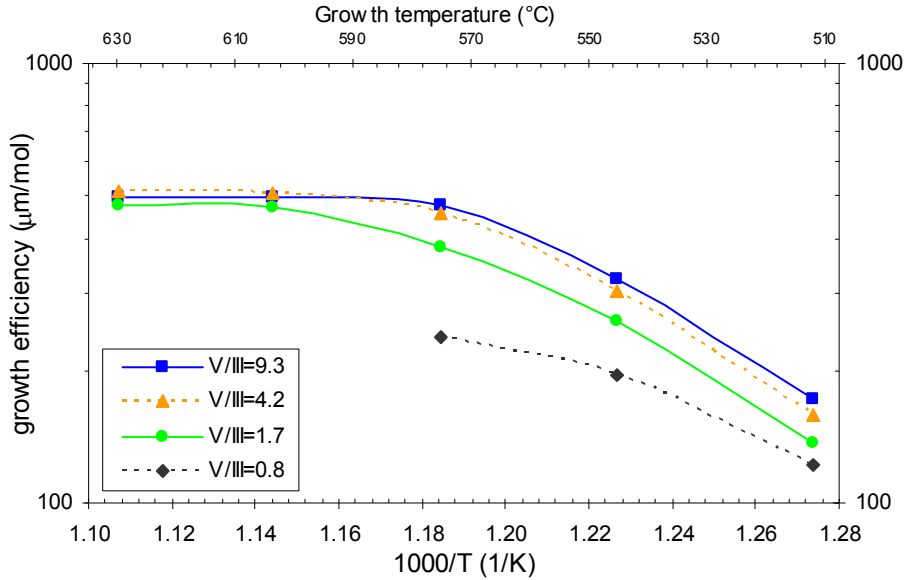


Figure 4-33: AlGaAs growth efficiency as a function of reciprocal temperature and input V/III ratio in the gas phase for constant III_{total} and $Al_g = 0.29$.

probability will decrease exponentially (see Eq. (3.16)). Fortunately, the peak current density is still high enough in these high-bandgap materials to warrant their use in multijunction solar cells.

Series of intrinsically C-doped AlGaAs samples were grown on 4" semi-insulating (100) GaAs wafers to a nominal thickness of 400-600 nm. The layers had V/III ratios varying from 9.3 to 0.8 with constant total group III molar flow (III_{total}), with TMAI = 23.8 $\mu\text{mol}/\text{min}$ and TMGa = 59.4 $\mu\text{mol}/\text{min}$. For each V/III ratio growth temperatures in the range of 630°C to 512°C were used. The TMAI/ III_{total} ratio in the gas phase (Al_g) was fixed to 0.29. Layers grown with V/III of 0.8 and T_{gr} above 570°C did not have a specular surface, as expected when growing with input V/III < 1 and a temperature that is too high. Determination of the growth rate was done by EpiTT in-situ reflectometry with a wavelength of 633nm. The EpiTT pyrometer signal was used to obtain the true wafer surface temperature, i.e. the real growth temperature T_{gr} .

The AlGaAs growth efficiency (growth rate over III_{total}) is temperature dependent below 600°C (see Figure 4-33). The activation energy for layers grown with V/III of 1.7 and higher is found to be 27 kcal/mol. For comparison we note that the activation energy for kinetically limited GaAs growth is between 25 and 31 kcal/mol [26]. Only for V/III smaller than unity a lower value of 19.6 kcal/mol is found. The growth efficiency also

Table 4-13: Aluminium fraction (Al_s) and carrier (carr.conc.) and carbon (C_s) concentration as a function of V/III ratio and T_{gr} for $Al_g=0.29$ on 4'' semi-insulating (001) GaAs. The concentrations are in units $\times 10^{19} \text{ cm}^{-3}$; #: on (001) Ge 6° off-oriented towards $\langle 111 \rangle$.

V/III	9.3			4.2	1.7			#1.7		0.8
T_{gr}	Al_s	Carr. conc.	C_s	Carr. conc.	Al_s	Carr. conc.	C_s	Al_s	C_s	Carr. conc.
630°C	0.33	0.3	0.8	0.6	0.24	6.0	51.2	0.23	50.7	–
601°C	0.33	0.2	0.8	0.6	0.19	5.6	65.3	0.17	46.7	–
571°C	0.31	0.5	1.2	2.5	0.13	6.5	60.1	0.11	35.4	5.1
542°C	0.22	1.4	3.1	3.6	0.07	6.6	42.5	0.06	24.0	5.5
512°C	0.14	1.1	2.9	2.9	0.04	6.0	24.5	0.04	15.3	6.2

decreases with V/III for ratios smaller than 4.2 and temperatures below 600°C. Growth at temperatures above 570°C with a V/III of 0.8 did not lead to smooth epitaxial layers. That datapoint is not included here.

Hall–van der Pauw measurements (300 K) were performed on the samples mentioned above to determine the carrier concentration in the layers. SIMS analysis was carried out on 2 samples consisting of a stack of AlGaAs layers grown with constant V/III (9.3 and 1.7) and III_{total} and varying T_{gr} on (100) GaAs to check the aluminium fraction in the solid (Al_s) and to compare the carbon concentration (C_s) to the measured carrier (hole) concentration. To investigate the substrate effect the same stack was grown on a (100) 6° $\langle 111 \rangle$ Ge substrate for V/III of 1.7. The results of these measurements are summarised in Table 4-13.

From Table 4-13 it is clear that at constant T_{gr} the carbon and hole concentration increase monotonically with decreasing V/III ratio (larger than one). In all cases, C_s is higher than the hole concentration. At a V/III ratio of 9.3 the hole and carbon content in the AlGaAs layers increase monotonically with decreasing temperature. Only at a temperature of 542 °C and lower, the hole concentration exceed 10^{19} cm^{-3} . At a V/III ratio of 4.2 the hole concentration already exceeds 10^{19} cm^{-3} for growth at 571 °C. With a further decrease of the V/III ratio to 1.7, hole concentrations are well above the 10^{19} cm^{-3} level for all temperatures. Also, here the temperature dependence has disappeared. At a V/III below unity and T_{gr} equal to 571 °C or less, hole concentrations also exceed 10^{19} cm^{-3} . Again, no real temperature dependence is observed. From the data collected in Table 4-13 we conclude that the electrically active carbon level saturates between $6\text{--}7 \times 10^{19} \text{ cm}^{-3}$ for an Al_g of 0.29. The highest value we obtained was $7 \times 10^{19} \text{ cm}^{-3}$ for $Al_g = 0.63$ (derived $Al_s \approx 0.53$) grown at 542 °C with V/III = 4.7. In the literature values of 7.5×10^{19} and $1.25 \times 10^{20} \text{ cm}^{-3}$ are reported, obtained at 650 and 530 °C, respectively and grown on (100) GaAs 2° off-oriented towards [110] with a V/III of about 2 and using AsH_3 [27].

In spite of the saturation of carrier concentration we observe, SIMS data indicates that C_s in the AlGaAs layers can be a factor of 2 to 10 higher. It is noted that C_s in the layers grown on 6° off-oriented Ge are around a factor of 1.6 lower than on exact GaAs. Misorientation has been documented to decrease carbon incorporation in AlGaAs [26][28].

Finally, it can be seen from Table 4-13 that the lowest temperature of 512°C does not lead to the highest carbon and hole concentrations. This is linked with the decrease in Al_s for low T_{gr} . Since the Al–C bond strength is larger than that of the Ga–C bond, fewer Al atoms in the solid imply less efficient carbon incorporation.

The Al_s behaviour also requires some discussion. At a V/III ratio of 9.3 Al_s starts decreasing at temperatures below 570°C . However, when using a V/III ratio of 1.7 at 630°C Al_s is already lower than the expected value for $Al_g = 0.29$. It can be seen that Al_s now decreases monotonically with decreasing growth temperature. A quantitative description of these phenomena is difficult. The growth rate reduction below 600°C with decreasing temperature is due to the fact that decomposition reactions on the surface are now growth rate limiting.

Our observations that Al_s reduces at reduced growth temperatures imply that the AlAs growth rate decreases relatively faster than the GaAs growth rate when T_{gr} decreases. This is consistent with the larger Al–C bond strength as compared to the Ga–C bond strength. We propose the removal of methyl groups from the adsorbed MO species as rate limiting step. In our reactor a clear transition point is noted at $V/III = 1.7$. Even at the highest growth temperature of 630°C , Al_s lies below the expected value. This indicates a change in the Al distribution coefficient. Since virtually no independent homogeneous decomposition of the group-III precursor occurs in the presence of TBAs (see §2.4), the decomposition of the group-III sources must be the result of an attack by H radicals produced during TBAs pyrolysis. We believe the change in Al distribution coefficient to be due to a combination of the higher Al–C bond strength and the smaller number of H radicals available at low V/III ratios.

The maximal electrically active carbon level is achieved for $V/III = 1.7$ and already at 630°C . It is clear that one requires an arsenic vacancy for carbon substitution. However, reducing the V/III ratio to 0.8 does not increase the hole concentration, it even slightly decreases. SIMS analysis was not performed on those samples but it is reasonable to assume that Al_s will be even less at this lower V/III ratio.

Substitutional or interstitial carbon donors or carbon precipitates in as-grown material might explain the discrepancy between C_s and the hole concentration, but there is no report of this in the literature for GaAs [29], so presumably they don't occur in AlGaAs

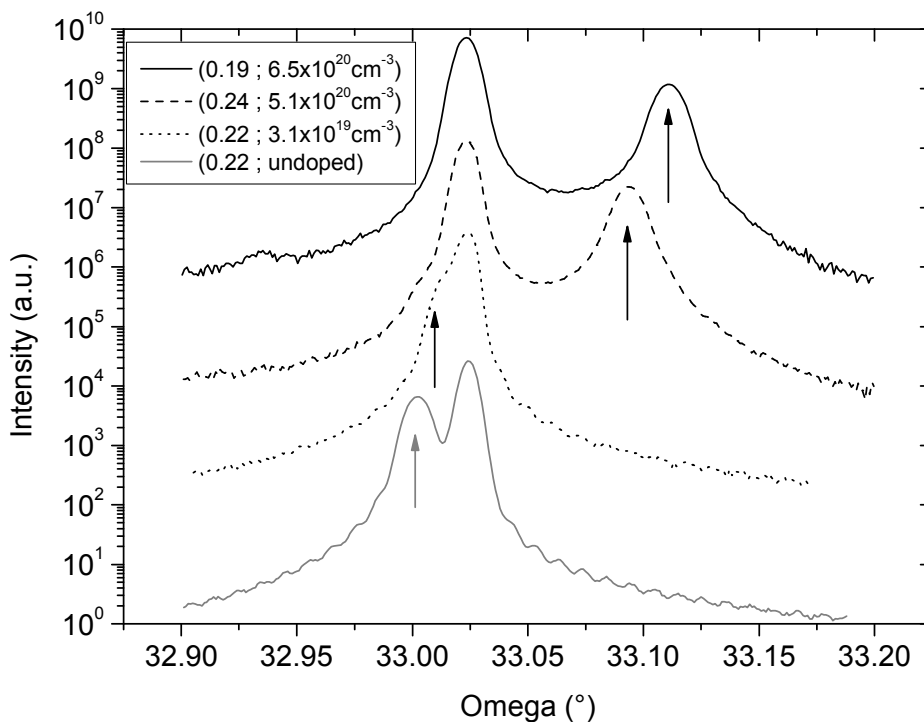


Figure 4-34: HRXRD $\omega/2\theta$ rocking curves for C-doped AlGaAs (Al_s ; C_s) on (1 0 0) GaAs. The arrow marks the AlGaAs peak position. The undoped curve is simulated.

either. The increasing lattice contraction observed in HRXRD spectra of 3 samples with Al_s around 0.22 but increasing C_s (Figure 4-34, undoped curve is simulated) suggest that the carbon is entirely substitutional (at least around this Al_s). If carbon is incorporated on interstitial sites, an effect on the lattice contraction would be expected. It is reported that carbon–hydrogen and carbon dimer complexes in as grown GaAs reduce the electrical activation degree of carbon acceptors [30]. We believe this to be true for AlGaAs as well.

Since tunnel junctions require very thin layers, two more samples were grown at 630 °C with a lower growth rate to gain better control of the deposited layer thickness. For $V/III = 1.7$ and $Al_g = 0.29$ a four times lower growth rate was used with respect to the equivalent sample in Table 4-13. The hole concentration was reduced from 6×10^{19} to $4 \times 10^{18} \text{ cm}^{-3}$. Apparently, lower growth rates yield lower doping levels, probably because now the methyl groups attached to the Al atom have more time to react with AsH and escape to the gas phase as CH_4 . Decreasing the V/III ratio to 1.3 resulted in a higher hole concentration of $8 \times 10^{18} \text{ cm}^{-3}$ which seems to confirm the assumption made above.

Room-temperature photoluminescence (RT-PL) with the 488 nm line of an argon laser was performed on all samples listed in Table 4-13. Only for V/III ratios of 4.2 or higher, a distinguishable PL signal was detected and it was more intense for higher V/III. Also, the full width at half maximum of the RT-PL signal increases for decreasing V/III ratio and decreasing growth temperature. The Al_s values deduced from RT-PL on samples with V/III of 9.3 and $T_{gr} \geq 571$ °C agree with the values determined from SIMS. Assuming the latter are accurate, acceptor levels of 32.0 and 28.5 meV are estimated for $Al_s = 0.22$ and 0.14, respectively, both samples having a carrier concentration higher than $1 \times 10^{19} \text{ cm}^{-3}$. Using an empirical formula to calculate the ionisation energy of C on an As site, E_a^C [31],

$$E_a^C(x) = 26.7 + 5.56x + 110x^{3.4}, \quad (4.7)$$

we obtain 28.6 and 27.6 meV, respectively. From the RT-PL peak wavelength for samples with V/III = 4.2, we can not determine the actual Al_s values seeing the acceptor level can not be resolved at room temperature. For $0 \leq x \leq 0.35$ ionisation energies lie between 26.7 and 31.7 meV. A few meV does not effect the composition very much so if we now assume a constant acceptor level of 28.2 meV for those 3 samples that have a carrier concentration higher than $1 \times 10^{19} \text{ cm}^{-3}$, we get approximate values of $Al_s = 0.33$, 0.33, 0.28, 0.16 and 0.10 (in order of decreasing T_{gr}) for the 5 samples with V/III = 4.2.

4.5.2 Tunnel junctions

GaAs tunnel junction

In industry, a combination of p^{++} AlGaAs / n^{++} InGaP is used as tunnel junction in multijunction solar cells. To avoid thin interface layers in the device by switching from one material to the other, we will only investigate As-based materials.

The first tunnel junction we realised uses GaAs layers. Due to conduction problems with intrinsically carbon doped GaAs, Zn is used in combination with Se. The p-n device is grown on 2" (100) n-type GaAs. The tunnel junction consists of 14 nm p-type ($7 \times 10^{19} \text{ cm}^{-3}$) on 14 nm n-type ($1 \times 10^{19} \text{ cm}^{-3}$) GaAs. Below the tunnel junction there is 500 nm Se-doped ($1 \times 10^{18} \text{ cm}^{-3}$) GaAs and above it 140 nm Zn-doped ($4 \times 10^{18} \text{ cm}^{-3}$) GaAs. On top there is a 170 nm Zn-doped ($7 \times 10^{19} \text{ cm}^{-3}$) contact layer. The whole stack is grown at 640 °C to avoid temperature ramp steps during growth of the critical layers. Also, no barriers are used to prevent Zn diffusion. The J - V curve for the (best) device is presented in Figure 4-35 along with a schematic of the layer structure described above.

The tunnel junction has a peak current density J_p of 82 A/cm² and specific resistance R_{sp} of 2.8 mΩ.cm². At 18 mA/cm², the voltage drop over the tunnel junction is 50 μV. However, the peak-to-valley ratio J_p/J_V is only 1.2. A typical value for J_p/J_V in GaAs is

Table 4-14: Performance of own GaAs tunnel junction compared to literature values.

Group	dopant		J_P (A/cm ²)	V_P (V)	J_P/J_V	R_{sp} (mΩ.cm ²)	V_V (V)
	p	n					
Imec [#]	Zn	Se	82	0.24	1.2	2.8	0.40
			70	0.30			
NREL [32]	Zn	Se	286			0.9	8.0
	C	Se	>360				
CNRS [33]	Zn	Sn	45		2.1	2	
† CNRS [34]	Be	Si	235			0.6	
† NTT Electrical Comm. Lab. [35]	Be	Si	0.84				
Typical values (Sze [36])				0.13	12		0.56

[#] Top row: best device; bottom row: average of 14 devices. † MBE grown

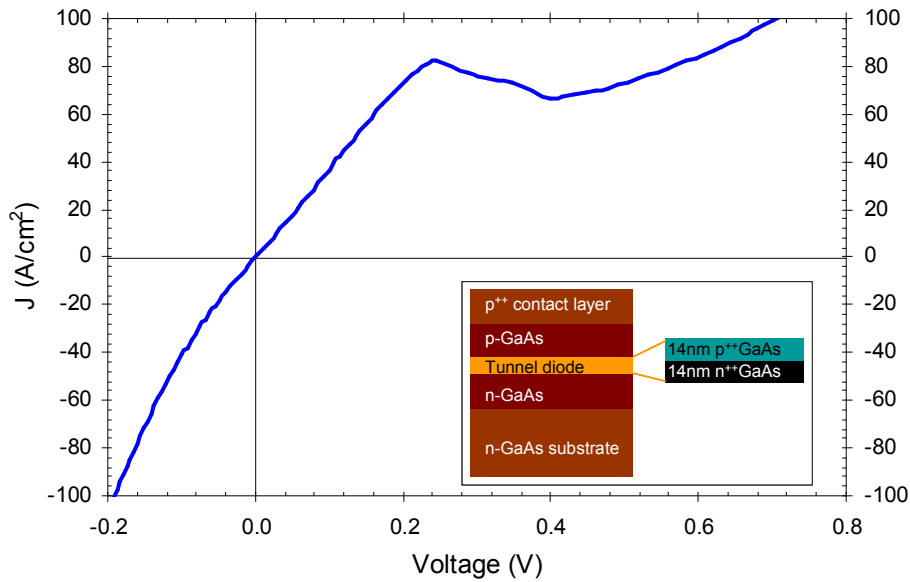


Figure 4-35: J - V curve of a GaAs tunnel junction, doped with Zn en Se. Inset: schematic representation of the layer structure.

12 according to Sze [36]. The low J_P/J_V ratio in our devices must be due to a large excess current caused by interface states and impurity levels in the bandgap most likely caused by Zn diffusion. This diffusion will also result in a decreased peak current. Table 4-14 gives an overview of some values found in literature. When applying this device in a tandem solar cell, the presence of barriers at either side of the tunnel junction (BSF top cell, window bottom cell) will increase the voltage drop due to an increase in R_{sp} .

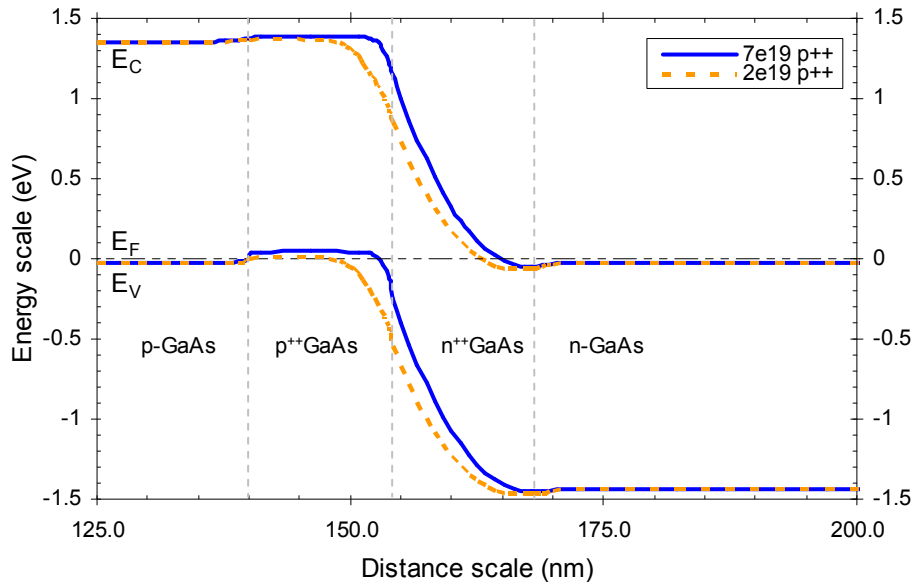


Figure 4-36: Energy band diagrams of a GaAs tunnel junction as a function of the doping level in the p^{++} layer. The distance scale starts from the top of the p -GaAs layer (see inset Figure 4-35). The n^{++} layer doping level is $1 \times 10^{19} \text{ cm}^{-3}$.

Figure 4-36 gives the energy band diagram of the GaAs tunnel structure described above in the case of the nominal doping levels and in the case of reduced doping level in the p^{++} layer due to Zn diffusion. For the simulation, PC1D, a one-dimensional program mainly used for the simulation of Si and Ge solar cells, was tried. It is clearly seen that in both cases the tunnel junction layers are degenerately doped. However, reduction of the p^{++} doping level does cause a slight broadening of the tunnel barrier width from 12 to 14.5 nm. Hence, the peak current will be decreased.

AlGaAs tunnel junction

To improve the performance of a multijunction solar cell, high-bandgap tunnel junctions are needed to minimise current generation losses in the underlying subcells due to optical absorption in the tunnel junction. Intrinsically carbon doped AlGaAs samples with $V/III = 9.3$ immediately resulted in high p -type doped material and therefore a tunnel junction was fabricated. The p^{++} AlGaAs layer ($T_{gr} = 542 \text{ }^\circ\text{C}$, $Al_g = 0.41$, $V/III = 7.6$) was calibrated on semi-insulating exact GaAs. A carrier concentration of $2.3 \times 10^{19} \text{ cm}^{-3}$ and an $Al_s = 0.32$ were recorded. The p - n tunnel junction itself is grown on $4''$ 6° off-oriented germanium and consists of $14 \text{ nm } 2 \times 10^{19} \text{ cm}^{-3} \text{ C:Al}_{0.3}\text{Ga}_{0.7}\text{As}$ on $14 \text{ nm } 2 \times 10^{18} \text{ cm}^{-3} \text{ Se:Al}_{0.2}\text{Ga}_{0.8}\text{As}$. The latter is about the highest n -type Hall carrier concentration we measured in $Al_x\text{Ga}_{1-x}\text{As}$. Three different layer structures were used (see Figure 4-37).

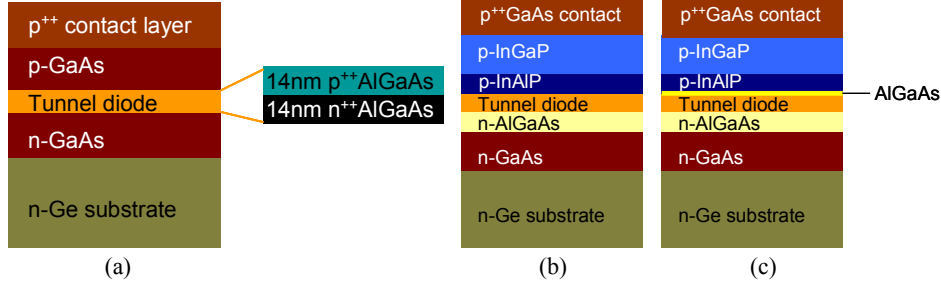


Figure 4-37: Schematic representation of the tunnel junction layer stacks of (a) *t1*, (b) *t2* and (c) *t3*. The tunnel diode layers are the same for the three structures.

Table 4-15: Performance comparison of our AlGaAs tunnel diode with devices from literature.

Group	dopant		J_p (A/cm ²)	V_p (V)	J_p/J_v	R_{sp} (mΩ.cm ²)	V_v (V)	
	p	n						
Imec p-Al _{0.3} Ga _{0.7} As/n-Al _{0.2} Ga _{0.8} As	<i>t1</i>		17.3	0.067	11.3	2.6	0.284	
	<i>t2</i>	C	Se	3.9	0.125	10.0	22.6	0.387
	<i>t3</i>			3.5	0.053	8.7	10.2	0.249
[†] CNRS: Al _{0.12} Ga _{0.88} As [34]	Be	Si	5	0.150		20		
[*] N.C. State Univ.: [37] Al _{0.14} Ga _{0.86} As	Ge	Te	0.04	0.12		23.4		
EMCORE : [38] p-Al _{0.9} Ga _{0.1} As/ n-In _{0.5} Al _{0.2} Ga _{0.3} P	C	Te	1.5			25		
Spectrolab : [39] p-AlGaAs/ n-InGaP			637	0.37	37	0.6	0.73	

[†] MBE grown, ^{*} LPE grown

The J - V curves are presented in Figure 4-38. The device parameters are summarised in Table 4-15 and compared to literature values. A good tunnel junction has a very high peak current and a low peak voltage. A peak current of 3 A/cm² is needed to accommodate a concentration factor of 200. Preferably, it has an even higher peak current for higher concentration factors.

The first device, *t1*, is sandwiched between 210 nm Zn:GaAs (4×10^{18} cm⁻³) and 240 nm Se:GaAs (1×10^{18} cm⁻³) on a 440 nm n-type buffer (Figure 4-37a). J_p equals 17.3 A/cm² at 67 mV. The peak-to-valley ratio is 11.3 and $R_{sp} = 2.6$ mΩ.cm². J_p is high enough to accommodate a tandem cell under up to 1000 suns concentration.

To simulate the tunnel junction behaviour in a tandem solar cell, a second device, *t2*, was made. The tunnel junction layers were grown in between 30 nm Si:Al_{0.8}Ga_{0.2}As (2×10^{18} cm⁻³) on Si:GaAs (2×10^{18} cm⁻³) and 50 nm Zn:InAlP (1×10^{18} cm⁻³) underneath 250 nm Zn:InGaP (1×10^{17} cm⁻³) (Figure 4-37b). J_p is seen to decrease to 3.9 A/cm² at an

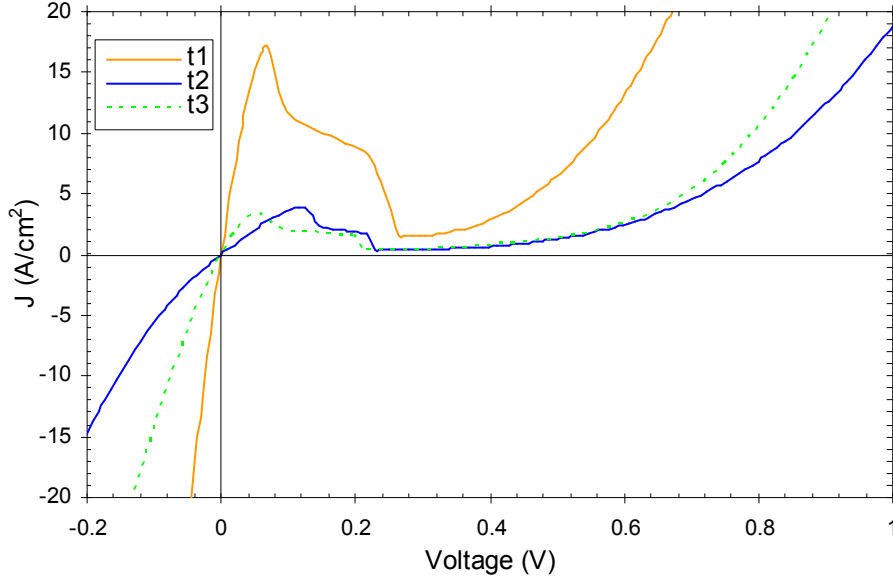


Figure 4-38: Four-points probe J - V measurement of structures $t1$, $t2$ and $t3$. For all structures, the doping level is $2 \times 10^{19} \text{ cm}^{-3}$ in the p^{++} layer, grown at $T_{gr} = 542^\circ\text{C}$.

increased V_p (125 mV), leading to an increase of the specific resistance by a factor 8.7. The peak-to-valley ratio remains essentially unchanged, indicating that these extra layers have not introduced more deep levels inside the junction or interface states.

To investigate the influence of postponing the switching from P to As following the deposition of the p^{++} C:Al_{0.3}Ga_{0.7}As layer, an additional 20 nm of p^+ Al_{0.3}Ga_{0.7}As (lower doped) was inserted in a third device, $t3$ (Figure 4-37c). There is a minor reduction of the peak current J_p and the peak-to-valley ratio of the device but the peak voltage V_p is influenced the most. The value is more than halved, resulting in an almost proportional reduction of R_{sp} . We believe this has got nothing to do with the moment of As→P switching itself, but is related to the insertion of that extra AlGaAs layer. Since the layer has practically the same composition (30 % Al), the lower doped additional layer reduces the effective doping level of the total p-type tunnel layer and hence the degeneracy V_p on the p-side (Eq. (3.22)). Through Eq. (3.21) the peak voltage V_p is reduced.

$$\text{Eq. (3.21):} \quad V_p \approx \frac{(V_p + V_n)}{3},$$

$$\text{Eq. (3.22):} \quad V_p \approx \frac{kT}{q} \left[\ln \left(\frac{N_A}{N_V} \right) + 0.35 \frac{N_A}{N_V} \right].$$

Now let us take a look at the band diagrams (simulated with PC1D). We have already established that off-orientation leads to lower carbon incorporation but the relation to the degree of electrical activation is unknown. It is therefore assumed in the following simulations that we have a carrier concentration of $2 \times 10^{19} \text{ cm}^{-3}$ in the C:AlGaAs layer.

For *t1*, a question arises. It is seen (Figure 4-39) that, due to the factor 10 difference in doping level, the n^{++} AlGaAs layer ($2 \times 10^{18} \text{ cm}^{-3}$) is completely depleted but is not degenerate. And yet, the tunnelling phenomenon occurs. In fact, an excellent *J-V* curve is obtained. Since the excess current is quite low ($J_P/J_V = 11.3$), a very large contribution of tunnelling via impurity levels can be ruled out as the main tunnelling path. So, either the n-type doping level is completely different from what we calibrated on SI-GaAs ($1.2 \times 10^{19} \text{ cm}^{-3}$ would make the layer degenerate) or electrons tunnel from the n-GaAs to the p^{++} AlGaAs but that barrier width (41 nm) is rather large and would result in a very low tunnelling probability. If a forward bias of 67 mV (the value corresponding to the peak current) is applied to the device, tunnelling from the n-GaAs is even impossible because the bands no longer overlap. Thus, the most likely explanation is that the Se-incorporation is much more efficient on off-oriented than on exact material and the actual doping level is higher than the calibrated one ($2 \times 10^{18} \text{ cm}^{-3}$). A doping level of $2 \times 10^{19} \text{ cm}^{-3}$ in the n^{++} AlGaAs layer would be high enough to have overlapping bands at 67 mV and thus allow for tunnelling to occur.

For *t2*, the same question arises. If the doping level in the n^+ $\text{Al}_{0.2}\text{Ga}_{0.8}\text{As}$ is indeed $2 \times 10^{18} \text{ cm}^{-3}$, the layer is again completely depleted without degeneracy being reached (Figure 4-40, “2/0.2 ; 14/14”-curve). For the same layer thicknesses degeneracy is reached if the doping level is minimal $6 \times 10^{18} \text{ cm}^{-3}$ (“2/0.6 ; 14/14”-curve). Another way of achieving overlapping bands is to broaden the layer instead of assuming a higher doping level. At the same time the thickness of the p^{++} $\text{Al}_{0.3}\text{Ga}_{0.7}\text{As}$ can be reduced (“2/0.2 ; 5/30”-curve).

From the simulations it is clear why the peak current is lower for the tunnel junction that is sandwiched between solar-cell-like layers. The $\text{Al}_{0.8}\text{Ga}_{0.2}\text{As}$ window of the bottom cell and the InAlP BSF of the top cell introduce additional barriers that can block the current. A crucial factor in the extent of this current blocking is the doping level of that window and BSF. The biggest (potential) problems are expected to occur for the holes at the top cell BSF / p^{++} AlGaAs interface. The barrier height is (apparently) the largest there and a variation in doping level of the BSF can substantially increase the barrier width. Furthermore, high p-doping of InAlP is not easy to obtain.

In literature, most often a p^{++} AlGaAs / n^{++} InGaP tunnel junction is used with standard thicknesses on the order of 14/14 nm or maybe a little thinner. In Figure 4-41 the band diagram using this combination of materials is compared to our all-AlGaAs tunnel

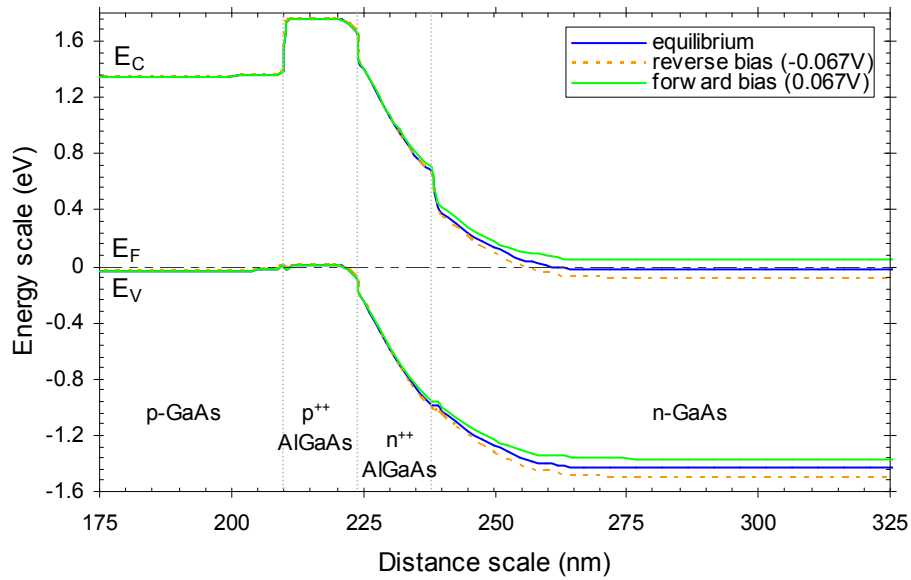


Figure 4-39: Simulation of the energy diagram for the t1-structure in thermal equilibrium and under forward and reverse bias of 67 mV.

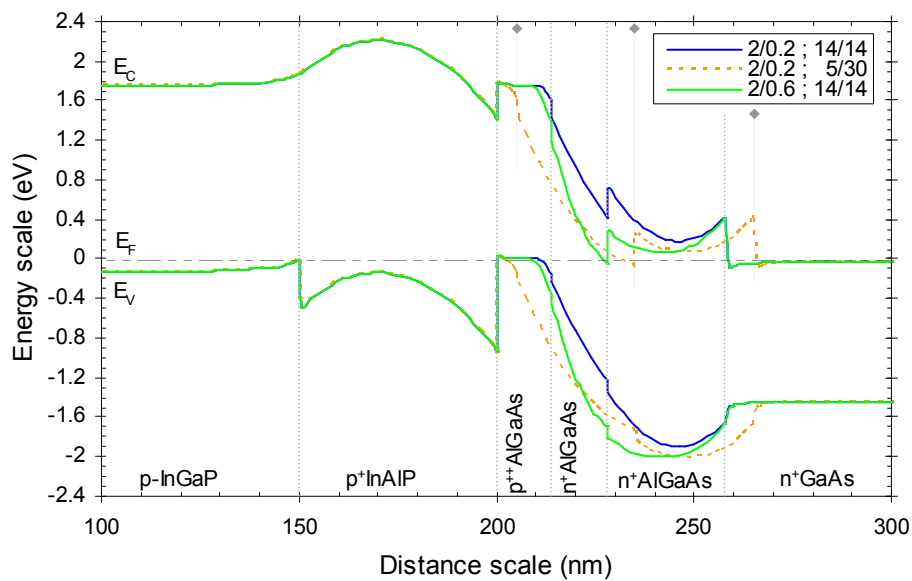


Figure 4-40: Simulated energy diagram for the t2-structure at equilibrium as function of a given “doping level ($\times 10^{19} \text{ cm}^{-3}$); layer thickness (nm)” combination for the $p^{++} \text{ Al}_{0.3}\text{Ga}_{0.7}\text{As} / n^{+} \text{ Al}_{0.2}\text{Ga}_{0.8}\text{As}$ tunnel junction. Interface indicator lines only refer to solid curves; for the dashed curve they are slightly shifted (see diamond arrows).

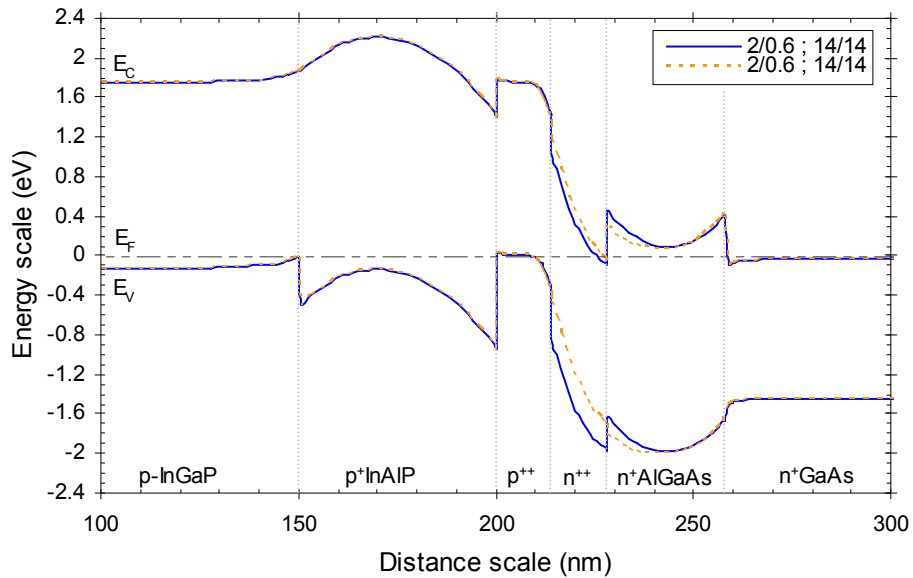


Figure 4-41: Comparison between InGaP (solid) and AlGaAs (dashed) n^{++} layers in the t_2 -structure for the same doping levels and layer thicknesses.

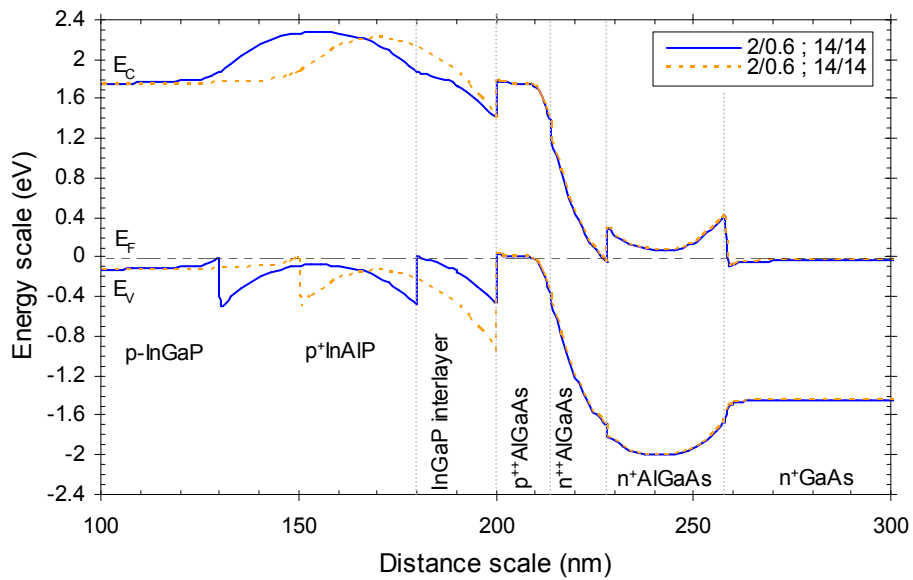


Figure 4-42: Comparison of band diagrams with (solid) and without (dashed) the interlayer.

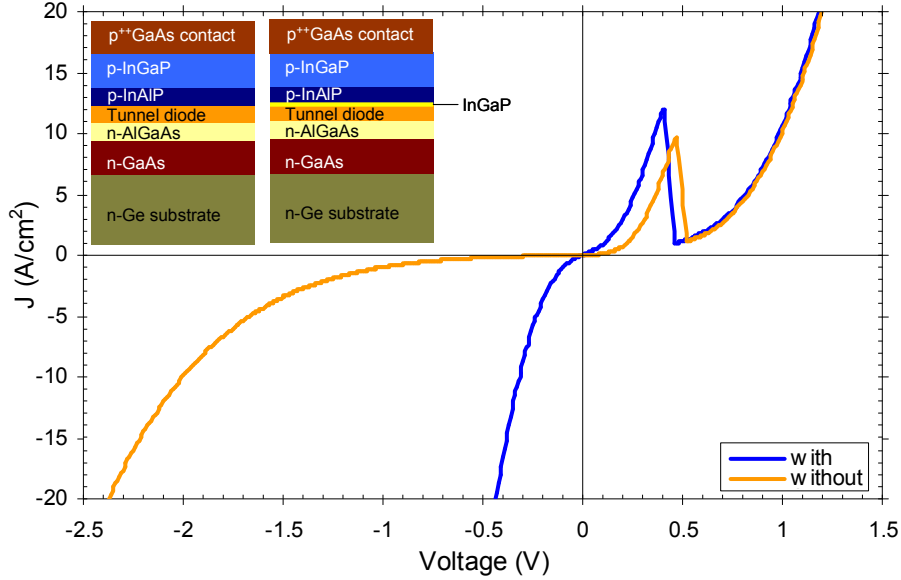


Figure 4-43: J - V curves of a t_2 -structure $\{14\text{nm } p^{++} (2 \times 10^{19} \text{ cm}^{-3}, 542^\circ\text{C})\}$ with and without InGaP interlayer.

Table 4-16: Growth parameters used for the tunnel junction layers of 6 test devices. A reproduction of t_2 is included: t_5 .

	Sample	t_4	t_5	t_6	t_7	t_8	t_9
p^{++}	thickness (nm)	10	14	10	5	5	5
	doping level ($\times 10^{19} \text{ cm}^{-3}$)	2	2	2	2	2	6
	T_{gr} ($^\circ\text{C}$)	542	542	571	571	571	630
	V/III	9.3	9.3	4.2	4.2	4.2	1.7
	Al fraction (approx.)	0.2	0.2	0.3	0.3	0.3	0.24
n^{++}	thickness	25	14	25	25	30	25
	other growth conditions	610 $^\circ\text{C}$, $2 \times 10^{18} \text{ cm}^{-3}$ (Se/V= 6.4×10^{-4}), V/III=16.9					

junction. It is not clear why using InGaP should be a better choice. When using an $\text{Al}_{0.8}\text{Ga}_{0.2}\text{As}$ window for the bottom cell, the barrier height for the electrons at the n^{++} InGaP / bottom cell window interface is even higher.

As growing low defect density InAlP after switching is more difficult than InGaP, we start with a thin InGaP layer and then continue with InAlP. This may have turned out advantageous as clarified by including that layer in our simulation (Figure 4-42). The holes have now three successive barriers to overcome but the barrier height is roughly halved and also the barrier width has greatly decreased. The InGaP interlayer's effect is

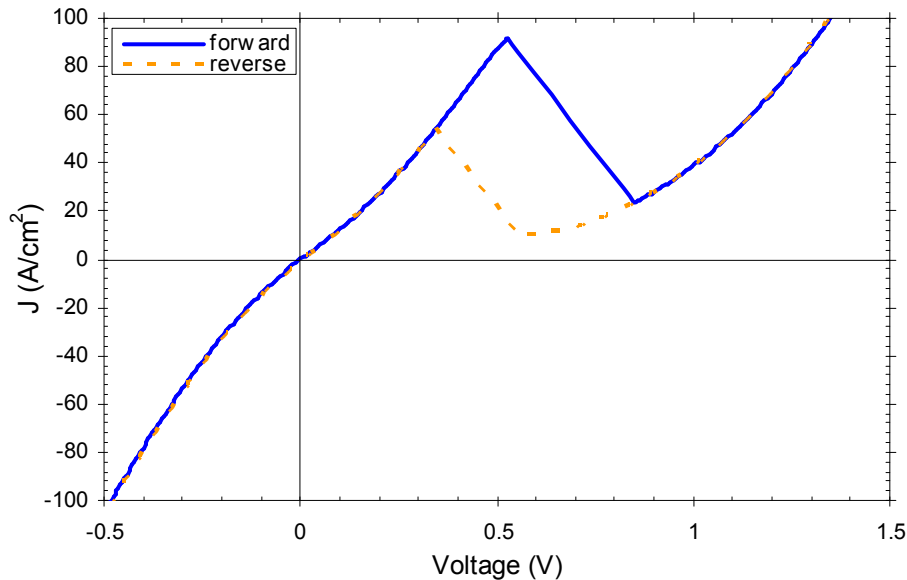


Figure 4-44: J - V curve for a $t9$ -structure $\{5 \text{ nm } p^{++} (6 \times 10^{19} \text{ cm}^{-3}, 630^\circ\text{C}), 25 \text{ nm } n^{++} (2 \times 10^{18} \text{ cm}^{-3}, 610^\circ\text{C})\}$ for forward and reverse voltage sweep.

clearly visible in Figure 4-43. Without the InGaP interlayer rectifying instead of ohmic behaviour is observed. The non-linearity in the structure with the InGaP interlayer (dark/blue curve) through the origin stems from a non-ohmic front contact (not enough Zn in contact layer). Using Au/AuZn instead of TiW/Au can correct for that.

Several structures (all containing the InGaP interlayer) were made to test the influence of the layer thicknesses of p^{++} and n^{++} tunnelling layer and the p^{++} doping level separately by changing growth temperatures and V/III ratio. The parameters of the structures that were grown are summarised in Table 4-16. Although a temperature calibration of the reactor was performed to yield the same wafer surface temperatures as with earlier calibrations, the results on the processed devices showed that a tunnel junction is very sensitive to the growth conditions. The reference tunnel junction, $t5$, only showed the characteristic of a bad Schottky-contact, whereas $t4$, $t7$ and $t8$ displayed disappointing normal diode behaviour. Devices $t6$ and $t9$ did show tunnelling, albeit that $t6$ only had $J_p = 0.46 \text{ A/cm}^2$ at 49 mV but with a good $J_p/J_V = 9.0$. $T9$ on the other hand had $J_p = 92.0 \text{ A/cm}^2$ at 527 mV also with a good $J_p/J_V = 9.2$ and an R_{sp} of $7.8 \text{ m}\Omega\cdot\text{cm}^2$. The negative resistance region was not discernable due to a high series resistance in (most likely) the device structure because the front contact did not display perfect ohmic behaviour, but also the leads of the measurement setup can contribute to it. This high series resistance is responsible for the difference (hysteresis) between the

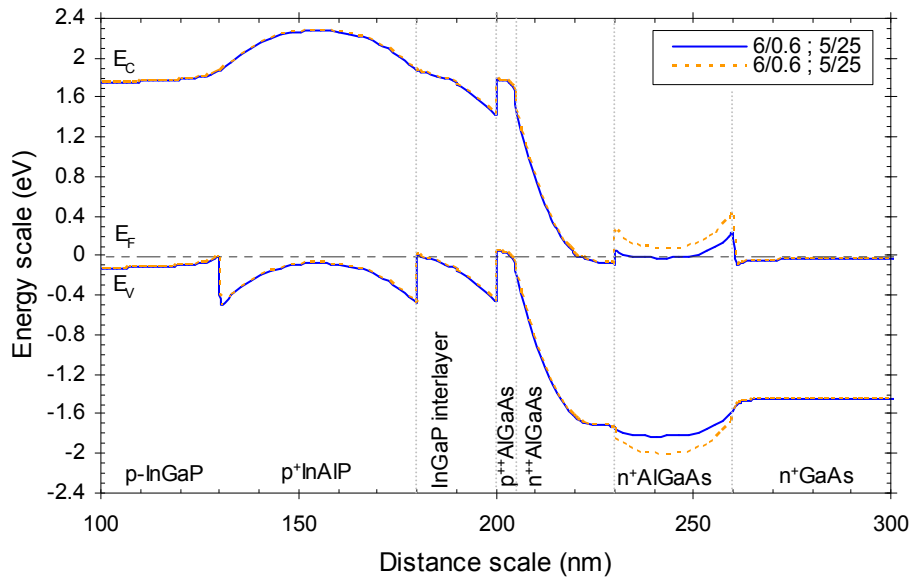


Figure 4-45: Comparison of band diagram of the best tunnel structure (dashed) with one where the $Al_{0.8}Ga_{0.2}As$ window of the bottom cell is replaced with $Al_{0.3}Ga_{0.7}As$ (solid).

forward and reverse voltage sweep around the peak area (Figure 4-44). By using a layer stack of Au/AuZn, the Schottky behaviour of the front contact can be improved to ohmic behaviour but not the rest of the series resistance effect that masks the negative resistance region. However, the main conclusion is that increased p-type doping in the tunnelling layer leads to higher peak currents. A recommendation for the future is to always use AuZn in the contact metal for this type of structure.

Given this result, obtained from a higher doped and thinner p^{++} layer combined with a thicker n^{++} layer, a next improvement could be envisaged by replacing the $Al_{0.8}Ga_{0.2}As$ window of the bottom cell by an $Al_{0.3}Ga_{0.7}As$ layer. The barrier for the electrons is substantially lowered while the barrier for the holes (deflection to keep them in the GaAs emitter) remains high enough. The simulation is shown in Figure 4-45. This should result in an even higher peak current, unless of course the bottle neck – as far as current is concerned – is not located at the top cell BSF / p^{++} tunnelling layer interface. Good temperature calibration for accurate high doping levels will be important. Although this experiment has not been carried out as part of the current study, it looks like an interesting topic for future research.

4.6 The InGaP/GaAs dual junction solar cell on Ge

Combining the InGaP and GaAs single junction cells into a monolithically stacked dual junction cell is now possible. As the *t2*-structure (see p.99) displays nice tunnelling behaviour, it is used to make our first $\text{In}_{0.495}\text{Ga}_{0.505}\text{P} / \text{In}_{0.01}\text{Ga}_{0.99}\text{As}$ dual junction solar cell (sample A). It simply consists of sequentially growing $\text{In}_{0.01}\text{Ga}_{0.99}\text{As}$ bottom cell, tunnel junction and $\text{In}_{0.495}\text{Ga}_{0.505}\text{P}$ top cell. Only a 3 nm thin InGaP interlayer is present between tunnel junction and InGaP top cell, meaning there is a large barrier (look back to Figure 4-42, p.103) for the holes to overcome in order to reach the tunnel junction.

This first attempt turned out to be a success: the solar cell parameters are not outstanding but a working dual junction InGaP / GaAs solar cell is obtained. It is not altogether surprising that the parameters are not first class, due to the cells not being current matched and the presence of defects on the surface (most likely due to dust particles since they have different sizes). The growth conditions of the layer stack are shown in Table 4-17. The best results for each cell size are presented in Table 4-18.

A second tandem structure, sample B, is fabricated with a thinner top cell for better current matching between top and bottom cell. The growth conditions are the same as for sample A. In literature, most often a 600 nm top cell is used. Sample B has a 700 nm thick InGaP cell. However, surprisingly, theoretical calculations show that 320 nm InGaP would in fact yield a current match. The realised J_{sc} would then be 15.0 mA/cm^2 , taking reflection and shadowing losses and real absorption coefficients into account.

Apart from in house quantification, cell B was also sent to the National Renewable Energy Laboratory (NREL), Golden (Co.), a recognized PV-calibration laboratory. Fill factor and V_{oc} values are in very good agreement with the in-house measurements but the efficiency turns out lower than what we measured due to a lower J_{sc} . This reflects the fact that the spectrum of our solar simulator is not optimal for high bandgap solar cells. The uniformity across the 4" germanium substrate is good. The efficiencies of the five cells on sample B – ranging from 0.25 cm^2 to 4 cm^2 in area– lie between 23.5 and 24.3 %, with the lower efficiencies for the cells near the edge of the wafer. So there is a trend due to a (small) temperature gradient during the layer deposition. On inspecting the J - V curves from Figure 4-46, no dip is found near the knee of the curves which means that the tunnel junction's peak current is indeed higher than the cell's short-circuit current.

Since in the spectral response setup the necessary filters to tune the bias light that is used are not available, only the spectral response of the current limiting cell can be measured. The InGaP top cell turns out to be current limiting in both cell A and B.

Table 4-17: Growth conditions for all $In_{0.495}Ga_{0.505}P / In_{0.01}Ga_{0.99}As$ tandem solar cells on Ge. No absolute T_{gr} values could be obtained via EpiTT because the signal was lost.

<i>Start layer structure</i>				<i>Layer structure continued</i>	
$In_{0.01}Ga_{0.99}As$ bottom cell				$In_{0.495}Ga_{0.505}P$ top cell	
BSF ($1 \times 10^{18} \text{ cm}^{-3}$)				BSF ($1 \times 10^{18} \text{ cm}^{-3}$)	
T_{gr} ($^{\circ}\text{C}$)	–		T_{gr} ($^{\circ}\text{C}$)	–	
V/III	37.4		V/III	82.1	
TMIn ($\mu\text{mol}/\text{min}$)	2.3		TMIn ($\mu\text{mol}/\text{min}$)	95.7	
TMAI ($\mu\text{mol}/\text{min}$)	24.8		TMAI ($\mu\text{mol}/\text{min}$)	76.6	
TMGa ($\mu\text{mol}/\text{min}$)	59.4				
Zn/III	0.35		Zn/III	0.28	
Base ($1 \times 10^{17} \text{ cm}^{-3}$)				Base ($1 \times 10^{17} \text{ cm}^{-3}$)	
T_{gr} ($^{\circ}\text{C}$)	–		T_{gr} ($^{\circ}\text{C}$)	–	
V/III	14.3		V/III	75.2	
TMIn ($\mu\text{mol}/\text{min}$)	2.3		TMIn ($\mu\text{mol}/\text{min}$)	95.7	
TMGa ($\mu\text{mol}/\text{min}$)	105.7		TMGa ($\mu\text{mol}/\text{min}$)	92.5	
Zn/III ($\times 10^{-3}$)	5.1		Zn/III ($\times 10^{-3}$)	5.1	
Emitter ($1-2 \times 10^{18} \text{ cm}^{-3}$)				Emitter ($1-2 \times 10^{18} \text{ cm}^{-3}$)	
T_{gr} ($^{\circ}\text{C}$)	–		T_{gr} ($^{\circ}\text{C}$)	–	
V/III	14.3		V/III	75.0	
TMIn ($\mu\text{mol}/\text{min}$)	2.3		TMIn ($\mu\text{mol}/\text{min}$)	95.7	
TMGa ($\mu\text{mol}/\text{min}$)	105.7		TMGa ($\mu\text{mol}/\text{min}$)	93.1	
Si/III ($\times 10^{-3}$)	2.1		Si/III ($\times 10^{-3}$)	9.4	
Window ($3 \times 10^{18} \text{ cm}^{-3}$)				Window ($3 \times 10^{18} \text{ cm}^{-3}$)	
T_{gr} ($^{\circ}\text{C}$)	–		T_{gr} ($^{\circ}\text{C}$)	–	
V/III	32.2		V/III	80.8	
TMIn ($\mu\text{mol}/\text{min}$)	2.3		TMIn ($\mu\text{mol}/\text{min}$)	95.7	
TMAI ($\mu\text{mol}/\text{min}$)	78.1		TMAI ($\mu\text{mol}/\text{min}$)	79.5	
TMGa ($\mu\text{mol}/\text{min}$)	20.1				
Si/III ($\times 10^{-3}$)	8.9		Se/V ($\times 10^{-4}$)	1.8	
AlGaAs tunnel junction					
Layer	n^{++}	p^{++}	Contact ($>10^{19} \text{ cm}^{-3}$)		
T_{gr} ($^{\circ}\text{C}$)	–	–	T_{gr} ($^{\circ}\text{C}$)	–	
V/III	18.7	7.6	V/III	14.3	
TMAI ($\mu\text{mol}/\text{min}$)	16.3	41.9	TMIn ($\mu\text{mol}/\text{min}$)	2.3	
TMGa ($\mu\text{mol}/\text{min}$)	66.1	59.4	TMGa ($\mu\text{mol}/\text{min}$)	105.7	
Se/V ($\times 10^{-4}$)	5.8		Se/V ($\times 10^{-3}$)	1.6	

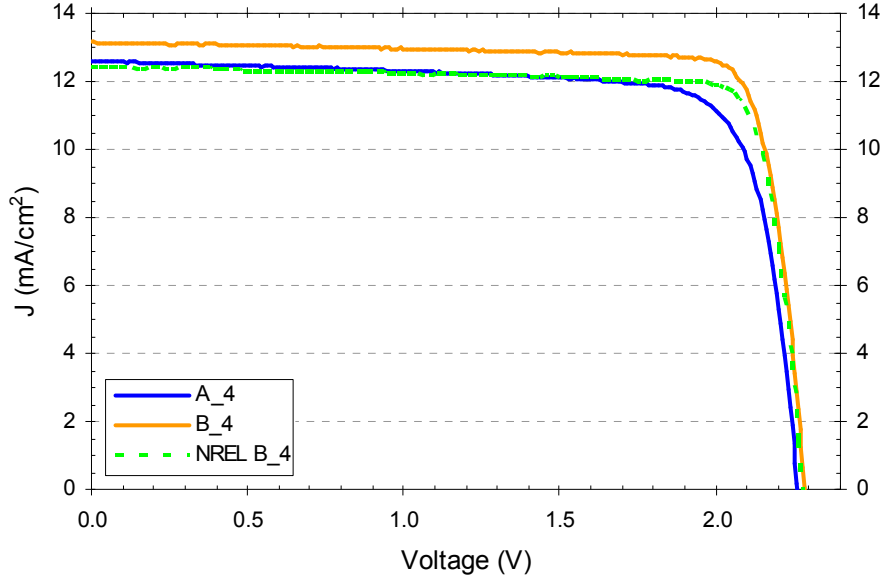


Figure 4-46: AM1.5G J-V curves of 4cm² tandem cells A and B plus the measurement by NREL.

Table 4-18: Comparison between samples A and B of the best cell's parameters for two sizes.

Sample	A_4	A_1	B_4	B_1	NREL B_4	NREL B_1
Reflectance _{400-900nm} (%)	2.9	2.9	2.5	2.5	–	–
J _{sc, measured} (mA/cm ²)	12.6	12.5	13.2	13.1	12.4	12.4
J _{sc, calculated from EQE} (mA/cm ²)	11.0	–	12.5	–	12.6	–
J _{sc, calculated from IQE} (mA/cm ²)	11.9	–	13.4	–	–	–
V _{oc} (V)	2.262	2.251	2.285	2.317	2.288	2.315
R _{s, upper limit} (Ω)	2.439	–	1.372	–	1.291	–
Fill factor (%)	78.6	81.8	84.2	84.3	84.4	84.5
Efficiency (%)	22.4	23.0	25.3	25.5	24.0	24.3

Obviously, the InGaP material quality is still in need of improvement because the bottom cell should be current limiting, especially in the case of cell A, which has the thickest InGaP layer. In Figure 4-47 the InGaP top cells' IQE are compared and the IQE of our best single junction InGaP cell is shown as a reference. Clearly, sample A's material quality is less good than that of sample B. The problem is largely situated at the back of the solar cell. Sample B has a material quality comparable to that of the single junction cell. The most obvious difference is a higher bandgap for cell B (see shorter absorption edge). Confirmation is found in the lower J_{sc} : 13.2 mA/cm² for cell B versus 13.6 mA/cm² for the single junction cell. In house measurement of EQE agrees with that of NREL, disregarding small spectral variations (see inset). Figure 4-48 shows the total EQE of the dual junction solar cell and of its components, as measured by NREL.

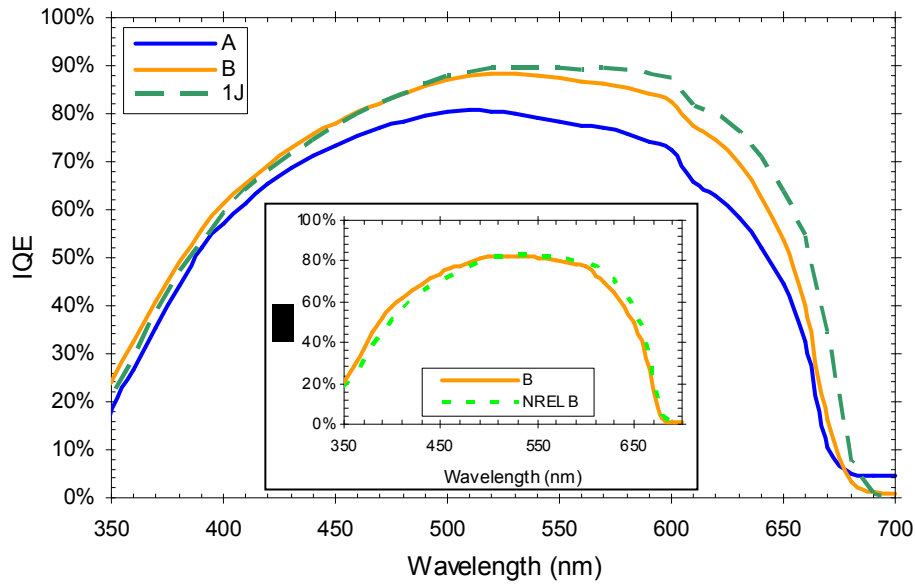


Figure 4-47: IQE of current limiting subcells (InGaP) in A and B and our best single junction InGaP reference. Inset: InGaP subcell EQE as measured in house and by NREL.

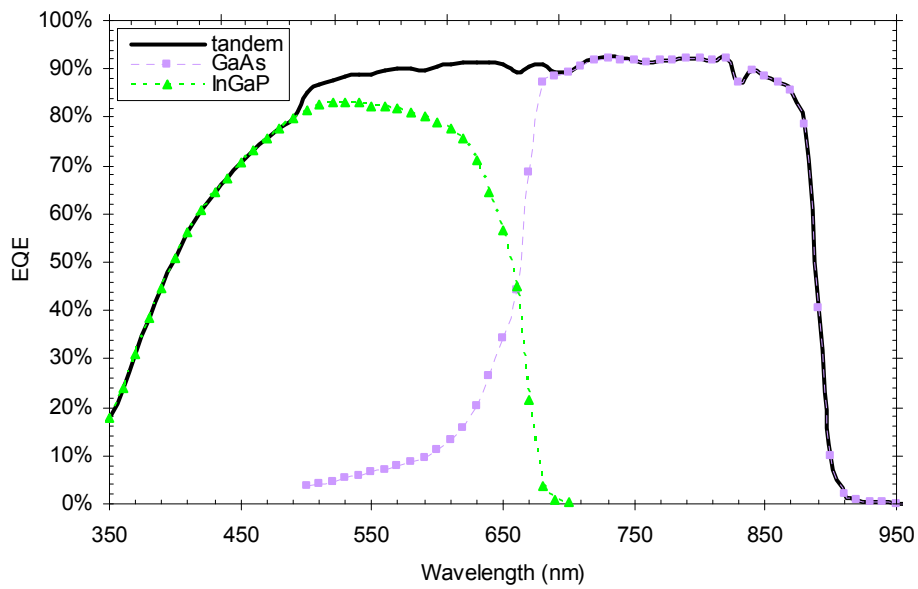


Figure 4-48: EQE of the total dual junction cell plus its components (NREL).

The hint of a shunt problem that is observable in the J - V curves and where R_{sh} is smaller for cell A than for B is also evidenced in the IQE measurement. Not only due to the lower IQE but also due to a measurable spectral response signal for wavelengths longer than the InGaP absorption edge (670 nm).

4.7 Summary and conclusions

N-type doping levels of the order 10^{19} cm^{-3} were obtained using Se as a dopant in GaAs. This was a requirement for realising ohmic contacts when making the transition from p-on-n to n-on-p solar cells. Also the contact resistance is below $1 \text{ m}\Omega\cdot\text{cm}^2$. Our p-on-n single junction GaAs solar cells on germanium are of world class, with efficiencies under AM1.5G of over 24 %. It was expected that better results would be achieved by using n-on-p cells due to the lower bulk resistivity of the material but to date, the results are only comparable. The fill factors are good; V_{oc} is lower but J_{sc} is higher, both due to the lower bandgap caused by slightly more indium in the layers of those samples.

The composition of InGaP and InAlP can be controlled well. Ordering is an effect that one can take into account when growing phosphides. It has an observable influence on the InGaP material parameters, but is less important for InAlP. Doping of InGaP is reliable and carbon and oxygen impurities in the material are low. Doping of InAlP has been more difficult to characterise and C and O concentrations in the material are high. Also long planar defects, originating at the InAlP / GaAs interface, were observed and are probably dependent on growth conditions. A best single junction InGaP solar cell of 14.2 % conversion efficiency was achieved – although the actual value might be a bit lower due to an overestimation (see NREL measurement dual junction cell) of the J_{sc} (13.6 mA/cm^2) – with a good value for V_{oc} (1.276 V) and fill factor (82.0 %). There is still room for improvement of both parameters, necessitating higher quality material. At first glance, TRPL measurements indicate a rather high recombination velocity, 3420 cm/s, at the base/BSF interface. However, higher values (5100 cm/s) than ours are reported in literature and simulations made by other authors indicate that reducing the interface recombination velocity below 10^4 cm/s does not sort much effect. A first test with remote hydrogen plasma passivation showed promising results

Intrinsic carbon doping of GaAs and AlGaAs was studied as function of growth temperature and V/III ratio. For GaAs, these experiments led to the derivation of the activation energy for growth using TMGa and TBAs, which is in the range of 34 to 38 kcal/mol. For AlGaAs growth with TMGa, TMAI and TBAs, the activation energy was determined to be 27 kcal/mol for V/III higher than 1.7 and the AlAs growth rate decreased relatively faster than that of GaAs. The carrier concentration was seen to increase with decreasing V/III ratio and decreasing growth temperature. Both parameters also had an effect on the Al fraction in the solid. For V/III = 9.3, a doping

level as high as $1.4 \times 10^{19} \text{ cm}^{-3}$ was reached at $542 \text{ }^\circ\text{C}$ and with an input TMAI/III of 0.29. With a low $V/\text{III} = 1.7$ and the same Al_g , the temperature dependence apparently disappears and carrier concentration saturates around $6\text{--}7 \times 10^{19} \text{ cm}^{-3}$, even at normal growth temperatures of $630 \text{ }^\circ\text{C}$.

A GaAs tunnel junction was realised with Zn- and Se-doping, yielding a peak current density of 82 A/cm^2 and a peak-to-valley ratio of only 1.2. AlGaAs tunnel diodes were realised with $J_p = 17.3 \text{ A/cm}^2$ and $J_p/J_V = 11.3$ for an C: $\text{Al}_{0.3}\text{Ga}_{0.7}\text{As}$ layer grown with $V/\text{III} = 9.3$ at $542 \text{ }^\circ\text{C}$ and sandwiched between GaAs layers. When clad in a solar cell-like layer stack J_p was 3.9 A/cm^2 and $J_p/J_V = 10.0$. Using a lower V/III of 1.7, hence, the higher p-doping level of $6\text{--}7 \times 10^{19} \text{ cm}^{-3}$ and adjusted layer thicknesses, 92.0 A/cm^2 was achieved with a peak-to-valley ratio of 9.2 for a high growth temperature of $630 \text{ }^\circ\text{C}$. It was also found that using AuZn in the front contact metal of these p-on-n structures is the best option.

Dual junction InGaP / GaAs solar cells on germanium were grown and processed, displaying good uniformity. The highest efficiency that we obtained was 24.3 % for a cell of 1 cm^2 . The 4 cm^2 cell had a conversion efficiency of 24.0 %. These first values are promising results.

4.8 References

- [1] Advanced Semiconductors Buyers' Guide 2005/2006, III-Vs Review.
- [2] Y. Li, "On the formation of antiphase domains in the system of GaAs on Ge", *Journal of Crystal Growth*, Vol. 163, 195-202 (1996).
- [3] M. D'Hondt et al., "High quality InGaAs/AlGaAs lasers grown on Ge substrates", *Journal of Crystal Growth*, Vol. 195, 655-659 (1998).
- [4] P. Modak, "Development of InAlGaP-based light-emitters on GaAs and Germanium substrates by means of MOCVD", Ph.D. dissertation, Intec – Ghent University, (2002).
- [5] J. Derluyn et al., "Comparison of MOVPE grown GaAs solar cells using different substrates and group-V precursors", *Journal of Crystal Growth*, Vol. 247, 237-244 (2003).
- [6] M. Yamaguchi et al., "Numerical analysis for radiation-resistant GaAs heteroface solar cell structures", *Journal of Applied Physics*, Vol. 57 (2), 537-544 (1985).
- [7] N. Dharmarasu et al., "Effect of proton irradiation on n⁺p InGaP solar cells", *Journal of Applied Physics*, Vol. 91 (5), 3306-3311 (2002).
- [8] G. Kunz and A. Wagner, "Internal series resistance determined of only one IV-curve under illumination", *Proceedings of the 19th European Photovoltaic Solar Energy Conference*, 2671-2674 (2004).
- [9] G.B. Stringfellow & G.S. Chen, "Atomic ordering in III/V semiconductor alloys", *Journal of Vacuum Science and Technology B*, Vol. 9 (4), 2182-2188 (1991).
- [10] R.P. Schneider et al., "Photoluminescence linewidths in metalorganic vapor phase epitaxially grown ordered and disordered InAlGaP alloys", *Journal of Applied Physics*, Vol. 72 (11), 5397-5400 (1992).
- [11] M. Zorn et al., "Correlation of InGaP (001) surface structure during growth and CuPtB-type bulk ordering", *Proceedings of Materials Research Society Symposium*, Vol. 583, 217-221 (2000).
- [12] T. Shitara et al., "Electronic properties of InGaP grown by solid-source molecular-beam epitaxy with a GaP decomposition source", *Applied Physics Letters*, Vol. 65 (3), 356-358 (1994).
- [13] M. Ikeda et al., "Selenium and zinc doping in Ga_{0.5}In_{0.5}P and (Al_{0.5}Ga_{0.5})_{0.5}In_{0.5}P grown by metalorganic chemical vapor deposition", *Journal of Applied Physics*, Vol. 66 (11), 5285-5289 (1989).
- [14] M. Quillec, Procion Analysis, private communication, February 19th, 2007.
- [15] A. Khan et al., "Deep level transient spectroscopy analysis of 10 MeV proton and 1 MeV electron irradiation-induced defects in p-InGaP and InGaP-based solar cells", *Japanese Journal of Applied Physics*, Vol. 41, 1241-1246 (2002).
- [16] A.R. Clawson, "Guide to references on III-V semiconductor chemical etching", *Materials Science and Engineering: R: Reports*, Vol. 31, 1-438 (2001).

-
- [17] T. Takamoto et al., "Structural optimization for single junction InGaP solar cells", *Solar Energy Materials and Solar Cells*, Vol. 35, 25-31 (1994).
- [18] M.-J. Yang et al., "Photoluminescence analysis of InGaP top cells for high-efficiency multijunction solar cells", *Solar Energy Materials and Solar Cells*, Vol. 45, 331-339 (1997).
- [19] S.R. Kurtz et al., "Passivation of interfaces in high-efficiency photovoltaic devices", *Materials Research Society Spring Meeting*, San Francisco, CA, (1999).
- [20] M.-J. Yang et al., "Photoluminescence analysis of InGaP top cells for high-efficiency multijunction solar cells", *Solar Energy Materials and Solar Cells*, Vol. 45, 331-339 (1997).
- [21] V.A. Gorbylev et al., "Hydrogen passivation effects in InAlGaP and InGaP", *Journal of Applied Physics*, Vol. 76 (11), 7390-7398 (1994).
- [22] J.Y. Lee et al., "Enhancement of a rectifying characteristic of InGaP diodes by hydrogenation", *Journal of Applied Physics*, Vol. 85 (1), 600-603 (1999).
- [23] K. Akahori et al., "Improvement of the MOCVD-grown InGaP-on-Si towards high-efficiency solar cell application", *Solar Energy Materials and Solar Cells*, Vol. 66, 593-598 (2001).
- [24] G. Wang et al., "PH₃/H₂ plasma passivation of metal-organic chemical vapor deposition grown GaAs on Si", *Journal of Applied Physics*, Vol. 88 (6), 3689-3694 (2000).
- [25] M. Longo et al., "Controlled intrinsic carbon doping in MOVPE-grown GaAs layers by using TMGa and TBAs", *Journal of Crystal Growth*, Vol. 248, 119-123 (2003).
- [26] Gerald B. Stringfellow, "Organometallic Vapour-Phase Epitaxy: Theory and Practice", 2nd edition, Academic Press, Boston, (1999).
- [27] J. van Deelen et al., "Parameter study of intrinsic carbon doping of Al_xGa_{1-x}As by MOCVD", *Journal of Crystal Growth*, Vol. 271, 376-384 (2004).
- [28] S. Leu et al., "C- and O-incorporation in (AlGa)As layers grown by MOVPE using TBAs", *Journal of Crystal Growth*, Vol. 195 (1-4), 98-104 (1998).
- [29] S.A. Stockman in "Properties of Gallium Arsenide", Eds. M.R. Brozel, G.E. Stillman, Short Run Press Ltd., Exeter, 1996.
- [30] J. Mimila-Arroyo et al., "Carbon acceptor doping efficiency in GaAs grown by metalorganic chemical vapor deposition", *Applied Physics Letters*, Vol. 79 (19), 3095-3097 (2001).
- [31] R. Heilmann et al., "Ionization energy of the carbon acceptor in Al_xGa_{1-x}As", *Semiconductor Science and Technology*, Vol. 5, 1040-1045 (1990).
- [32] K.A. Bertness et al., "Tunnel junction interconnects in GaAs-based multijunction solar cells", *Proceedings of the 1st World Conference on Photovoltaic Energy Conversion*, 1859-1862 (1994).

-
- [33] P. Basmaji et al., "GaAs tunnel junction grown by metalorganic vapor-phase epitaxy for multigap cascade solar cells", *Journal of Applied Physics*, Vol. 62 (5), 2103-2106 (1987).
 - [34] P. Bouchaib et al., "Use of molecular beam epitaxy for the achievement of low resistance intercell contacts in multiband gap solar cells", *Journal of Vacuum Science and Technology*, Vol. 19 (2), 145-147 (1981).
 - [35] C. Amano et al., "20.2% efficiency $\text{Al}_{0.4}\text{Ga}_{0.6}\text{As}/\text{GaAs}$ tandem solar cells grown by molecular beam epitaxy", *Applied Physics Letters*, Vol. 51 (24), 1998-2000 (1987).
 - [36] S.M. Sze, "Physics of Semiconductor Devices", 2nd edition, John Wiley & Sons Inc., New York, (1981).
 - [37] S.M. Bedair et al., "AlGaAs tunnel diode", *Journal of Applied Physics*, Vol. 50 (11), 7267-7268 (1979).
 - [38] P.R. Sharps et al., "AlGaAs/InGaAlP tunnel junctions for multijunction solar cells", *Proceedings of the 28th IEEE Photovoltaic Specialists Conference*, 1185-1188 (2000).
 - [39] R.R. King et al., "High-efficiency space and terrestrial multijunction solar cells through bandgap control in cell structures", *Proceedings of the 29th IEEE Photovoltaic Specialists Conference*, 776-781 (2002).

Chapter 5

Metamorphic materials

5.1 Introduction

In the previous chapter solar cells lattice-matched to the substrate were discussed. If we now look back to Table 3-1, the bandgaps that need to be combined to realise maximal conversion efficiency for a dual junction solar cell are not those of the lattice-matched materials. The optimal bandgap combination can be calculated but depends strongly on the spectrum and the assumptions made for the calculations. Table 5-1 presents yet another set of values under a different spectrum [1]. One thing is clear, to improve the conversion efficiencies to values as high as possible, the condition of lattice-matching the subcells will have to be relaxed. A transition to metamorphic (lattice-mismatched) materials is mandatory, since substrates are not available with just any lattice constant. Some of the active cell materials can be lattice-matched to the substrate if special design approaches are used (inverted structures) but then the substrate will (most likely) have to be removed during further processing of the solar cell. Usually, a germanium substrate will be used and metamorphic layers will be deposited on it. The subcells can be lattice-matched to one another but this is certainly not a requirement.

Obtaining high quality metamorphic material is only manageable by using appropriate buffer layers to accommodate the (large) lattice-mismatch between substrate and layers. Several approaches are possible but they all have the same objective: bending threading dislocations (TD) to prevent them from propagating into the active layers of the device. The threading dislocation density (TDD) has to be on the order of 10^6 cm^{-2} or below in order for recombination to be limited by (primarily) non-dislocation related bulk Shockley-Read-Hall (non-radiative) recombination [2,3].

Table 5-1: The maximal energy conversion efficiency and the corresponding optimal set of bandgaps $E_{G,i}$ ($i=1$ is the top of the stack) for tandem cells with n stacked cells under AM1.5D (1 sun, no angular restriction, no reflector).

n	η (%)	$E_{G,1}$ (eV)	$E_{G,2}$ (eV)	$E_{G,3}$ (eV)	$E_{G,4}$ (eV)
1	32.5	1.13			
2	44.1	0.94	1.64		
3	49.7	0.71	1.16	1.83	
4	53.6	0.71	1.13	1.55	2.13

5.2 Buffer layers

5.2.1 Critical thickness

In this work a metamorphic dual junction solar cell on germanium will be demonstrated, where the subcells are made of $\text{In}_{0.17}\text{Ga}_{0.83}\text{As}$ (1.18 eV) and $\text{In}_{0.65}\text{Ga}_{0.35}\text{P}$ (1.68 eV). Combining these two materials should yield solar cells with conversion efficiencies of 34.2 % under AM0 spectral conditions and 41.8 % under AM1.5D illumination (500 suns) (see Figure 1-8). Both materials are lattice-matched to each other, having lattice constants of 5.7225 and 5.7224 Å, respectively, but are lattice-mismatched to Ge (5.6577 Å). The lattice-mismatch f between layers and substrate is defined as

$$f = \frac{a_l - a_s}{a_s}, \quad (5.1)$$

where a_s and a_l are the lattice constants of the substrate and the deposited layer. A mismatch of 1.14 % between substrate and layers is calculated in the case of the materials mentioned above.

A layer that is deposited onto a substrate with a different lattice constant and without applying a suitable buffer, will first be elastically deformed. The in-plane lattice constant of the layer, $a_{//}$, will adapt itself to the lattice constant of the substrate but the perpendicular lattice parameter will change in such a manner as to keep the (lattice) cell volume of the non-deformed material. If $a_l > a_s$, then $a_{//} < a_l$ and the deposited layer will be compressively stressed. In the other case the layer will be under tensile strain.

When the built up strain energy becomes larger than the dislocation generation energy, the layer will start to relax. The relaxation degree R is defined as

$$R = \frac{a_{//} - a_s}{a_l - a_s}. \quad (5.2)$$

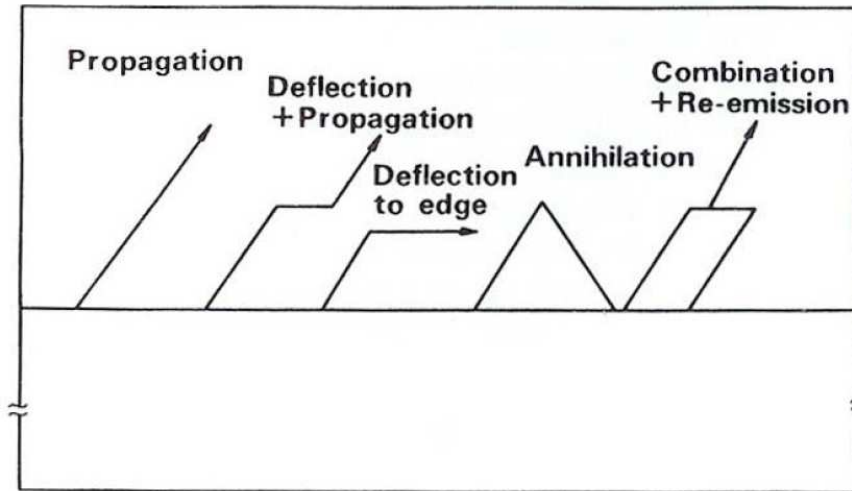


Figure 5-1: Mechanisms of dislocation interaction in lattice-mismatched material.

Three cases are possible for a layer with lattice constant larger than the substrate's :

- (1) Perfectly strained: $a_{//} = a_s$ and $a_{\perp} = \frac{a_l(1-\nu) - 2\nu a_{//}}{1-\nu} \Rightarrow R = 0$
- (2) Partially relaxed: $a_l > a_{//} > a_s$ and $a_{\perp} > a_l \Rightarrow 0 < R < 1$
- (3) Completely relaxed: $a_{//} = a_{\perp} = a_l \Rightarrow R = 1$

with ν the Poisson ratio.

Many types of lattice defects can be generated when the deposited layer starts to relax via dislocation formation. All dislocations can be characterised by their Burgers vector. Stacking faults e.g. are two-dimensional defects. Edge and screw dislocations are linear defects. Several dislocations can be combined to form other types of dislocations with a mixed edge and screw character. A typical example in zinc-blende crystals is the 60° dislocation, 60° being the angle between dislocation line and Burgers vector.

Dislocation lines can only end at the crystal surface or on other dislocations if the total sum of Burgers vectors is zero. In this way they can form loops or half-loops ending at the surface. Dislocations can interact in a variety of ways of which several are presented in Figure 5-1. When a dislocation penetrates the growing surface they are called threading dislocations and can propagate through the entire layer stack that is grown. This type of defect is unwanted since they cause a local disruption of the crystal lattice leading to dangling bonds; these may be occupied by impurity atoms, mostly leading to deep states in the bandgap and, hence, non-radiative recombination pathways.

Threading dislocations can also move within the crystal. They are nucleated at the growing surface and can then glide in the $\{111\}$ planes under the influence of strain. Misfit dislocations are created by that process at the interface between two layers to partially alleviate the stress. The layer thickness at which elastic deformation of the lattice can no longer accommodate misfit strain and the first misfit dislocations are formed is called the critical thickness. Matthews and Blakeslee [4] (M&B) derive an implicit expression for the critical thickness h_c by balancing the tension in the dislocation line with the force exerted on it by misfit stress. This model uses the concept of mechanical equilibrium of the system of dislocations. With a number of approximations and assumptions they obtain

$$h_c = \frac{a_l}{\kappa\sqrt{2}\pi f} \cdot \frac{1-\nu/4}{1+\nu} \cdot \left[\ln\left(\frac{h_c\sqrt{2}}{a_l}\right) + 1 \right], \quad (5.3)$$

where ν is the Poisson ratio of the layer and κ a factor that equals 2 for a single layer, 4 for a sandwiched layer (the top layer having the same lattice constant as the bottom one) or 8 if the strained layer is incorporated in a superlattice. The value for h_c that follows from Eq. (5.3) is a minimum value because nucleation barriers towards the formation of misfit dislocations are not taken into account [5]. The layer can be grown thicker than the critical thickness if there are such barriers; these layers are called metastable.

Another model was developed by People and Bean [6] (P&B) and takes the point of view of energy balance. They use the equilibrium condition between the strain energy density of the layer and the energy density associated with that dislocation-generating mechanism which is of minimum energy in the absence of threading dislocations. Screw dislocations turn out to be of minimum energy with the edge dislocation density exceeding the screw energy density by a small factor $\beta \sim 1/(1-\nu)$. P&B derive the following expression

$$h_c = \frac{a_l}{32\sqrt{2}\pi f^2} \cdot \frac{1-\nu}{1+\nu} \cdot \ln\left(\frac{h_c\sqrt{2}}{a_l}\right). \quad (5.4)$$

Their incentive for making the model was that they observed that the actual critical thickness of a layer can be more than an order of magnitude larger than that calculated by the M&B model.

In a reaction to P&B, Dodson and Taylor [7] (D&T) argue that its use as a model to calculate the critical thickness is incorrect because P&B use a restrictive expression for the dislocation energy and an energy balance that is not taken with respect to the entire strained lattice. Furthermore, screw dislocations can not relieve tetragonal strain [5] which occurs in a cubic lattice whereas P&B assume they do because they are of minimum formation energy.

A distinction can be made, based on the sign of the stress present in the layer [5]. Compressive strain ($f > 0$) gives rise to the formation of perfect 60° dislocations via the nucleation of half-loops while tensile strain ($f < 0$) results in stacking faults.

According to the M&B model, an $\text{In}_{0.17}\text{Ga}_{0.83}\text{As}$ layer has a critical thickness of 7.8 nm on a germanium substrate, whereas it is 84.9 nm in the P&B model. For an $\text{In}_{0.65}\text{Ga}_{0.35}\text{P}$ layer we calculate 7.5 nm and 79.9 nm, respectively. In view of D&T's reaction to the P&B model, those values are deemed incorrect. In any case, both values for the layer thicknesses are too small to grow a thick solar cell layer. It is obvious that a buffer layer is needed when transitioning from one lattice constant to another.

5.2.2 Sorts of buffers

The aim of a buffer layer is to prevent dislocations from propagating into the active layers of a device when growing e.g. lattice-mismatched material. The simplest way to try and achieve this is to grow a thick uniform layer with the lattice constant of the desired active layer material. This approach is based on the opportunities a dislocation gets to bend towards the edge of the sample or to interact with other dislocations. When more dislocations are "neutralised" as the layer gets thicker, this probability decreases due to the reduced dislocation density and a saturation of the effect occurs. Another option is to grade the lattice constant from the substrate to the active layer value. Possibilities to do this are the use of

- (1) a step graded buffer,
- (2) a lineary graded buffer or
- (3) a strained superlattice.

In a step graded buffer the lattice constant is adjusted in steps from one layer to the next until the desired lattice constant is reached. When the interfaces are sharp, dislocations can be deflected into the plane of the interface and, thus, be stopped from propagating into the active layers. To prevent the formation of new dislocations but at the same time create enough tension in the layer to bend existing dislocations, special care has to be given to the lattice-mismatch between the buffer layers. A value of 0.13 % is mentioned for the mismatch between successive layers [8].

The lineary graded buffer is a sort of special case of the step graded buffer, namely one where the number of steps is infinity. By controlling the source gasses the lattice constant of the buffer is varied lineary and continuously. Although there are no interfaces in this buffer scheme, dislocations are bent because they tend to propagate in the direction of the smallest lattice constant, which is in our case towards the substrate. It is shown both theoretically and experimentally that at the top of the lineary graded buffer a dislocation free ($< 10^5\text{-}10^6\text{ cm}^{-2}$, TEM detection limit) layer will exist, that, however, remains under tension [9]. The thickness of that dislocation free layer z_{df} remains constant while the film grows and is equal to $w-z_c$, with w the total film

thickness and z_c the distance from the substrate/buffer interface up to the point in the buffer where the density of dislocations in equilibrium is enough to cancel the mismatch. Thus, relaxation of the material is not 100 % at the top of the buffer and therefore the in-plane lattice constant will be smaller than the lattice constant of a free-standing layer with the same composition. This means that for a given composition of the active layer, the buffer will have to overshoot this value in order to end up with the same (in-plane) lattice constant.

The strained superlattice (SSL) consists of alternating thin layers that in this case, obviously, have different lattice constants. Here, the remark that was made in the case of a step graded buffer concerning the lattice-mismatch between composing layers, also holds. Because the SSL has more interfaces than a step graded buffer, it should be more efficient in neutralising dislocations. The grading mechanism is based on grading the mean lattice constant a_{SSL} of one period of the SSL, which is calculated as follows

$$a_{SSL} = \frac{d_1 a_1 + d_2 a_2}{d_1 + d_2}, \quad (5.5)$$

where d_i and a_i represent the thickness and lattice constant of the i^{th} layer. So either the lattice constant of the layers (composition) or the thicknesses can be adjusted within one SSL period.

5.2.3 Buffer comparison

Only step and linearly graded buffer layers were tested in this work. All buffers were grown on 4" (100) Ge 6° off-oriented towards <111> at low pressure (76 torr). The growth temperature of all buffer structures was 650 °C, except for one that was grown at 570 °C. Only for the step graded buffers, some samples were annealed in the reactor at 690 °C under TBAs after growth of the reference layer (always the same growth conditions, see p.125). Growth rates in the range of 4.6 to 14.6 Å/s were used and V/III ratios between 10 and 26.

The details of the buffers used in this study are mentioned in Table 5-2. On top of every buffer the reference layer with the same (desired) composition was grown. This was always deposited at 650 °C. "High V_{gr} " means a doubled group-III flux during the growth of buffer layer with respect to "low V_{gr} "-samples. For the step graded buffers the number of layers used to go from the lattice-matched to the reference layer are given with the mismatch between successive steps. Thickness refers to the total thickness of that number of layers. The linearly graded buffers consist of 1 layer in which the In concentration is ramped continuously to the desired level, so also the mismatch between lattice-matched and reference layer is gradually built up to 1.14 %. For one linearly and one step graded buffer, the In concentration was intentionally overshoot by about 10% to what is required. Annealing experiments were performed only on step graded buffers to test the influence of high temperature on layer relaxation and buffer quality.

Table 5-2: Overview of buffer details, grown at 650 °C.

Sample	Buffer type	layers	step mismatch	Thickness (μm)	V _{gr}	Remarks
r0418	none					
r0419	linear	1		1.0	low	
r0422 [#]	linear	1		1.0	low	
r0423	linear	1		2.0	low	
r0425	linear	1		2.0	high	
r0448	linear	1		2.4	high	10 % overshoot In fraction
r0424	step	11	0.10 %	2.0	low	
r0426	step	11	0.10 %	1.0	low	
r0460	step	9	0.12 %	1.8	low	
r0461	step	9	0.12 %	1.8	low	20 min anneal at 690°C
r0462	step	6	0.14 %	1.2	low	<ul style="list-style-type: none"> • 0.21% mismatch between 5th and 6th layer, • 0.28% between 6th and reference layer. • Anneal at 690°C for 30 min. ◦ 0.14% mismatch between lattice-matched and 1st and also between 6th and 7th layer.
r0463	step	7	0.21 %	1.4	high	<ul style="list-style-type: none"> ◦ 10 % overshoot In fraction in 7th layer. ◦ Anneal at 690°C for 30 min.

[#] grown at 570 °C

Table 5-3: Measurement results of the reference layer analysis on the buffers from Table 5-2.

Sample	In fraction ref. layer	relaxation	ω _{FWHM} (arcsec)	σ (arcsec)	In fraction lattice-matched to ref. layer	Remarks
r0418 [#]	0.180	78.4 %	855.6	230.0	0.142	
r0419	0.181	81.0 %	493.3	25.3	0.147	
r0422 [#]	0.192	74.3 %	636.8	13.2	0.144	
r0423	0.185	89.2 %	420.2	25.7	0.165	
r0425	0.182	84.8 %	429.8	10.5	0.154	
r0448	0.176	80.3 %	420.8	46.6	0.142	10% In overshoot
r0424	0.179	82.3 %	443.2	69.8	0.148	
r0426	0.182	84.5 %	477.5	25.1	0.154	
r0460	0.180	82.9 %	456.3	45.8	0.149	
r0461	0.179	85.2 %	375.3	49.1	0.153	20 min anneal at 690°C
r0462	0.176	78.2 %	364.1	34.7	0.153	30 min anneal at 690°C
r0463	0.187	86.6 %	368.7	36.6	0.162	<ul style="list-style-type: none"> •10% In overshoot •30 min anneal at 690°C

[#] only 2 RSM measurements

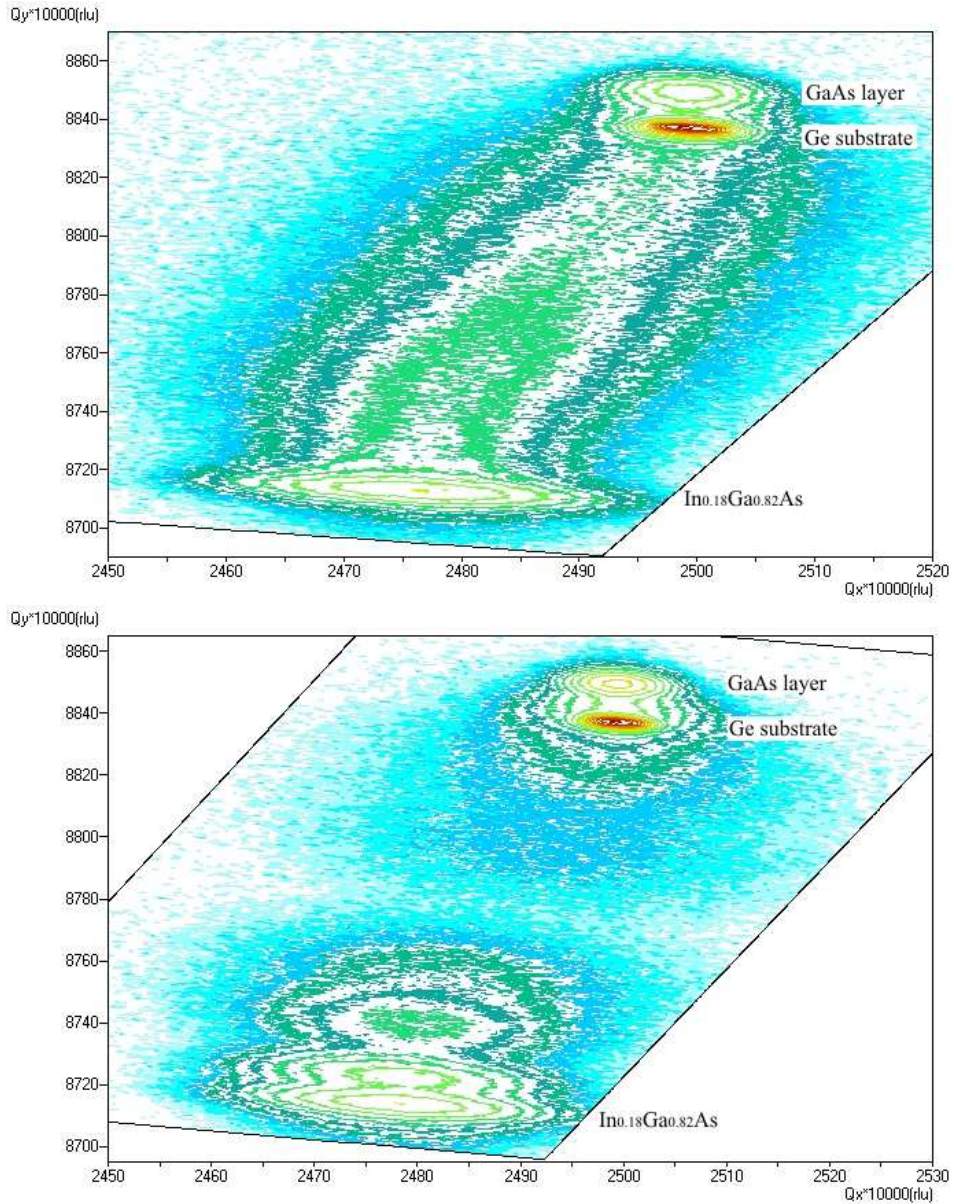


Figure 5-2: HRXRD reciprocal space map of linearly (top) and step (bottom) graded InGaAs buffers on germanium. In both pictures the Ge, GaAs and $\text{In}_{0.18}\text{Ga}_{0.82}\text{As}$ peak are indicated. For the linear grade a continuous diffraction signal is detected whereas for the step buffer the peaks of the individual steps are visible, especially near the top where the layers were thicker.

The growth rate calibration was done by depositing several $\text{In}_x\text{Ga}_{1-x}\text{As}$ single layers with $0 < x < 0.2$ and measuring the growth rate via EpiTT in-situ reflectometry at 633 nm. Increasing the indium concentration in the material was achieved by increasing the TMIn molar flux in the gas phase while keeping the TMGa and TBAs flow constant. Hence, the growth rate and V/III ratio were not identical for $\text{In}_x\text{Ga}_{1-x}\text{As}$ layers with different x when depositing step graded buffers and were continuously ramped in the case of linearly graded buffers.

The top of every buffer was a 600 nm reference layer, deposited at 650 °C. The full width at half maximum of its ω -peak, determined from a HRXRD (115) reciprocal space map (RSM, examples see Figure 5-2), was used as a measure of the crystalline layer quality and, thus, the buffer quality. On most samples four or more RSMs were taken and a standard deviation was calculated. These results are presented in Table 5-3 along with the In fraction and relaxation degree of the reference layer and the composition of the $\text{In}_x\text{Ga}_{1-x}\text{As}$ alloy that can be grown lattice-matched to it.

Now, conclusions will be drawn from Table 5-2 and Table 5-3. From the peak width of r0418 it is clear that a buffer layer is needed. Comparing r0419 and r0422 shows that reducing the growth temperature is detrimental for the layer quality. This is due to the lower relaxation degree in r0422. Thicker buffer layers give better layer quality, irrespective of growth rate, because dislocations will have had more time to interact or bend. Thick linearly graded buffers (r0423, r0425, r0448) seem to yield slightly better material than step graded ones (r0424, r0460). The high temperature annealing of step graded buffer and reference layer improves the quality considerably. In general, the longer a buffer is kept in relaxation enhancing conditions, the better the material quality.

Figure 5-3 shows the cross-section TEM image in the dark-field (002) two-beam diffraction condition for a linearly graded buffer similar to r0448 but integrated in a device. A high dislocation density can be found in the graded InGaAs region. Most dislocations have line directions along [110] or [1-10]. Deviations from these line directions exist, which results in some upward bending, but all of them are blocked due to dislocation interaction. The net result is that all dislocations (in this analysed piece) are confined to the buffer region. Analysis of a large area of the sample in plan-view TEM confirms that no single dislocation reaches the sample surface. We can conclude that the threading dislocation density in the whole wafer will most likely be on the order of the TEM detection limit (10^5 - 10^6 cm⁻²).

By applying the **g.b** invisibility criterion (**g**: incident beam direction, **b**: Burgers vector) it is found that all dislocations are 60° dislocations. Screw dislocations or 90° dislocations were not observed. This agrees with the fact that compressive strain gives rise to 60° dislocations. The bright line (contrast) almost at the top of the image is due to stress in that layer with 10 % overshoot of the indium concentration.

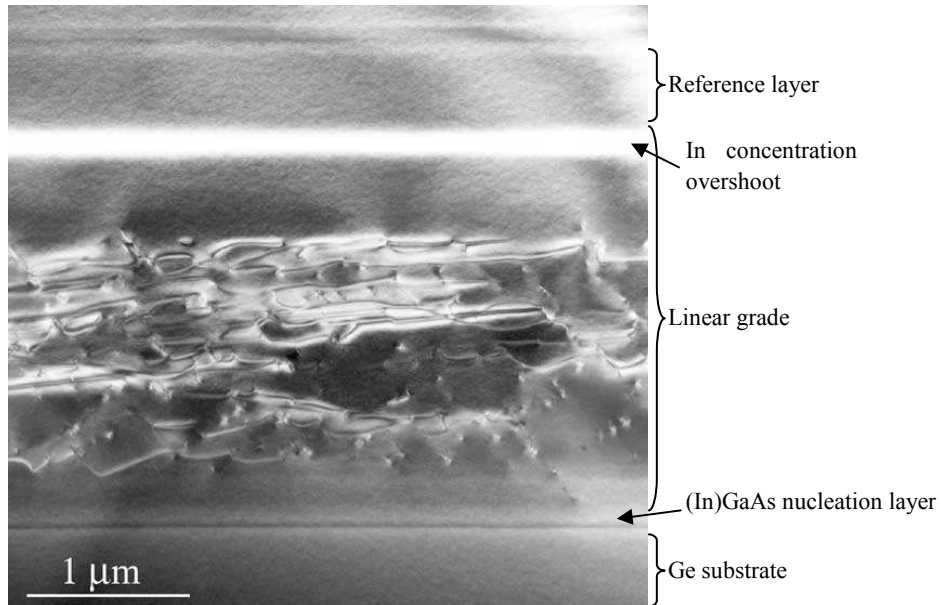


Figure 5-3: Dark-field (002) two-beam diffraction TEM cross-section of linear grade r0448.

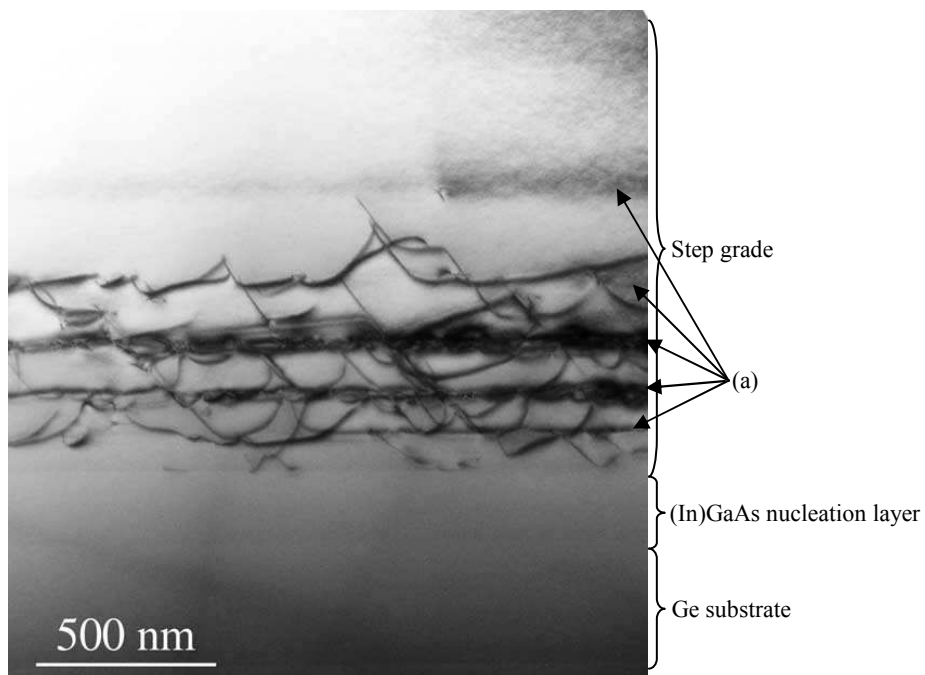


Figure 5-4: Bright-field (002) two-beam diffraction TEM cross-section of step buffer r0462.

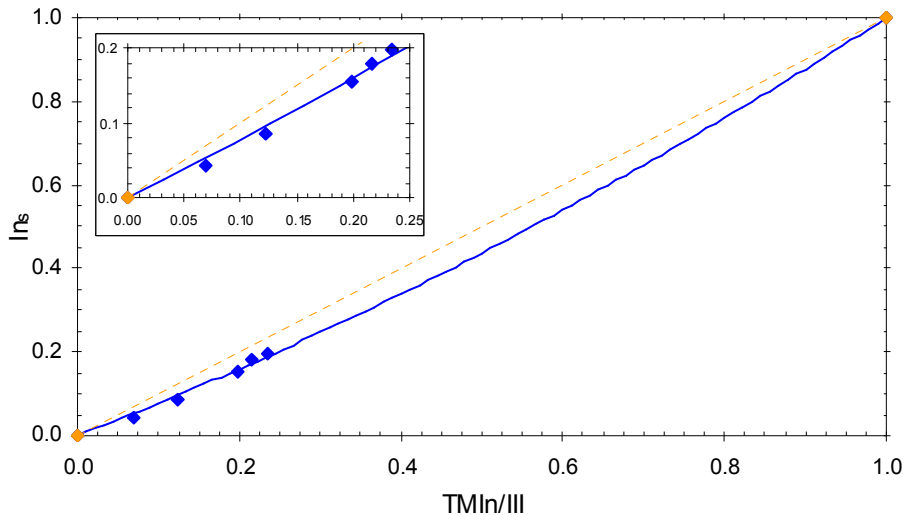


Figure 5-5: Parabolic fit to indium fraction in the solid phase (In_s) as a function of $TMIn/III$ ratio in the input gas phase (solid curve). The data for $TMIn/III = 0$ and 1 are obvious points and the broken line is a linear fit through them. Inset: magnification of the calibration points.

Figure 5-4 shows the cross-section TEM image in the bright-field (002) two-beam diffraction condition for a step graded buffer similar to r0462 but integrated in a device. A high dislocation density can be found in the graded InGaAs region but this time the dislocations pile up at certain heights in the sample. These are (most likely) the interface positions of the steps. The conclusions as described for Figure 5-3 also hold for this sample, thus, the threading dislocation density is on the order of the TEM detection limit (10^5 - 10^6 cm^{-2}) or below.

5.3 $In_{0.17}Ga_{0.83}As$ single junction solar cell

5.3.1 Composition

As mentioned above, the growth rate calibration was done by depositing $In_xGa_{1-x}As$ single layers with $0 < x < 0.2$ and measuring the growth rate via EpiTT in-situ reflectometry at 633 nm. Increasing the indium concentration in the material was achieved by increasing the TMIn molar flux in the gas phase while keeping the TMGa and TBAs flow constant. Hence, the growth rate and V/III ratio were not identical for $In_xGa_{1-x}As$ layers with different x . In Figure 5-5 it is seen that a parabolic relationship between the In composition in the solid and that in the gas phase is in good agreement with the datapoints.

Table 5-4: Overview of the different metamorphic single junction n-p InGaAs cell structures with their intended layer compositions.

Sample	A	B	C, D	E
Contact	In _{0.14} Ga _{0.86} As 260 nm	In _{0.15} Ga _{0.85} As 260 nm	In _{0.16} Ga _{0.84} As 270 nm	In _{0.16} Ga _{0.84} As 270 nm
Window (30 nm)	In _{0.14} Al _{0.69} Ga _{0.17} As	In _{0.15} Al _{0.68} Ga _{0.17} As	In _{0.16} Al _{0.67} Ga _{0.17} As	In _{0.16} Al _{0.67} Ga _{0.17} As
Emitter	In _{0.15} Ga _{0.85} As 230 nm	In _{0.16} Ga _{0.84} As 230 nm	In _{0.16} Ga _{0.84} As 235 nm	In _{0.16} Ga _{0.84} As 235 nm
Intrinsic layer	–	–	–	In _{0.16} Ga _{0.84} As 210 nm
Base	In _{0.15} Ga _{0.85} As 2.77 μm	In _{0.16} Ga _{0.84} As 2.78 μm	In _{0.16} Ga _{0.84} As 2.91 μm	In _{0.16} Ga _{0.84} As 2.70 μm
BSF (50 nm)	In _{0.15} Al _{0.25} Ga _{0.60} As	In _{0.16} Al _{0.25} Ga _{0.59} As	In _{0.16} Al _{0.25} Ga _{0.59} As	In _{0.16} Al _{0.25} Ga _{0.59} As
Anneal step	–	30 min at 690°C	C: – D: 20min at 690°C	–
Buffer	2.4 μm, linear, In-overshoot	1.2 μm, step, high growth rate	2.2 μm, linear, In-overshoot	2.2 μm, linear, In-overshoot
Substrate	p-Ge	p-Ge	p-Ge	p-Ge

No separate doping calibration runs were performed for this material. Dimroth et al. [10] mention that the doping behaviour of In_{0.17}Ga_{0.83}As with SiH₄ and DMZn is similar to that of GaAs, so it was assumed that it would also be the case for the dopants we use (SiH₄, H₂Se and DEZn). We therefore immediately proceeded to grow a metamorphic InGaAs solar cell by using the same dopant fluxes as for the lattice-matched GaAs solar cell. Before we present the solar cell performance, we will first discuss the growth details of the samples and the analysis results of the grown layers.

5.3.2 Solar cell structures and growth details

Table 5-4 gives an overview of the metamorphic n-p single junction InGaAs solar cell structures that were grown. As seen in §5.2, the composition of the alloy that can be grown lattice-matched to the InGaAs virtual substrate (= germanium substrate + InGaAs buffer and top layer) is different from that of the virtual substrate's top layer. The in-plane lattice constant is smaller than that of a free-standing top layer due to incomplete relaxation. We tried to account for that difference as much as possible. For this reason, the In concentration in the active layers of the solar cell is lower than 17 %.

Samples A and B were grown right after the buffer test samples. Buffer r0448 was used for sample A and a modified version of r0462 (it was grown with the high growth rate; see §5.2.3) for sample B. Samples C, D and E were made quite some time after that. They were deposited on a modified version of r0448. The In concentration overshoot was larger and at the same time the buffer was made a bit thinner.

Table 5-5: Active layer growth details for single junction metamorphic InGaAs solar cells.

Sample	A	B	C, D, E	A	B	C, D, E
BSF ($1 \times 10^{18} \text{ cm}^{-3}$)				Emitter ($1-2 \times 10^{18} \text{ cm}^{-3}$)		
T_{set} ($^{\circ}\text{C}$)	720	720	720	T_{set} ($^{\circ}\text{C}$)	690	690
T_{gr} ($^{\circ}\text{C}$)			660	T_{gr} ($^{\circ}\text{C}$)		630
V/III	25.3	25.0	25.4	V/III	10.8	10.7
TMIn ($\mu\text{mol}/\text{min}$)	24.6	26.1	26.1	TMIn ($\mu\text{mol}/\text{min}$)	23.0	24.6
TMAI ($\mu\text{mol}/\text{min}$)	30.4	30.4	30.4	TMGa ($\mu\text{mol}/\text{min}$)	105.7	105.7
TMGa ($\mu\text{mol}/\text{min}$)	73.2	73.2	70.9	Si/III ($\times 10^{-3}$)	2.4	2.4
Zn/III	0.24	0.23	0.24			
Base ($1 \times 10^{17} \text{ cm}^{-3}$)				Window ($3 \times 10^{18} \text{ cm}^{-3}$)		
T_{set} ($^{\circ}\text{C}$)	690	690	690	T_{set} ($^{\circ}\text{C}$)	720	720
T_{gr} ($^{\circ}\text{C}$)			630	T_{gr} ($^{\circ}\text{C}$)		660
V/III	10.8	10.7	10.5	V/III	26.3	26.0
TMIn ($\mu\text{mol}/\text{min}$)	23.0	24.6	26.1	TMIn ($\mu\text{mol}/\text{min}$)	23.0	24.6
TMGa ($\mu\text{mol}/\text{min}$)	105.7	105.7	105.7	TMAI ($\mu\text{mol}/\text{min}$)	79.6	79.6
Zn/III ($\times 10^{-3}$)	8.6	8.5	8.4	TMGa ($\mu\text{mol}/\text{min}$)	20.5	20.5
				Si/III ($\times 10^{-3}$)	7.3	7.2
Intrinsic layer			only for E	Contact ($> 10^{19} \text{ cm}^{-3}$)		
T_{set} ($^{\circ}\text{C}$)			690	T_{set} ($^{\circ}\text{C}$)	650	650
T_{gr} ($^{\circ}\text{C}$)			630	T_{gr} ($^{\circ}\text{C}$)		590
V/III			10.5	V/III	10.8	10.7
TMIn ($\mu\text{mol}/\text{min}$)			26.1	TMIn ($\mu\text{mol}/\text{min}$)	23.0	24.6
TMGa ($\mu\text{mol}/\text{min}$)			105.7	TMGa ($\mu\text{mol}/\text{min}$)	105.7	105.7
				Se/V ($\times 10^{-3}$)	2.3	2.3

Before growth of sample D's active layers, the InGaAs virtual substrate was annealed for 20 min at 690 $^{\circ}\text{C}$ whereas for sample C it was not. Sample E was different from sample C only by the insertion of a 210 nm intrinsic InGaAs layer between the base and the emitter. The base was made thinner by the same amount to keep the cell thickness constant. The aim of inserting this intrinsic region was to broaden the space charge region which should lead to an improved carrier separation and better performance, as was demonstrated by Dimroth et al. [10] in the case of a p-n versus p-i-n structure.

In Table 5-5 the growth details of the active layers of all samples are summarised. The real wafer surface temperature T_{gr} is determined from the EpiTT pyrometer signal. During growth it decreases because the wafer bends due to (usually) compressive stress. Since there is only one measurement position along the radius of the wafer, the value therefore is only an approximation at that position. A small temperature gradient can exist across the wafer which can affect the composition uniformity of the layers.

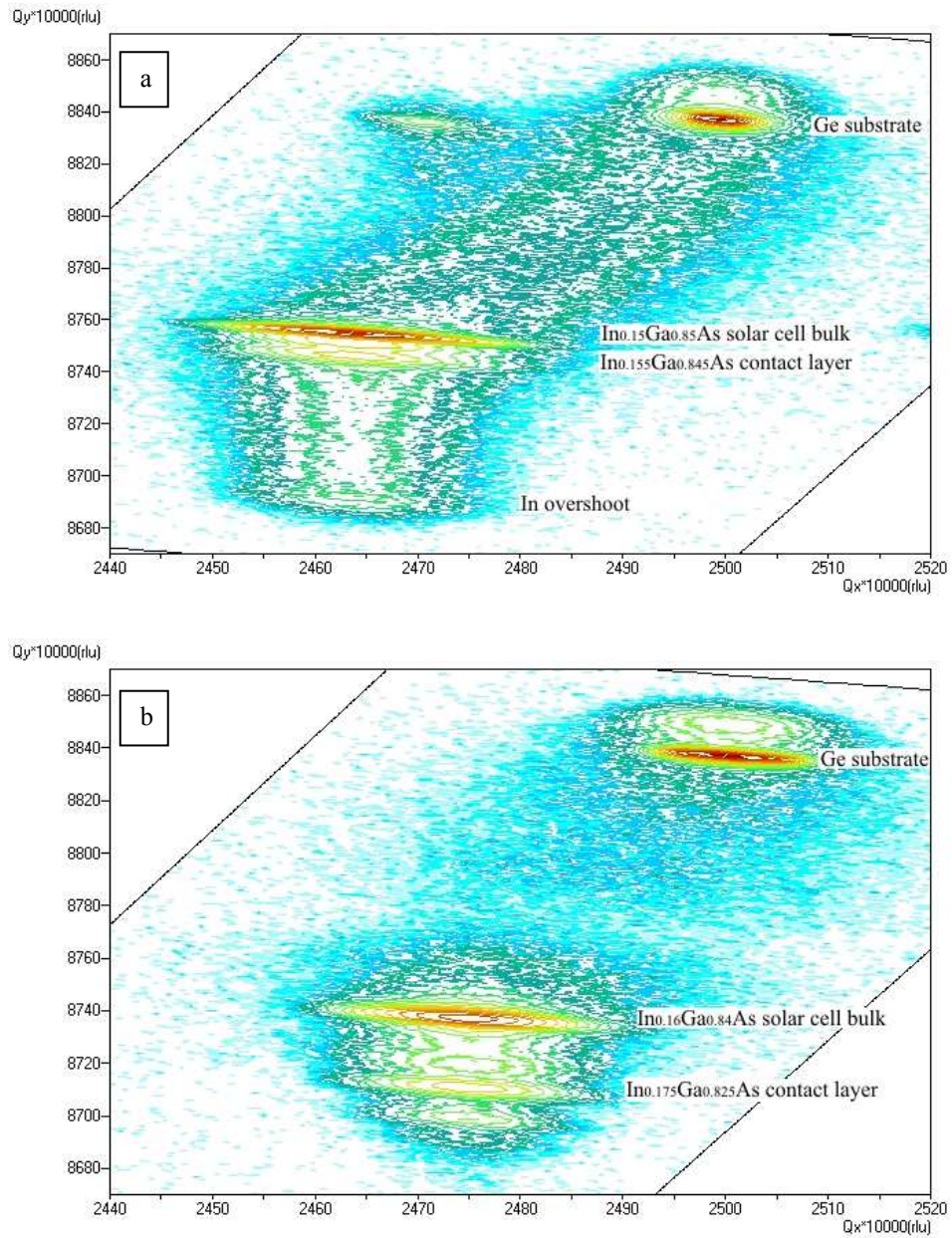


Figure 5-6: HRXRD reciprocal space map of solar cell (a) A and (b) B, with indication of measured composition and type of layer.

A reciprocal space map of sample A and B is shown in Figure 5-6a and b, respectively. For sample A, the continuous linear grade from the germanium substrate to higher indium concentrations is visible. From a certain point on, the remainder of the buffer – up to the overshoot of the In concentration and down again – is grown strained to the already grown part, as was described in §5.2.2. The peak position of the InGaAs solar cell bulk, having a 15.1 % In content, shows this is grown almost perfectly strained on top of the buffer. The peak of the contact layer is seen just below the bulk peak. Reducing the In percentage in the solar cell bulk to match the lattice constant of the buffer finish layer seems to have worked well. For sample B, the thin first couple of layers of the step graded buffer are not distinguishable but the uppermost layers are. Here also, the uppermost part of the buffer is grown strained on the bottom part. The InGaAs bulk – 16.2 % In – layer's peak position shows it is grown almost perfectly strained on the buffer structure. The contact layer peak is also indicated.

A crude attempt can be made to separate out the spread of peaks due to finite size effects and lattice tilts. This analysis was performed by PANalytical on the reciprocal space map of sample A and is based on the calculation of mosaic spread and lateral correlation length. It turns out that the spreading of the peak appears to be due to relatively large regions of crystal (microns dimensions) with slightly different tilts. This is a typical result for a relaxed buffer layer. A lateral correlation length of 2 to 30 μm is estimated and the mosaic spread is 0.07° to 0.08° , where the spread in the peak is primarily due to tilting of the diffracting planes. To estimate the dislocation density, we now assume that the lateral correlation length defines the mosaic block size and that each block contains one threading dislocation. A threading dislocation density (TDD) of 1.1×10^5 to $2.5 \times 10^7 \text{ cm}^{-2}$ is calculated for sample A. The lower range of this result agrees with the value obtained from the TEM study and indicates that the TDD in the material is most likely on the order of 10^5 - 10^6 cm^{-2} or less.

5.3.3 Radius of curvature

As mentioned in the previous paragraph, the layers are under compressive stress after growth and cooling down causing the sample to bend. Across the 4" wafer HRXRD ω -scans of the substrate peak were performed in a $6 \times 6 \text{ cm}^2$ grid. Due to the wafer curvature the ω peak position is offset. This is shown in Figure 5-7. At the wafer centre the peak position is measured at the Bragg angle ω because the crystallographic planes are parallel to the sample stage. If the stage is moved over a distance r , the lattice planes are no longer parallel to the sample stage. In the sample stage coordinate system, the peak position is now offset by an amount α , measured at an angle ω' , with $\omega = \omega' + \alpha$. By plotting $-\alpha$ as a function of sample stage displacement, the bending can be visualised (Figure 5-8). The curvature is cylinder-like, with the cylinder axis parallel to a direction 45° from the primary flat of the wafer and perpendicular to the substrate step edges. The white line in Figure 5-8 represents the direction of the step edges.

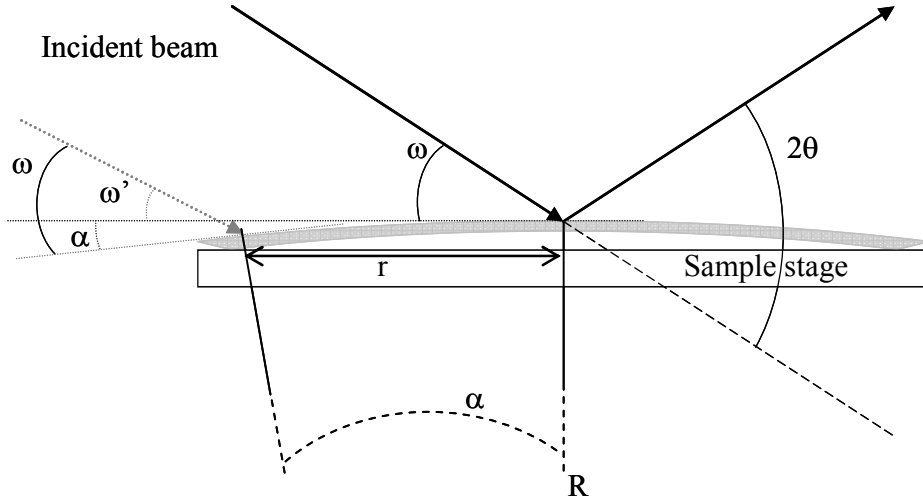


Figure 5-7: Determination of radius of curvature from HRXRD measurement.

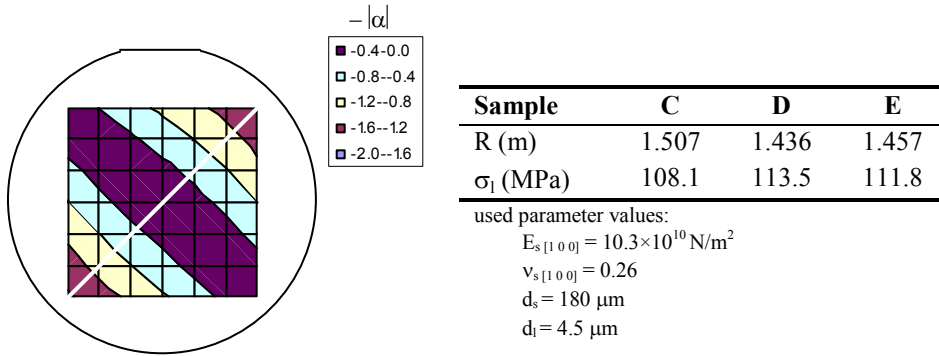


Figure 5-8: Visualisation of the wafer curvature by plotting “-|α|”. Table: radius of curvature and stress in structures C, D and E.

The distance r between wafer centre and measurement position can be approximated as follows. The angle between the surface normal in both positions is also equal to α . Their intersection defines the radius of curvature R . The displacement r can now be expressed as $r = R \cdot \tan(\alpha) \approx R \cdot \alpha$. If we now plot r as a function of α , the slope of the curve yields R . The layer stress σ_l , which causes the bending, can then be calculated from [11]:

$$\sigma_l = \frac{E_s d_s^3}{6(1-\nu_s) R d_l^2 \left(1 + \frac{d_s}{d_l}\right)}, \quad (5.6)$$

Table 5-6: Comparison of the InGaAs bandgap deduced from HRXRD and spectral response.

Sample	A	B	C	D	E
In fraction (from HRXRD)	0.151	0.162	0.160	0.172	0.161
$E_G^{\#}$ (from In fraction)	1.21 eV	1.19 eV	1.19 eV	1.18 eV	1.19 eV
E_G (from absorption edge)	1.20 eV	1.19 eV	1.18 eV	1.18 eV	1.18 eV

$$^{\#}E_G = 0.4(1-x)^2 + 0.7(1-x) + 0.324, \text{ with } x \text{ the indium fraction}$$

Table 5-7: Performance of metamorphic InGaAs solar cells under AM1.5G illumination. The cell area is denoted as “_<area in cm²>”.

Sample	A_0.25	A_4	B_4	C_4	D_4	E_4
Reflectance _{400-1000nm} (%)	9.9	9.9	11.6	3.5	3.3	3.0
$J_{sc, \text{ measured}}$ (mA/cm ²)	33.5	33.4	29.9	37.0	36.5	36.8
$J_{sc, \text{ calculated from EQE}}$ (mA/cm ²)	–	32.0	31.3	34.3	34.4	34.6
$J_{sc, \text{ calculated from IQE}}$ (mA/cm ²)	–	37.1	37.8	37.4	37.5	37.6
V_{oc} (V)	0.786	0.785	0.774	0.752	0.766	0.770
R_s , upper limit (Ω)	–	4.135	–	1.523	1.397	4.003
Fill factor (%)	63.3	46.1	26.1	61.1	61.7	45.6
Efficiency (%)	16.7	12.1	6.1	17.0	17.3	12.9

where E_s , ν_s and d_s are the substrate's Young's modulus, Poisson ratio and thickness, respectively, and d_l is the layer thickness. In the table next to Figure 5-8 values for R and σ_l are given in the case of samples C, D and E. The radius of curvature is calculated from the α -values measured along the white diagonal and lies in the range of 1.43 to 1.51 m. The stress in the layer causing the wafer bending at room temperature is around 0.11 GPa. Due to the flexible Ge substrate, no problems occur during processing.

5.3.4 In_{0.17}Ga_{0.83}As single junction cell performance

The internal quantum efficiencies of all 5 cells are very good and few differences are to be seen. The cells do not all have the same absorption edge, indicating minor differences in bandgap and, hence, In composition. These are summarised in Table 5-6 and are in good agreement with the values obtained from HRXRD reciprocal space mapping.

Even though all cells show a comparable IQE (low bias light intensity), they do not behave similarly under AM1.5G illumination (see Table 5-7 and Figure 5-10). The first cells, A and B, have a rather high average reflection due to a non-optimised ARC, causing J_{sc} to be lower than it could be. The A_4 fill factor is bad due to a high series resistance and is even worse for B_4, which seems to have an extremely high R_s . The resulting efficiencies, 12.1 and 6.1 % respectively, are low to very low. Uniformity across the 4" wafer is not outstanding because there is a noticeable size-effect that

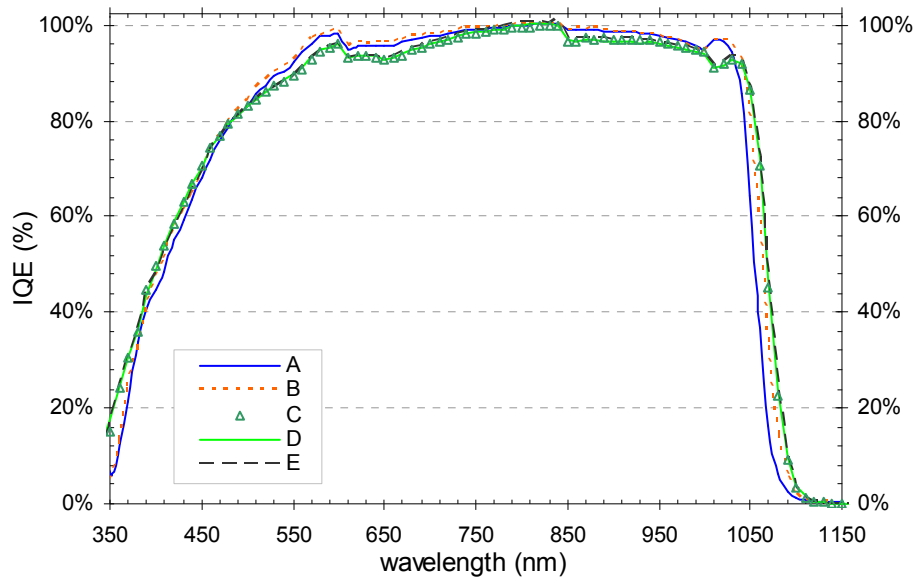


Figure 5-9: IQE derived from spectral response of metamorphic $In_{0.17}Ga_{0.83}As$ solar cells.

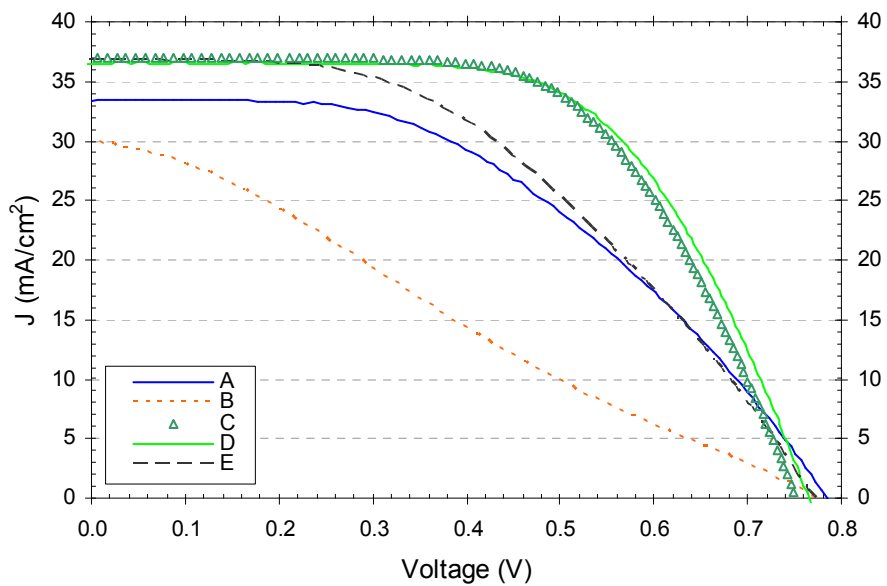


Figure 5-10: Measured I-V curves for 4 cm^2 metamorphic $InGaAs$ solar cells under the AM1.5G solar spectrum.

Table 5-8: Comparison between our cells and literature values.

Sample	Structure	% In	V_{oc} (V)	J_{sc} (mA/cm ²)	Fill factor (%)	Efficiency (%)
C_4	n-p	16.0	0.752	37.0	61.1	17.0
	p-n	20	0.697	30.1	67.7	14.2
Dimroth et al. [#]	p-i-n	17	0.785	33.8	77.8	20.6
	n-i-p	17	0.786	36.4	79.1	22.6

[#] 1 cm² cells

reduces efficiency for larger cells through a reduction in fill factor for cells A and B. An example is given for cell A (compare A_0.25 and A_4). For the best 0.25 cm² B-cell, the fill factor increase is less spectacular: FF now equals 30.8 %, resulting in an efficiency of 7.0 %. Surprisingly enough, the results for 1 cm² cells were not as good as those of the 4 cm² cells. This is most likely due to either a lack of relevant statistical data, small variations in the processing flow, the cells being processed on regions of different material quality or a combination of all of the above.

The later realised cells C, D and E had a much lower average reflection in the indicated wavelength interval. This was achieved by interpolating literature data to obtain an approximation of the index of refraction for the In_{0.16}Al_{0.67}Ga_{0.17}As window and the In_{0.16}Ga_{0.84}As emitter in order to calculate adjusted values for the ARC layer thicknesses. The cells were grown with a more uniform temperature distribution across the substrate. Improved fill factor and reduced series resistance are the immediate results for cells C and D. Here also, the same observations are made regarding the size effect of the cell as for cells A and B, although the spreading was not as large. Not enough cells are made to perform statistical analysis and draw a meaningful conclusion.

Cell E on the other hand, although having comparable J_{sc} and V_{oc} values, has a lower fill factor and a higher R_s than cell C and D. The insertion of that intrinsic region in E's layer stack does not improve the cell performance. This contradicts what was reported by Dimroth et al. [10] in the case of p-n versus p-i-n cells. Their n-i-p cells were even better than the p-i-n cells. When comparing our cells to theirs (Table 5-8), the main conclusion is that a fill factor improvement to 79 % would yield cells of comparable efficiency. Assuming the other parameters remain constant, 22.0 % conversion efficiency is possible. In this case the efficiency is comparable to the best n-i-p result.

Reducing R_s is already one solution to obtaining a higher fill factor. Also the material quality can probably be improved (recombination at interfaces and/or in the bulk). Dark current measurements reveal an ideality factor between 1.6 and 1.7.

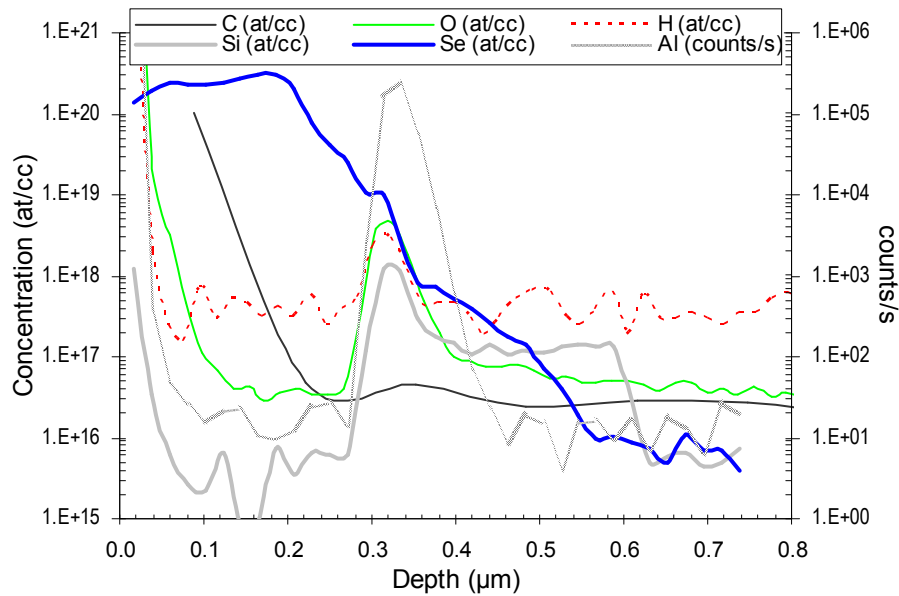
5.3.5 SIMS analysis of $\text{In}_{0.17}\text{Ga}_{0.83}\text{As}$ single junction solar cell

Sample A (Figure 5-11) and B (Figure 5-12) were analysed by SIMS (Probion Analysis). The quantification of the atomic concentrations of the different elements was done with their GaAs standards. A small error is therefore expected since our material contained a minimum indium fraction of 15 % in the bulk.

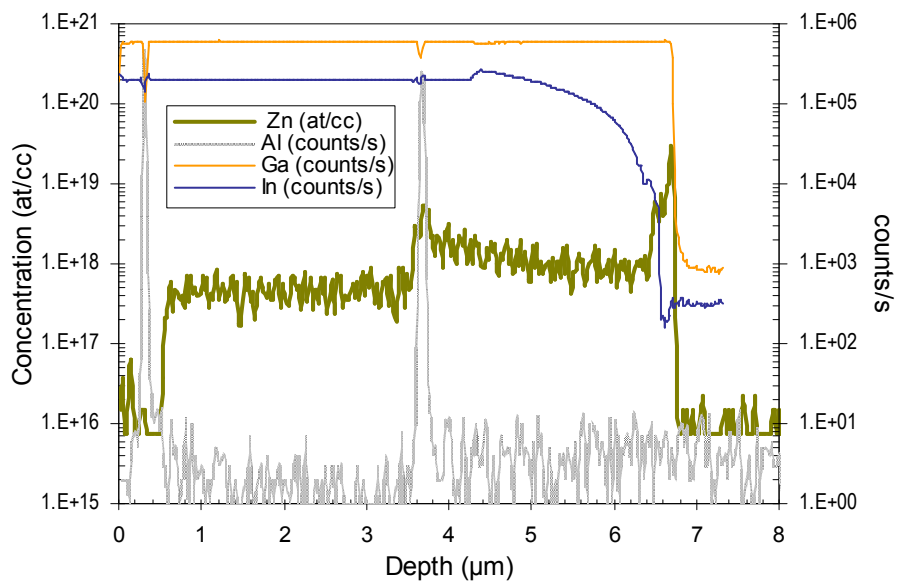
A detail of the detection of C, O, H, Si and Se is shown for both samples in the figures labelled “a”. The different layers are clearly distinguishable when comparing the SIMS measurement to the growth details of the layer structure given in §5.3.2. After the initial surface effects due to contamination of the sample, the O concentration remains constant below $6 \times 10^{16} \text{ cm}^{-3}$ (probably the detection limit) in the InGaAs bulk and only shows a spike in the Al containing window (and presumably also in the BSF). The H concentration exhibits a similar behaviour ($\sim 4 \times 10^{17} \text{ cm}^{-3}$). The C concentration is lower than $4 \times 10^{16} \text{ cm}^{-3}$ in the InGaAs bulk but has a surprisingly high value in the contact layer. This might be the result of the decrease in T_{gr} to increase the Se doping level in the contact layer.

The Se signal is constant for about two thirds of the contact layer – where T_{gr} is also constant – and then decreases. That point was the end of the temperature ramp and the lower Se signal is simply the result of a higher T_{gr} . Although the window and emitter were doped with Si only, a sizeable Se signal is detected in those layers, indicating Se diffusion took place. Most likely this happened when ramping down from the window’s high T_{gr} to the contact layer’s low T_{gr} . The window Si concentration was larger than that of the emitter although that was not intended. To grow the window layer on the emitter, the temperature is ramped up. The increasing Si signal means that more Si is incorporated into the growing layer and hence the cracking efficiency of SiH_4 has risen. This might be an indication that the growth temperature near the top of the device was lower than at the start of the active layers. A possible explanation for this is the bending of the substrate during growth which results in a lower surface temperature because contact with the susceptor is lost.

The Zn profile and that of the matrix elements Al, Ga and In for both samples is shown in the figures labelled “b”. The reader can easily distinguish the solar cell layers from the buffer layer by observing the Al signal. Zn incorporation is comparable in both samples and on the order of $4 \times 10^{17} \text{ cm}^{-3}$. No real evidence is found that the Zn concentration in the buffer changed as a result of the 20 minutes annealing step that sample B underwent. The In profile shows distinct differences. It is clearly seen that a linearly graded buffer with overshoot was used in sample A and a step graded one without overshoot in sample B.

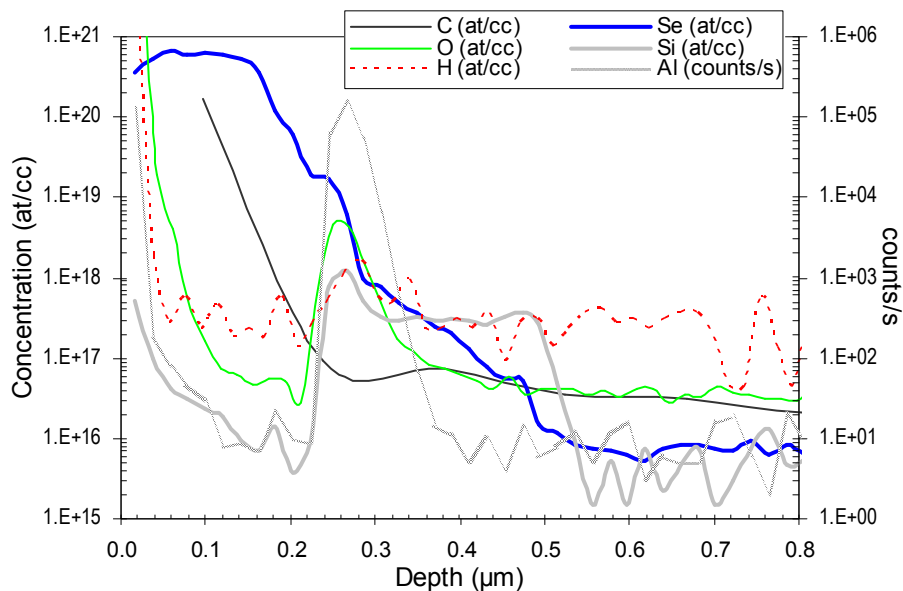


(a)

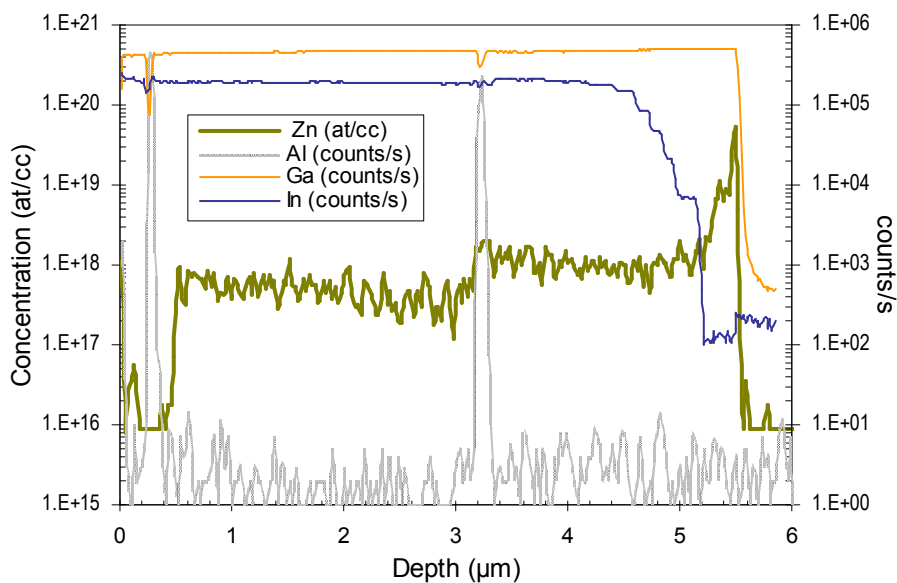


(b)

Figure 5-11: SIMS analysis of solar cell A. (a) Detail of C, O, H, Si and Se detection in contact, window, emitter and (partial) base layer. (b) Detection of Zn and matrix elements (Al, Ga, In) throughout the entire structure. The linear grade of the buffer is clearly visible, as are the position of window and BSF (see Al signal).



(a)



(b)

Figure 5-12: SIMS analysis of solar cell B. (a) Detail of C, O, H, Si and Se detection in contact layer, window, emitter and (partial) base. (b) Detection of Zn and matrix elements (Al, Ga, In) throughout the entire structure. The steps of the graded buffer are clearly visible, as are the position of window and BSF (see Al signal).

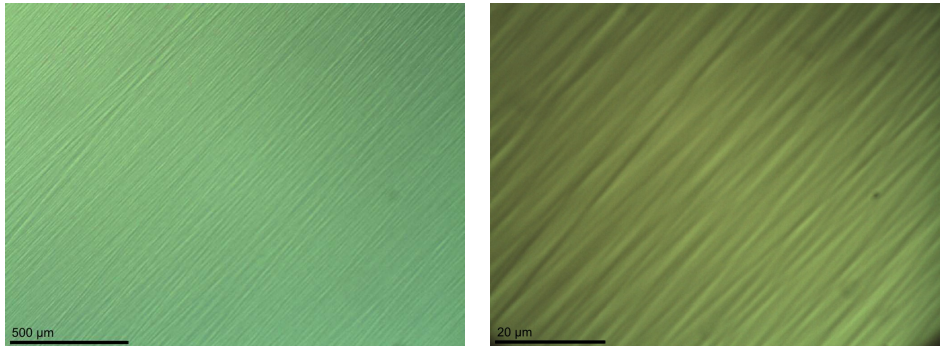


Figure 5-13: Nomarski microscopy image of metamorphic $\text{In}_{0.16}\text{Ga}_{0.84}\text{As}$ solar cell surface after growth, magnified 5 (left) and 100 (right) times.

5.3.6 Laser beam induced current measurement

Looking through a microscope, it is seen that the sample surface is not flat (Figure 5-13). The question now rises if there is increased recombination at the edges of the features on the surface. Laser beam induced current (LBIC) measurements were performed on a finished solar cell. The scanned area measured $800 \times 800 \mu\text{m}$ and the step size was $2 \mu\text{m}$. The laser wavelength was 850 nm. The first scan is performed in short-circuit conditions; the current value I_1 is recorded for each step. The second scan is performed while applying a 250 mV forward bias to the cell. When the laser illuminates a spot with a small shunt resistance, the recorded current value I_2 is lower than the short-circuit value (see figure p.40). When plotting the ratio I_1/I_2 for each set of coordinates, power losses due to shunt paths or regions with increased recombination can be visualised. This is seen in Figure 5-14. The intensity gradient from left to right in this plot is due to non-uniformity of the laser intensity during the long measurement time.

In the LBIC measurement the line pattern can be vaguely distinguished but no shunt paths are introduced due to the surface roughness. A better approach to analyse these surface features could be to perform higher resolution LBIC scans on smaller areas and on different spots on the cell.

5.3.7 Time-resolved photoluminescence

On top of an InGaAs virtual substrate a p-type double heterostructure (DH) ($\text{In}_{0.17}\text{Al}_{0.25}\text{Ga}_{0.58}\text{As} / \text{In}_{0.17}\text{Ga}_{0.83}\text{As} / \text{In}_{0.17}\text{Al}_{0.25}\text{Ga}_{0.58}\text{As}$) is grown, capped with a highly p-doped $\text{In}_{0.17}\text{Ga}_{0.83}\text{As}$ layer. The DH is Zn-doped to the level that is used in base and BSF of the solar cells to discover the minority carrier lifetime and the interface recombination velocity. $\text{In}_{0.17}\text{Ga}_{0.83}\text{As}$ layer thicknesses are 800, 400 and 200 nm and a bandgap of 1.17 eV is confirmed with RT-PL. The $\text{In}_{0.17}\text{Al}_{0.25}\text{Ga}_{0.58}\text{As}$ is 50 nm thick, the cap layer 40 nm.

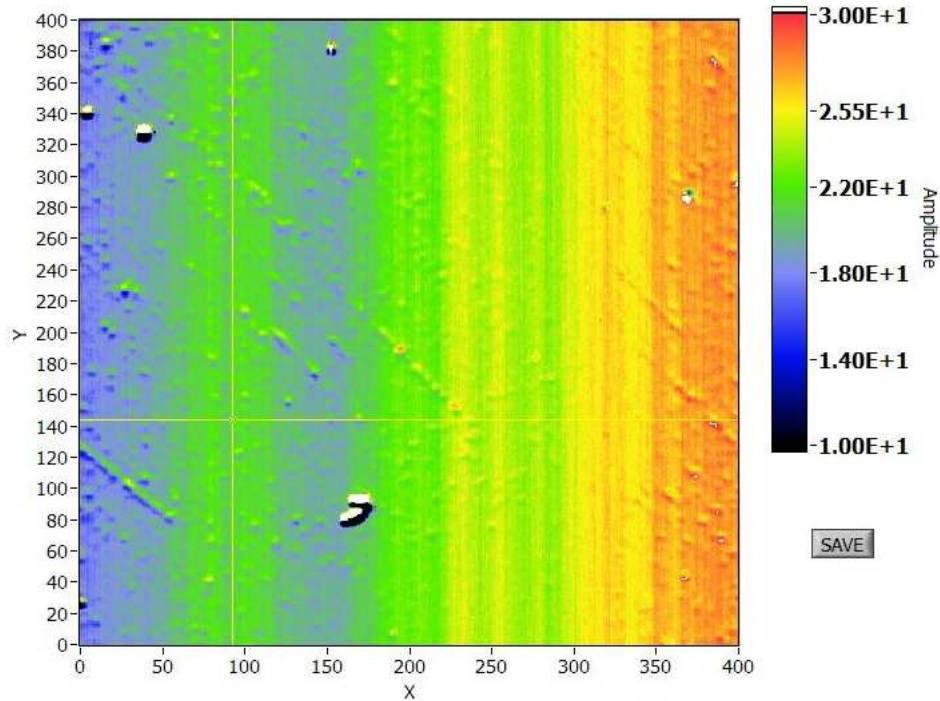


Figure 5-14: Screen capture of the processed laser beam induced current (LBIC) measurements, showing the resulting visualisation of I_1/I_2 . The gradient from left to right in this picture is due to reduced laser intensity uniformity during the long scanning period. The axis scale is the step number.

The samples were analysed by Probian Analysis. They used a Ti:Sa laser with a pulse repetition rate of 82 MHz at 720 nm. The spot size was about 50 μm and the excitation power was 1 mW. Effective carrier lifetimes of 9.7, 7.3 and 4.3 ns are deduced for a layer thickness of 800, 400 and 200 nm, respectively. Using the same method as described in §4.4.4, $\tau_{\text{eff, bulk}} = 18.1$ ns and $S = 1753$ cm/s are calculated. Assuming $D_e = 170$ cm²/s [12] we find $L_e = 17.6$ μm . In case of a 2.9 μm base layer of the solar cell, τ_{eff} would be 14.8 ns.

Yamaguchi and Amano [2] derive an expression for the minority carrier diffusion length associated with recombination at a dislocation – for GaAs grown on silicon– under the assumption that the dislocations are uniformly distributed in the layer:

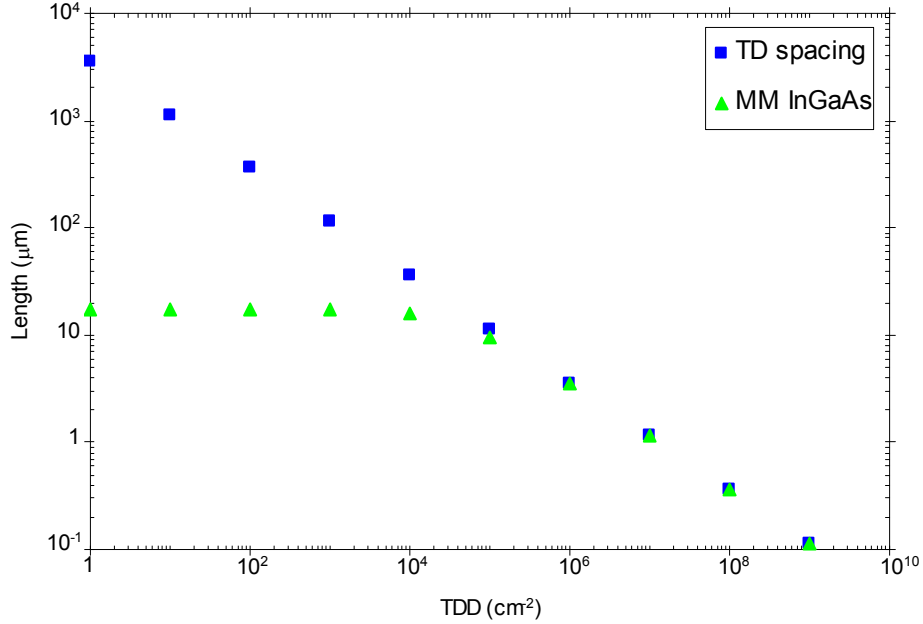


Figure 5-15: Threading dislocation spacing L_d and metamorphic (MM) InGaAs effective diffusion length L_{eff} as function of threading dislocation density (TDD) (after [2]).

$$\frac{1}{L_d^2} = \frac{\pi^3}{4} N_d, \quad (5.7)$$

where L_d is the dislocation-limited diffusion length (also considered as threading dislocation spacing) and N_d the dislocation density (in “per cm²”). This relation is plotted in Figure 5-15. The effective diffusion length L_{eff} in the layer is given by

$$\frac{1}{L_{eff}^2} = \frac{1}{L_e^2} + \frac{1}{L_d^2}, \quad (5.8)$$

with L_e the non-dislocation-limited diffusion length. L_{eff} is determined by the smaller of L_d and L_e . Eq. (5.8) is plotted in the same figure using the above calculated value for L_e (17.6 μm) and assuming in first approximation that it is not dislocation limited. However, if τ_{eff_bulk} is dislocation limited, Eq. (5.7) yields an upper limit of 7.2×10^4 cm⁻² to the threading dislocation density (TDD) in the analysed In_{0.17}Ga_{0.83}As layers. Comparison between this result and the ones from the TEM study and the HRXRD RSM analysis again confirms that the TDD is on the order of or below 10^5 - 10^6 cm⁻².

5.4 $\text{In}_{0.65}\text{Ga}_{0.35}\text{P}$ single junction solar cell

5.4.1 Material characterisation

$\text{In}_{0.65}\text{Ga}_{0.35}\text{P}$

The $\text{In}_{0.65}\text{Ga}_{0.35}\text{P}$ alloy can be grown lattice-matched to $\text{In}_{0.17}\text{Ga}_{0.83}\text{As}$. Initial composition tests were performed by recalculating the molar flows from the $\text{In}_{0.495}\text{Ga}_{0.505}\text{P}$ starting point. Immediately, HRXRD RSM analysis showed that In concentrations of around 65 % are obtained. Since an $\text{In}_{0.65}\text{Ga}_{0.35}\text{P}$ single junction will be grown on an $\text{In}_{0.17}\text{Ga}_{0.83}\text{As}$ virtual substrate (or on the $\text{In}_{0.17}\text{Ga}_{0.83}\text{As}$ solar cell to make a tandem), no calibration of the compounds with compositions lying between starting and end point was carried out. An electron diffraction pattern taken on the bulk InGaP of the metamorphic tandem cell (see §5.6) shows that the layer is not ordered.

Again, it is observed that Zn-doping causes a reduced In incorporation in the solid. For the same TMIIn/III ratio of 0.65 in the input gas phase an In fraction of 0.656 and 0.636 is measured for a DEZn/III ratio 0.0057 and 0.17 in the input gas phase, respectively, at a growth temperature of 605 °C. *C-V* measurements on these layers, grown on germanium and semi-insulating GaAs, returned carrier concentrations of $2.43 \times 10^{17} \text{ cm}^{-3}$ and $2.01 \times 10^{18} \text{ cm}^{-3}$, respectively. Doping with SiH_4 with a SiH_4/III ratio of 0.0005 resulted in a carrier concentration of $1.77 \times 10^{17} \text{ cm}^{-3}$. The $\text{In}_{0.65}\text{Ga}_{0.35}\text{P}$ doping behaviour appears to be similar to that of $\text{In}_{0.495}\text{Ga}_{0.505}\text{P}$.

$\text{In}_{0.644}\text{Al}_{0.356}\text{P}$

The $\text{In}_{0.644}\text{Al}_{0.356}\text{P}$ alloy can be grown lattice-matched to $\text{In}_{0.65}\text{Ga}_{0.35}\text{P}$. It turns out to be difficult to obtain conclusive results on the doping behaviour of this material. The assumption is made that this behaviour is also similar to that of its lattice-matched counterpart.

5.4.2 Solar cell structure and growth details

The metamorphic single junction $\text{In}_{0.65}\text{Ga}_{0.35}\text{P}$ solar cell was grown on the same $\text{In}_{0.17}\text{Ga}_{0.83}\text{As}$ virtual substrate as the single junction InGaAs solar cell C. The layer structure and the growth details of the active layers are presented in Table 5-9 and Table 5-10, respectively.

The HRXRD reciprocal space map of the grown solar cell is shown in Figure 5-16. Here also, the linearly graded buffer is seen, as well as the overshoot in indium concentration. Furthermore, the InGaP bulk peak and that of the contact layer are visible. The mosaic spread determined from this RSM is $0.06^\circ \pm 0.01^\circ$. The lateral correlation length is of the order 0.2 to 1 μm . The calculated threading dislocation density is then supposedly between $1 \times 10^8 \text{ cm}^{-2}$ and $2.5 \times 10^{11} \text{ cm}^{-2}$, which seems to be rather high.

Table 5-9: Overview of the metamorphic single junction InGaP cell structure.

Sample	A	thickness
Contact	In _{0.17} Ga _{0.83} As	300 nm
Window	In _{0.64} Al _{0.36} P	30 nm
Emitter	In _{0.65} Ga _{0.35} P	100 nm
Base	In _{0.65} Ga _{0.35} P	1.0 μm
BSF	In _{0.64} Al _{0.36} P	50 nm
Buffer	linear, In-overshoot	2.2 μm
Substrate	p-Ge	180 μm

Table 5-10: Growth details of the active layers of the metamorphic single junction In_{0.65}Ga_{0.35}P solar cell.

Sample	A	A	A
BSF ($1 \times 10^{18} \text{ cm}^{-3}$)		Emitter ($1-2 \times 10^{18} \text{ cm}^{-3}$)	Contact ($>10^{19} \text{ cm}^{-3}$)
T _{set} (°C)	655	T _{set} (°C)	655
T _{gr} (°C)		T _{gr} (°C)	
V/III	50.6	V/III	48.3
TMIn (μmol/min)	124.4	TMIn (μmol/min)	124.4
TMAI (μmol/min)	55.4	TMGa (μmol/min)	63.9
Zn/III	0.29	Si/III ($\times 10^{-3}$)	2.9
		Se/V ($\times 10^{-3}$)	1.8
Base ($1 \times 10^{17} \text{ cm}^{-3}$)		Window ($3 \times 10^{18} \text{ cm}^{-3}$)	
T _{set} (°C)	655	T _{set} (°C)	655
T _{gr} (°C)		T _{gr} (°C)	
V/III	47.0	V/III	49.3
TMIn (μmol/min)	124.4	TMIn (μmol/min)	124.4
TMGa (μmol/min)	69.4	TMAI (μmol/min)	60.0
Zn/III ($\times 10^{-3}$)	2.8	S/III ($\times 10^{-3}$)	4.8

5.4.3 Solar cell performance

The ARC for the single junction InGaP cell was calculated by approximating the refractive index of the In_{0.64}Al_{0.36}P window layer by using that of In_{0.48}Al_{0.52}P (lattice matched to Ge). For the determination of the In_{0.65}Ga_{0.35}P bulk refractive index, a layer of that material was analysed by ellipsometry. From this measurement the refractive index n and the extinction coefficient k could be derived and also the absorption coefficient α of the material.

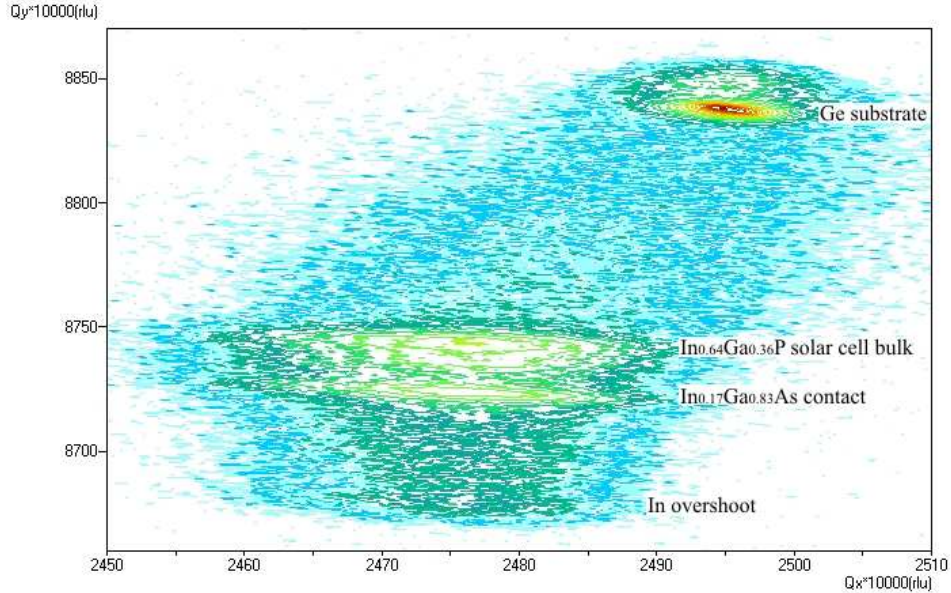


Figure 5-16: HRXRD reciprocal space map of metamorphic InGaP solar cell on linearly buffer.

Table 5-11: Performance of 4 cm² metamorphic InGaP solar cell under AM1.5G illumination.

Reflectance _{400-750nm} (%)	1.5	\approx	V _{oc} (V)	1.228
J _{sc, measured} (mA/cm ²)	15.4	\approx	R _{s, upper limit} (Ω)	1.333
J _{sc, calculated from EQE} (mA/cm ²)	18.3	\approx	Fill factor (%)	80.3
J _{sc, calculated from IQE} (mA/cm ²)	19.4	\approx	Efficiency (%)	15.2

Table 5-11 presents the characteristic parameters of a 4 cm² metamorphic In_{0.65}Ga_{0.35}P solar cell recorded under the AM1.5G solar spectrum. The I - V curve (a) under this spectrum is shown in Figure 5-17, along with the device's IQE (b). The efficiency of our first 4 cm² metamorphic InGaP solar cell is 15.2 %. Comparing the short-circuit current calculated from the cell's EQE with the measured value reveals quite some current loss. A possible explanation for this observation is enhanced recombination at the interfaces. Although a high interface recombination velocity for the rear interface is deduced from TRPL measurements (see next paragraph), the spectral response of the cell indicates that the front interface recombination is a more severe limiting factor. Nevertheless, the IQE is good for a high lattice-mismatched material. Values over 88 % and up to 100 % are obtained in the 500 to 700 nm range of the spectral response. From the absorption edge at 730 nm a bandgap energy of 1.70 eV is calculated, corresponding to 63 % indium in the alloy, which is in good agreement with the 63.5 % obtained from the HRXRD reciprocal space map. A value of 1.228 V is recorded for the V_{oc} .

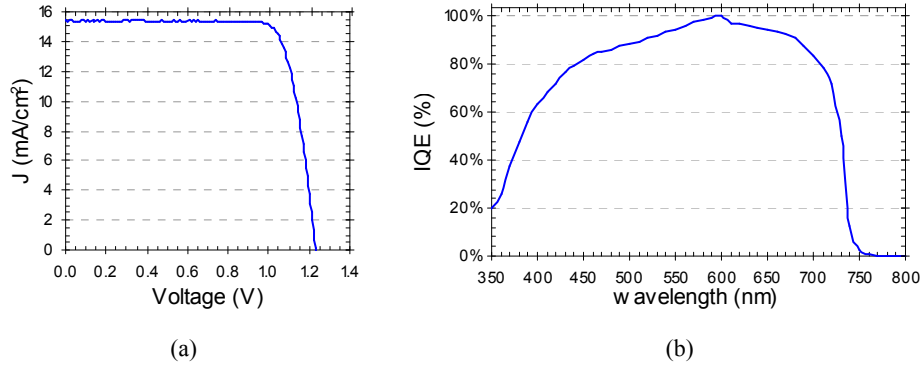


Figure 5-17: (a) I - V characteristic under AM1.5G illumination and (b) IQE of 4 cm² metamorphic InGaP single junction solar cell.

According to Eq. (3.7) the theoretical maximal fill factor calculated from this value is 89.9 %. We observe a good fill factor of 80.3 % but it is clear that a reduction in the cell's series resistance, which for this cell has a value of 1.333 Ω , will already lead to an increase of the FF. Also, improving the material quality will result in an even higher value and it will also increase V_{oc} .

5.4.4 Time-resolved photoluminescence

On top of an InGaAs virtual substrate a p-type double heterostructure (DH) ($\text{In}_{0.64}\text{Al}_{0.36}\text{P}$ / $\text{In}_{0.65}\text{Ga}_{0.35}\text{P}$ / $\text{In}_{0.64}\text{Al}_{0.36}\text{P}$) is grown, capped with a highly p-doped $\text{In}_{0.17}\text{Ga}_{0.83}\text{As}$ layer. The DH is Zn-doped to the levels that are used in the base and BSF of the solar cell to determine the minority carrier lifetime and the interface recombination velocity. $\text{In}_{0.65}\text{Ga}_{0.35}\text{P}$ layer thicknesses were 800, 400 and 200 nm and a 1.69 eV bandgap was determined with RT-PL. The $\text{In}_{0.64}\text{Al}_{0.36}\text{P}$ was 50 nm thick, the cap 40 nm.

The samples were analysed by Probian Analysis. They used a Ti:Sa laser with a pulse repetition rate of 82 MHz at 720 nm. The spot size was about 50 μm and the excitation power was 1.5 mW. They noticed an increasing lifetime with increasing excitation power, typical of recombination centres which saturate at high excitation. Effective carrier lifetimes of 0.33, 0.43 and 0.27 ns are deduced for a layer thickness of 800, 400 and 200 nm, respectively. Since "800 nm" gives a worse value than "400 nm", this data point is not used for the derivation of τ_{eff_bulk} and S . Using the same method as described in §4.4.4, $\tau_{eff_bulk} = 1.06$ ns and $S = 27562$ cm/s are calculated. Assuming $D_e = 100$ cm²/s [13] (it is probably lower for metamorphic material) we find $L_e = 3.2$ μm . Using this value for L_e and assuming that it is not dislocation limited, Eq. (5.8) is plotted in Figure 5-18. If τ_{eff_bulk} is dislocation limited, an upper limit of 1.3×10^6 cm⁻² to the threading

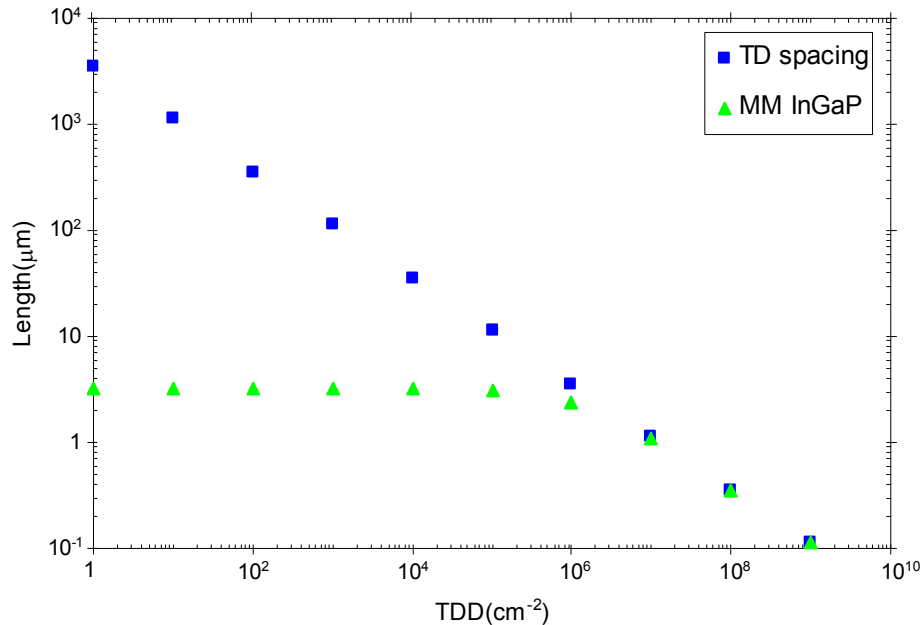


Figure 5-18: Effective diffusion length for metamorphic (MM) InGaP and threading dislocation spacing as a function of threading dislocation density (TDD).

dislocation density (TDD) in the analysed $\text{In}_{0.65}\text{Ga}_{0.35}\text{P}$ layers is deduced, two orders of magnitude lower than the crude HRXRD approximation. Since our buffer quality is good (see TEM p.126), $1.3 \times 10^6 \text{ cm}^{-2}$ is likely to be a more accurate value for the TDD.

5.5 AlGaAs tunnel junction

In literature several combinations are used to make the tunnel junction that connects the $\text{In}_x\text{Ga}_{1-x}\text{P}$ top cell with the $\text{In}_x\text{Ga}_{1-x}\text{As}$ bottom (or middle) cell. Sinharoy et al. [14] use a low bandgap $\text{In}_x\text{Ga}_{1-x}\text{As}$ tunnel junction. Patton et al. [15] use a high bandgap AlGaAs / InGaP tunnel junction. Our approach is to test whether the AlGaAs tunnel junction that was used in the dual junction lattice-matched to Ge, can be integrated strained in a metamorphic layer structure.

5.5.1 Influence of strain

Obviously, the tunnel junction will be under tensile strain when it is sandwiched between layers with a larger lattice constant. Since a tunnel diode is usually around 30 nm thick, one can wonder if the critical thickness is not surpassed. Therefore, the

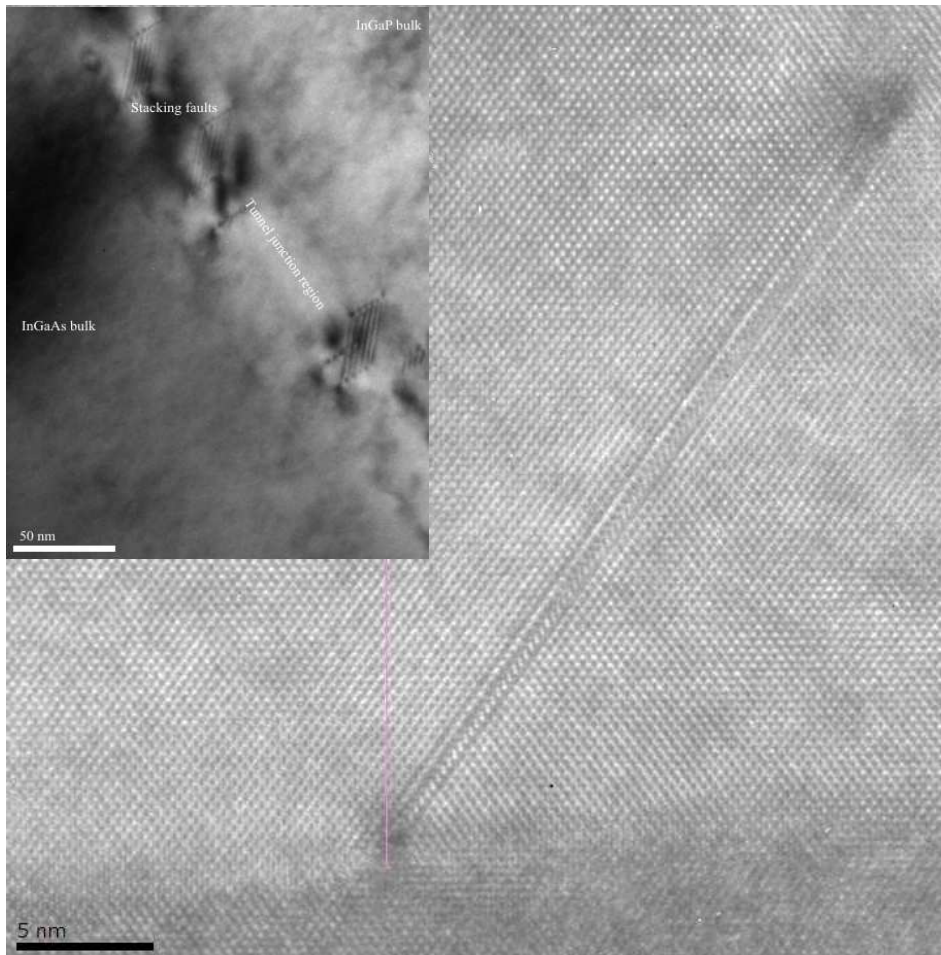


Figure 5-19: TEM image of a stacking fault in the AlGaAs tunnel junction. Inset: TEM image of a larger area of the tunnel junction region in the metamorphic dual junction solar cell showing the formation of several stacking faults in a $\{1\ 1\ 1\}$ plane due to the tensile strain in the layers.

critical thickness is calculated according to the model of Matthews and Blakeslee (M&B) on the one hand and People and Bean (P&B) on the other. For the calculation it is assumed that the tunnel junction is entirely made of $\text{Al}_{0.2}\text{Ga}_{0.8}\text{As}$ and that it is sandwiched between $\text{In}_{0.17}\text{Ga}_{0.83}\text{As}$ layers. From Eqs. (5.3) and (5.4) critical thicknesses of 18 and 79 nm are calculated, respectively. In §5.2.1 it was explained that P&B is believed to be an incorrect calculation. Therefore the M&B calculation will give a more accurate result. The sandwiched tunnel junction will most likely relax although there is a possibility that it stays in a metastable state. However, the transmission electron microscopy image of the tunnel junction region in the metamorphic dual junction solar

cell (Figure 5-19) proves that the tunnel junction region does indeed relax under the tensile strain and the formation of stacking faults in a $\{111\}$ plane is observed. Such stacking faults also influence the electrical behaviour (J_p/J_V) of the tunnel junction.

Strain is known to cause a change in the bandgap energy. This could be beneficial for the performance of the tunnel junction if the change is a reduction, since the tunnelling probability increases with decreasing bandgap. The device is under biaxial strain: the in-plane strain is tensile whereas the strain perpendicular to the surface is compressive.

A simple zeroth order approximation is to use the shift of the unstrained bandgap E_G due to hydrostatic pressure as expressed in [16]:

$$\frac{dE_G}{dP} = \frac{-3a}{c_{11} + 2c_{12}}. \quad (5.9)$$

Here a is the interband hydrostatic deformation potential energy in eV and c_{ij} are the elastic stiffness constants of the layer under stress. Filling in $a = -10.85$ eV (value for 22 % Al), $c_{11} = 1.19 \times 10^{11}$ Pa and $c_{12} = 5.44 \times 10^{10}$ Pa (c_{ij} for 20 % Al) in Eq. (5.9) yields 0.143 eV/GPa. If we now assume that the pressure on the layer can be approximated by the residual stress in the layer underneath, for example -0.108 GPa (see §5.3.3; the strain parallel and perpendicular to the layer have opposite sign), a bandgap reduction of 15.4 meV is calculated for $\text{Al}_{0.2}\text{Ga}_{0.8}\text{As}$.

From an interpolation between the pressure dependence of the GaAs and AlAs bandgaps it is possible to write for $\text{Al}_x\text{Ga}_{1-x}\text{As}$ [16]

$$\frac{dE_G}{dP} = (10.7 - 1.3x) \times 10^{-2} \frac{\text{eV}}{\text{GPa}}. \quad (5.10)$$

A bandgap reduction of 11.3 meV is now calculated for $\text{Al}_{0.2}\text{Ga}_{0.8}\text{As}$.

Another formula suggested for the $\text{Al}_x\text{Ga}_{1-x}\text{As}$ (hydrostatic) pressure dependence is [17]

$$\frac{dE_G}{dP} = (10.7 - 2.7x) \times 10^{-2} \frac{\text{eV}}{\text{GPa}}. \quad (5.11)$$

This formula leads to a bandgap reduction of -11.0 meV for $\text{Al}_{0.2}\text{Ga}_{0.8}\text{As}$. However, those authors emphasise that one has to exert caution in applying these data.

Calculations including biaxial strain were performed by Logothetidis et al. [18] for $\text{Al}_x\text{Ga}_{1-x}\text{As}$ layers on (001) GaAs substrates. In the absence of strain, the spin-orbit interaction splits the sixfold degenerate multiplet with orbital symmetry Γ_{15} into a fourfold $P_{3/2}$ multiplet and a twofold $P_{1/2}$ multiplet. Transitions from the $P_{3/2}$ multiplet (these bands are labelled $v1$ and $v2$) to the conduction band correspond to the direct bandgap E_G in the absence of strain. When the material is under strain, the degeneracy

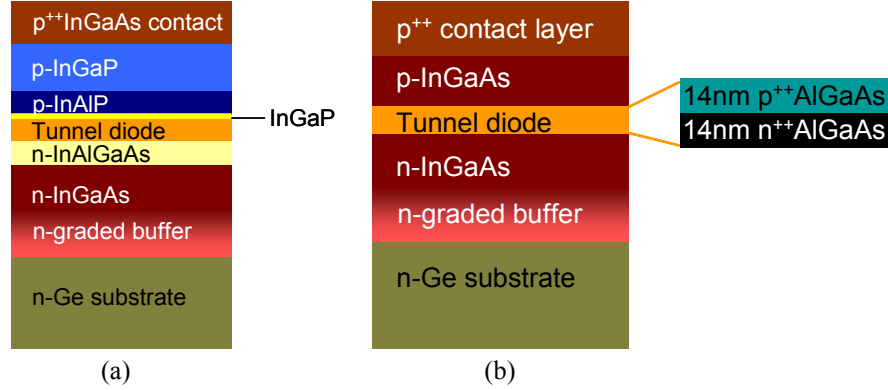


Figure 5-20: Schematic representation of AlGaAs tunnel junction between metamorphic layers (a) with and (b) without simulation of (partial) solar cell stack.

of the v_1 and v_2 bands is lifted and the $P_{3/2}$ multiplet splits into two twofold levels. The bandgap change is given by

$$\Delta E_G^{v_1} = \left(-2a \frac{c_{11} - c_{12}}{c_{11}} + b \frac{c_{11} + 2c_{12}}{c_{11}} \right) \cdot f, \quad (5.12)$$

with a and b the hydrostatic and shear deformation potentials, respectively, and f the lattice-mismatch given by Eq. (5.1). For $\text{Al}_{0.2}\text{Ga}_{0.8}\text{As}$, a and b are calculated to be -7.24 and -1.86 eV, respectively. The lattice-mismatch between $\text{In}_{0.17}\text{Ga}_{0.83}\text{As}$ and $\text{Al}_{0.2}\text{Ga}_{0.8}\text{As}$ is given by $f = -0.0117$. Substituting these values in Eq. (5.12) yields a (more accurate) bandgap reduction of 50.5 meV when biaxial stress is taken into account. Considering the tunnel junction layers' partial strain relaxation by stacking fault formation, the real bandgap reduction value will probably be smaller.

5.5.2 Tunnel junction analysis

The same approach as for the lattice-matched test structures was followed here. The tunnel junction layers (14 nm $p^{++} 2 \times 10^{19} \text{ cm}^{-3}$ and 14 nm $n^{++} 2 \times 10^{18} \text{ cm}^{-3}$) were grown on the top part of the metamorphic bottom cell: 30 nm $\text{Si:In}_{0.17}\text{Al}_{0.66}\text{Ga}_{0.17}\text{As}$ ($2 \times 10^{18} \text{ cm}^{-3}$) on $\text{Si:In}_{0.17}\text{Ga}_{0.83}\text{As}$ ($2 \times 10^{18} \text{ cm}^{-3}$). Then a thin metamorphic Zn:InGaP interlayer was deposited before growth of the bottom part of the metamorphic top cell: 50 nm $\text{Zn:In}_{0.65}\text{Al}_{0.35}\text{P}$ ($1 \times 10^{18} \text{ cm}^{-3}$) underneath 250 nm $\text{Zn:In}_{0.65}\text{Ga}_{0.35}\text{P}$ ($1 \times 10^{17} \text{ cm}^{-3}$). Finally, a contact layer was added to the structure. This is shown schematically in Figure 5-20a.

The (forward swept) J - V curve for a tunnel junction having a Au/TiW front contact is shown in Figure 5-21. Strange behaviour is observed. There is no resistance-like profile around zero bias. Instead, diode-like behaviour is observed for both negative and positive voltage (see inset), probably indicating the existence of a Schottky barrier in the

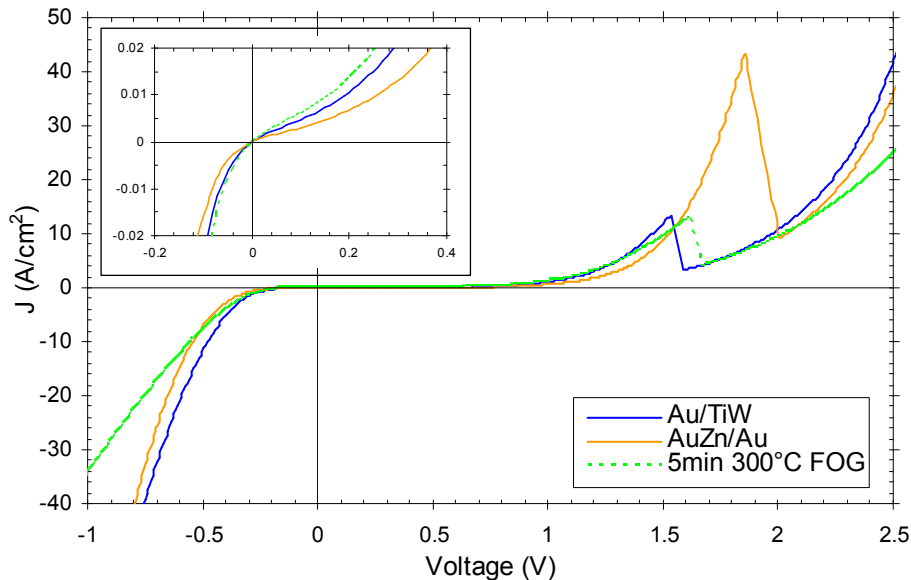


Figure 5-21: *J-V* curves for an AlGaAs tunnel junction with Au/TiW and AuZn/Au front contact and for the sample with Au/TiW contact that was annealed at 300 °C for 5 minutes. Inset: Magnification of the curve in the -0.2 to 0.4 V range with *J* still in A/cm².

structure. Nevertheless, tunnelling occurs, albeit at large positive voltage with a peak of 13.5 A/cm² at 1.533 V. The peak-to-valley ratio is now only 4.2 whereas it was more than double in the lattice-matched case. This is probably caused by a combination of stacking faults in and threading dislocations (not blocked by the graded buffer on Ge) penetrating the active layers.

Next, the sample was annealed in forming gas at 300 °C for 5 minutes because it was believed that passivated dopants in the contact layer were partially responsible for the occurrence of the barrier(s) (Schottky contact?). As can be seen from the figure, the only effect was an increase of the series resistance of the device. The problem must lie elsewhere in the structure. A second processing was done whereby a AuZn/Au contact was applied. Unfortunately, the barrier problem was not solved. However, a higher peak current was obtained, 43.5 A/cm² at 1.855 V, although it is not really clear why changing the contact metal would influence the peak current.

Figure 5-21's inset is a magnification of the -0.2 to 0.4 V region. Here it is seen that a metamorphic dual junction solar cell, made with this tunnel junction, for a current of 17 mA/cm² would have a voltage drop of around 0.27 V if a Au/TiW contact is used and around 0.34 V if a AuZn/Au contact is used. Obviously, these values are unacceptable for a high performance device.

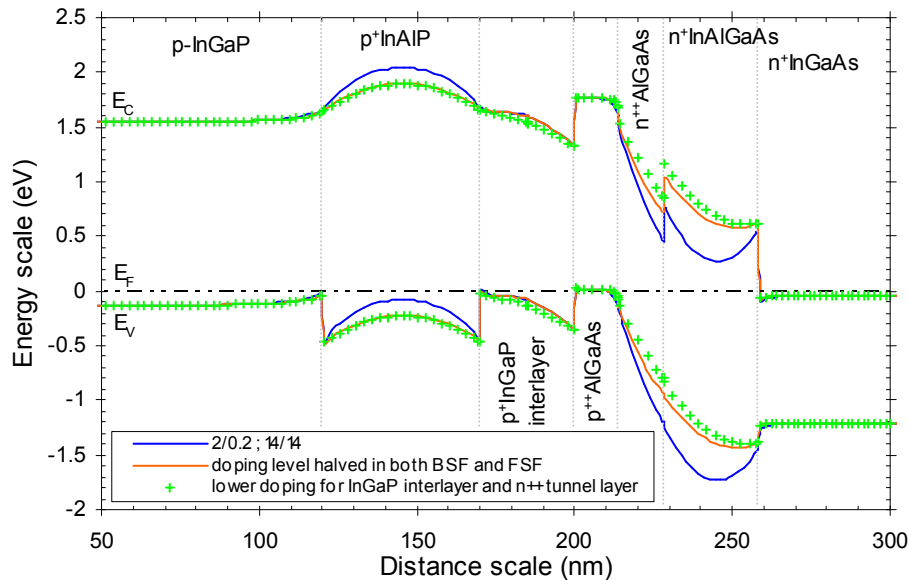


Figure 5-22: Energy diagram simulation of p^+/n^{++} AlGaAs tunnel junction in metamorphic material. The dark (blue) solid curve is the simulation for the grown device with “doping level ($\times 10^{19} \text{ cm}^{-3}$); layer thickness (nm)” combination as indicated in the figure. The light (orange) solid curve illustrates the influence of lower doping levels in “BSF” and “window”. The “+”-curve has reduced doping level in the n^{++} layer and the InGaP interlayer.

The energy band diagram simulation is plotted in Figure 5-22 for the grown tunnel junction (dark/blue curve) and for hypothetical cases where the doping level in certain layers is reduced. Here, again, there is the matter of the actual doping level of the n^{++} AlGaAs tunnel junction layer (see §4.5.2). It is seen in the simulation of the grown device that the conduction band bending in the n^+ InAlGaAs layer is insufficient to allow for tunnelling of electrons from the n^+ InGaAs into this “well”. On the p-side, the valence band bending of the p^+ InAlP is barely high enough. A hypothetical structure is simulated to investigate the influence of doping level in those layers (light (orange) curve). It is observed that a lower doping level has a detrimental effect on the “well depth” and, hence, on the transmission of carriers through those layers. We therefore propose that the barrier-like behaviour arises from insufficiently doped InAlGaAs and/or InAlP layers. Another simulation with reduced doping levels in InGaP interlayer and n^{++} AlGaAs tunnel junction layer illustrates an increase in barrier width for the holes going from interlayer to tunnel junction.

Table 5-12: Characteristic parameters of an AlGaAs tunnel junction in metamorphic material and of devices reported in literature.

Group	dopant		J_p (A/cm ²)	V_p (V)	J_p/J_v	R_{sp} (m Ω .cm ²)	V_v (V)	
	p	n						
Imec	Au/TiW		13.5	1.533	4.2	–	1.586	
	annealed		C	Se	13.0	1.613	3.2	1.662
	AuZn/Au		43.5	1.855	4.8	–	2.003	
†Motorola Labs. [19]			17500	0.575	9.2	–	0.760	
In _{0.53} Ga _{0.47} As/In _{0.52} Al _{0.48} As (on GaAs)								
†Ohio State Univ. [20]			C	Si	5900	0.31	0.05	
In _{0.69} Ga _{0.31} As (on InP)								

† MBE grown

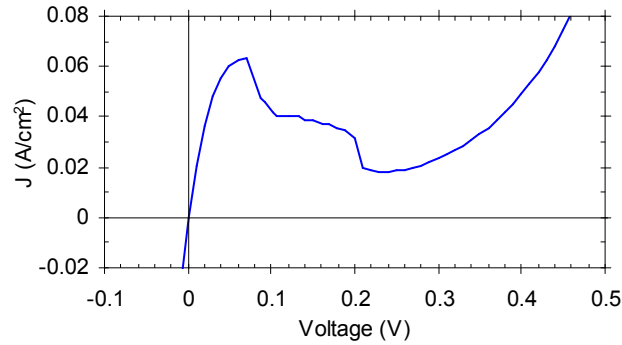


Figure 5-23: J - V curve of an AlGaAs tunnel junction between In_{0.17}Ga_{0.83}As layers.

Our measurement results are presented in Table 5-12, together with some results from literature. These values can not be compared to one another due to the large difference in bandgaps of around 1 eV between the tunnel junction materials. Higher peak current for lower bandgap material is consistent with the bandgap dependence of the tunnelling current. The J - V curves from those two groups do not show the existence of barrier-like behaviour but instead have a nice resistance-like profile around zero voltage bias, continuing up to the peak voltage, the latter occurring at considerably lower values.

To investigate the origin of the strange behaviour of our device, several structures were grown. A first test structure was simply to grow the AlGaAs tunnel diode embedded in metamorphic InGaAs layers (see Figure 5-20b), a structure similar to the first test we did in the lattice-matched case. The band diagram is much like that of the lattice-matched structure (see Figure 4-39, p.102). The J - V measurement is presented in Figure 5-23. The device has a J_p of only 63 mA/cm² at 0.07 V. The valley is at 0.24 V, J_p/J_v

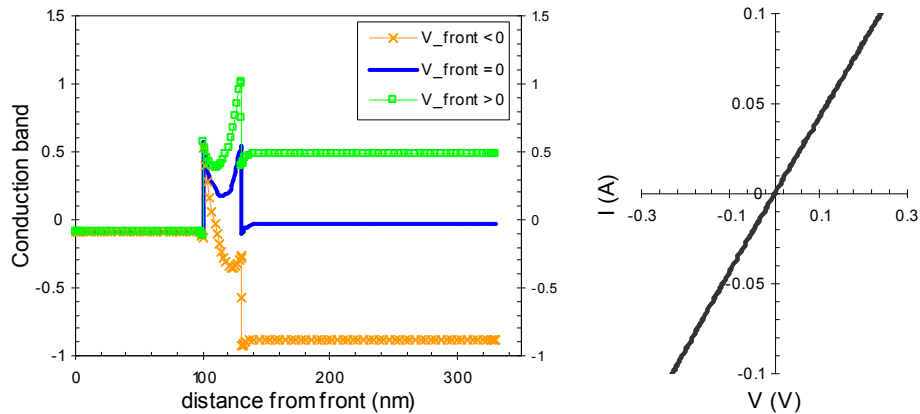


Figure 5-24: Results for transmission through $\text{In}_{0.17}\text{Al}_{0.66}\text{Ga}_{0.17}\text{As} / \text{In}_{0.17}\text{Ga}_{0.83}\text{As}$ interface. Left: Change of conduction band position as a function of applied bias for a circuit resistance of 10Ω (arbitrary value). Right: Measured I - V curve.

equals 3.4 and R_{sp} is $1.1 \Omega \cdot \text{cm}^2$. The peak current is very low and also R_{sp} is at least a factor 100 higher than in the lattice-matched case. However, it is believed that the tunnel junction (the stacking faults in it) is not the main cause for the barrier-like behaviour.

A second structure was grown to test the transmission through the interface between $\text{In}_{0.17}\text{Al}_{0.66}\text{Ga}_{0.17}\text{As}$ and $\text{In}_{0.17}\text{Ga}_{0.83}\text{As}$. This is the bottom part of the structure in Figure 5-20a, but where an n-type contact layer is directly deposited on the InAlGaAs layer. Since in an all-n-type device the current is carried by electrons in the conduction band (CB), only the change of CB position is shown in Figure 5-24 (left) for a sweep of the bias voltage. No problems are expected and this is confirmed in the I - V curve in the figure on the right: the structure behaves as a resistor.

The last structure grown, tested the interface between the p^{++} AlGaAs and the metamorphic InGaP interlayer. On a p-type Ge substrate a p-type InGaAs buffer was deposited. On top of this buffer a 10^{17} cm^{-3} InGaAs layer was grown. Then the p^{++} AlGaAs was deposited, followed by the metamorphic InGaP interlayer (high 10^{17} cm^{-3}). Finally a lower doped InGaP layer (10^{17} cm^{-3}) was grown which was capped by the contact layer (10^{19} cm^{-3}). In this case, the current is governed by hole transport in the valence band (VB). Only a change in VB position is therefore shown in Figure 5-25 (left). There is a high and wide barrier for holes between the contact layer and the InGaP that might cause problems concerning current blocking. This is exactly what is seen in the I - V curve (right figure). For negative applied voltages, current is able to pass through the structure. Holes coming from the InGaAs-side of the structure can tunnel through

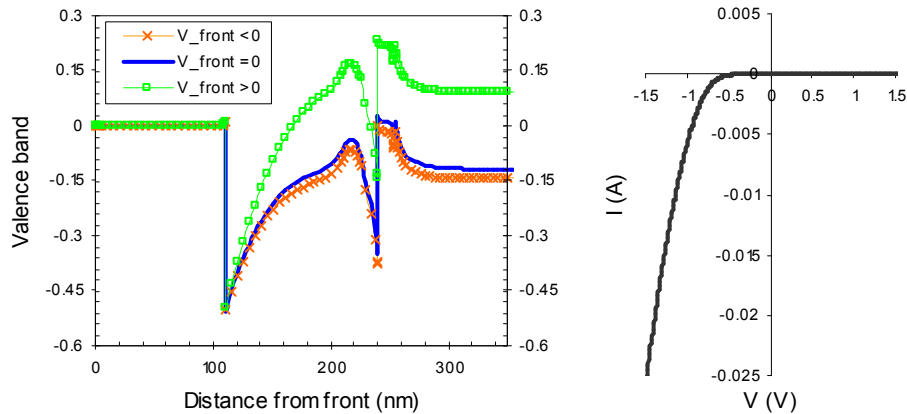


Figure 5-25: Results for transmission through InGaP interlayer / p^{++} AlGaAs interface. Left: Change of valence band position as a function of applied bias for a circuit resistance of 10Ω (arbitrary value). Right: Measured I-V curve.

the barrier between p^{++} AlGaAs and InGaP once the well starts to fill. The holes then arrive already at the half height of the barrier separating them from the contact layer. Because the width of the barrier is still large at that position, it is suspected that the holes surpass it due to some kind of thermionic emission, giving rise to the measured current at negative voltages. For positive voltages, the holes come from the contact-side of the structure. The barrier is just too high and too broad for the holes to end up at the other side of it and so the current is blocked, as is also seen in the measurement.

From these three experiments we believe we can conclude that neither the tunnel junction nor the two interfaces under test are the causing the problems in the full tunnel junction structure. To definitively exclude the interface from the third test structure, this structure should be regrown with a higher doped InGaP (10^{18} cm^{-3}) layer under the contact layer. This will significantly decrease the barrier width at that interface. Furthermore, other test structure should be made that test the interface between the InGaP interlayer and the InAlP and the interface between the InAlP and the InGaP bulk.

5.6 $\text{In}_{0.65}\text{Ga}_{0.35}\text{P}/\text{In}_{0.17}\text{Ga}_{0.83}\text{As}$ tandem solar cell

Despite the strained AlGaAs tunnel junction's unusual behaviour, a metamorphic dual junction solar cell was grown. The growth details are presented in Table 5-13. A small error was discovered in the growth recipe: the TMAI molar flux in the n^{++} AlGaAs layer was too high compared to the stand-alone devices, giving rise to 40 % Al in the n^{++} layer

Table 5-13: Metamorphic $In_{0.65}Ga_{0.35}P/In_{0.17}Ga_{0.83}As$ tandem solar cell growth details.

<i>Start layer structure</i>				<i>Layer structure continued</i>			
$In_{0.17}Ga_{0.83}As$ bottom cell				$In_{0.65}Ga_{0.35}P$ top cell			
BSF ($1 \times 10^{18} \text{ cm}^{-3}$)				BSF ($1 \times 10^{18} \text{ cm}^{-3}$)			
T_{gr} ($^{\circ}C$)				T_{gr} ($^{\circ}C$)			
V/III		25.1		V/III		50.6	
TMIn ($\mu\text{mol}/\text{min}$)		27.6		TMIn ($\mu\text{mol}/\text{min}$)		124.4	
TMAI ($\mu\text{mol}/\text{min}$)		30.4		TMAI ($\mu\text{mol}/\text{min}$)		55.4	
TMGa ($\mu\text{mol}/\text{min}$)		70.9		Zn/III		0.29	
Zn/III		0.23					
Base ($1 \times 10^{17} \text{ cm}^{-3}$)				Base ($1 \times 10^{17} \text{ cm}^{-3}$)			
T_{gr} ($^{\circ}C$)				T_{gr} ($^{\circ}C$)			
V/III		10.5		V/III		47.0	
TMIn ($\mu\text{mol}/\text{min}$)		26.1		TMIn ($\mu\text{mol}/\text{min}$)		124.4	
TMGa ($\mu\text{mol}/\text{min}$)		105.7		TMGa ($\mu\text{mol}/\text{min}$)		69.4	
Zn/III ($\times 10^{-3}$)		8.4		Zn/III ($\times 10^{-3}$)		2.8	
Emitter ($1-2 \times 10^{18} \text{ cm}^{-3}$)				Emitter ($1-2 \times 10^{18} \text{ cm}^{-3}$)			
T_{gr} ($^{\circ}C$)				T_{gr} ($^{\circ}C$)			
V/III		10.5		V/III		48.3	
TMIn ($\mu\text{mol}/\text{min}$)		26.1		TMIn ($\mu\text{mol}/\text{min}$)		124.4	
TMGa ($\mu\text{mol}/\text{min}$)		105.7		TMGa ($\mu\text{mol}/\text{min}$)		63.9	
Si/III ($\times 10^{-3}$)		2.4		Si/III ($\times 10^{-3}$)		4.7	
Window ($3 \times 10^{18} \text{ cm}^{-3}$)				Window ($3 \times 10^{18} \text{ cm}^{-3}$)			
T_{gr} ($^{\circ}C$)				T_{gr} ($^{\circ}C$)			
V/III		25.8		V/III		49.3	
TMIn ($\mu\text{mol}/\text{min}$)		26.1		TMIn ($\mu\text{mol}/\text{min}$)		124.4	
TMAI ($\mu\text{mol}/\text{min}$)		79.6		TMAI ($\mu\text{mol}/\text{min}$)		60.0	
TMGa ($\mu\text{mol}/\text{min}$)		19.8		S/V ($\times 10^{-4}$)		1.0	
Si/III ($\times 10^{-3}$)		7.1					
AlGaAs tunnel junction							
Layer	n^{++}	p^{++}		Contact ($>10^{19} \text{ cm}^{-3}$)			
T_{gr} ($^{\circ}C$)				T_{gr} ($^{\circ}C$)			
V/III	12.6	7.6		V/III		10.4	
TMAI ($\mu\text{mol}/\text{min}$)	44.0	41.9		TMIn ($\mu\text{mol}/\text{min}$)		27.6	
TMGa ($\mu\text{mol}/\text{min}$)	66.1	59.4		TMGa ($\mu\text{mol}/\text{min}$)		105.7	
Se/V ($\times 10^{-4}$)	6.4	-		Se/V ($\times 10^{-3}$)		1.8	

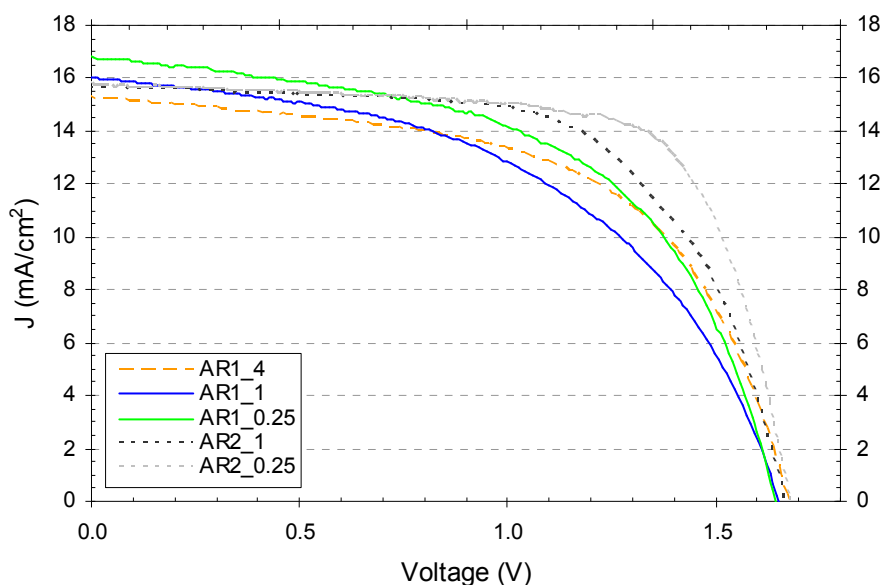


Figure 5-26: Metamorphic dual junction solar cell J-V curves under AM1.5G illumination. Cell area is denoted as “<_area in cm²>”. Two ARCs were used: AR1 refers to MgF₂/ZnS and AR2 to Si₃N₄.

Table 5-14: Metamorphic InGaP/InGaAs tandem solar cell characteristic parameters.

Sample	AR1_4	AR1_1	AR2_1	AR1_0.25	AR2_0.25
Reflectance _{400-1000nm} (%)	1.5		7.4		
J _{sc, measured} (mA/cm ²)	15.2	16.0	15.7	16.8	15.8
J _{sc, calculated from EQE} (mA/cm ²)	12.5	–	13.2	–	–
J _{sc, calculated from IQE} (mA/cm ²)	13.1	–	14.1	–	–
V _{oc} (V)	1.675	1.653	1.666	1.645	1.680
R _{s, upper limit} (Ω)		–	–	–	–
Fill factor (%)	57.1	49.8	63.1	54.7	70.1
Efficiency (%)	14.6	13.2	16.5	15.1	18.6

instead of 20 %. This, however, did not significantly change the band line-up (see dark (blue) curve in Figure 5-22), although it may have a small impact on the peak current.

All parameters are summarised in Table 5-14 for cells of 4, 1 and 0.25 cm². Two different ARCs were used. First a single layer Si₃N₄ coating (AR2) was deposited on two cells because the deposition tool for the MgF₂/ZnS double layer coating (AR1) was temporarily unavailable. Later, the standard double layer coating was deposited on the remaining cells. As can be seen from the table, the reflection is higher for the single

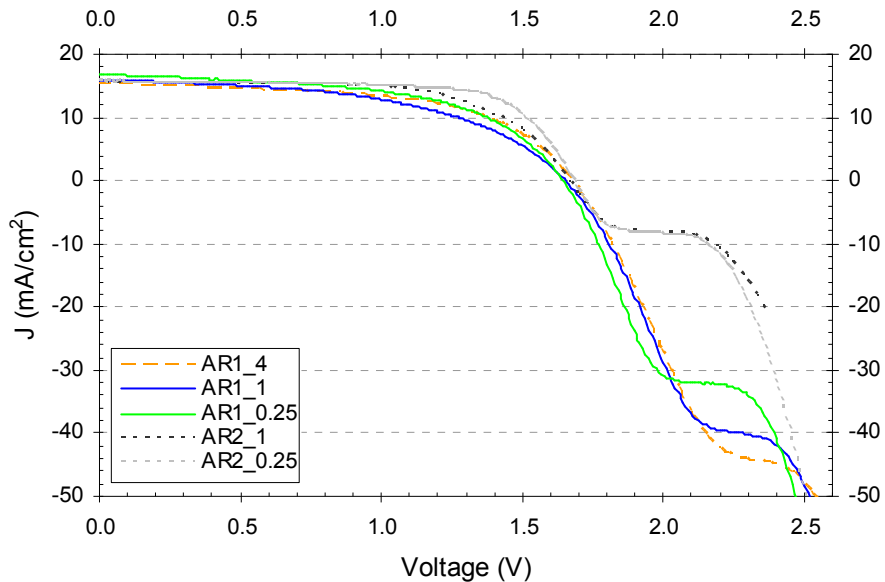


Figure 5-27: Effect of the tunnel diode beyond V_{oc} on the characteristic of a metamorphic dual junction solar cell.

layer coating, resulting in a lower short-circuit current for the same cell size. However, it is clear from the J - V curves in Figure 5-26 (AM1.5G) that applying a Si_3N_4 coating appears to have a positive effect on cell performance due to a higher fill factor. Most likely, hydrogen from the Si_3N_4 layer diffused into the top cell where it passivated defects, thus reducing the number of shunt paths and the series resistance in the cell. In the future, looking into a double-layer ARC with Si_3N_4 may be interesting.

The cells have V_{oc} of around 1.664 V only. This is too low for a tandem cell consisting of single junction cells that have a V_{oc} of 1.22 and 0.76 V for InGaP and InGaAs cell, respectively. When put in series, a V_{oc} of around 1.98 V should be obtained. Obviously, as might have been expected, a (large) voltage drop exists over the tunnel junction due to its non-ideal behaviour. When inspecting the J - V curves beyond the open-circuit value, the effect of the tunnel junction can be observed (Figure 5-27). Looking back to the inset of Figure 5-21, the transition from negative current to the value of the short-circuit current for the tunnel junction by itself is not as abrupt as when it is incorporated into a tandem cell. Really puzzling is the fact that the voltage hop occurs around non-zero current. As mentioned before, there is more Al in the n^{++} layer of the tunnel diode which undoubtedly affects its peak current but it is reasonable to expect a similar behaviour. It is therefore not understood why the voltage offset does not occur gradually around $J = 0$.

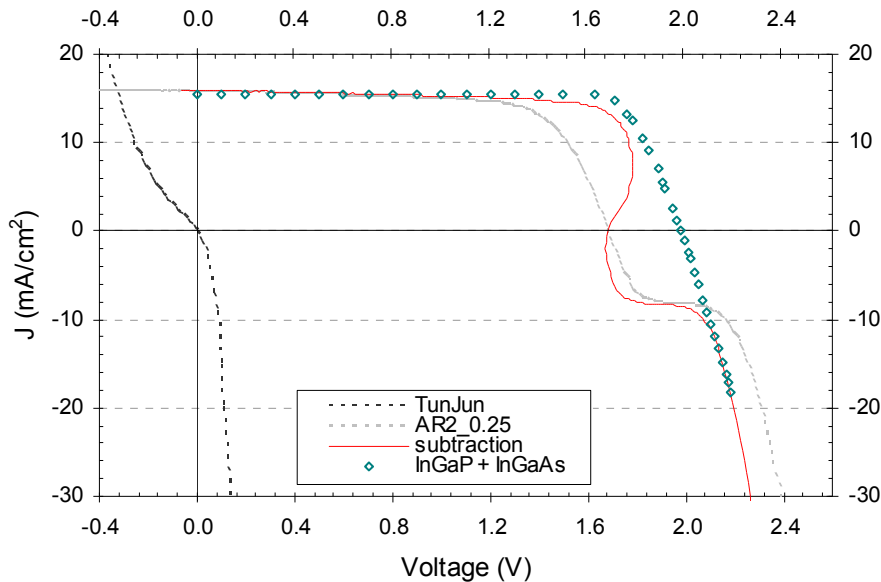


Figure 5-28: Comparison between the J - V curves of the subtraction (solid, red) of the tunnel junction influence from the tandem cell characteristic and the sum (diamond) of the two composing subcells' characteristics.

Here also, there is another effect clearly noticeable due to using a Si_3N_4 coating: the transition from “tunnel junction in forward bias operation” to “tunnel junction in reverse bias operation” when sweeping up the voltage during measurement of an illuminated solar cell's J - V characteristic, occurs at much lower currents. This, too, is probably related to hydrogen passivation of defects during deposition of the ARC.

An attempt is made to filter out the influence of the tunnel junction by subtracting the voltage loss over the device from the voltage over the entire tandem cell. This procedure is shown in Figure 5-28 for cell AR2_0.25. When the solar cell J - V curve is displayed according to the photovoltaic convention, the tunnel junction J - V curve (TunJun) is mirrored around the J -axis due to the inverse polarity of the layers in the stack. The subtraction results in the solid (red) curve. Such behaviour is not possible. This phenomenon is caused by the sudden voltage jump in the J - V curve whereas the transition in the tunnel junction characteristic is more gradual. A better result is found (diamond curve) by simply adding the curves of the two metamorphic single junction cells. Presumably, external factors dictate an almost constant voltage offset and also trigger this abrupt voltage jump.

5.7 Summary and conclusions

To accommodate the large lattice-mismatch between the germanium substrate and the metamorphic layers, step and linearly graded InGaAs buffers were investigated. It was concluded that the best material quality (without annealing) is obtained on thick buffers ($\sim 2 \mu\text{m}$) and linear ones are slightly better than step graded ones. Annealing the buffer at high temperature even further improves the material quality due to more interaction between dislocations, inducing a higher degree of relaxation. As evidenced from TEM images, the grown buffer layers are effective in bending the dislocations, thus preventing them from threading into the device layers that can be deposited on top of the buffers. An estimate for the threading dislocation density in such layers is 10^6 cm^{-2} or below.

It is seen for cell B (Figure 5-10) which has a step graded buffer, that the annealing treatment gives rise to an increase in the cell's series resistance and thus reduces its performance. However, in the case of a linearly graded buffer, cell D, no such behaviour is observed. It is not sure if there is a link between buffer type and electrical properties upon annealing.

A linear grade was chosen for the growth of the metamorphic $\text{In}_{0.17}\text{Ga}_{0.83}\text{As}$ and $\text{In}_{0.65}\text{Ga}_{0.35}\text{P}$ single junction solar cells. The best efficiency obtained for 4 cm^2 cells on an unannealed buffer is 17.0 and 15.2 %, respectively.

Using the lattice-matched AlGaAs tunnel junction in the metamorphic stack produced an extra barrier in the structure, which manifested itself in the J - V curve as a large voltage offset. The exact origin of this phenomenon remains to be determined. TEM analysis showed that the tunnel junction layers are (partially?) relaxed under the strain by forming stacking faults. Still, a peak current density of 13.5 A/cm^2 was obtained, which is higher than in the lattice-matched structure with the AlGaAs grown under the same conditions. Possibly this is a strain effect.

Nevertheless, the $\text{In}_{0.65}\text{Ga}_{0.35}\text{P} / \text{In}_{0.17}\text{Ga}_{0.83}\text{As}$ dual junction solar cell on Ge was grown with an AlGaAs tunnel junction. The barrier influences the solar cell characteristic. A low efficiency is the result. It is also discovered that using Si_3N_4 as the ARC improves the cell parameters. Working towards a double-layer ARC using a Si_3N_4 layer can be an interesting future development. The best efficiencies are recorded for the 0.25 cm^2 cells: 15.1 % with an MgF_2/ZnS coating and 18.6 % with the Si_3N_4 coating. A 4 cm^2 cell with MgF_2/ZnS coating reaches 14.6 % conversion efficiency. Adding the J - V curves of the separate subcells shows that the dual junction cell has the potential to reach a higher efficiency, if the problem with the voltage offset is solved.

5.8 References

- [1] A. Martí et al., “Limiting efficiencies for photovoltaic energy conversion in multigap systems”, *Solar Energy Materials and Solar Cells*, Vol. 43, 203-222 (1996).
- [2] M. Yamaguchi and C. Amano, “Efficiency calculations of thin-film GaAs solar cells on Si substrates”, *Journal of Applied Physics*, Vol. 58 (9), 3601-3606 (1985).
- [3] S.A. Ringel et al., “Single junction InGaP/GaAs solar cells grown on Si substrates with SiGe buffer layers”, *Progress in Photovoltaics: Research and Applications*, Vol. 10, 417-426 (2002).
- [4] J.W. Matthews and A.E. Blakeslee, “Defects in epitaxial multilayers: I. Misfit dislocations”, *Journal of Crystal Growth*, Vol. 27, 118-125 (1974).
- [5] M.R. Leys, “Metal organic vapour phase epitaxy for the growth of semiconductor structures and strained layers”, 78-85 in *Low-dimensional structures in semiconductors – From basic physics to applications*, Eds. A.R. Peaker, H.G. Grimmeiss, Plenum Press, New York (1991).
- [6] R. People and J.C. Bean, “Calculation of critical layer thickness versus lattice mismatch for $\text{Ge}_x\text{Si}_{1-x}/\text{Si}$ strained-layer heterostructures”, *Applied Physics Letters*, Vol. 47 (3), 322-324 (1985).
- [7] B.W. Dodson and P.A. Taylor, “Atomistic Monte Carlo calculation of critical layer thickness for coherently strained siliconlike structures”, *Applied Physics Letters*, Vol. 49 (11), 642-644 (1986).
- [8] M. D’Hondt, “Ontwikkeling van MOVPE-gebaseerde InGaAs/InP fotodetectoren en laserdioden voor golflengten boven $1.65\mu\text{m}$ ”, Ph.D. dissertation, Intec – Ghent University, (1998).
- [9] J. Tersoff, “Dislocations and strain relief in compositionally graded layers”, *Applied Physics Letters*, Vol. 62 (7), 693-695 (1993).
- [10] F. Dimroth et al., “MOVPE grown $\text{Ga}_{1-x}\text{In}_x\text{As}$ solar cells for GaInP/GaInAs tandem applications”, *Journal of Electronic Materials*, Vol. 29 (1), 42-46 (2000).
- [11] N. Schwarzer and F. Richter, “On the determination of film stress from substrate bending: Stoney’s formula and its limits”, <http://archiv.tu-chemnitz.de/pub/2006/0011/index.html>, (2006).
- [12] <http://www.ioffe.rssi.ru/SVA/NSM/Semicond/GaInAs/electric.html>
- [13] S.R. Kurtz et al., “Passivation of interfaces in high-efficiency photovoltaic devices”, *Materials Research Society Spring Meeting*, San Francisco, CA, (1999).
- [14] S. Sinharoy et al., “1.62eV/1.2eV InGaP/InGaAs dual junction solar cell development on lattice-mismatched GaAs”, *Proceedings of the 28th IEEE Photovoltaic Specialists Conference*, 1285-1288 (2000).

-
- [15] M.O. Patton et al., "Development of a high efficiency metamorphic triple junction 2.1eV/1.6eV/1.2eV AlGaInP/InGaAsP/InGaAs space solar cell", Proceedings of the 29th IEEE Photovoltaic Specialists Conference, 1027-1030 (2002).
- [16] F.H. Pollak, "Electronic deformation potentials of AlGaAs", 77-78 in "Properties of Gallium Arsenide", Eds. M.R. Brozel, G.E. Stillman, Short Run Press Ltd., Exeter, (1996).
- [17] V.A. Wilkinson and A.R. Adams, "Pressure effects on the energy band parameters of AlGaAs", 82-85 in "Properties of Gallium Arsenide", Eds. M.R. Brozel, G.E. Stillman, Short Run Press Ltd., Exeter, (1996).
- [18] S. Logothetidis et al., "Effect of biaxial strain on exciton transitions of Al_xGa_{1-x}As epitaxial layers on (001) GaAs substrates", Journal of Applied Physics, Vol. 66 (5), 2108-2113 (1989).
- [19] J.H. Lewis et al., "Metamorphic In_{0.53}Ga_{0.47}As/ In_{0.52}Al_{0.48}As tunnel diodes grown on GaAs", Proceedings of the IEEE 27th International Symposium on Compound Semiconductors, 143-148 (2000).
- [20] O. Kwon et al., "High performance, metamorphic In_xGa_{1-x}As tunnel diodes grown by molecular beam epitaxy", IEEE Electron Device Letters, Vol. 24 (10), 613-615 (2003).

Chapter 6

Summary and outlook

6.1 Introduction

Our society is based on energy and the demand is ever increasing. According to the “World Energy Outlook 2006” of the International Energy Agency, the global energy consumption in 2005 amounted to 15.3 TW. It is projected that this will rise with one quarter by 2015 and that we will need 22.7 TW by 2030 if the present energy source usage profile is maintained. Implementing several policy measures can reduce this number with 10 %.

At the moment we rely, for the most part, on fossil fuels to provide in our energy needs. Bearing in mind that combustion of these fossil fuels will lead to still higher concentrations of CO₂, a green house gas, in our planet’s atmosphere, alternative energy sources are mandatory to slow down (or even stop) global warming.

Renewable energy sources present the safest and most environmental friendly solution to produce electrical energy. Of all the options, solar energy has the largest potential: the practical onshore solar energy potential is 600 TW. Assuming an overall conversion efficiency of 10 %, 60 TW can be generated. If we are to realise a substantial portion of this potential, all solar cell technologies will have to co-exist. Thin-film and crystalline silicon will be dominant in areas with few hours of direct sunlight (cloudy skies) and can be integrated into buildings and on rooftops, whereas III-V concentrator technology will be dominant in areas with ample direct sunlight for utility-scale electricity production. In this work, we focus on the realisation of high-efficiency III-V solar cells.

Theoretical calculations show that the maximal conversion efficiency with a single junction is about 29 % under AM1.5G illumination and 26 % under AM0. Using

multiple junctions increases this conversion efficiency to over 40 % under AM1.5G. Under concentration even higher theoretical efficiencies are possible. The III-V material system offers the broadest selection of bandgaps for realising such high-efficiency multijunction solar cells.

Growing a defect free multijunction solar cell on one substrate requires that the used materials are lattice-matched. This monolithic approach considerably reduces the number of candidate materials that can be used and it is no longer possible to select an optimal bandgap combination. Furthermore, in a monolithic stack considerable attention has to be given to current matching of the different junctions and also to the interconnects between them, i.e. the tunnel junctions. The best results are obtained with the InGaP / GaAs / Ge triple junction solar cell. The Imec concept for this high-efficiency cell is to mechanically stack an InGaP / GaAs dual junction solar cell on top of a Ge bottom cell. In this way, the full potential of the Ge bottom cell can be used.

In recent years, one has relaxed the constraint of only using lattice-matched materials so more optimal bandgap combinations become accessible and higher efficiencies come within reach. Due to the lattice-mismatch in this metamorphic approach, adequate buffer structures are needed to prevent threading dislocations from propagating into the active layers of the device. Threading dislocations in the active layers can not be completely avoided but when their concentration is low enough ($< 5 \times 10^5$ to 10^6 cm⁻²), high efficiencies become a reality under concentrated sunlight due to saturation of the defects.

The first part of the work during this doctoral thesis consisted of the optimisation of the n-on-p single junction In_{0.01}Ga_{0.99}As solar cell and the development of an n-on-p In_{0.495}Ga_{0.505}P single junction solar cell, both lattice-matched to a germanium substrate. Then an AlGaAs tunnel junction was made to allow for the fabrication of an In_{0.495}Ga_{0.505}P / In_{0.01}Ga_{0.99}As dual junction solar cell.

The final part of the work was in making the transition to metamorphic materials. For this purpose a good buffer layer was developed. On this buffer layer the single junction In_{0.17}Ga_{0.83}As and In_{0.65}Ga_{0.35}P metamorphic solar cells were realised. The existing AlGaAs tunnel junction was used to achieve the end goal of the research, a working In_{0.65}Ga_{0.35}P / In_{0.17}Ga_{0.83}As dual junction metamorphic solar cell on Ge.

6.2 Results

Before concentrator photovoltaics became an additional incentive for III-V solar cell development, space applications were the main driving force. Due to lower radiation induced degradation in np-InGaP solar cells and due to the lower bulk resistivity of n-type material, allowing for a thinner emitter, this order has become the preferred one.

Our lattice-matched p-on-n single junction GaAs solar cells on germanium are of world class, with an efficiency of 24.5 % under AM1.5G. High n-type doping of GaAs (10^{19} cm^{-3}) has been achieved using H_2Se as a dopant source. So far, the efficiencies of our n-on-p GaAs cells, 23.9 % for the best 4 cm^2 cell, are only comparable to those pn-cells. Fill factors are good (83.4 %); V_{oc} is lower but J_{sc} is higher, both due to the lower bandgap caused by slightly more indium in those cells. However, recently, a 24.7 % efficient n-on-p cell was obtained.

Good control of InGaP and InAlP composition is demonstrated. Doping of InGaP is found to be reliable, InAlP-doping is more challenging. Contrary to InGaP, C and O impurity concentrations in InAlP are high. Growth conditions are probably very important for high quality material. A best single junction InGaP solar cell of 14.2 % conversion efficiency was achieved with a good J_{sc} (13.6 mA/cm^2), V_{oc} (1.276 V) and fill factor (82.0 %). TRPL measurements on a p-type InGaP / InAlP double heterostructure lead to an interface recombination velocity of 3420 cm/s at the base / BSF interface and an effective InGaP bulk lifetime of 4.94 ns.

Intrinsic carbon doping of GaAs and AlGaAs was studied as function of growth temperature and V/III ratio. For AlGaAs grown at 542 °C with V/III = 9.3 a doping level as high as $1.4 \times 10^{19} \text{ cm}^{-3}$ was reached. For low V/III ratios (1.7) and independent of temperature, saturation occurs around $6\text{--}7 \times 10^{19} \text{ cm}^{-3}$, even at 630 °C.

A GaAs tunnel junction was realised with Zn- and Se-doping, displaying a peak current density of 82 A/cm^2 and a peak-to-valley ratio of 1.2. With intrinsic carbon doped AlGaAs, tunnel diodes were realised with $J_p = 17.3 \text{ A/cm}^2$ and $J_p/J_V = 11.3$ for C:Al_{0.3}Ga_{0.7}As grown with V/III = 9.3 at 542 °C and between GaAs layers. When used in a solar cell-like structure, J_p was 3.9 A/cm^2 and J_p/J_V 10.0. For V/III = 1.7 at 630 °C and adjusted layer thicknesses, 92.0 A/cm^2 was achieved in this lay-out with a peak-to-valley ratio of 9.2. It should be noted that using AuZn in the front contact gives better ohmic behaviour of the tunnelling structures.

Dual junction InGaP / GaAs solar cells on germanium were fabricated using the 3.9 A/cm^2 tunnel junctions. The cells displayed good uniformity. The highest efficiency that we obtained was 24.3 % for a cell of 1 cm^2 . The 4 cm^2 cell had a conversion efficiency of 24.0 %.

For the fabrication of metamorphic cells, step and linearly graded InGaAs buffers were investigated. As evidenced from TEM images, the buffer layers are effective in bending the dislocations. Threading dislocation densities of 10^6 cm^{-2} or less are estimated. The best material quality (without annealing) is obtained on thick buffers ($\sim 2 \mu\text{m}$) and linear ones are slightly better than step graded ones. Annealing the buffer leads to more relaxation and thus better material quality can be obtained.

A linear grade was chosen for the growth of the metamorphic $\text{In}_{0.17}\text{Ga}_{0.83}\text{As}$ and $\text{In}_{0.65}\text{Ga}_{0.35}\text{P}$ single junction solar cells. The best efficiency obtained for 4 cm^2 cells on an unannealed buffer is 17.0 and 15.2 %, respectively. Looking at the device performance, annealing the buffer before growth of the solar cell has a different effect depending on the buffer type.

Using the lattice-matched AlGaAs tunnel junction in a metamorphic stack produced an extra barrier in the structure, which manifested itself in the J - V curve as a large voltage offset. The exact origin of this phenomenon remains to be determined. TEM analysis showed that relaxation occurred in the tunnel junction layers by stacking fault formation. Still, a 13.5 A/cm^2 peak current density is obtained, which is higher than in the lattice-matched structure for the same AlGaAs growth conditions. This might be a strain effect.

One $\text{In}_{0.65}\text{Ga}_{0.35}\text{P} / \text{In}_{0.17}\text{Ga}_{0.83}\text{As}$ dual junction solar cell on Ge was grown with this AlGaAs tunnel junction. The barrier influences the solar cell characteristic, resulting in a low efficiency due to a shifted maximum power point. It is also observed that using Si_3N_4 as the ARC improves cell parameters. The best efficiencies are recorded for the 0.25 cm^2 cells: 15.1 % with an MgF_2/ZnS coating and 18.6 % with the Si_3N_4 coating. A 4 cm^2 cell with MgF_2/ZnS coating reaches 14.6 % conversion efficiency.

6.3 Outlook

6.3.1 Industry outlook

With no longer only public but also political awareness of the potential impact of traditional energy sources on the (future) climate, renewable energy production is stepping more onto the foreground. Solar power has the potential to be the key element in renewable energy production if photovoltaic technologies can generate electricity at genuinely competitive rates and especially III-V concentrator photovoltaics (CPV) show great potential in getting there.

Third-generation photovoltaics in general aim at reducing costs by significantly increasing efficiencies but maintaining the economic and environmental cost advantages of thin-film deposition techniques. Increasing the cell's efficiency above the Shockley-Queisser limit (for single-bandgap devices) requires multiple energy level devices. To this end, several approaches have been proposed:

- 1) Increasing the number of energy levels in the cell
- 2) Multiple carrier pair generation per high energy photon or single carrier pair generation with multiple low energy photons
- 3) Capturing carriers before thermalisation

A well-known example of the first strategy is the multijunction solar cell. These cells consist of p-n junctions in different semiconductors placed on top of each other with the highest bandgap intercepting the light first. By choosing appropriate bandgaps and thicknesses, the incident spectrum can be absorbed in a more efficient way. The most (commercially) successful solar cell of this type is the $\text{In}_{0.495}\text{Ga}_{0.505}\text{P} / \text{In}_{0.01}\text{Ga}_{0.99}\text{As} / \text{Ge}$ triple junction cell. Further improvements can be made by allowing lattice-mismatched (metamorphic) materials in order to access more optimal bandgap combinations. Recently, solar cells of both types were demonstrated that have surpassed the 40 % efficiency milestone. An efficiency of 40.7 % [1] was measured for a metamorphic triple junction $\text{In}_{0.56}\text{Ga}_{0.44}\text{P} / \text{In}_{0.08}\text{Ga}_{0.92}\text{As} / \text{Ge}$ cell under AM1.5D at 240 suns. The lattice-matched $\text{In}_{0.495}\text{Ga}_{0.505}\text{P} / \text{In}_{0.01}\text{Ga}_{0.99}\text{As} / \text{Ge}$ triple junction cell has now reached 40.1 % [1] under AM1.5D at 135 suns. A variation on the metamorphic cell is the inverted metamorphic (IMM) structure in which the top cell is grown first and the substrate is removed (and can potentially be reused) during processing after bonding to a cheap carrier. This opens up the possibility for flexible thin-film high-efficiency III-V solar cells. With this approach, Emcore's $\text{AlInGaP} / \text{In}_{0.01}\text{Ga}_{0.99}\text{As} / \text{In}_{0.3}\text{Ga}_{0.7}\text{As}$ IMM cell operates at a record conversion efficiency of 31.9 % [2] under the AM0 space spectrum whereas NREL's $\text{In}_{0.5}\text{Ga}_{0.5}\text{P} / \text{GaAs} / \text{In}_{0.3}\text{Ga}_{0.7}\text{As}$ IMM cell operates at a record conversion efficiency of 33.8 % under the 1 sun AM1.5G spectrum and already achieves 38.9 % at 81 suns which could have been higher if the front contact grid had been optimised [3]. According to Spectrolab, multijunction cell architectures using four, five or even six junctions have the potential to increase practical terrestrial concentrator cell efficiencies to over 45 % or even to 50 %. An important consequence for concentrator cells using more than three junctions is that these cells have higher voltage and lower current, thus reducing series resistance losses. A conversion efficiency of 35.7 % at 256 suns [4] was obtained for a 4-junction $\text{AlGaInP} / \text{AlGaInAs} / \text{GaInAs} / \text{Ge}$ solar cell. At Fraunhofer ISE, a 5-junction $\text{AlGaInP} / \text{GaInP} / \text{AlGaInAs} / \text{GaInAs} / \text{Ge}$ solar cell has been demonstrated with a V_{oc} of 5.2 V [5]. They plan to introduce GaInNAs as a 6th junction between Ge and GaInAs . Due to the low current of the 6-junction cell, the intrinsic defects in GaInNAs do not limit the performance of this junction anymore. Still other researchers are investigating the $\text{InN} / \text{GaN} / \text{AlN}$ material system because these compounds are all nearly lattice-matched and they cover the entire spectrum of interest. Especially the possibility of a component cell with a bandgap of 2.4 eV or greater looks promising to achieve 50 % conversion efficiency with a multijunction cell. Recently, a V_{oc} of 2.1 V was demonstrated for a 2.5 eV $\text{In}_{0.28}\text{Ga}_{0.72}\text{N}$ solar cell [6].

The above mentioned cells are all of the monolithically 'in-series' stacked type (only two terminals for the whole stack). Another multijunction configuration is the mechanical stack, in which each subcell has two terminals. This is the path Imec has chosen: developing a triple junction cell consisting of an $\text{In}_{0.495}\text{Ga}_{0.505}\text{P} / \text{In}_{0.01}\text{Ga}_{0.99}\text{As}$ dual junction cell mechanically stacked on top of a Ge single junction cell.

The US Defense Advanced Research Projects Agency (DARPA) goes one step further. They use the advantages of having separate subcells (i.e. utilising the full potential) but integrate a lateral optical concentrator, which splits the incident solar spectrum into several bands, into the architecture, allowing a much broader choice of materials. The fact that the cells are “stacked” next to each other enables plug-and-play so that existing components can be easily swapped for improvements. Combining 93 % optical efficiency with 42.9 % sum of efficiencies the subcells (5 junctions) yields 39.9 % at a concentration of 20 suns and 50 % efficient modules are envisaged by the continued development of optics and cells [7].

Another approach consists of using a strain-balanced quantum well (SB-QW) structure. Lower bandgap material is inserted into the bulk of a (single junction) solar cell to extend the absorption window to longer wavelengths, thus increasing the generated photocurrent. The reason behind a strain-balanced structure is to prevent the introduction of dislocations since the QW material usually has a different lattice constant compared to the host material. Using this technique, an InGaP / GaAs tandem solar cell has been constructed containing an InGaAs / GaAsP SB-QW structure integrated into the bottom GaAs cell and with a conversion efficiency of 30.6 % at 54 suns [8].

The second strategy can be realised using an up- or a down-converter. An up-converter (UC) is a device that absorbs at least two below-bandgap photons and emits one above-bandgap photon. The UC is placed behind a (single junction) solar cell and therefore does not interfere with the incident spectrum on the front of the cell. Hence, even a low-efficiency UC increases the efficiency via a small current boost. A down-converter (DC) on the other hand, absorbs a photon of at least twice the bandgap and emits two photons. Because it is placed in front of the cell, the DC’s quantum efficiency needs to be greater than one. This may require the implementation of quantum dot (QD) structures since QDs are prone to impact ionisation and hence give rise to a process with $QE > 1$ more easily [9].

The third (final) strategy for increased solar cell efficiency is to collect photogenerated carriers at elevated energies (‘hot’) before they thermalise by phonon interaction in the lattice. This allows higher voltages to be achieved by the cell. Hot carrier solar cells are made of an absorber material that slows the rate of carrier cooling and allows carrier extraction from the device through selective energy contacts that accept only a very narrow range of energies. These cells are very promising but are still a long way from demonstration [9].

It is obvious that III-V concentrator cells do indeed hold the key to utility-scale electricity production. Proving the reliability of III-V concentrator cells has now become important work. Recently, an unencapsulated single junction GaAs CPV module has

been tested under concentrations up to 1000 suns. Although the module was inadvertently exposed to condensation (cover not waterproof) before the high-flux experiments started, no evidence of visible or measurable degradation was found after several high-flux exposures [10] which is a very encouraging result.

In Castilla La Mancha, Spain, ISFOC (Instituto de Sistemas Fotovoltaicos de Concentración) has started a 3MW CPV demonstration project based on III-V semiconductors to prove that CPV is a viable and reliable way to generate 'clean' electricity. Among the companies that have been selected to install CPV systems are Isofoton (Spain), Concentrix Solar (Germany), SolFocus (USA), Emcore (USA) and Arima Eco (Taiwan) [11]. Another major III-V CPV project (2 MW) is GreenVolts' "GV1" installation in Tracy, San Francisco, which will provide interesting information on CPV performance in a slightly cloudier climate [12]. Emcore (USA) has announced being awarded several production orders to supply CPV cells or complete power systems, e.g an order from Green & Gold Energy (GGE) for 3 million solar cells (worth \$24 million) for use in GGE's SunCube™ terrestrial CPV system (105 MW) [13] and for additional solar cell receiver assemblies (worth \$39 million) [14], an order for the supply of 60MW of solar power systems that are scheduled for deployment in Ontario, Canada over the next three years [15] and they have signed a memorandum of understanding with SunPeak Solar for the supply of between 200 MW and 700 MW of solar power systems that are scheduled for deployment in utility-scale solar power projects of which construction is expected to begin in early 2009 in the southwestern region of the United States [16]. Another company, Solar Systems (Australia), will demonstrate its unique, world leading design incorporating space technology in a 154 MW solar power station (worth \$420 million) in north-west Victoria, Australia, connected to the national grid using high performance solar cells [17].

Much will depend on the success of these and other projects to bring the industry closer towards large-scale commercial deployment of CPV technologies.

6.3.2 Future work at imec

First results obtained on lattice-matched dual junction and metamorphic single and dual junction solar cells are very promising. Of course, further work is needed to optimise their performance. In what follows, future steps in their development are discussed briefly.

Slight modifications to the single junction GaAs cell can be made to improve the performance of the n-on-p configuration beyond that of the p-on-n configuration. N-type InGaP / InAlP double heterostructures need to be grown to determine the effective bulk lifetime in the InGaP emitter and the recombination velocity at the emitter/window interface. Also, further investigation on the influence of growth conditions on the phosphide material quality can be useful to realise higher performances of the InGaP

single junction cell. A first defect passivation test with a hydrogen plasma showed promising results. The design of experiments can still be carried out. Concerning the dual junction cell, more attention needs to be devoted to current matching of the subcells. Also more experiments with the tunnel diodes and its cladding layers (window bottom cell and BSF top cell) can help to improve the tandem cell's performance.

For the metamorphic materials, fabricating InGaAs and InGaP n-type double heterostructures can also yield valuable information on the emitter bulk lifetime and the window/emitter interface recombination velocity. Tests can also be performed to better control the residual stress in the layers, if that is indeed possible. A closer look has to be taken at the tunnel junction required for the metamorphic dual junction cell. On the one hand the "barrier problem" needs to be resolved and on the other hand intrinsic carbon doping of $\text{In}_{0.17}\text{Al}_{0.25}\text{Ga}_{0.58}\text{As}$ will need to be studied to make the tunnel diode "strain free". An appealing option – also for lattice-matched cells – to improve cell performance might be the development of a double-layer anti-reflection coating using Si_3N_4 as one of the layers. In that way, hydrogen defect passivation may be obtained as a bonus. A final test for the metamorphic cells is to characterise them under a concentrated spectrum to get a better idea of their performance under operating conditions, i.e. to assess the quality of the cells.

This work is but the beginning towards building up the know-how of making (lattice-matched and metamorphic) multijunction III-V solar cells. The first results are promising. More experiments are needed to fine-tune the growth process and to better understand its influence on device characteristics. Some issues also need to be investigated further to find the solutions to overcome current limiting factors in the cell design.

6.4 References

- [1] R.R. King et al., “Metamorphic concentrator solar cells with over 40 % conversion efficiency”, Proceedings of the International Conference on Solar Concentrators for the Generation of Electricity or Hydrogen, to be published (2007).
- [2] M. Stan et al., “Recent advances in the performance of multijunction space solar cells”, Proceedings of the 22nd European Photovoltaic Solar Energy Conference, 101-105 (2007).
- [3] J.F. Geisz et al., “High-efficiency GaInP/GaAs/InGaAs triple junction solar cells grown inverted with a metamorphic bottom junction”, Applied Physics Letters, Vol. 91, 023502 1-3 (2007).
- [4] R.R. King et al., “New horizons in III-V multijunction terrestrial concentrator cell research”, Proceedings of the 21st European Photovoltaic Solar Energy Conference, 124-128 (2006).
- [5] M. Meusel et al., “Development and production of European III-V multijunction solar cells”, Proceedings of the 22nd European Photovoltaic Solar Energy Conference, 16-21 (2007).
- [6] O. Jani et al., “Effect of phase separation on performance of III-V nitride solar cells”, Proceedings of the 22nd European Photovoltaic Solar Energy Conference, 64-67 (2007).
- [7] A. Barnett et al., “Milestones towards 50% efficient solar cell modules”, Proceedings of the 22nd European Photovoltaic Solar Energy Conference, 95-100 (2007).
- [8] A. Ioannides et al., “Advances in strain balanced quantum well tandem solar cells”, Proceedings of the 22nd European Photovoltaic Solar Energy Conference, 221-224 (2007).
- [9] G. Conibeer, “Third-generation photovoltaics”, Materials Today, Vol. 10 (11), 42-50 (2007).
- [10] D. Faiman et al., “Outdoor tests of a 100 cm² GaAs dense array CPV module from 1× – 1000× in the Negev desert”, Proceedings of the 22nd European Photovoltaic Solar Energy Conference, 132-135 (2007).
- [11] <http://compoundsemiconductor.net/cws/article/news/31939>
- [12] <http://compoundsemiconductor.net/cws/article/news/31735>
- [13] http://www.emcore.com/news_events/release?y=2007&news=163
- [14] http://www.emcore.com/news_events/release?y=2008&news=187
- [15] http://www.emcore.com/news_events/release?y=2007&news=172
- [16] http://www.emcore.com/news_events/release?y=2008&news=180
- [17] <http://www.solarsystems.com.au/154MWVictorianProject.html>

List of publications

Journal contributions

Y. Mols, M.R. Leys, E. Simons, J. Poortmans, G. Borghs, “Study of intrinsically carbon doped AlGaAs layers for tunnel diodes in multijunction solar cells”, Journal of Crystal Growth, Vol. 298, 758-761 (2007).

J. Derluyn, K. Dessen, G. Flamand, Y. Mols, J. Poortmans, G. Borghs, I. Moerman, “Comparison of MOVPE grown GaAs solar cells using different substrates and group-V precursors”, Journal of Crystal Growth, Vol. 247, 237-244 (2003).

G. Brammertz, Y. Mols, S. Degroote, M. Leys, J. Van Steenberghe, G. Borghs, M. Caymax, “Selective epitaxial growth of GaAs on Ge by MOCVD”, Journal of Crystal Growth, Vol. 297, 204-210 (2006).

G. Brammertz, Y. Mols, S. Degroote, V. Motsnyi, M. Leys, G. Borghs, M. Caymax, “Low-temperature photoluminescence study of thin epitaxial GaAs films on Ge substrates”, Journal of Applied Physics, Vol. 99, (2006).

Conference contributions

Y. Mols, M.R. Leys, J. van der Heide, N.E. Posthuma, L. Zhao, G. Flamand, J. Poortmans and G. Borghs, “Development of metamorphic dual junction solar cells”, 22nd European Photovoltaic Solar Energy Conference and Exhibition (2007).

Y. Mols, M.R. Leys, E. Simons, J. Poortmans, G. Borghs, “Study of intrinsically carbon doped AlGaAs layers for tunnel diodes in multijunction solar cells”, 13th International Conference on Metalorganic Vapor Phase Epitaxy (MOVPE) (2006).

Y. Mols, M.R. Leys, J. Poortmans, G. Borghs, “Comparison of buffers for metamorphic In_{0.17}Ga_{0.83}As solar cells on germanium”, 11th European Workshop on Metalorganic Vapor Phase Epitaxy (MOVPE) (2005).

J. Derluyn, K. Dessen, G. Flamand, Y. Mols, J. Poortmans, G. Borghs, I. Moerman, “Comprehensive study of GaAs solar cells using different substrates and group-V precursors”, 11th International Conference on Metalorganic Vapor Phase Epitaxy (MOVPE) (2002).

G. Flamand, E. Simons, Y. Mols, J. Poortmans, “Technology development and demonstration of a one-side contacted, very thin GaAs solar cell”, 19th European Photovoltaic Solar Energy Conference and Exhibition (2004).

G. Brammertz, M. Caymax, Y. Mols, S. Degroote, M. Leys, J. Van Steenbergen, G. Winderickx, "Selective epitaxial growth of GaAs on Ge substrates with a SiO₂ pattern", 210th Meeting of the Electrochemical Society (2006).